UNIVERSITÉ DE LILLE 1 – SCIENCES ET TECHNOLOGIES

École doctorale Sciences de la Matière, du Rayonnement et de l'Énergie
Discipline : Science des matériaux

Sink efficiency calculation of dislocations in irradiated materials by phase-field modelling

Hadrien ROUCHETTE

Soutenue le 9 février 2015

Constitution du jury :

M. Emmanuel CLOUET	CEA-Saclay	Rapporteur
M. Yann LE BOUAR	CNRS/ONERA	Rapporteur
M. Antoine AMBARD	EDF-R&D	Examinateur
M. Christophe DOMAIN	EDF-R&D	Examinateur
M. Pär OLSSON	KTH-Suède	Examinateur
M. Laurent PIZZAGALLI	Université de Poitiers	Examinateur
M. Alexandre LEGRIS	Université de Lille-1	Directeur de thèse
M. Ludovic THUINET	Université de Lille-1	Encadrant de thèse

Résumé

L'objectif de ce travail est le développement d'une méthode numérique pour simuler la diffusion de défauts cristallographiques mobiles dans les métaux irradiés, ainsi que leur absorption par les puits, afin de mieux anticiper l'évolution microstructurale de ces matériaux. Un intérêt particulier a été porté au cas de l'interaction entre les défauts ponctuels et les dislocations. Les méthodes de champ de phases sont bien adaptées à ce problème, puisqu'elles peuvent tenir compte des effets élastiques des dislocations sur la diffusion de ces défauts dans les cas les plus complexes. Le modèle de champ de phases présenté dans ce travail a été adapté pour prendre en compte la création des défauts par irradiation ainsi que leur absorption par les cœurs de dislocation à l'aide d'un nouveau paramètre d'ordre associé à la morphologie du puits. La méthode a d'abord été validée dans différents cas de référence en comparant les forces de puits obtenues numériquement aux solutions analytiques disponibles dans la littérature. Elle a ensuite été appliquée aux dislocations dans le zirconium en faisant varier leur orientation, et en tenant compte des propriétés anisotropes du cristal et des défauts ponctuels, obtenus récemment par des calculs à l'échelle atomique. L'analyse des résultats démontre que l'anisotropie de forme des défauts ponctuels favorise l'absorption des lacunes par les boucles basales, ce qui est cohérent avec la croissance du zirconium sous irradiation expérimentalement observée. Enfin, l'étude rigoureuse des boucles de dislocation révèle que les simulations par champ de phases sont plus précises que les solutions analytiques dans des domaines de densités réalistes.

Summary

The aim of this work is to develop a modelling technique for diffusion of crystallographic migrating defects in irradiated metals and absorption by sinks to better predict the microstructural evolution in those materials. The phase field technique is well suited for this problem, since it naturally takes into account the elastic effects of dislocations on point defect diffusion in the most complex cases. The phase field model presented in this work has been adapted to simulate the generation of defects by irradiation and their absorption by the dislocation cores by means of a new order parameter associated to the sink morphology. The method has first been validated in different reference cases by comparing the sink strengths obtained numerically with analytical solutions available in the literature. Then, the method has been applied to dislocations with different orientations in zirconium, taking into account the anisotropic properties of the crystal and point defects, obtained by state-of-the-art atomic calculations. The results show that the shape anisotropy of the point defects promotes the vacancy absorption by basal loops, which is consistent with the experimentally observed zirconium growth under irradiation. Finally, the rigorous investigation of the dislocation loop case proves that phase field simulations give more accurate results than analytical solutions in realistic loop density ranges.

Remerciements

Je ne saurais rendre justice à ceux qui m'ont soutenu qu'en rédigeant dans ma langue maternelle.

Je tiens tout d'abord à adresser un remerciement pour les enseignants et formateurs avec qui j'ai travaillé au cours de ma scolarité. J'en profite pour remercier les contributeurs d'Openclassrooms[1] qui m'ont permis de m'autoformer en programmation, contribuant de manière inestimable à ce doctorat. J'ai une pensée pour ceux qui développent les outils libres et ouverts qui m'ont permis de mener à bien ce travail.

J'adresse mes remerciements sincères à tous les doctorants avec qui j'ai partagé le bureau 226. J'apporte mes encouragement ceux qui poursuivent leur thèse, et je les félicite par avance de leurs prochains succès. J'ai également une pensée pour les anciens occupants, en particulier Julien Boisse, pour tous nos échanges enrichissants, en particulier à propos de AWK et GNUPLOT, de l'univers du champ de phases.

Je remercie Andrée Debacker pour avoir contribué à mon intégration à l'UMET, accompagné dans la découverte des outils du laboratoire, à m'avoir fait découvrir GIT et pour sa contribution à la parallélisation du code de champ de phases.

Je remercie Christophe Domain et Antoine Ambard qui m'ont proposé ce sujet, puis pour avoir montré leur intérêt pour mon travail et pour leurs remarques gratifiantes.

Je tiens à remercier tout particulièrement Alexandre Legris et Ludovic Thuinet, qui ont toujours fait preuve d'enthousiasme à propos de mon sujet et de mon travail, pour m'avoir soutenu dans les moments difficiles, pour tout ce qu'ils m'ont appris, pour tous les conseils et les gratifications.

Je remercie mes parents et ma sœur, ainsi que le reste de ma famille, qui ont toujours été là pour moi, qui m'ont inculqué mes valeurs et qui ont fait de moi ce que je suis aujourd'hui.

Finalement, je remercie tous ceux qui, au cours de ces trois années, chacun à leur manière, ont contribué à tous les bons souvenirs que je garderai de cet épisode de ma vie.

[1] Anciennement *Site du Zéro* : http://openclassrooms.com/

Contents

Nomenclature

B_s Absorption bias of sink s

C_{ijkl} elastic constants of the homogeneous system

D_{ref} PF reference diffusion coefficient

D_i diffusion coefficient of species i

E_f PD formation energy

E_{el} elastic energy of the system

F total free energy

F_B^n Boltzmann factor of configuration n

F_{chem} chemical energy of the system

G_{ij} Green function

I_n modified Bessel function of the nth order of the first kind

J^s Average PD flux to the sink s

$J^{\mathrm{abs}}(\mathbf{r})$ local PD flux to the sink s

J^{prod} Average flux of PDs produced by a source region

J_s Average flux of point defects to the sink s

K_i^0 generation rate of the ith defect type due to irradiation

K_n modified Bessel function of the nth order of the second kind

K_{ij} Reaction rate constant between the ith and jth defect type

M Atomic mobility

N_{at} number of atoms by unit volume

P_{ij} elastic dipole tensor

R radius or width of the reservoir

S^{ext} Surface of the reservoir

T	Temperature in K
V	Volume of the domain
V_{at}	atomic volume
X^{RT}	PD site fraction that corresponds to $\bar{X}$ in the rate-theory model (see section 1.3.1)
X^s	Equilibrium PD site fraction in the sink s
X_i^s	concentration of i at the surface of the sink s
$Z_{\mathrm{vol}}^{\mathrm{sph}}$	Sink efficiency of a spherical sink, per unit volume, in units of m
Z_i^s	sink efficiency of a sink s for a PD of type i
Ω_i	relaxation volume of the defect i
$\bar{X}_i$	atomic site fraction of the ith defect type
$\boldsymbol{\nabla}$	gradient operator
ϵ_{ij}^{00}	tensor of the Vegard coefficients
ϵ_{ij}^{d0}	Stress free strain tensor of the order parameter associated with the dislocation stress field
η	Order parameter associated with the dislocation stress field
λ	Order parameter associated with the sink region, i.e. the zone where the PDs are absorbed
λ^{eff}	Local sink efficiency coefficient
$\mathbf{D}$	PD diffusion coefficient tensor in a dilute solution
μ	shear modulus
μ_{chem}	chemical potential of the PD
μ_{el}	elastic potential of the PD
ν	Poisson coefficient
ν_n	multiplicity of the SIA of type n
ρ_{vol}	Sink volumetric density, in units of m^{-3}
ρ_l	Dislocation line density, in units of m^{-2}
ρ_s	sink density of type s
$\sigma_{xy}(\mathbf{r})$	Stress field in direction x, y
θ	accelerated convergence algorithm time period, in calculation time steps

$\varepsilon_{ij}(\mathbf{r})$ total strain in the system

$\mathbf{b}$ Burgers vector

$\mathbf{n}$ Vector normal to the dislocation habit plane

ξ *ad hoc* value that sets the homothetic transformation value in the accelerated convergence algorithm

a_0 PF grid spacing

k_B Boltzmann constant

r'_0 Higher minor radius limit of the spherical or toroidal sink

r_0 sink radius

r_L Torus major radius or dislocation loop radius

t_0 PF reference time

u_i displacement field in direction i

PWSCF planewave pseudopotential code

QE Quantum Espresso

SIESTA Spanish Initiative for Electronic Simulations with Thousands of Atoms

VASP Vienna Ab Initio Package

PKA primary knock-on atom

DAD Diffusion anisotropy difference

DFT density functional theory

dpa displacement per atom

FFTW Fastest Fourier transform in the West

GB grain boundary

GGA Generalised Gradient Approximation

HVEM high velocity electron microscopy

K Kelvin

LDA Local Density Approximation

MD Molecular dynamics

MPI Message passing interface

OKMC Object Kinetic Monte Carlo

PAW Projector Augmented Wave

PBM Production Bias Model

PFRS PF model equivalent to that of Rauh and Simon

PWR pressurized light water reactor

RS Rauh and Simon

RT (Standard) Rate-theory

SAS Shape Anisotropy of SIAs

SIA self-interstitial atom

SIPA Stress Induced Preferential Absorption

TEM transmission electron microscopy

PD point defect

PF phase field

USPP Ultra Soft Pseudo Potential

Introduction

The behaviour of metals under irradiation is still not fully understood. Nuclear industry has been building and operating nuclear power plants since the 60's, and still, structural materials remain the limiting parameter in ageing, durability and safety. Much attention has been given to materials located close to the reactor core, as they are continuously submitted to neutron irradiation. It has been found out that it accelerates materials properties deterioration. As more recent project expect to build fast neutron reactors, as well as fusion reactors, which generate very high energy neutrons and fast ions, the behaviour of irradiated materials remains a key issue for future industrial development. However, the older pressurized water reactors are still a major concern. Their ageing demands expensive work in order to remain reliable, an thus, avoid being stopped. On one hand, direct effort is committed for repairing and testing, while on the other hand, studies are carried out to better understand and predict future evolution of irradiated materials. Better knowledge means better decisions.

Direct testing is expensive and time consuming. Recent computer improvement allowed to simulate larger systems, for longer time scales, and with more complex evolution rules. The new trend relies on the multiscale modelling strategy: low space and short time scale methods will produce results that can be used in higher scale methods. Iteration of this process makes it virtually possible to link atomic scale simulations with macroscopic system simulations, and evolution prediction for several decades. Research is ongoing to improve these interactions between modelling techniques. As the materials properties degradation is mainly due to the formation of microstructural defects (voids, dislocation loops), the nucleation and growth of those defects should be properly understood and evaluated prior to assess the validity of the predictions. The capacity of a given microstructural defect (called sink in the following) to absorb migrating defects will be defined as the *sink efficiency* (see section 1.3) and depends on the sink shape, density and the point defect (PD) properties.

The present work is dedicated to one method of the multiscale modelling strategy, one link of the chain: phase-field (PF) modelling. This manuscript will describe the advancement made on the modelling of various microstructural defects called sinks in metals during irradiation. To this end, chapter 1 will give a more detailed description of the various analytical and numerical methods dedicated to their study. Starting from atomic scale data, the goal is to evaluate the capacity of microstructural extended defects to absorb smaller migrating point defects, in order to predict the evolution of the microstructure. The obtained results can then be used in a larger scale model for long term prediction, but the method already

gives good advice on physical phenomena taking place in irradiated metals.

In chapter 2 will be presented a new PF method that has been developed in order to simulate the creation, diffusion and absorption by sinks of migrating PDs. The reader will be regularly referred to this part, as it gathers the details of the method, while the following chapters will be dedicated to the applications of the model.

In chapter 3, the reliability of the PF model will be tested in the case of the PD absorption by straight dislocations. The PF results will be systematically compared with some reference cases for which analytical solutions for sink efficiencies are known. The validation of the method will ensure the reliability for following chapters.

While the previous chapter is a generic study of sink efficiency calculation by PF, chapter 4 will be applied to the practical case of hexagonal zirconium. This chapter will illustrate how to use state-of-the-art atomic scale simulation results in the PF model. It will bring new insights on the evolution of this metal under irradiation.

Finally, while the two previous chapters will be focused on straight dislocations, chapter 5 will go beyond this 2D geometrically simplified case and consider dislocation loops instead. This defect is commonly observed under irradiation, and is a 3D problem in nature, which makes its modelling more difficult. As the PF model described in chapter 2 is not limited to 2D simulations, we will present results obtained in various cases: for the toroidal sink without elasticity, the dislocation loop with isotropic elasticity and apply the model to the case of dislocation loops in zirconium. The literature on loop sink efficiency calculation is still limited. As a consequence, this chapter will follow a systematic procedure, in order to study each case separately. This will allow to better understand the effect of each parameter on loop sink efficiency.

Chapter 1

Irradiated materials – Modelling techniques

Contents

The main advantage of simulation over experimentation lies in its capacity to explore space and time domains forbidden to the experimenter. For example, it is still impossible to directly study the collision cascade due to its size (few tens of cubic nanometers) and its lifetime (up to the nanosecond) [1, p. 140]. In addition, most irradiation created defects (point defects and small defect clusters) still cannot be observed by means of microscopy or atom probe tomography.

The following chapter will be dedicated to the presentation of the main features of irradiated materials (section 1.1) and the existing modelling techniques available to simulate those materials (section 1.2). In particular, we will focus on the *rate theory* model, which needs to be provided with the properties of microstructural PD sinks: the sink efficiencies. Finally, the methods to evaluate the sink efficiency of straight dislocation lines and dislocation loops available in the literature will be detailed in section 1.3.

1.1 Irradiated materials

For power plant components, nuclear industry relies mostly on metallic alloys. This choice has been made due to the knowledge of industrial metallurgy, the capacity to build large structures, and the good mechanical properties of metals. Metallic alloys present are good compromise between hardness and fracture toughness. This provides to the nuclear device a good reliability: instead of breaking, the structure is first expected to deform plastically, and generate small cracks. Those damages would lead to minor leaks that can be over-viewed by surveillance teams.

However, under irradiation by high energy neutrons (and heavy ions), the mechanical properties and dimensional stability of metals deteriorate: they get brittle and their shapes evolve, even without applied stress. These phenomena must be understood and quantified in order to predict the ageing of nuclear power plants. This section will focus on some of the causes of these detrimental effects.

1.1.1 Irradiation damage

Irradiation of a material with high energy particles creates particle-atom collisions [2]. During a collision, kinetic energy is transferred to an atom of the crystal lattice (called the *primary knock-on atom* (PKA)). The energy transferred to the PKA will be dissipated by further collisions with surrounding atoms. If the kinetic energy transfer is low, the atom will return to its original crystallographic site, and energy will be dissipated into heat. If the energy of the PKA is higher than the *displacement energy* (a few tens of eV, depending on the metal [1]), the atom may experience a *displacement* (see Fig. 1.1): the PKA will go far enough from the original site, which will now host a vacancy. In the simplest case possible, the PKA becomes a *self-interstitial atom* (SIA). As a consequence, particle collision can create a Frenkel pair, i.e. a vacancy and a self-interstitial atom far enough from each other to counterbalance their natural affinity. This type of defect generation (creation of Frenkel pairs by irradiation) is typical of *high velocity electron microscopy* (HVEM,

$\geq$ 1 MeV electrons).

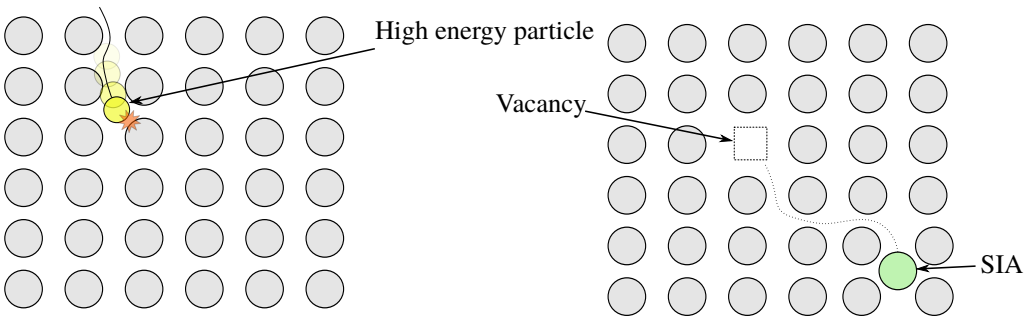

Figure 1.1: Schematics representing of the creation of a Frenkel pair (one vacancy and one SIA) by collision between a lattice atom and a high energy particle.

For heavier particles bombardment (neutrons or ions), irradiation creates a more complex phenomenon. The PKA may have a kinetic energy far higher than the displacement energy. Further collisions between the PKA and idle atoms may transfer more kinetic energy, and exceed the displacement energy limit E_d. As a consequence, other atoms may experience displacement, and even collide and displace other atoms. This complex process of energy transfer by collisions is called the *damage cascade*. In that case, more than one Frenkel pair can be created by a collision between the heavy particle and the PKA.

The dose rate for a given particle bombardment at a fixed temperature is defined as [1]:

$$R = N_{\text{at}} \int_{E_i=0}^{E_i \to \infty} \phi(E_i)\, \sigma_D(E_i)\, \mathrm{d}E_i \tag{1.1}$$

with N_{at} the number of atoms per unit volume, ϕ the flux of incident particles and σ_D the cross section of displacement. Hence, the total accumulated damage is:

$$\mathrm{dpa}(t) = N_{\text{at}} \int_0^t \int_{E_i=0}^{E_i \to \infty} \phi(E_i, t) \sigma_D(E_i)\, \mathrm{d}E_i\, \mathrm{d}t \tag{1.2}$$

This quantity defines the number of atoms that have been displaced from their original crystallographic site.

A frequently used simplified equation is given by [2]:

$$\mathrm{dpa}(t) = \frac{0.4(T - Q_{\text{el}})}{T_{d,\text{eff}}} \tag{1.3}$$

where Q_{el} is the fraction of total kinetic energy T of the PKA which goes into electronic excitation and $T_{d,\text{eff}}$ the effective displacement threshold energy, i.e. the minimum displacement energy averaged over all directions.

Recent models even consider that the damage cascade will produce directly other defects [3–6], such as *defect clusters*. These defect clusters are aggregates of either vacancies or SIAs. The aggregation of monodefects creates new objects

with properties different from those of the constitutive point defects [1]. A brief overview of those defects is given in the next section.

1.1.2 Irradiation defects

The main consequences of irradiation of metals are:

- damage generated by high-energy particle collision,
- nucleation and growth of specific crystallographic defects.

Metallic alloys owe their ductility mainly to the deformation by dislocation slip mechanism [7, 8]. The dislocation mobility is limited by the interference with crystallographic defects in the microstructure. The higher the defect density, the lower the dislocation mobility, hence, the harder the crystal. We have seen in section 1.1.1 that irradiation leads to microstructural defects creation. These defects interfere with the dislocation movement, and as such, leads to crystal hardening and embrittlement.

Here is given a non exhaustive list of some crystallographic defects due to irradiation defects aggregation:

Voids (also called *cavities* [9]) 3D aggregates of vacancies which lead to *swelling* (see Fig. 1.2), that is an isotropic dilatation of the material [10–12].

Stacking fault tetrahedra 3D vacancy-type defect that appears in fcc crystals [13]. Their origin is not clear: they may come from vacancy defects or from the splitting of Frank dislocation loops [1].

Dislocation loops 2D defects that can be of vacancy or interstitial nature. Their nucleation and growth are basically due to the aggregation of defects in the shape of a platelet laying in a dense plane [1].

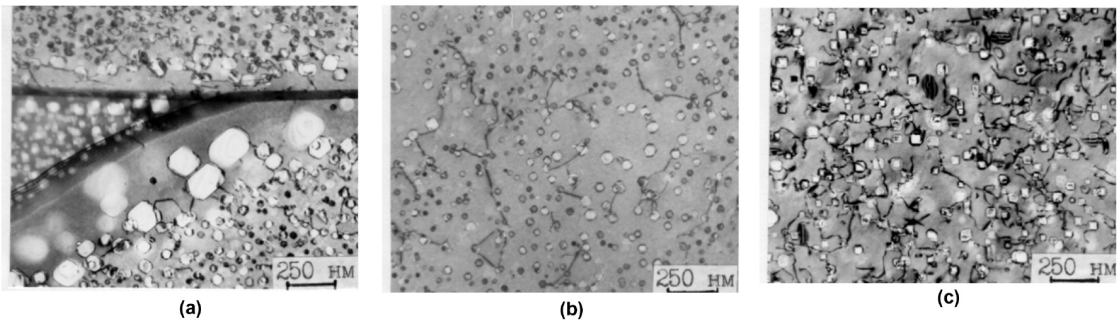

Figure 1.2: Microstructure of neutron irradiated nickel observed with transmission electron microscopy (TEM): (a) 2–3% cold worked (CW), 673 K, 9 dpa, (b) 2–3% CW, 823 K, 17 dpa, (c) 15–20% CW, 823 K, 11 dpa (From [12]). Voids appear as clear circles. Void mean diameters are 30-40 nm, densities are between 10^{19} and 10^{21} m^{-3}.

The evolution of the density and size of such defects must be properly understood in order to predict the material ageing during irradiation. As a consequence, modelling techniques constitute essential tools to understand irradiated materials.

1.2 Modelling techniques

In order to better explain the relevance of the present work, we will present the main available techniques to model irradiated materials. It should be noted that we will only give a brief overview of the advantages and limits of each method, in order to understand the role of a phase-field approach. For further explanations, the reader should refer to cited references (review by Was [1, p. 133]). A summarising diagram is given in Fig. 1.4.

1.2.1 *Ab initio*/DFT

Recent improvements in computational power and techniques allowed the scientific community to numerically solve the Schrödinger equation for system of several atoms. With reasonable assumptions, the simplification of the algorithm based on the *density functional theory* (DFT) enables to simulate hundreds of atoms [14, 15]. According to the Born-Oppenheimer approximation, the electrons are so much lighter than nuclei that they reach their ground state before the nuclei move. The problem is then described as moving electrons and fixed ions, or electrons at ground state, and slowly moving ions, depending on the time scale. Owing to the Hohenberg-Kohn theorems, the many-electrons are described in terms of electron density ρ_{el} instead of wave functions. The ground state of the electrons, i.e. the density function that corresponds to the minimum of the system energy functional, is found using a variational approach. Assuming that the exchange-correlation energy functional $E_{xc}[\rho_{el}]$ is known, it is possible to solve the Schrödinger equation. Different forms of E_{xc} exist, depending on the assumptions. The common ones are:

- the *Local Density Approximation* (LDA), that considers only the electron density function;
- the *Generalised Gradient Approximation* (GGA), that designates a family of methods which have in common the fact that E_{xc} also depends on the gradient of the electron density. It is considered to be more reliable to describe metallic crystals.

The first drawback is to require much computational power, even for small systems (few hundreds of atoms). As a consequence, only perfect crystals or small systems with high defect densities can be modelled.

The main advantage of the technique is to rely on few adjustable parameters. As a consequence, it is the most accurate method for atomic-scale property calculation. This method provides precious information for larger scale simulations: the formation energy of atomic-scale defects (SIAs, vacancies, defect clusters, etc.), shape properties of those defects [16–18], and migration properties (activation energies).

1.2.2 Binary collision approximation model (BCA)

To simulate the collision cascade that takes place in a crystal [1], the first models only consider the interaction between two colliding atoms, regardless of the environment. This approximation allows to compute the shape and size of a damage cascade with reasonable computational cost. As the mean free path of a given atom increases with its velocity, the PKA and the first collided atoms will travel along relatively long distances between two collisions. On the opposite, the late stage displaced atoms, which have lower energy, will dissipate their energy close to their initial site. As a consequence, the damage cascade does not have a spherical shape. Instead, it generally consist of a bunch of scattered high damage regions (also called *subcascades*).

Another particular feature that is taken into account in the BCA model is the *channelling*. Along certain crystallographic directions, the linear density of atoms can be relatively low. These directions allow a high energy atom to migrate for a longer distance before a collision. This phenomenon will also affect the cascade shape, by increasing the distance between subcascades.

The BCA model doesn't allow to compute further stages of the damage cascade, that is the post-collision *annealing* stage that occurs just after the high disorder stage (the *quench phase*, see Fig. 1.3). These stages need a proper simulation of the system relaxation and atomic diffusion.

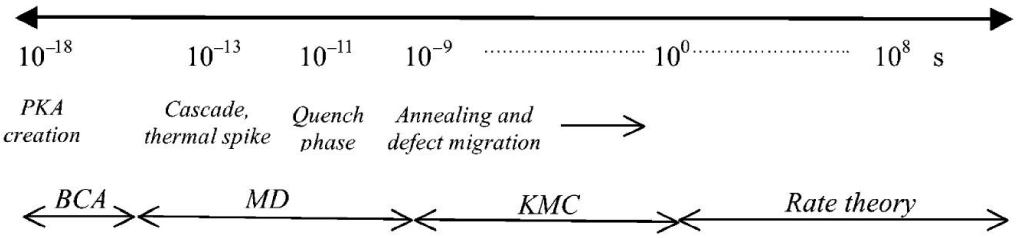

Figure 1.3: Time-scale for radiation damage evolution and corresponding simulation methodologies (from [1]).

1.2.3 Molecular dynamics (MD)

Another way of simulate the damage cascade is *molecular dynamics* that describes every atom as a mass with location and speed coordinates. The interaction between atoms are modelled by means of an phenomenological energetic potential (even if a DFT potential is sometimes used), that is fitted on various experimental and atomic-scale simulation data. The net force on each atom is computed and used in the second Newton law. Each atom acceleration is deduced, and applied on its speed vector. The incrementation of the process with short time steps ($\sim 10^{-15}$ s) allows to simulate the evolution of the system over hundreds of picoseconds.

This method naturally takes into account any movement of defects (including diffusion), considering any stress field in the system. As a consequence, the quench phase (the material self healing) can be considered. MD has been ex-

tensively used to simulate displacement cascades in various crystallographic systems [19–21]. However, the high computational cost for large systems forbids the simulation of a full cascade annealing (from a few nanoseconds up to the second, see Fig. 1.3). In that case, other techniques, such as *kinetic Monte Carlo* models can be used (see 1.2.4). In addition, the potential chosen for computing the forces on each atom has to be fitted on a given number of parameters. The computed long range effects are due to the propagation of short range interactions. It is then impossible to decorrelate the effect of stress on the system evolution. Comparative studies of various potential functions are regularly published by specialists [22].

As an atomic scale simulation method, MD can provide precious information about small defects: formation energy, shape properties, diffusion paths and migration energies. The main drawback is that these quantities are strongly dependent on the chosen interatomic potential.

1.2.4 Object Kinetic Monte Carlo (OKMC)

The *Object Kinetic Monte Carlo* derives from Monte Carlo techniques that have the common feature to use random numbers to predict the occurrence of events. It generally considers a population of objects, and physical events that can affect those objects: for example particle diffusion or phase transformation (see for example [23, 24]). The word "kinetic" indicates that (i) the time is taken into account, and (ii) the system evolves following a physical path. The main principle of the method is to compare the mean residence time between each of those events in order to deduce their probability. The occurrence of those events will be considered as a probability distribution. The mean time necessary to trigger an event is generally deduced from an Arrhenius frequency Γ_i, which depends on the activation energy of the event:

$$\Gamma_i = \nu_i \exp\left(\frac{-A_i}{k_B T}\right), \tag{1.4}$$

where A_i is the activation energy, ν_i the attempt frequency, T the temperature and k_B the Boltzmann constant. Typical events that can be taken into account for irradiated materials are the diffusion of point defects, and capture of a defect by another one. The activation energy of each one of those cases should be known. The probability of occurrence of each event can be deduced from the frequency distribution. A random event is numerically picked, the system experiences this event, and the frequency distribution of the system has to be computed again. The iteration of the technique allows to simulate the evolution of a system during several seconds. The main advantage of the technique is that an event occurs at each iteration. As a consequence, the simulated time can reach several seconds. However, it should be noted that the duration of a given iteration depends on the number of possible events, and their respective frequency. As a consequence, the computation processing time for a given simulated physical time strongly depends on the number of defects in the system: the more defects are in the system, the shorter the duration of the time step.

The OKMC technique generally doesn't take into account the influence of the stress field on the evolution of the system. In this case, the stress field is provided

as an input to the model [25–27].

1.2.5 Mean field simulation

The *reaction rate theory* [28], also called *rate theory* (RT) [1,10,29], *cluster dynamics* [30], or *radiation damage theory* (RDT) [31] models the irradiated material as a mean medium in which defects are uniformly distributed. The objective is to solve the evolution equation on defect populations, regardless of spatial considerations. The spatial part of the diffusion equation is replaced by average reaction terms between uniformly distributed defects such as:

$$\dot{\bar{X}}_i = K_i^0 - \sum_{i,j} K_{ij} \bar{X}_i \bar{X}_j, \tag{1.5}$$

where $\bar{X}_i$ is the atomic fraction of the ith defect type, K_i^0 the generation rate of the ith defect type due to irradiation and K_{ij} the reaction constant between the ith and jth defect type. The defect type can either refer to point defects, defect clusters or microstructural defects such as dislocations, grain boundaries, surfaces (also called “defect sinks” or “sinks”).

The RT problem can then be described as a system of numerous coupled equations (as many equations as defect types). The RT has proven to be useful to predict materials evolution for long term irradiation (up to tens of years) [1, 31]. The main difficulty of this non linear technique is to determine the proper reaction constants K_{ij} for relevant reactions (as well as the generation rates K_i^0). As the spatial distribution of defects is not computed by the method, the reaction rate constant K_{ij} has to incorporate the local phenomena such as diffusion, close- and long-range interactions. The model then relies on lower scale methods in order to determine those parameters.

The ability of sinks to absorb PDs is of primary importance to determine microstructure evolution, since sinks may grow during irradiation and induce structural changes like swelling, shrinkage, radiation growth or radiation induced creep. In a metallic material containing an atomic fraction $\bar{X}_i$ of defect i at steady state, the rate of absorption J_i^s by a sink of type s and density ρ_s is given by:

$$J_i^s = Z_i^s \rho_s D_i (\bar{X}_i - X_i^s), \tag{1.6}$$

with D_i the diffusion coefficient of species i, X_i^s the concentration of i at the surface of the sink (supposed in general to be equal to its thermal equilibrium value X_i^{th}) and Z_i^s the sink efficiency. The sink strength corresponds to $Z_i^s \rho_s$.

Up to now, reaction rates between defects have been calculated by analytical and numerical means. As the present work is a new technique for computing defect capture, other methods will be presented in the following.

A summarising diagram of the different modelling techniques is given in Fig. 1.4.

1.3 Sink efficiency

The mean field simulations need to be provided the proper sink efficiencies in order to predict the evolution of irradiated materials. This section is dedicated to

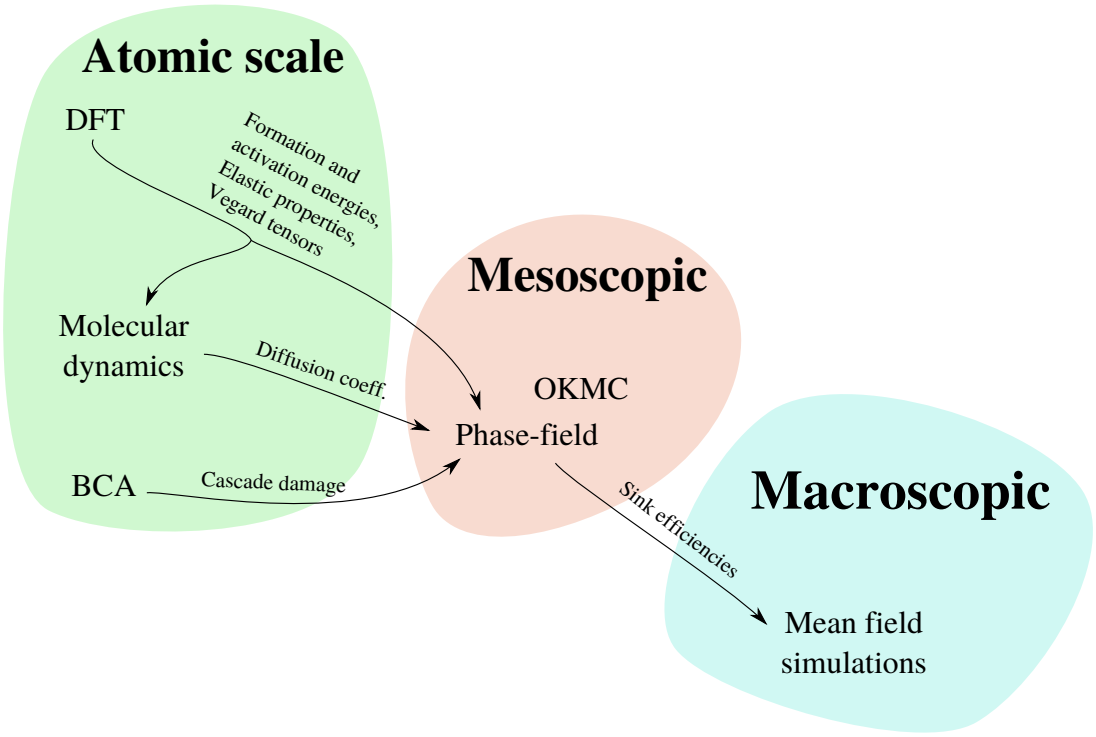

Figure 1.4: Diagram of the multiscale modelling method: the lower scale methods give results that can be used as input in higher scale techniques. As a consequence, it becomes possible for higher spatial and time scale techniques to be provided atomic properties.

the description of the sink efficiency definition and calculation techniques. This part will focus on the particular case of straight dislocation lines and dislocation loops.

1.3.1 Definition

The sink efficiency Z_i^s reflects the tendency of a sink s to absorb a migrating defect i. Different models have been proposed for sink efficiency calculation. In general, the method consists in a resolution of the diffusion equation of PDs around the considered sink using different boundary conditions. To this end, a *reservoir* (or sink-free region) is defined, i.e. a representative average volume around the sink, free of any other microstructural defect. The main parameters influencing the capture efficiency are then: (i) the geometry and volume of the sink, (ii) the geometry and volume of the reservoir, (iii) the properties of the diffusion tensor (isotropic/anisotropic) of the species and (iv) the existence or not of a diffusion drift generated for instance by an elastic stress gradient. In general, two spatial parameters are introduced, namely the sink radius or width r_0 and the radius or width of the reservoir R (typically the mean half distance between sinks) that is related to the sink density ρ_s. Assuming simple situations (isotropic diffusion and no elasticity), a compilation of Z_i^s expressions is given by Nichols [28].

Let's consider a RT model with only one type of migrating defect. The kinetic equation for the PD population $\bar{X}_i$ is:

$$\dot{\bar{X}}_i(t) = K_i^0 - \sum_s Z_i^s \rho_s D_i (\bar{X}_i(t) - X_i^s) \tag{1.7}$$

If only one sink type is considered, Eq. (1.7) becomes:

$$\dot{\bar{X}}_i(t) = K_i^0 - Z_i^s \rho_s D_i (\bar{X}_i(t) - X_i^s) \tag{1.8}$$

For $t \to \infty$, the differential equation (1.8) reaches a steady state:

$$\dot{\bar{X}}_i = 0 \;\Rightarrow\; \bar{X}_i(t \to \infty) = \frac{K_i^0}{Z_i^s \rho_s D_i} + X_i^s \tag{1.9}$$

Z_i^s must then be defined so that:

$$Z_i^s = \frac{K_i^0}{\rho_s D_i \left[\bar{X}_i(t \to \infty) - X_i^s\right]} \tag{1.10}$$

As this definition is the most rigorous one, we will see that different models have been developed in order to estimate the sink efficiency of various sink types. The following sections will be dedicated to the case of straight dislocations and dislocation loops, as those defects are almost omnipresent in irradiated metals. At this stage, it is important to emphasise that for a given sink, the choice of the boundary conditions can lead to different expressions of Z_i^s: it should be noted that the arbitrary choice of the shape of the sink and sink-free region is a limit shared by all models.

We will see that from a more general point of view, the sink efficiency Z_i^s can be defined as:

$$Z_i^s = \frac{K_i^0}{\rho_s D_i \left(X^{\mathrm{RT}} - X_i^s\right)} \tag{1.11}$$

with X^{RT} a given PD site fraction that corresponds to $\bar{X}$ in the rate-theory model, but will be used in various ways in the sink efficiency calculation methods. This quantity is necessary in order to unify the different methods that will be presented in the following sections.

1.3.2 Analytical models for straight dislocations

Analytical expressions have been proposed for sink efficiency obtained after resolution of the diffusion equation of PDs around the considered sink using different boundary conditions. To this end, a reservoir is generally defined (or sink-free region), i.e. a representative average volume around the sink and free of any other microstructural defect.

When elastic interactions are neglected, the boundary conditions can be decomposed as three main systems: Laplace's, Poisson's and Wiedersich's. At very low sink densities, the results obtained are equivalent.

1.3.2.1 Laplace model

The sink is modelled as a volume (spherical for a void, cylindrical for a straight dislocation) with fixed composition X^s at its boundaries. Generally, the concentration X^s is taken equal to the thermal equilibrium concentration. The surrounding medium (the "reservoir" or "sink-free region") has a given shape, generally the same as the sink, with a larger volume. The sink-free region volume V is chosen so that $V = 1/\rho^s$. For example, in the case of the cylindrical sink, the sink-free region is cylinder-shaped, with a radius $R = \sqrt{1/(\pi\rho_l)}$ where ρ_l is the dislocation line density (in m^{-2}). On the outer boundary of the sink-free region S^{ext}, a composition X^∞ is fixed (see Fig. 1.5):

$$\begin{aligned} X(S^s) &= X^s \\ X(S^{\mathrm{ext}}) &= X^\infty = X^{\mathrm{RT}} \end{aligned} \tag{1.12}$$

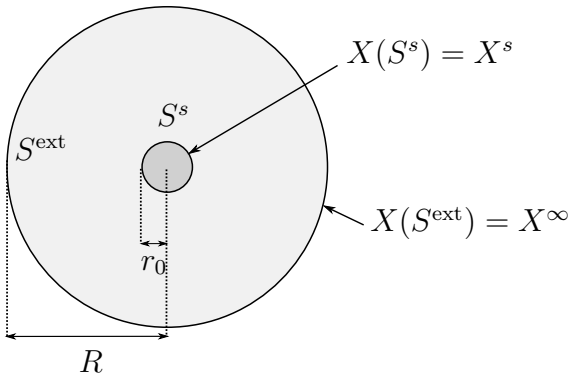

Figure 1.5: Laplace model in the case of the cylindrical sink. The system is represented as a cut normal to the cylinder axis.

The Laplace equation is solved in the volume V located between both boundaries:

$$\nabla^2 X = 0 \tag{1.13}$$

The sink efficiency Z is deduced from the total incoming flux J_s at the sink surface:

$$Z^{\mathrm{Lap}} = \frac{J_s}{\rho_s D(X^\infty - X^s)} \tag{1.14}$$

This model assumes that any defect created by irradiation is created "far from the sink", i.e. that the sink density is low. For higher sink densities, the Poisson or Wiedersich models are more realistic. Anyway, the Laplace model is the most used one, on one hand because the analytical solution is easier to obtain, on the other hand because the numerical resolution of Eq. (1.13) leads to faster convergence than for the next models.

1.3.2.2 Poisson model

The geometry of the system is the same as in the Laplace model (see section 1.3.2.1), as well as the fixed composition at the sink surface S^s. However, instead of a fixed composition at the sink-free region surface, the PD are generated by a uniform source term K^0 that simulates uniform PD creation. The system is considered isolated, as a consequence, the sink free-region surface S^{ext} is assumed to forbid any incoming PD flux (see Fig. 1.6):

$$\begin{aligned} X(S^s) &= X^s \\ \boldsymbol{\nabla} X \cdot \mathbf{S}^{\text{ext}} &= 0 \end{aligned} \tag{1.15}$$

where $\boldsymbol{\nabla}$ is the gradient operator and $\mathbf{S}^{\text{ext}}$ the vector normal to the surface S^{ext}.

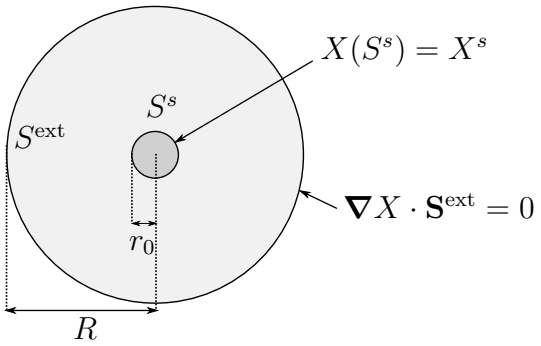

Figure 1.6: Poisson model in the case of the cylindrical sink. The system is represented as a cut normal to the cylinder axis.

The steady state solution is then:

$$\nabla^2 X = K^0 \tag{1.16}$$

The composition $X^\infty = X^{\text{RT}}$ at the outer boundary S^{ext} is deduced from Eq. (1.16) with conditions (1.15). The efficiency is calculated as:

$$Z^{\text{Pois}} = \frac{J_s}{\rho_s D(X^\infty - X^s)} \tag{1.17}$$

It should be emphasised that in this case, $J_s = K^0 V$. The value deduced from Eq. (1.16) is X^∞, while it is J_s in the Laplace model. The main limit of the Poisson model is that the deduction of X^∞ can be ambiguous apart from simple cases. If the value of X is not uniform along the surface S^{ext}, an arbitrary choice has to be made. The Wiedersich formulation will avoid this problem, while keeping realistic irradiation conditions.

1.3.2.3 Wiedersich model

The Wiedersich model considers the system geometry and boundary conditions as the Poisson system (see Fig. 1.6 and Eq. (1.16)). The difference with the Poisson model lies in the sink efficiency definition:

$$Z^{\mathrm{W}} = \frac{J_s}{\rho_s D(\bar{X} - X^s)}, \tag{1.18}$$

where $\bar{X} = X^{\mathrm{RT}}$ is the average composition in the sink-free volume:

$$\bar{X} = \frac{1}{V}\int_V X \,\mathrm{d}V \tag{1.19}$$

This model is more demanding than the previous ones, as it is needed to spatially solve Eq. (1.16) and integrate Eq. (1.19). Like the previous models, the analytical solution of those equations can only be derived for simple cases. Nevertheless, in comparison with the previous methods, this model is considered to be the most realistic one [28].

1.3.2.4 Summary

The sink efficiencies calculated by Laplace, Poisson and Wiedersich models have been respectively noted Z^{Lap}, Z^{Pois} and Z^{W}. Their expressions as well as the main assumptions of the models are summarized in Table 1.1. The equivalent table is given for the spherical sink centred in a spherical reservoir (Tab. 1.2). The sink efficiency of the spherical sink $Z^{\mathrm{sph}}_{\mathrm{vol}}$ is in the dimension of a length. When $R \to \infty$, the sink efficiency corresponds to the *asymptotic Laplace solution*:

$$Z^{\mathrm{Lap\ asymp}}_{\mathrm{vol}} \simeq 4\pi r_0 \tag{1.20}$$

1.3.2.5 Model of Rauh and Simon

As the elastic drift is thought to be one of the driving forces for swelling in irradiated face-centred-cubic crystals [10, 29], the elastic interaction between the dislocation line and the point defect has been taken into account by several authors (Margvelashvili et al. [32], Rauh et al. [33], Ham [34], Wolfer et al. [35]).

In Rauh and Simon model, the dislocation is an infinite cylindrical sink with radius r_0 centred in a cylindrical sink-free region with radius R (see Fig. 1.7). The diffusion of point defects is affected by the stress field of the edge dislocation whose core coincides with the central axis of the cylindrical sink. Their work is focused on isotropic elastic properties (both for the crystal and PD shape). This means that the PDs are considered as dilatation centres that generate an isotropic strain around them. Like in the Laplace model, $K_0 = 0$ and irradiation is taken into account by imposing the suitable Dirichlet conditions at the domain boundaries:

$$X(R, \theta) = X(R) \tag{1.21}$$

The composition at the boundary of the reservoir is set at a fixed value $X(R)$ independent from θ, this hypothesis being valid provided that R is high enough.

The boundary condition at the dislocation core $r = r_0$ is:

$$X^s(r = r_0) = X^{\mathrm{th}} \exp\left[-\frac{\mu^{\mathrm{iso*}}_{\mathrm{el}}(r = r_0)}{k_B T}\right], \tag{1.22}$$

where X^{th} is the thermal equilibrium concentration of defect in the matrix in the absence of elasticity, k_B the Boltzmann constant, T the temperature in Kelvin and $\mu^{\mathrm{iso*}}_{\mathrm{el}}$ the local elastic potential. For an elastically isotropic crystal with an

Table 1.1: Description of the different analytical models with their boundary conditions (BC), sink efficiency Z and flux expression J^s for the straight dislocation without elasticity. r_0 is the cylindrical sink radius, R the cylindrical reservoir radius and $f_d = (r_0/R)^2$.

	Laplace	Poisson	Wiedersich
Equation	$D\nabla^2 X = 0$	$D\nabla^2 X + K_0 = 0$	$D\nabla^2 X + K_0 = 0$
BC	$X(r_0) = X^{th}$	$X(r_0) = X^{th}$	$X(r_0) = X^{th}$
	$X(R) = X^{th} + \frac{K_0 R^2 \ln(R/r_0)}{2D}$	$\frac{\partial X}{\partial r}(R) = 0$	$\frac{\partial X}{\partial r}(R) = 0$
Z	$\frac{2\pi}{\ln(f_d^{-1/2})}$	$\frac{2\pi}{\ln(f_d^{-1/2}) + \frac{1}{2}(f_d - 1)}$	$\frac{2\pi(1-f_d)}{\ln(f_d^{-1/2}) - \frac{3}{4} + \frac{1}{4} f_d (4 - f_d)}$
J^s	$Z^{\mathrm{Lap}} D \rho_l (X(R) - X^{th})$	$Z^{\mathrm{Pois}} D \rho_l (X(R) - X^{th})$	$Z^{\mathrm{W}} D \rho_l (\bar{X} - X^{th})$
X^{RT}	$X(R)$	$X(R)$	$\bar{X}$

Table 1.2: Description of the different analytical models with their boundary conditions (BC), sink efficiency Z_{vol} and flux expression J^s for the spherical sink without elasticity. r_0 is the sphere radius and $f_d = (r_0/R)^2$.

	Laplace	Poisson	Wiedersich
Equation	$D\nabla^2 X = 0$	$D\nabla^2 X + K_0 = 0$	$D\nabla^2 X + K_0 = 0$
BC	$X(r_0) = X^{th}$	$X(r_0) = X^{th}$	$X(r_0) = X^{th}$
	$X(R) = X^{th} + \frac{K_0 R^2 \ln(R/r_0)}{2D}$	$\frac{\partial X}{\partial r}(R) = 0$	$\frac{\partial X}{\partial r}(R) = 0$
$Z_{\mathrm{vol}}^{\mathrm{sph}}$	$4\pi r_0 \frac{R}{R - r_0}$	$4\pi r_0 \frac{R}{R - r_0}$	$4\pi r_0 \frac{1 - f_d^{3/2}}{1 - 1.8 f_d^{1/2} + f_d^{3/2} - 0.2 f_d^3}$
J^s_{sph}	$Z_{\mathrm{vol}}^{\mathrm{sph}} D \rho_s (X(R) - X^{th})$	$Z_{\mathrm{vol}}^{\mathrm{sph}} D \rho_s (X(R) - X^{th})$	$Z_{\mathrm{vol}}^{\mathrm{sph}} D \rho_s (\bar{X} - X^{th})$
X^{RT}	$X(R)$	$X(R)$	$\bar{X}$

isotropic Vegard tensor (pure dilatation centres), the reduced elastic potential $\mu_{\mathrm{el}}^{\mathrm{iso}*}(r,\theta)$ (see Fig. 1.7 for the meaning of θ relative to the edge dislocation orientation) can be expressed as:

$$\mu_{\mathrm{el}}^{\mathrm{iso}*}(\mathbf{r}) = \mu_{\mathrm{el}}^{\mathrm{iso}*}(r,\theta) = \frac{\mu b(1+\nu)\Omega}{3\pi(1-\nu)k_B T}\,\frac{\sin\theta}{r}, \tag{1.23}$$

where μ is the shear modulus, ν the Poisson coefficient, Ω the relaxation volume of the defect, T the temperature and k_B the Boltzmann constant.

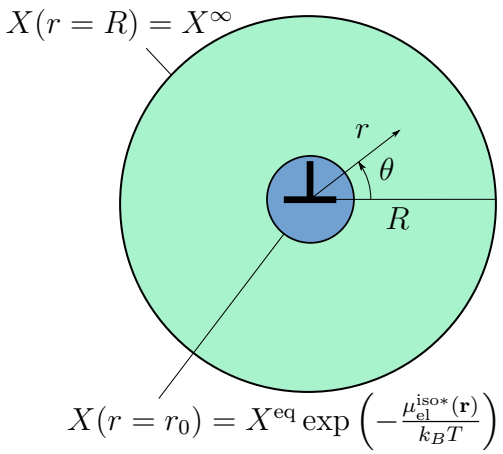

Figure 1.7: Schematics of the Rauh and Simon model for the straight dislocation. The system is represented as a cut normal to the cylinder axis. The diffusion equation (1.24) is solved in the green region.

An elastic drift term is added to the Fick diffusion equation. For the case of purely edge dislocation, the equation describing the steady state can be written as:

$$\nabla^2 X + \boldsymbol{\nabla}\left[X\cdot\boldsymbol{\nabla}\mu_{\mathrm{el}}^{\mathrm{iso}*}\right] = 0 \tag{1.24}$$

As the elastic potential depends on the angle θ, this problem is now a true 2D problem, while the previous cases without elasticity were solved in 1D, as only one space dimension was relevant. As a consequence, the solution is much harder to obtain. Under these conditions and the supplementary assumption that $\bar{X} \gg X^{th}$, the PD flux at the sink per unit volume can be written as:

$$J^s = Z_{\mathrm{el}}^{RS}\rho_l D(X^{\infty} - X^s) \tag{1.25}$$

where

$$Z_{\mathrm{el}}^{RS} = z_0(R) + 2\sum_{n=1}^{\infty}(-1)^n z_n(R) \tag{1.26}$$

and

$$z_n(R) = \frac{2\pi I_n(\frac{L}{2r_0})I_n(\frac{L}{2R})}{I_n(\frac{L}{2r_0})K_n(\frac{L}{2R}) - I_n(\frac{L}{2R})K_n(\frac{L}{2r_0})} \tag{1.27}$$

where I_n and K_n are the modified Bessel functions of the nth order of the first and second kind, respectively.

This model takes into account the effect of elastic interactions on the sink efficiency. However, it is limited to the case of the straight edge dislocation in a fully isotropic crystal. In most cases, this result will not reflect the complexity of anisotropic crystal and the properties of dislocations (screw or mixed character, dislocation loops).

1.3.3 Numerical techniques for straight dislocations

Recently, the sink efficiency calculations called for new needs:

- less symmetrical topologies must be explored (dislocation loops),
- the anisotropies of the properties should be handled more easily (elastic properties, diffusion coefficients, etc.),
- a drift term (elastic, electric) should be taken into account.

The sink efficiencies of more complex systems must be evaluated by numerical means, when the analytical solutions cannot be found. Different modelling techniques have been developed:

- solving the diffusion equation with the Laplace, Poisson or Wiedersich conditions, for various sink geometries, or
- calculating the mean capture time of a given migrating defect by atomic scale techniques, in particular OKMC.

1.3.3.1 Numerical solution of the continuous diffusion equation

This method relies on the solution of the Fick diffusion equation with a proper set of boundary conditions (see Sec. 1.3.2).

In most works, the solution is found with the boundary conditions of Laplace (fixed concentration away from the sink, sink efficiency deduced from the flux, see section 1.3.2.1) [25,36,37]. This method has been used to take the elastic effects into account by solving the elastodiffusion equation (1.24) in a given geometry (for the case of the dislocation, see Fig. 1.7). Analytical works relied on the assumptions that the crystal properties were isotropic and the point defect could be modelled as a dilatation centre. More recent works considered the influence of anisotropy of the crystal and of the point defect shape in its equilibrium (Chang et al. [25]) and saddle point configuration on sink efficiency (Tomé et al. [38], Skinner et al. [39], Seif et al. [40], Smetniansky–De Grande et al. [41]).

Chang et al. [25] present a generic technique to calculate the sink efficiency of straight dislocations: the dislocation-point defect interaction energy is computed by molecular statics (see section 1.2.3) with empirical potential in an fcc

copper lattice. This approach allows to consider anisotropic elastic properties of fcc-copper and the shape of the PDs The elastic field was used in order to compute the PDs diffusion using Eq. (1.24), solved with *finite elements method* (FEM). Calculation with molecular statics allowed to take into account the splitting of the dislocation core as partial dislocations. Chang et al. studied the effect of the shape of the core and the reservoir on the bias (see Fig. 1.8). They show that the sink efficiencies of dislocations are underestimated by analytical solutions (see sec. 1.3.2.5). Nevertheless, they considered only Laplace boundary conditions (fixed composition at the reservoir and sink boundaries) for their calculations, and the technique has never been applied to dislocation loops. In addition, their method needs to be provided with the elastic potential field of PDs prior to the sink efficiency calculation. To our knowledge, Tomé et al. [38] constitutes the only team that used the Wiedersich conditions (uniform irradiation, sink efficiency deduced from average concentration, see Sec. 1.3.2.3), which are the most realistic ones.

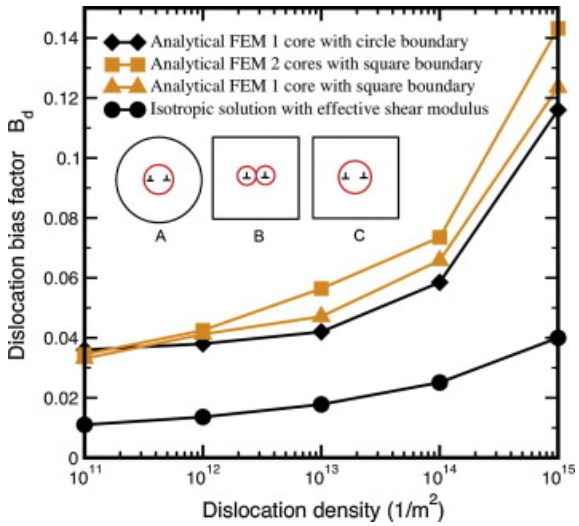

Figure 1.8: Analytical solution of B_d at 873 K as a function on dislocation density considering different geometries and methods. Illustration of different boundaries are shown in inner figures (from [25]). (A) One core with circle boundary; (B) two cores with square boundary; and (C) one core with square boundary. Red circles represent the inner core, black circle and squares represent the outer boundaries.

1.3.3.2 Kinetic Monte Carlo method

Another method has been developed in parallel with the previous ones. The main idea is to simulate the behaviour of one independent migrating defect in a medium, with external periodic boundary conditions. The defect is generated and migrates in a box with fixed dimensions and properties. This migrating defect can be absorbed by one or more sinks. The sink region is freely defined, as well as the diffusion properties of the migrating defect. The result of each simulation is the "time of survival" between creation and absorption of the defect. This time is proportional to the number of jumps needed to reach a sink. A large number

of such simulations are performed to obtain the mean survival time of a given migrating defect in the microstructure.

$$k^2 = Z\rho_s = \frac{2n}{d_j^2 \langle n_j \rangle} \tag{1.28}$$

where $\langle n_j \rangle$ is the average number of steps performed by the defect before being annihilated at the sink, n is the dimensionality of the motion (1D, 2D or 3D) and d_j is the jump distance. The sink efficiency is inversely proportional to the survival time: the higher the survival time, the lower the sink efficiency.

OKMC method has proved to be efficient for the calculation of sink efficiencies (see Sec. 1.2.4). It has been applied on the case of spherical [23], cylindrical [26] and toroidal sinks [24, 42], with isotropic or anisotropic diffusion properties.

The model is almost equivalent to the continuous diffusion equation with Wiedersich conditions (see Sec. 1.3.3.1). The main difference between the continuous and OKMC methods is that while the first one describes the problem in the eulerian way (spatially averaged fluxes), the second one is its lagrangian equivalent (the step-by-step tracking of one isolated defect).

The elastic drift effect on diffusion could be considered by the OKMC technique [27], by extending the work of [25, 26, 36, 40, 43–45] to 3D geometries, but in those conditions, elasic interactions would need to be provided with the elastic potential field of the PD around the dislocation loop as the dislocation stress field will affect the jump orientation probability of defects. In those conditions, the model would need to be provided with the elastic potential field of the PD around the dislocation loop, obtained from preliminary analytical or numerical calculations. In general, calculations are performed using an atomic scale interatomic potential (see section 1.3.3.1). The use of the molecular statics to map the elastic potential field at the equilibrium configuration is improved to also take into account the elastic potential of the saddle-point configuration. In this case, the jump direction probability will be affected by the stress field and the saddle point configuration shape.

1.3.4 Sink efficiency of dislocation loops

The case of perfect straight dislocations has been the subject of extensive studies for more than 50 years. While dislocation loops are commonly observed defects in irradiated metals, their migrating defect sink efficiencies have been much less studied than the case of straight dislocations, due to their 3D nature. In order to better understand the microstructure evolution of irradiated metals, dislocation loops should benefit of the same efforts as those dedicated to straight dislocation lines. Most of the studies previously mentioned (see Sec. 1.3.2 and 1.3.3) are limited to the case of pure straight dislocations. Indeed, unlike straight dislocations, dislocation loops cannot be simulated in a 2D calculation domain. As a consequence, the calculation of migrating defect flux to a toroidal sink, even without elasticity, is much more challenging.

1.3.4.1 Analytical model for dislocation loops

The dislocation loop is approximated as a toroidal sink, with minor radius r_0 and major radius r_L. In this case, elastic effects are neglected. The loop is consid-

ered isolated in an infinite medium. Nichols [28] gives an expression of the sink efficiency of such a sink:

$$Z_{\mathrm{vol}}^{\mathrm{Ni}}(r_0, r_L) = \frac{4\pi^2 \left({r_L}^2 - {r_0}^2\right)^{\frac{1}{2}}}{\ln(8r_L/r_0)} \tag{1.29}$$

This equation is supposed to be a good approximation if $r_L \gtrsim 3r_0$ and $r_L \ll R = [3/(4\pi\rho_L)]^{1/3}$ with ρ_{vol} the loop density. As the solution is derived considering that the loop radius is very small in comparison with the volume from which the sink drains defects, the expression is valid only for very low loop densities. One can see that Eq. (1.29) is undefined if $r_L < r_0$ (see also Fig. 1.9). In order to solve this problem, Seeger et al. [46] give another expression for Z which they claim to be more accurate than Eq. (1.29) for $r_L \simeq r_0$:

$$Z_{\mathrm{vol}}(r_0, r_L) = \frac{4\pi^2 r_L}{\ln(8r_L/r_0)} \tag{1.30}$$

With this solution, Z tends to take infinite values for $8r_L/r_0 \to 1$. Such a system is closer to the sphere than the open torus. In spite of this limitation, the solution remains relevant.

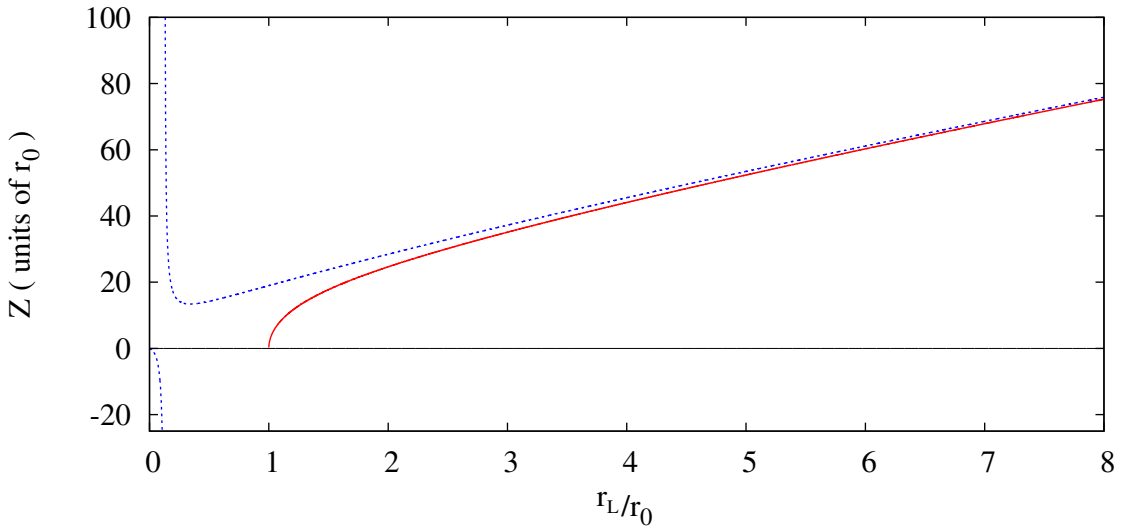

Figure 1.9: Analytical solutions for the toroidal sink as a function of r_L/r_0. Plot of Eq. (1.29) (solid line) and Eq. (1.30) (dashed line). One can see the limits of those solutions for low r_L/r_0 values. Eq. (1.29) is undefined if $r_L < r_0$ while Eq. (1.30) tends to take infinite values for $8r_L/r_0 \to 1$ and negative values for $8r_L/r_0 < 1$.

Finally, it should be emphasised that, unlike straight dislocations, the sink efficiencies proposed here are independent on the loop density ρ_L, i.e. the number of loops per unit volume. This fact should be put to the test in the present work by considering experimentally observed loop densities.

Like in the case of the straight dislocation, the dislocation loop stress field may have a strong influence on the PD diffusion and absorption. While the stress

field generated by an isolated straight dislocation can be analytically derived for some specific cases [7], the dislocation loop case remains a tricky issue. In most analytical works, a solution to this problem is proposed under the assumption that the loop is elastically equivalent to a spherical inclusion [47, 48].

1.3.4.2 Numerical models for dislocation loops

The shape of the dislocation loop induces various difficulties: (i) the diffusion problem cannot be solved in 2D (as for the case of straight dislocation), (ii) the stress field of a circular loop is not as available as for the straight dislocation.

Continuous models As the analytical solution for toroidal geometries are hard to obtain, numerical techniques seem to be the best way to study the case of dislocation loops. Dubinko et al. proposed a model of loop as a toroidal sink embedded in a toroidal reservoir with fixed concentrations at its boundaries (Laplace model) [37]. This model takes into account the elastic stress field of the loop on the diffusion of PDs. The diffusion equation is solved in the fully isotropic properties case (diffusion and elastic properties). In particular, it is shown that the choice of the sink-free volume shape can strongly affect the calculated sink efficiencies. In addition, they proposed a mechanism that allows the coexistence of both interstitial and vacancy loops in hcp crystals. Nevertheless, the application of the technique demands to know the elastic energy of a given point defect in any location around the dislocation loop. This illustrates the interest of considering numerical methods with no topological constraints.

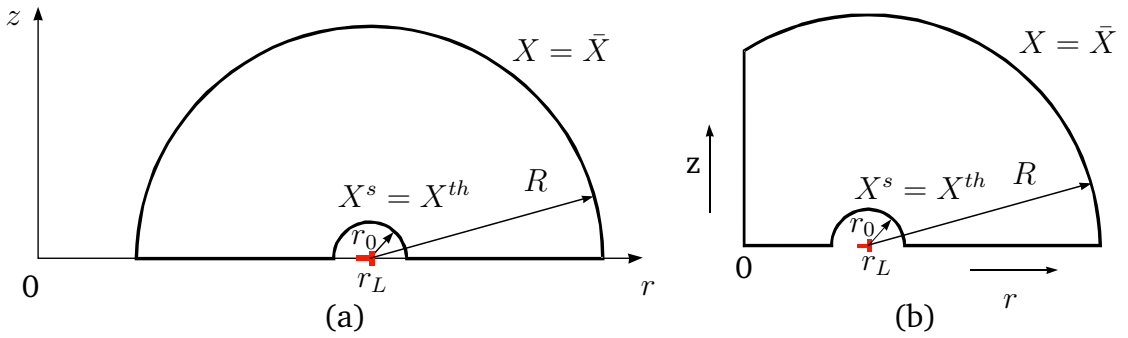

Figure 1.10: Disposition of the coordinate system used for the toroidal reservoir: (a) $r_L > R_{\text{ext}}$, (b) $r_L < R_{\text{ext}}$ (from [37]).

In this system, the following equation is solved:

$$\frac{\partial X}{\partial t} = D\Delta X + \frac{D}{k_B T}\boldsymbol{\nabla} E \cdot \boldsymbol{\nabla} X + \frac{D}{k_B T} X \Delta E, \tag{1.31}$$

where D is the diffusion coefficient and $E(\mathbf{r})$ is the interaction energy of the point defect with the stress field. For the dislocation loop, the elastic interaction energy is then approximated as:

$$E^{\mathrm{el}}(r,z) = -\frac{\mu b(1+\nu)\Omega}{3\pi(1-\nu)}\frac{1}{\sqrt{(r+r_L)^2+z^2}} \times \left(\frac{r_L^2-r^2-z^2}{(r_L-r)^2+z^2}E_e(k)+K_e(k)\right), \tag{1.32}$$

where $E_e(k)$ and $K_e(k)$ are the complete elliptic integrals of the first and second kind, respectively. r and z are respectively the cylindrical coordinates in the habit plane of the loop and normal to this plane (see Fig. 1.10). The origin is located in the centre of the torus. The parameter k is defined by:

$$k(r,z) = \frac{4r\,r_L}{(r+r_L)^2+z^2} \tag{1.33}$$

The elastic potential (Eq. (1.32)) is considered in equation (1.31).

Dubinko showed that the shape of the sink-free region can strongly affect the computed sink efficiency (see Fig. 1.11). Further numerical methods should be designed to avoid this limitation.

The limits of the model are: (i) all the properties are considered isotropic, (ii) the Laplace boundary conditions are used, (iii) the reservoir shape is an arbitrary choice and (iv) the model has to be provided the stress field of the dislocation loop. In this case, the stress field can be analytically obtained, but one can see that (1.32) is already very complex. As a consequence, this approach cannot be generalised to elastically anisotropic systems, for which an analytical solution is not necessarily available.

Discrete methods OKMC techniques have also been used with success for both isotropic and anisotropic diffusion [24, 42], but only in cases without elasticity. This model has the advantage of recreating the boundary conditions close to those of Wiedersich (more realistic volumetric defect generation). The results are compared with analytical solution (1.30) and show acceptable agreement for low loop density and high loop radius r_L.

In order to take elasticity into account, the OKMC model would need the stress field of the dislocation loop as an input data. As a consequence, the previous calculation of the stress field in complex cases remain a limitation on this model as well.

As explained in section 1.3.3.2, OKMC models need to be provided with the elastic potential of each PD in the microstructure.

1.3.5 Absorption bias

Earlier works on the swelling of fcc crystals assumed that the nucleation of voids were due to the aggregation of supersaturated vacancies into voids [10, 29, 35]. The voids can persist only if the *net flux* of SIA to voids is negative (that is, if voids absorb more vacancies than SIAs). The net flux is the difference between the SIA and vacancy flux. A microstructural defect receiving a balanced input flux of both SIAs and vacancies will get a zero net flux. As a consequence, the defect size would not evolve or even exist. It means that a vacancy-type defect must receive

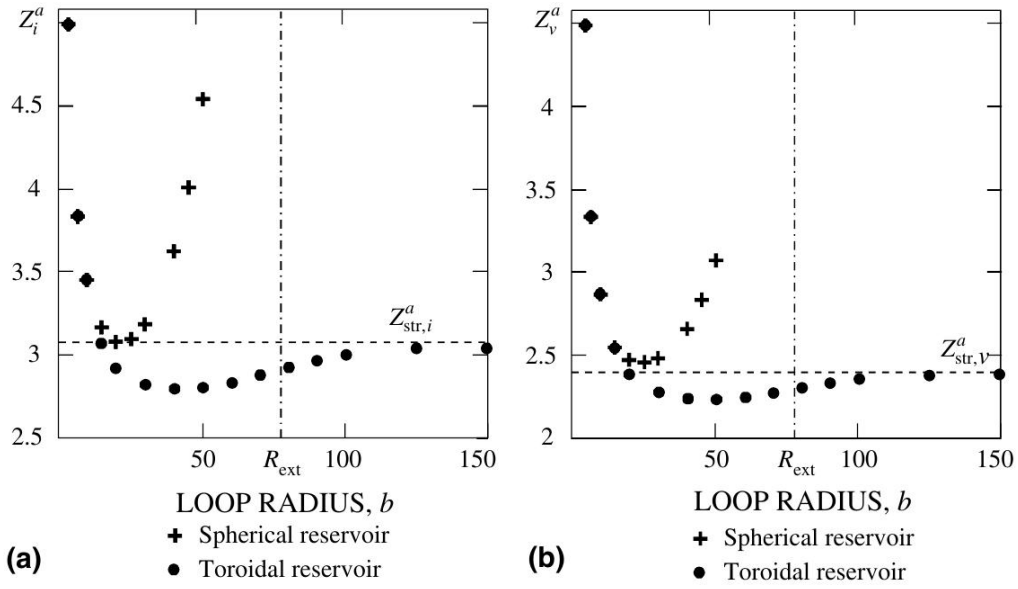

Figure 1.11: Interstitial and vacancy absorption efficiency, Z_i (a) and Z_v (b) as a function of the loop radius for toroidal and spherical reservoir, calculated for $R = 78b$ (with b the Burgers vector norm). Dashed lines represent absorption efficiencies of straight dislocation, according to Eq. (1.26). From [37] (detailed input data given in the article). Although in this case, the spherical and toroidal reservoir do not have the same volume, both solutions are equivalent at low dislocation loop radius, they display a significant difference for radii above a few tens of b. It should even be emphasised that in the case of the spherical reservoir, the sink efficiency tends to the infinite for a loop radius r_L close to the radius of the spherical reservoir R_{ext}. This is due to the fact that in this case, the minimal distance between the toroidal sink and the spherical reservoir boundary tends to zero.

a negative net flux of SIAs in order exist in a material, if it was not present prior to irradiation. The sink bias B_s in a system with only monovacancies and SIAs is defined as:

$$B_s = \frac{Z_i^s - Z_v^s}{Z_i^s} = 1 - \frac{Z_v^s}{Z_i^s} \tag{1.34}$$

where Z_v^s and Z_i^s are the sink efficiencies of sink s for vacancies and SIAs, respectively. A sink with a positive bias will have a tendency to absorb more SIAs than vacancies.

1.3.5.1 Elastic dislocation bias model

According to the *dislocation bias theory* [10, 32, 35, 37], the supersaturation of vacancies is due to the higher flux of SIAs to the dislocations, that leads to a lower SIA concentration in the matrix. The origin of the stronger affinity of SIAs for dislocations could be explained by the higher absolute relaxation volume of the SIA than the vacancy. As a consequence, the elastic attraction of SIAs to the dislocation is stronger than that of the vacancy. The SIAs absorbed by dislocations do not

annihilate with vacancies anymore. The fraction of vacancies left behind have the opportunity to aggregate and form voids, while SIAs would form interstitial dislocation loops that will cause dislocation slip obstruction. This mechanism would then cause swelling and embrittlement. Experimental works give indications that the model gives the right predictions, at least for high and moderate dislocation densities [29].

1.3.5.2 Diffusion anisotropy difference

Woo and Goesele [49, 50] assumed than another cause of preferential absorption of SIAs by certain sinks is due to the diffusion anisotropy of PDs. The model was developed to explain the growth of hcp crystals, and was based on the following assumptions:

- the SIAs diffuse faster in directions parallel to the basal plane rather than perpendicular to it,
- the vacancies diffuse isotropically in the crystal,
- the dislocations are the main sink, and are considered straight,
- the dislocations lines have no preferential orientation.

With the previous assumptions, vacancies are equally absorbed by any dislocation line in the crystal. As a consequence, the vacancy flux is the same for any dislocation orientation. On the opposite, Woo et al. showed that SIAs are more prone to be absorbed by dislocations normal to the basal plane, rather than by dislocations parallel to it. In fact, dislocations contained in the basal plane are parallel to one of the fast diffusion directions. It gives a lower probability for those dislocations to intercept a SIA along its diffusion path (see Fig. 1.13). Dislocation normal to the basal plane can absorb SIAs with no off-plane jumps. Those dislocations will receive a higher SIA flux than the others. As the vacancy flux is independent of the dislocation orientation, dislocations normal to the basal plane will receive a positive net flux (of SIAs), while dislocations parallel to the basal plane will receive a negative net flux. As a consequence, the diffusion anisotropy can be a cause of an absorption bias for sinks with a particular geometry (in the previous case, linear dislocations).

If we consider a straight dislocation oriented along the z axis in a cartesian basis, the PD flux absorbed by the dislocation, as a function of D_x and D_y the diffusion coefficients of the PD in x and y direction respectively, is given as:

$$I^{\mathrm{Woo}} = \bar{D} X(r=R) \frac{2\pi}{\ln\left[\frac{R}{r_0} f\left(\frac{D_x}{D_y}\right)\right]} \tag{1.35}$$

with $\bar{D} = \sqrt{D_x D_y}$, and:

$$f(\omega) = \left(\frac{\omega^{1/2} + \omega^{-1/2}}{2}\right)^{-1/2} \left(\frac{\omega^{1/4} + \omega^{-1/4}}{2}\right)^{-1} \tag{1.36}$$

The sink efficiency Z is deduced:

$$Z^{\mathrm{Woo}} = \frac{2\pi}{\ln\left[\frac{R}{r_0} f\left(\frac{D_x}{D_y}\right)\right]} \tag{1.37}$$

In this paragraph, we consider that angle ϕ is the rotation angle of the axis $\langle c \rangle$ around x, i.e. the angle between the dislocation line orientation $\mathbf{l} = \mathbf{z}$ and $\mathbf{c}$ (see Fig. 1.12). Hence, $D_x = D_a$ and $D_y = D_a \cos^2\phi + D_c \sin^2\phi$, where D_a is the diffusion coefficient of SIAs parallel to the basal plane, and D_c perpendicular to it. If the vacancy has isotropic diffusion and the SIA diffuses faster in the basal plane, then $Z_v(\phi) = Z_v = Z_{\mathrm{Lap}}$ and $Z_i(\phi)$ is given by Eq. (1.37). From Eq. (1.37), we have $Z_i(\phi_1) < Z_i(\phi_2) \leqslant Z_i(\phi = 0) = Z_v$ if $\phi_2 < \phi_1 \leqslant 90°$. In other words, the bias will be higher for dislocations with a low angle with the $\langle c \rangle$ axis. According to the authors, expressions (1.37) and (1.34) are valid if $0.1 < D_a/D_c < 10$ and the dislocation density is low (Laplace conditions).

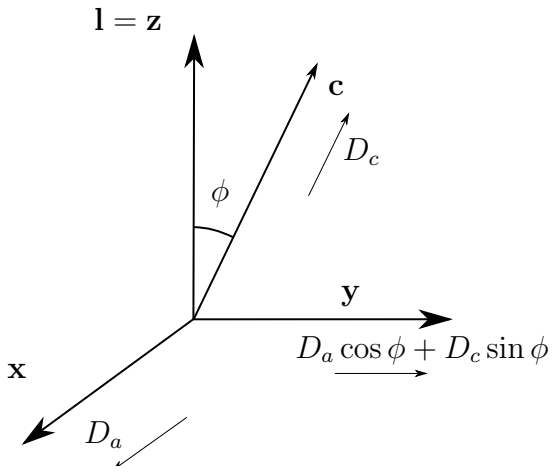

Figure 1.12: Description of the Woo and Goesele model for DAD. The dislocation line is oriented towards axis $\langle z \rangle$.

The main application of the models is the growth of hcp crystals under irradiation (see section 4.1.3.1), as case that will be studied in chapter 4.

1.3.5.3 Production bias model

In the 90's, another bias origin is proposed by Woo [3,51–54]: the *production bias model* (PBM). The main assumption is that the irradiation cascade produces defect clusters as well as Frenkel pairs. These clusters may have different properties from the single defect of the same nature. In addition, the fraction of vacancies and interstitials in clusters can differ significantly. As a consequence, the clusters may act as nuclei for larger defects. Indirect evidences of these assumptions have been brought by swelling experiments performed using various irradiation particles, that led to different swelling rates. It was shown that the irradiating particle type has a strong influence on the microstructure evolution, even for the same damage (see Fig. 1.14).

Another important assumption concerning the PD clusters has been proposed by other authors [55]: the SIA clusters may appear as small dislocation loops that

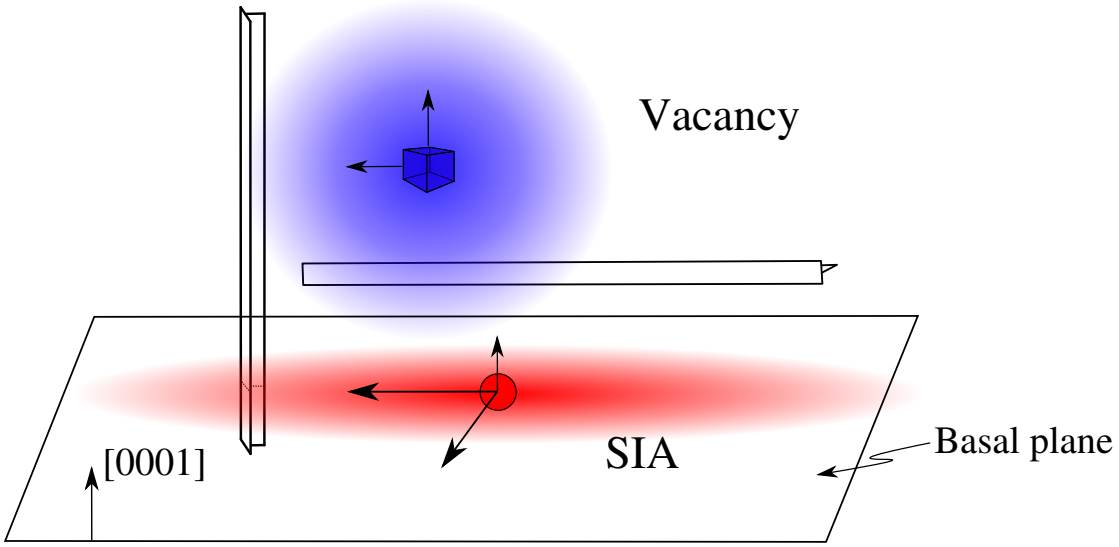

Figure 1.13: Schematics illustrating the faster absorption of SIAs by dislocations perpendicular to the basal plane. The 3D-diffusing vacancy has the same probability to be absorbed by both dislocations. On the opposite, the dislocation normal to the basal plane has a higher probability to intercept the SIA diffusion path, as the SIA stays close to the basal plane.

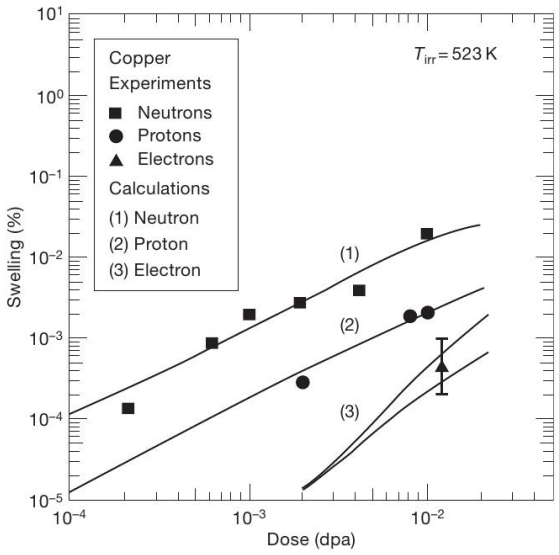

Figure 1.14: Experimentally measured and calculated effect of recoil energy on void swelling in pure copper irradiated with 2.5 MeV electrons, 3 MeV protons, and fission neutrons (from [31]).

diffuse mostly along a unique dense direction (pseudo 1D-diffusion). On the opposite, the vacancy clusters were assumed to be immobile, or unstable [6]. As a consequence, the sink shape and orientation would have a strong influence on SIA clusters capture, while it would have little effect on single vacancy and vacancy clusters absorption. For example, a 1D-diffusing defect has a higher probability to be absorbed by dislocation lines or grain boundaries normal to its fastest diffusion direction. On the opposite, voids aligned along fast diffusion directions would have a lower probability to absorb 1D-diffusing clusters, while still absorbing vacancies. In other words, the sink efficiency of a given defect population is dependent on its distribution and orientation. In this case, vacancy-type defects organise themselves to minimise their sink efficiency with respect to SIA-type defects (see Fig. 1.15, 1.16 and 1.18).

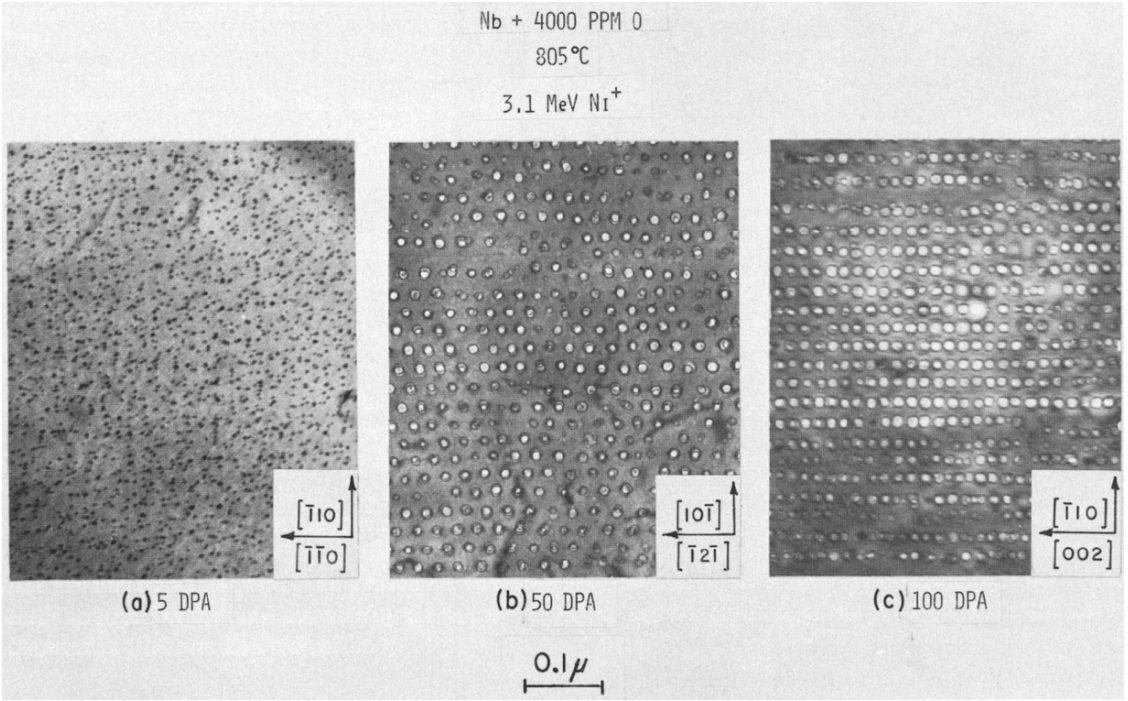

Figure 1.15: Ordered void array in bcc Nb + 4000 at.ppm O after 5, 50 and 100 dpa at 805°C (from [56]).

This theory has been applied in order to explain the swelling of fcc crystals and alignment of vacancy-type defects [58] in heavy particle irradiated fcc crystals [59] (see Fig. 1.17). Woo describes this phenomenon as a “Darwinian selection” [60]: any “misplaced” (outside the optimal lattice) vacancy defect will receive a relatively high SIA flux and vanish, while “screened” defects will survive. An equivalent theory including 1D-diffusing defects was proposed by Dubinko and Turkin [61]. This last theory is still under development [62].

It must therefore be noted that the generalisation of the conclusions achieved by the PBM are still under debate. In particular, Evans [63] made an extensive investigation of the limits of the model, and showed that several cases of voids lattice formation cannot be explained by 1D-diffusing SIA defects. In addition,

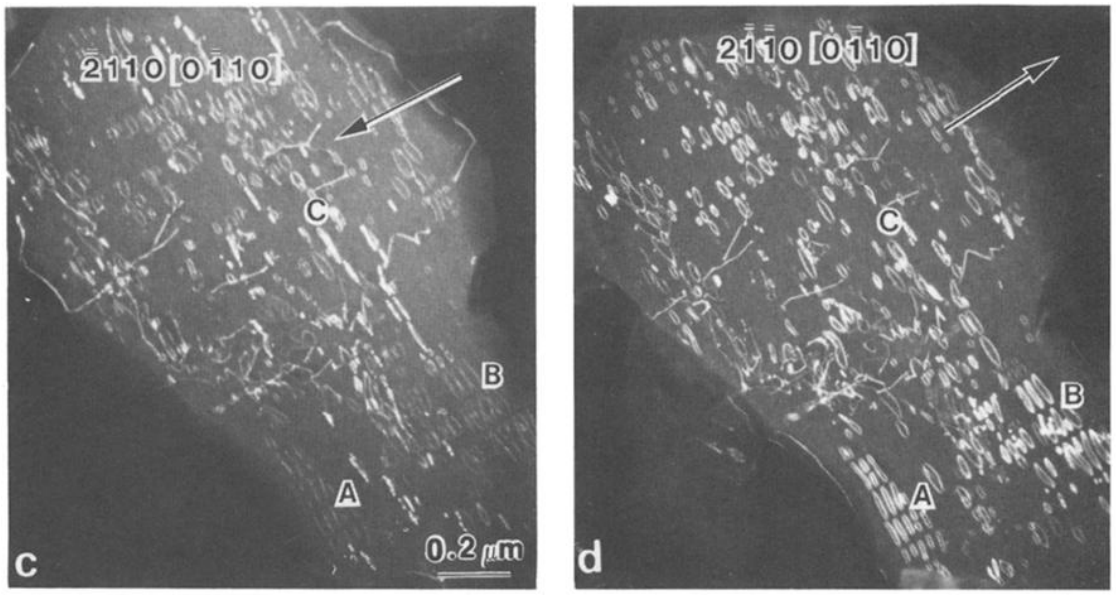

Figure 1.16: Loop ordering in neutron irradiated 64 % cold-worked titanium (from [57]).

vacancy-type clusters alignment has already been observed in electron irradiated copper [59], where no primary clusters are produced by collisions (see Sec. 1.1.1).

1.4 Summary

Up to date, much work has been dedicated to evaluate the sink efficiency of straight dislocations. The sink efficiency has been calculated by analytical and numerical means, with and without elasticity. However, to our knowledge, Tomé et al. [38] is the only team to have computed the sink efficiency of straight dislocations in the scope of the Wiedersich model. In addition, most calculations limited themselves to the case of pure edge dislocations. Finally, there has been no systematic study of the effect of the boundary conditions on the sink efficiency of straight dislocations with elasticity. This point is the first one addressed in this work.

Since to the best of our knowledge, there has been no calculation of the sink efficiency of dislocation loops in the framework of the Wiedersich model, either with or without elasticity, it is necessary to perform a study of the effect of the boundary conditions on the sink efficiency of dislocation loops. In addition, when the elasticity is taken into account in the calculation of sink efficiencies, the properties of the system have always been considered isotropic [37]. The second objective of this work is therefore to compute the sink efficiency of dislocation loops with and without elasticity (either isotropic or anisotropic), in the case of the Wiedersich boundary conditions.

To summarise, from the state-of-the-art compilation exposed in section 1.3, the objectives of the current work can be described as follows:

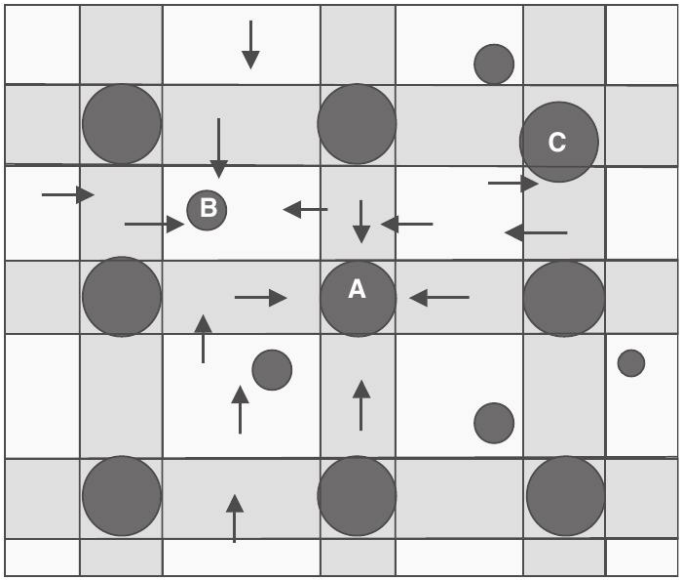

Figure 1.17: 2D schematic diagram of a void lattice depicting the cylindrical volumes lying along close-packed directions between voids that contain the only 1D migrating clusters that can interact with the voids. The shadowing effect (light grey regions) preserves the voids at the intersection of the cylinders A, since only the crowdions migrating in the adjacent cylinders in the direction of the cylinder axis can diminish the voids, while the voids B outside of the shadowed regions of the lattice voids A (white regions) are exposed to a much higher flux of SIA crowdions and should disappear. This effect also tends to facilitate better alignment of partially aligned voids C (from [64]).

- Calculate and compare sink efficiency of the straight dislocation with various boundary conditions,
  - without elasticity,
  - with isotropic elasticity,
  - with anisotropic elasticity,
  - for various slip systems (habit plane and Burgers vector).
- Calculate the sink efficiency of dislocation loops with the boundary conditions of Wiedersich,
  - without elasticity,
  - with isotropic elasticity,
  - with anisotropic elasticity,
  - for various slip systems.

In order to answer these problems, a new model has been developed. For our objectives, the main needed features are described as follows:

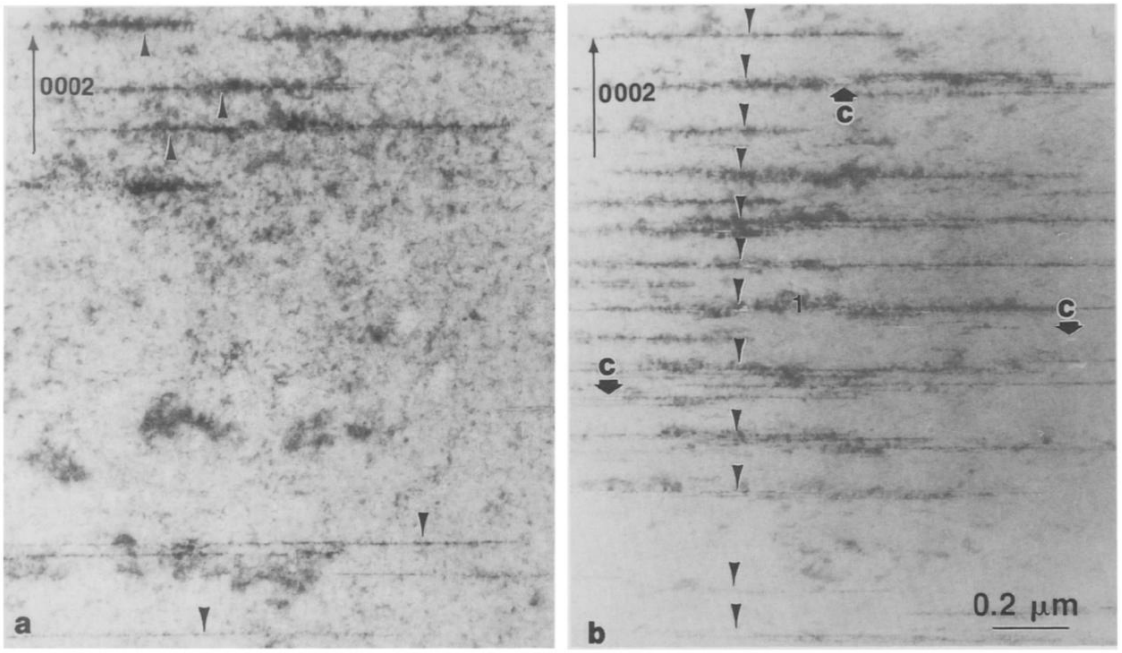

Figure 1.18: Comparison of radiation damage in pure (about 99.99% purity) and impure (about 99.8% purity) Zr irradiated at 573 K to 30 dpa: (a) high purity Zr; (b) impure Zr. Basal plane c-component loops (arrowed) are produced in each case although there are many more, along with cavities (labelled C), in the impure material. Diffracting vector $= [0002]$, beam direction close to $[1\bar{2}10]$. Basal vacancy loops are aligned in the basal plane (from [65]).

- Straight dislocation
  - Analytical
    - No elasticity [28]
    - Isotropic elasticity [33, 35]
  - Numerical
    - No elasticity [42]
    - Isotropic elasticity [37]
    - Anisotropic elasticity [25, 38]
- Dislocation loops
  - Analytical
    - No elasticity [28, 66]
  - Numerical
    - No elasticity [42]
    - Isotropic elasticity [37]

Figure 1.19: Summary of the sink efficiency calculations available in the literature. It should be noted that in the case of straight dislocations, no systematic study of the effect of boundary conditions has been made.

- The boundary conditions must be freely defined, in order to create Laplace or Wiedersich boundary conditions.
- The system should be able to take into account the shape of the sink, either cylindrical or toroidal.
  - in addition, the model should be applicable to various types of sinks (cylinder, torus, voids, surfaces, grain boundaries).
- The stress field of a straight dislocation and dislocation loop must be calculated,
  - in the case of isotropic or anisotropic elasticity,
  - for any dislocation slip system.
- The sink efficiency must be calculated with and without elasticity. As a consequence, the model should be able to consider the elastic effects on PD diffusion, as well as neglect them.

In the next chapter, we will propose a model that can handle those conditions.

Chapter 2

A new phase-field model for sink efficiency calculation

Contents

As we have seen in the previous chapter, the calculation of the sink efficiency of microstructural defects is a major concern for long term predictions. In this work, the goal is to propose a new method in order to compute the sink efficiency of dislocation lines and loops, taking into account anisotropic elastic interactions with the PD. In order to address this problem, we have chosen to follow a PF approach: it can take into account anisotropic elasticity, consider irradiation and PD absorption, and model dislocations, as it will be shown in section 2.1.

Then, our new model will be presented in detail: the *order parameters* of the problem in section 2.2, the calculation of the total system free energy in section 2.3 and the kinetic equation associated with PD diffusion in section 2.4. Using this model, it will be possible to simulate the creation, diffusion and absorption of PDs. This will allow us to deduce the sink efficiency of a sink for each PD type, as described in section 2.5. In order to optimise the computational time, an accelerated convergence algorithm has been developed and is detailed in section 2.6. Finally, we will enumerate the advantages and the limits of this new PF model, in comparison with existing ones from the literature.

2.1 Phase field models: state-of-the-art

Cahn and Hilliard proposed the first approach that led to the PF method as it is seen nowadays [67]. The method is based on the solution of spatial continuous equations. This assumption of a continuous medium induces that the dimensions considered are large compared to the interatomic distance. The microstructure is described by spatial functions: the *order parameters*. The value of a given order parameter is a local property of the microstructure. For example, an order parameter η can be a function of existence of a given precipitate in a matrix: the precipitate is located where the value of η is 1, while the matrix correspond to the region where η is 0. The interface between the precipitate and the matrix corresponds to the volume with intermediate values. It is then not necessary to explicitly consider the location of the interfaces, as it is given by the order parameter function. If several order parameters η_i are used, a complex microstructure can be described.

From the order parameters and the properties of the microstructural objects they describe, it is possible to compute the free energy functional F of the system. As a consequence, the energetic potential f can be deduced as the functional derivative of the free energy functional:

$$f_i(\mathbf{r}) = \left(\frac{\delta F}{\delta \eta_i}\right)_{\eta_{j\neq i},T,P} \tag{2.1}$$

The system evolution is governed by the minimisation of the total system free energy of the system. The Cahn-Hilliard [67] and Allen-Cahn [68] equations assume that the evolution speed is proportional to its driving force. A kinetic equation can be defined for each order parameter. If the average value must be conserved during evolution (total heat, atomic concentration), it is a *conserved order parameter*. On the opposite, the average value can be non conservative (shape function of the grain volume or precipitate with a given crystallographic orientation, volume sheared by a dislocation [69, 70]), it is then a *non-conservative order parameter*.

The solution of each kinetic equation on each order parameter allows to predict the temporal evolution of the system, and gives access to the full "history" of this evolution.

In the next sections, we will focus on the particular cases of dislocations mod-

elled by PF, and the use of PF to model the irradiated materials.

2.1.1 The modelling of dislocations in phase-field

PF models generally consider volumetric objects in order to predict the composition evolution and shape modification of the system. It is hard to consider linear objects such as dislocation lines and loops. In 2001, dislocations have first been modelled in PF by Finel et al. [69] and Wang et al. [70]. The innovative idea was to consider the sheared volume as an order parameter, instead of the dislocation core region. To this end, they used a result established by Nabarro [71] that shows that the stress field created by a dislocation loop is equivalent to that of a platelet whose border corresponds to the dislocation loop core, with thickness d (see Fig. 2.1) and a stress-free strain ϵ_{ij}^{d0} defined as:

$$\epsilon_{ij}^{d0} = \frac{1}{2d}\left(b_i\, n_j + b_j\, n_i\right) \tag{2.2}$$

with b_i and n_j respectively the i^{th} component of the Burgers vector $\mathbf{b}$ and the j^{th} component of the unit vector $\mathbf{n}$ normal to the habit plane of the loop (see also Fig. 2.1).

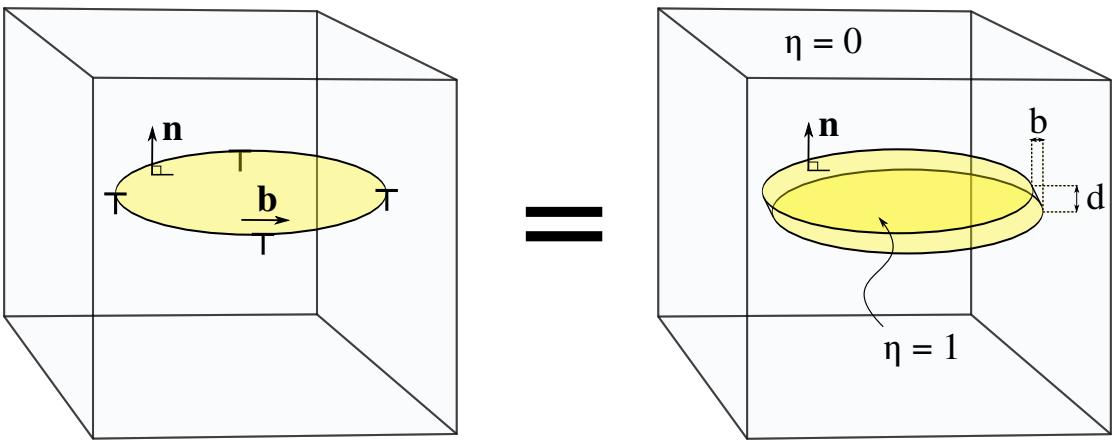

Figure 2.1: Dislocation loop as modelled in the PF approach. The platelet with normal $\mathbf{n}$ and ϵ_{ij}^{d0} defined in Eq. (2.2) is equivalent to the dislocation loop with the same normal and Burgers vector $\mathbf{b}$. d is the platelet thickness and $\mathbf{n}$ the unit vector normal to the dislocation habit plane.

This property enables to compute the stress field of any dislocation loop in any slip system. In the PF approach, this allows to model any dislocation loop by a volume (the platelet) instead of a linear object (the dislocation core). In order to describe the platelet, an order parameter η is defined: its value is 1 inside the platelet, and 0 outside. In the case of glissile dislocations, the value of η can be seen as the number of times the region has been sheared by a dislocation. For sessile interstitial dislocation loops, the value of η is the thickness of atomic layers added to the region, in units of b/d. Now that the loop is described as a volume, it

is possible to compute the stress field of this loop by means of the microelasticity theory of Khatchaturyan [72] (see section 2.3 for further explanation).

The advantages of the method are numerous:

- the capacity to model any shape of dislocation loop, as long as the dislocation loop remains in its habit plane;
- the definition of the dislocation properties can be freely determined (Burgers vector orientation and value, habit plane orientation, loop nature);
- the calculation of the stress/strain field are possible for any slip system, whatever the host crystal elastic properties (isotropic/anisotropic).

It must be emphasised that this technique allows to model not only glissile dislocations (Burgers vector contained in the habit plane), but also sessile dislocations (Burgers vector non-parallel to the habit plane). In the case where there are several slip systems, there must be one order parameter by slip system. As a consequence, each parameter $\eta_{(\mathbf{b},\mathbf{n})}$ is associated with a unique couple $(\mathbf{b},\mathbf{n})$.

This technique has been applied to the case of dislocation slip, cold-work hardening [70], precipitate hardening [69], but also to the case of sessile interstitial dislocation loops [73, 74].

2.1.2 Phase-field model of irradiated materials

Some authors have already applied the PF method to the case of irradiated microstructures. Millett et al. studied mostly the aggregation of vacancies and inert gases in metals and ceramics [75]. The main objectives were to understand the growth of voids in the vicinity of grain boundaries [76], the interaction between vacancies and inert gases [77–79], the growth and percolation of gas bubbles in the grain boundaries of ceramic nuclear fuel [78, 80] and the effect of voids on the thermal conductivity [81–83]. From a technical point of view, those works relied, on one hand, on the solution of the diffusion equation of vacancies and inert gases in the matrix, and on the other hand, on the evolution of a non conserved order parameter that corresponds to the shape function of the voids. The voids were considered as "vacancy precipitates" whose vacancy composition were close to 100 % and a concentration of inert gas high in comparison with the matrix. Another remarkable feature is used in some of those works: the introduction of defect sinks in grain boundaries (GB) [76]. In this work, vacancies and SIAs are submitted to the following equation:

$$\frac{\partial X}{\partial t} = \boldsymbol{\nabla} \cdot \left(M \boldsymbol{\nabla} \frac{1}{N_{\mathrm{at}}} \frac{\partial F}{\partial X} \right) + \xi(\mathbf{r},t) + P(\mathbf{r},t) - R_{iv}(\mathbf{r},t) - S^{\mathrm{GB}}(\mathbf{r},t), \tag{2.3}$$

where M is the atomic mobility, N_{at} the number of atoms by unit volume, ξ a noise function dedicated to the generation of inhomogeneities, P the point defect rate creation, R_{iv} the local recombination rate function and S^{GB} the local sink flux to the grain boundary. The sink flux function S^{GB} is defined as [78]:

$$S^{\mathrm{GB}}(\mathbf{r},t) = S_r[1 - \Phi(\mathbf{r})]\,[X(\mathbf{r},t) - X^{\mathrm{eq}}] \tag{2.4}$$

where the parameter S_r is a reaction constant, Φ the sink order parameter function, equal to 0 inside the GB, 1 outside and X^{eq} the local grain boundary PD concentration. It must be noted that the function S^{GB} in nonzero only where $\Phi = 0$, this means that the sink does absorb only in the grain boundary. This technique allowed to adapt the capacity of PF to model the coarsening of precipitate in a supersaturated matrix to the case of voids. The specific features of this work are then:

- the annihilation of SIAs and vacancies,
- the generation of PDs by irradiation,
- the absorption of PDs by sinks (GBs in this case).

Another team has studied the case of SIAs and vacancies absorption by interstitial loops, and the growth of the loop by climbing [73, 74]. In this case, the loop growth is driven by free energy minimisation, but is also limited by mass conservation: the loop should grow only if SIAs are absorbed. To this end, they considered the dislocation loop as a "phase" with the equilibrium at 100 % SIA fraction. The driving force of absorption of SIAs is due to the SIA supersaturation in the matrix. The chemical energy of SIAs in the matrix is higher than in the loop, as a consequence, the loop will absorb the SIAs. Vacancies are also introduced in the system, and annihilate with the SIAs through a second-order reaction kinetic:

$$R_{iv}(\mathbf{r}, t) = K_{iv} X_i(\mathbf{r}, t) X_v(\mathbf{r}, t), \tag{2.5}$$

where R_{iv} is the annihilation functional, X_i and X_v the site fractions of SIA and vacancy, respectively, and K_{iv} the second-order reaction constant. As a consequence, the absorption of vacancies by the loop will generate: (i) the shrinkage of the interstitial loop, (ii) a vacancy composition gradient that will act as a driving force for vacancy diffusion towards the loop. In this model, the effects of the dislocation loop stress field on the defect diffusion have been taken into account (see section 2.1.1). Hu and Henager have shown that the elastic interaction do accelerate the growth of the dislocation loop. In addition, the loop that begun with a circular shape, did tend to a square geometry. This effect was never experienced in irradiated samples. The model still raises some criticisms:

- the chemical fractions are overestimated ($\bar{X}_i \sim 10^{-4} \sim 10^{19}\,\mathrm{cm}^{-3}$);
- PDs can be absorbed at any interface of the platelet, and not only the core region, that corresponds to the platelet *border*;
- according to the free energy definition, the loop shape and volume is able to change without PD absorption;
- In the case of perfect loops, the "inside" of the platelet should be equivalent to the matrix. This is not guaranteed in the model.

Finally, it must be emphasised that this model was was not developed in order to calculate sink efficiencies.

2.1.3 Dislocation climb by PD absorption

Very recently, Geslin has been studying the climb of straight dislocations due to vacancy absorption in hot metals [84, 85]. The new model developed allows to solve some of the limits of the previous ones by Hu and Henager:

- The PDs are absorbed only close to the dislocation core;
- the "inside" of the platelet does not affect the movement of PDs;
- the dislocation "platelet" is not allowed to grow without absorbing defects.

However, this model was dedicated to the absorption of thermal vacancies by edge dislocations. There have been no consideration for the absorption of other types of defects. A surprising result of this work is that the elastic interaction between the dislocation and the PDs does decrease the absorbed flux of PDs.

2.1.4 Summary

The presented models shown that the PF method is able to handle various effects:

1. the calculation of a dislocation stress field, in an elastically isotropic or anisotropic crystal (see sec. 2.1.1),
2. the PD diffusion taking into account the elastic interaction between the dislocations and the PDs,
3. the creation of PDs by irradiation and their absorption by microstructural sinks (see section 2.1.2).

In the following, we will present our PF model, which relies on these particular features described in this section.

2.2 System description: definition of the order parameters

In the following, we describe the 3 main steps required to build a PF model, i.e. the definition of:

- the order parameters,
- the energy functional,
- the evolution equation.

The computational approach used in this work rests on a PF model which is upgraded to take into account the creation of PDs by irradiation, the elastic drift in PD diffusion and their absorption by localized sinks.

In this section, three order parameters will be defined:

1. the PD site fraction X, which are created by irradiation, migrate in the crystal and are absorbed by sinks;

2. the parameter η, which is associated with the dislocations loop and allows to generate the corresponding stress field;

3. the parameter λ associated with the sink region, i.e. the zone where the PDs are absorbed.

2.2.1 PD site fraction X

We consider a single crystal with a PD site fraction field $X(\mathbf{r})$ interacting with dislocations which act as PD sinks. In this work, PDs are created by irradiation at a uniform and constant generation rate K_0, and absorbed locally by the dislocation cores. Only Frenkel pairs are considered, which means that $X(\mathbf{r})$ refers either to vacancies or SIAs. Nevertheless, this technique can be easily adapted to the diffusion of various migrating defects (defect cluster, 1D-diffusion crowdion, etc.) to a sink. Moreover, it is assumed that the chemical and elastic interactions between these vacancies and SIAs have no influence on the resulting sink efficiencies. As a consequence, the definition of only one conserved order parameter field X, corresponding to either vacancy or SIA site fraction, is required in the simulations. This parameter will correspond to SIA or vacancy, depending on the elastic and diffusion properties.

In order to properly define the SIA site fraction, we consider the *dumbbell* site fraction, that is two atoms sharing the same atomic site. As a consequence, a volume that contains n atoms and m SIAs can be described as containing m dumbbells and $n - m$ single atoms on n substitutional sites. In a cell containing $n + m$ atoms, the dumbbell site fraction in the volume is then m/n, that is the number of SIAs divided by the *number of substitutional sites* (see Fig. 2.2). In the case of vacancies, the site fraction can be defined without ambiguity.

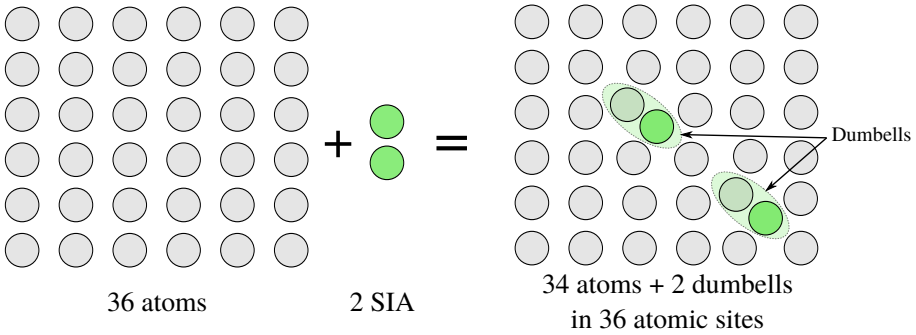

Figure 2.2: Equivalence between SIA and dumbbell fraction for $m = 2$ and $n = 36$. The example illustrates the difference between site and atomic fractions.

2.2.2 Dislocation platelet η

In order to calculate the sink efficiency of a dislocation, its stress field must be accurately computed, since it modifies the diffusion of the migrating species around it. The linear nature of the dislocation makes it hard to model in PF. Effective models have already been proposed in the past to calculate correctly the stress field of dislocation loops and lines (see section 2.1.1). Instead of a line, the dislocation loop will be modelled as a volume. Modelling dislocation loops as volumes can be performed in PF models by using the equivalence demonstrated by Nabarro [7] (see Fig. 2.1): a platelet of thickness d characterised by a stress-free strain ϵ_{ij}^{d0} generates the same stress field as a dislocation loop embracing this platelet along its perimeter provided that its stress-free strain ϵ_{ij}^{d0} is defined by Eq. (2.2).

Any type of dislocation (perfect edge, screw or mixed) can then be modelled by PF. In PF models, d is usually replaced by the grid spacing a_0 in equation (2.2). This method will be validated in section A.1.

Any type of dislocations can then be modelled by means of the order parameter $\eta(\mathbf{r})$ equal to 1 inside the platelet and 0 outside. If a dislocation loop is modelled, $\eta(\mathbf{r})$ increases sharply from 0 to 1 along the direction normal to its habit plane. Conversely, $\eta(\mathbf{r})$ gradually changes from 1 to 0 along a diffuse interface of width W and located at the dislocation core along a line crossing the loop and contained in its habit plane. W is typically of the order of 2-3 numerical cells in PF models. To conclude, the elastic properties of the dislocation loop in PF are defined by ϵ_{ij}^{d0} and its shape by the order parameter η.

2.2.3 The order parameter λ

Dislocations in PF methods is well-known, as mentioned in section 2.1.1, but the correct modelling of the sink behaviour of a dislocation is still a challenge, even if attempts towards this goal is proposed in [73, 74, 84, 85]. In order to avoid the limits of the previous works, another method is presented in this chapter, which introduces an additional order parameter $\lambda(\mathbf{r})$ equal to 0 in the matrix and 1 in the capture zone of the sink. It is then possible to explore various sink geometries: cylindrical for straight dislocation in chapter 3 and 4, spherical and toroidal in chapter 5. The composition in the sink is maintained at a constant value X^s by adding an absorption flux $J^{\text{abs}}(\mathbf{r})$ to the PD conservation equation as explained in section 2.4.

The capture zone of the dislocations is supposed to be circular, of radius r_0 and located around the dislocation cores (Fig. 2.3a)).

Order parameters $\eta(\mathbf{r})$, $\lambda(\mathbf{r})$ and the shear stress $\sigma_{xy}(\mathbf{r})$ (calculated using the microelasticity model described in section 2.3) are plotted in Fig. 2.4 along $y = y_1 + a_0$ for the case depicted in Fig. 2.3 c) and $N = 64$. $\sigma_{xy}(\mathbf{r})$ displays extremal values close to the dislocation cores, in a region where linear elasticity is not valid. We therefore choose r_0 in our simulation in such a way that the sink encompasses these non-physical extrema in order to suppress their influence on the diffusion fields. Rigorously speaking, r_0 will refer in the following parts to the equivalent radius corresponding to the volume occupied by the grid cells absorbing PDs, i.e. for which $\lambda(\mathbf{r})$ is different from 0.

The combination of the two fields $\eta(\mathbf{r})$ and $\lambda(\mathbf{r})$ (Fig. 2.3 c)) constitutes an

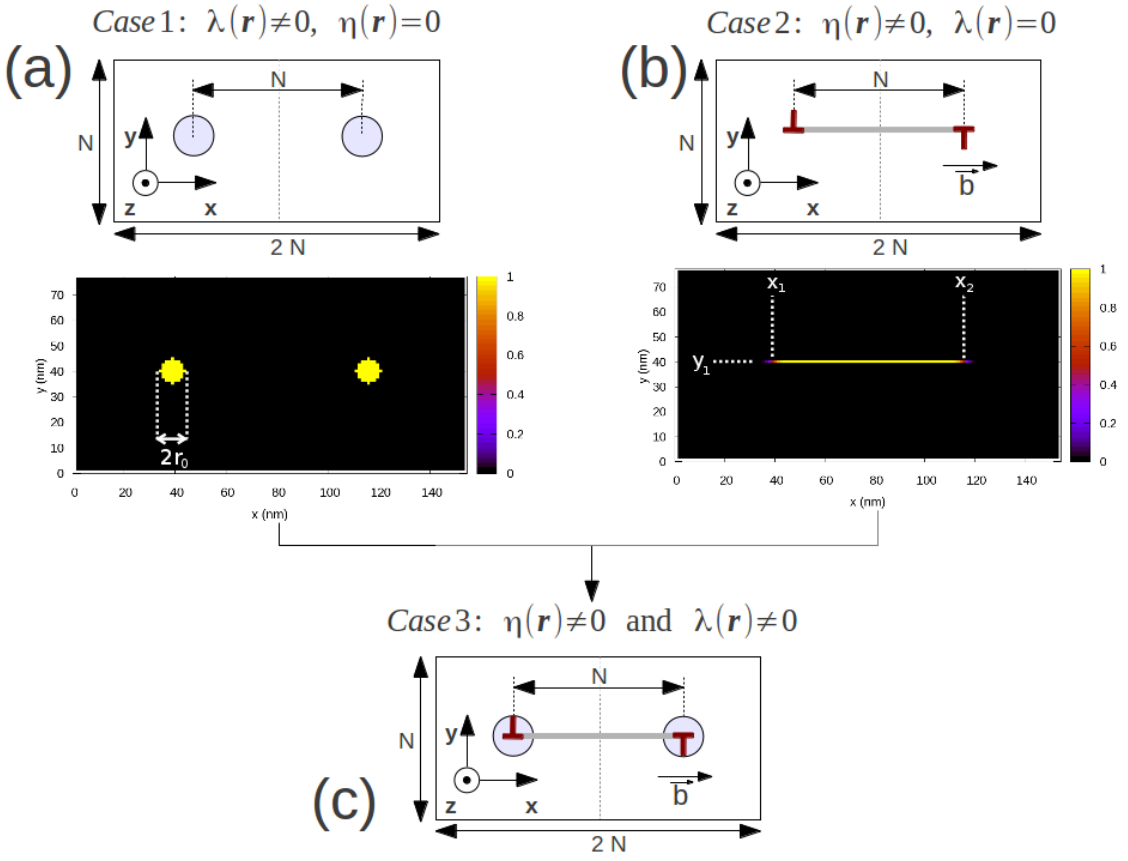

Figure 2.3: Example of the definition of the order parameters $\eta(\mathbf{r})$ and $\lambda(\mathbf{r})$ in the case of straight dislocations. Considering only η (resp. λ) in the calculation domain leads to case 1 (resp. 2). a) the dislocation is an absorbing sink without associated stress field ($\eta = 0$). b) the dislocation interacts with PDs via its stress field but is not an absorbing sink ($\lambda = 0$). c) the superposition of $\eta(\mathbf{r})$ and $\lambda(\mathbf{r})$ allows to model a dislocation as a sink which generates its own stress field.

original numerical approach to calculate realistic dislocation sink efficiencies by taking properly into account its stress field.

It must be emphasised that two distinct parameters are associated with the dislocation cores:

(i) the core thickness W already used in the previous PF models dedicated to dislocations and related to the core energy E_{core} (it is set at a few PF cells to allow dislocation glide)

(ii) the new parameter r_0 associated with the dislocation capture zone which allows PDs absorption from all around the core.

This last parameter corresponds to a new degree of freedom in the PF model. It allows a good control of the sink geometry, which is essential to correctly calculate the sink efficiency.

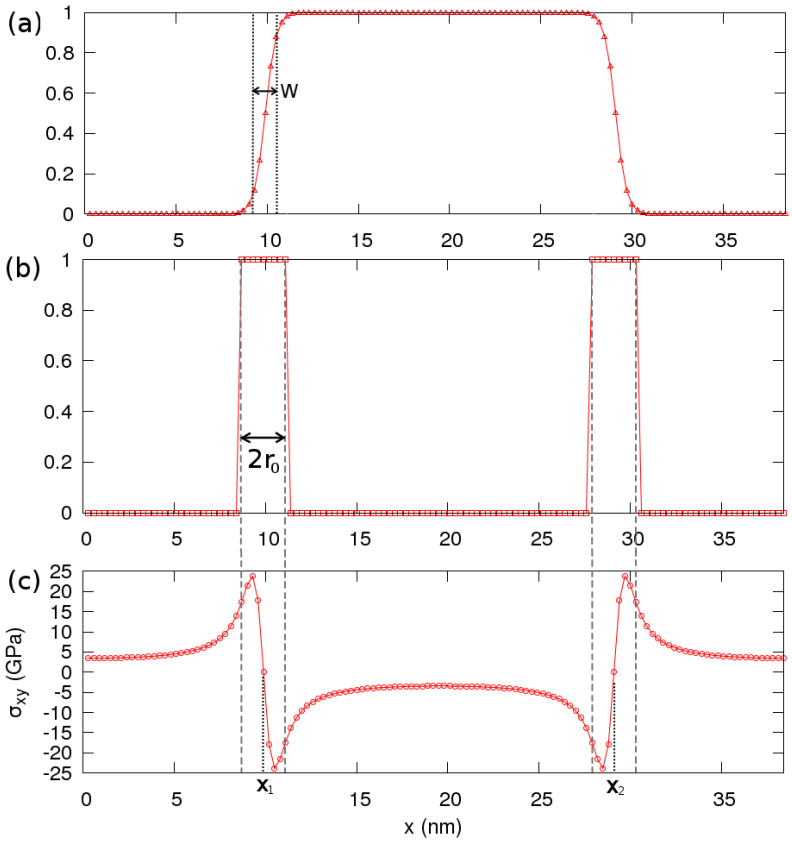

Figure 2.4: Profiles of a) $\eta(\mathbf{r})$, b) $\lambda(\mathbf{r})$ and c) $\sigma_{xy}(\mathbf{r})$ along $y = y_1 + a_0$.

2.3 Energy of the system

The total free energy F of the system is given by:

$$F = F_{\text{chem}}(X) + E_{\text{el}}(X, \eta) + E_{\text{core}}(\eta) \tag{2.6}$$

F_{chem} and E_{el} are respectively the chemical and elastic energy of the system and E_{core} is the core energy of the dislocation lines.

If we consider the defect-free crystal as the reference, then the excess chemical free energy of the system of volume V due to the point defect fraction X under the assumption of the ideal solution is given by [1]:

$$F_{\text{chem}} = \frac{1}{V_{\text{at}}} \int_V E_f X + k_B T[X \ln(X) + (1 - X) \ln(1 - X)] \, \mathrm{d}V \tag{2.7}$$

V_{at} is the atomic volume, E_f is the PD formation energy, k_B is the Boltzmann constant and T is the temperature of the system.

Following Hu et al. [86] who computed composition inhomogeneities due to stress gradients near structural defects, the Khachaturyan method [72] is employed to calculate the strain energy of the system (supposed to be elastically homogeneous) in which the PD composition is not uniform due to the presence

of the dislocations. We assume that the stress-free lattice parameter a obeys the Vegard law and the reference state for strain calculation is chosen as the matrix free of any PDs or structural defects. The local stress-free strain due to the site fraction of PDs $X(\mathbf{r})$ is therefore given by:

$$\varepsilon^0_{ij}(\mathbf{r}) = \epsilon^{00}_{ij}\ X(\mathbf{r}), \tag{2.8}$$

where ϵ^{00}_{ij} is the tensor of the Vegard coefficients. If the PD is considered as an isotropic dilatation centre, the strain of the perfect lattice induced by PDs is usually given in terms of relaxation volume Ω, which is related to the Vegard coefficients through the following relation:

$$\mathrm{Tr}(\epsilon^{00}) = \Omega/V_{\mathrm{at}} \tag{2.9}$$

If PDs are supposed to act as pure dilatation centres, then $\epsilon^{00}_{ii} = \frac{1}{a}\frac{\partial a}{\partial X} = \Omega/3V_{\mathrm{at}}$ and $\epsilon^{00}_{ij} = 0$ if $i \neq j$. In general, ϵ^{00}_{ij} is not isotropic and can be obtained from atomic scale simulations (*ab initio* or molecular dynamics, see sections 1.2.3 and 1.2.1). The effect of the PD shape (isotropic and anisotropic) will be illustrated in chapter 4.

Similarly, the local stress-free strain associated with dislocations ε^d_{ij} is given by equation (2.2) multiplied by the order parameter $\eta(\mathbf{r})$:

$$\varepsilon^d_{ij}(\mathbf{r}) = \epsilon^{d0}_{ij}\ \eta(\mathbf{r}) \tag{2.10}$$

This leads to the total elastic energy of the system:

$$E_{\mathrm{el}} = \frac{1}{2}\int_V C_{ijkl}\left[\varepsilon_{ij}(\mathbf{r}) - \varepsilon^0_{ij}(\mathbf{r}) - \varepsilon^d_{ij}(\mathbf{r})\right]\cdot\left[\varepsilon_{kl}(\mathbf{r}) - \varepsilon^0_{kl}(\mathbf{r}) - \varepsilon^d_{kl}(\mathbf{r})\right]\mathrm{d}V, \tag{2.11}$$

where C_{ijkl} are the elastic constants of the homogeneous system and $\varepsilon_{ij}(\mathbf{r})$ is the total strain. $\varepsilon_{ij}(\mathbf{r})$ can be decomposed into two parts, $\varepsilon_{ij}(\mathbf{r}) = \bar{\varepsilon}_{ij} + \delta\varepsilon_{ij}(\mathbf{r})$, $\delta\varepsilon_{ij}(\mathbf{r})$ being the heterogeneous part of the strain and $\bar{\varepsilon}_{ij}$ the average strain. Since the system is supposed to be elastically homogeneous, the average strain is given by:

$$\bar{\varepsilon}_{ij} = \epsilon^{00}_{ij}\ \bar{X} + \epsilon^{d0}_{ij}\ \bar{\eta}, \tag{2.12}$$

where $\bar{X}$ and $\bar{\eta}$ are respectively the volume average values of $X(\mathbf{r})$ and $\eta(\mathbf{r})$.

$\delta\varepsilon_{ij}(\mathbf{r})$ derives from the displacement field u_i which is obtained by solving the following equation in the Fourier space:

$$C_{ijkl}\frac{\partial^2 u_k}{\partial r_j \partial r_l}(\mathbf{r}) = C_{ijkl}\left[\epsilon^{00}_{kl}\frac{\partial X}{\partial r_j}(\mathbf{r}) + \epsilon^{d0}_{kl}\frac{\partial \eta}{\partial r_j}(\mathbf{r})\right] \tag{2.13}$$

The core energy E_{core} of dislocations is described in previous PF models as a sum of a potential term and a gradient energy term [70, 84]:

$$E_{\mathrm{core}}(\eta) = \int_V \left\{\alpha f[\eta(\mathbf{r})] + \beta\left[\mathbf{n}\wedge\boldsymbol{\nabla}\eta(\mathbf{r})\right]^2\right\}\mathrm{d}V \tag{2.14}$$

where $\boldsymbol{\nabla}$ stands for the gradient operator, α and β are parameters chosen in order to fit the core energy and produce a core thickness of a few numerical cells. In the literature, $f[\eta(\mathbf{r})]$ is given under the form of a double-well potential ($\eta(\mathbf{r})^2[1-\eta(\mathbf{r})]^2$) [84] or a periodic crystalline energy ($\sin^2[\pi\eta(\mathbf{r})]$) which is zero when η takes integer values [70]. The second term takes into account spatial variations of η only in the habit plane. From equation (2.14), it is obvious that the core expression E_{core} is independent of X. A specific choice for an expression of E_{core} is not required in this work, as justified in section 2.4.

2.4 Kinetic equation

In this work, the dislocation lines remain immobile during the simulation, i.e. the climb due to PDs absorption is not taken into account to calculate the sink efficiencies. As a consequence, the two fields $\eta(\mathbf{r})$ and $\lambda(\mathbf{r})$ do not evolve with time and only the kinetic equation of $X(\mathbf{r})$ is considered.

The local PD flux $\mathbf{J}$, which is derived from the minimisation of the total free energy F, is given by:

$$\mathbf{J}(\mathbf{r}) = -\frac{1}{V_{\text{at}}}\mathbf{M}\cdot\boldsymbol{\nabla}\mu(\mathbf{r}) \tag{2.15}$$

where μ is the local energetic potential per atom defined by:

$$\mu(\mathbf{r}) = V_{\text{at}}\frac{\delta F}{\delta X}(\mathbf{r}) = \mu_{\text{chem}}(\mathbf{r}) + \mu_{\text{el}}(\mathbf{r}) \tag{2.16}$$

with:

$$\mu_{\text{chem}}(\mathbf{r}) = V_{\text{at}}\frac{\delta F_{\text{chem}}}{\delta X}(\mathbf{r}), \tag{2.17}$$

and:

$$\mu_{\text{el}}(\mathbf{r}) = V_{\text{at}}\frac{\delta E^{\text{el}}}{\delta X}(\mathbf{r}) = V_{\text{at}}\epsilon^{00}_{ij}\sigma_{ij}(\mathbf{r}), \tag{2.18}$$

where $\sigma_{ij}(\mathbf{r})$ is the elastic stress field defined as $C_{ijkl}[\varepsilon_{kl}(\mathbf{r}) - \varepsilon^0_{kl}(\mathbf{r}) - \varepsilon^d_{kl}(\mathbf{r})]$.

As the core energy E_{core} does not depend on X, this term disappears in the potential expression.

μ_{chem} is calculated from equation (2.7):

$$\mu_{\text{chem}}(\mathbf{r}) = E_f + k_B T \ln\left[\frac{X(\mathbf{r})}{1-X(\mathbf{r})}\right] \tag{2.19}$$

As we consider only very low PD concentrations ($1 - X \simeq 1$), Eq. (2.19) becomes:

$$\mu_{\text{chem}}(\mathbf{r}) = E_f + k_B T \ln\left[X(\mathbf{r})\right] \tag{2.20}$$

We assume that the PD mobility can be written as:

$$\mathbf{M}(X) = \frac{X}{k_B T}\mathbf{D} \tag{2.21}$$

where $\mathbf{D}$ is the PD diffusion coefficient tensor in a dilute solution.

Classically, in PF models, the evolution of a conserved order parameter is governed by the Cahn-Hilliard equation which ensures the minimisation of the total free energy F of the system [67]. This conservation equation has to be modified in our case to take into account: (i) the PD creation due to irradiation and characterised by the point defect generation rate K_0 (assumed constant and uniform in this work, but the generalisation would be straightforward) and (ii) the PD absorption at the sink represented by the flux $J^{\text{abs}}(\mathbf{r})$. This leads to:

$$\frac{\partial X}{\partial t}(\mathbf{r},t) = \boldsymbol{\nabla} \cdot [\mathbf{M}(X) \cdot \boldsymbol{\nabla}\mu(\mathbf{r},t)] + K_0 - J^{\text{abs}}(\mathbf{r},t) \tag{2.22}$$

The following expression is adopted for $J^{\text{abs}}(\mathbf{r})$:

$$J^{\text{abs}}(\mathbf{r},t) = \lambda(\mathbf{r})\ \lambda^{\text{eff}}\ [X(\mathbf{r},t) - X^s] \tag{2.23}$$

where X^s is the PD site fraction at the surface of the sink. Expression (2.23) ensures that $J^{\text{abs}}(\mathbf{r},t)$ is zero in the whole volume except inside the sink. Moreover, the composition inside the sink is maintained at X^s by absorbing all the PDs in excess at each time step if $\lambda^{\text{eff}} = 1/\Delta t$, Δt being the calculation time step. This expression is similar to the one proposed in [76], i.e. Eq. (2.4). Another possibility would be to reset the composition of PDs in the sink at a constant value after each time step without explicitly writing the flux of absorbed PDs in equation (2.22), the difference between the target and the actual value being recorded in order to access to the absorbed flux.

Equation (2.22) is valid whatever the position of the grid cell in the simulation domain (inside or outside the sink) and constitutes a convenient way to solve the diffusion equation whatever the spatial arrangement of the sinks. We will see that the methodology used here gives accurate results concerning the sink efficiency in sections 3.2.1 and 5.1.

The relation between J^s (Eq. (1.6)) and $J^{\text{abs}}(\mathbf{r})$ is given by:

$$J^s = \frac{1}{V}\int_V J^{\text{abs}}(\mathbf{r})\,\mathrm{d}V \tag{2.24}$$

Due to the specific expression of the chemical potential gradient ($\boldsymbol{\nabla}\mu_{\text{chem}} = k_B T \frac{1}{X}\boldsymbol{\nabla}X$ from equation (2.20)), the divergence term in equation (2.22) can be modified as follows:

$$\begin{aligned}\boldsymbol{\nabla}\cdot\left(\frac{X}{k_BT}\mathbf{D}\cdot\boldsymbol{\nabla}\mu\right) &= \boldsymbol{\nabla}\cdot\left(\frac{X}{k_BT}\frac{1}{X}k_BT\mathbf{D}\cdot\boldsymbol{\nabla}X + \frac{X}{k_BT}\mathbf{D}\cdot\boldsymbol{\nabla}\mu_{\text{el}}\right)\\ &= \boldsymbol{\nabla}\cdot\mathbf{D}\cdot\boldsymbol{\nabla}X + \boldsymbol{\nabla}\cdot\left(\frac{X}{k_BT}\mathbf{D}\cdot\boldsymbol{\nabla}\mu_{\text{el}}\right)\end{aligned} \tag{2.25}$$

Equation (2.30) is solved numerically with an explicit algorithm in the Fourier space, which implies periodic conditions at the boundaries of the calculation domain. This method is particularly suitable to deal with the elastic drift, since the Fourier transform of $\mu_{el}(\mathbf{r})$ have the following simple form valid whatever the symmetry properties of the crystal and PDs:

$$\widetilde{\mu_{el}}(\tilde{\mathbf{q}}) = B_X(\tilde{\mathbf{q}})\tilde{X}(\tilde{\mathbf{q}}) + B_\eta(\tilde{\mathbf{q}})\tilde{\eta}(\tilde{\mathbf{q}}) \tag{2.26}$$

with

$$B_X = \sigma_{ij}^{00}\epsilon_{ij}^{00} - \tilde{q}_i\sigma_{ij}^{00}G_{jm}(\tilde{\mathbf{q}})\sigma_{mn}^{00}\tilde{q}_n, \tag{2.27}$$

and

$$B_\eta = \sigma_{ij}^{d0}\epsilon_{ij}^{00} - \tilde{q}_i\sigma_{ij}^{d0}G_{jm}(\tilde{\mathbf{q}})\sigma_{mn}^{00}\tilde{q}_n, \tag{2.28}$$

where $\tilde{f}(\tilde{\mathbf{q}})$ is the Fourier transform of f, $\tilde{\mathbf{q}}$ is the wave vector, $\tilde{q}_i$ its coordinate in the i^{th} direction, $G_{ij}(\tilde{\mathbf{q}})$ is the Fourier transform of Green function (defined by $[G_{ij}(\tilde{\mathbf{q}})]^{-1} = C_{imjl}\tilde{q}_m\tilde{q}_l$), σ_{ij}^{00} and σ_{ij}^{d0} are respectively related to eigenstrains ϵ_{ij}^{00} and ϵ_{ij}^{d0} by Hooke law.

It should be noted that simplification in Eq. (2.25) spares some computational time, but is not necessary. As a consequence, this model is not limited to the ideal solution approximation.

Considering simplification in Eq. (2.25), equation (2.22) can be rewritten as:

$$\frac{\partial X}{\partial t} = \boldsymbol{\nabla}\cdot\mathbf{D}\cdot\boldsymbol{\nabla}X + \frac{\mathbf{D}}{k_BT}\boldsymbol{\nabla}\cdot(X\boldsymbol{\nabla}\mu_{\mathrm{el}}) + K_0 - J^{\mathrm{abs}} \tag{2.29}$$

Equation (2.29) is solved in the Fourier space, which is particularly suitable to deal with the elastic drift:

$$\begin{aligned}\widetilde{\frac{\partial X}{\partial t}}(\tilde{\mathbf{q}},t) =& -\tilde{q}_iD_{ij}\tilde{q}_j\tilde{X}(\tilde{\mathbf{q}},t)\\ &+\sum_i \frac{1}{k_BT}\, i_c\tilde{q}_i\,\mathfrak{F}\left\{D_{ij}X(\mathbf{r},t)\,\mathfrak{F}^{-1}\left[i_c\tilde{q}_i\widetilde{\mu_{\mathrm{el}}}(\tilde{\mathbf{q}},t)\right]\right\}\\ &+\tilde{K}_0 - \tilde{J}^{\mathrm{abs}}(\tilde{\mathbf{q}},t),\end{aligned} \tag{2.30}$$

where $\tilde{f}$ is the Fourier transform of the f function, $\mathfrak{F}(f) = \tilde{f}$ and $\mathfrak{F}^{-1}(\tilde{f}) = f$. $\tilde{\mathbf{q}}$ is the wave vector, $\tilde{q}_i$ its coordinate in the i^{th} direction and i_c the number defined as $(i_c)^2 = -1$.

Using dimensionless units, equation (2.30) becomes:

$$\begin{aligned}\widetilde{\frac{\partial X}{\partial t^*}}(\tilde{\mathbf{q}}^*,t^*) =& -\tilde{q}_i{}^*D_{ij}^*\tilde{q}_j{}^*\tilde{X}(\tilde{\mathbf{q}}^*,t^*)\\ &+\sum_i\, i_c\tilde{q}_i^*\,\mathfrak{F}\left\{D_{ij}^*X(\mathbf{r}^*,t^*)\,\mathfrak{F}^{-1}\left[i_c\tilde{q}_i^*\widetilde{\mu_{\mathrm{el}}^*}(\tilde{\mathbf{q}}^*,t^*)\right]\right\}\\ &+\tilde{K}_0^* - \tilde{J}^{\mathrm{abs}*}(\tilde{\mathbf{q}}^*,t^*),\end{aligned} \tag{2.31}$$

with:

$$
\begin{aligned}
&\tilde{\mathbf{q}}^* = a_0\ \tilde{\mathbf{q}} \\
&r^* = r/a_0 \\
&t^* = t/t_0 \text{ with } t_0 = a_0^2/D_{\mathrm{ref}} \\
&D_{ij}^* = D_{ij}/D_{\mathrm{ref}} \\
&\mu_{\mathrm{el}}^* = \mu_{\mathrm{el}}/k_B T \\
&K_0^* = t_0 K_0 \\
&J^{\mathrm{abs}*} = t_0 J^{\mathrm{abs}}
\end{aligned}
\tag{2.32}
$$

with D_{ref} a reference diffusion coefficient which is set for the whole system.

The PF method has been implemented in FORTRAN90. The Fourier transform are done by the parallel MPI version of the FFTW 3.3.3 library.

In the case of isotropic diffusion, $D_{ij} = D$ so Eq. (2.31) becomes:

$$
\begin{aligned}
\widetilde{\frac{\partial X}{\partial t^*}}(\tilde{\mathbf{q}}^*, t^*) = &- D^* \tilde{\mathbf{q}}^* \tilde{X}(\tilde{\mathbf{q}}^*, t^*) \\
&+ \sum_i i_c D^* \tilde{q}_i^*\ \mathfrak{F}\left\{ X(\mathbf{r}^*, t^*)\ \mathfrak{F}^{-1}\left[i_c \tilde{q}_i^* \widetilde{\mu_{\mathrm{el}}^*}(\tilde{\mathbf{q}}^*, t^*) \right] \right\} \\
&+ \tilde{K}_0^* - \tilde{J}^{\mathrm{abs}*}(\tilde{\mathbf{q}}^*, t^*),
\end{aligned}
\tag{2.33}
$$

In the following chapters, isotropic diffusion will mostly be considered. However, anisotropic diffusion calculation will be presented in section 3.2.2.

2.5 Sink efficiency deduction

In each simulation, only one type of sink and PD is considered, so the sink efficiency Z_i^s will be simply noted Z in the following parts. As a preliminary remark, since $K_0 = J^s$ at steady state, the value of Z can be deduced from equation (1.6):

$$
Z = \frac{K_0}{D\rho_s(\bar{X} - X^s)} \tag{2.34}
$$

Equation (2.34) can be used to calculate Z from the PF simulations since K_0, D, ρ_s and X^s are inputs of the PF model and $\bar{X}$ is an output. Then, the computation of the PD average composition at steady state allows to deduce the sink efficiency. It is valid for calculation domains containing only one sink. However, it is possible to take into account any number p of sinks with the following expression, consistent with Eq. (2.24):

$$
Z_s = \frac{J_s}{D\rho_s(\bar{X} - X^s)}, \tag{2.35}
$$

with J_s the average incoming flux to sink s defined in Eq. (2.24). With only one sink in the system, we have $J_s = K_0$, hence Eq. (2.34) and (2.35) are equivalent in this particular case. Equation (2.35) allows to compute the sink efficiency of any number of sinks in the same domain. It will be used in chapter 5.

One can remark that the dimension of Z depends on the dimension of ρ_s, as other variables have fixed dimensions. In the case of straight dislocations, ρ_s (or ρ_l for dislocations) is in m^{-2} so Z is dimensionless. In PF, the straight dislocation is modelled as a 2D system, the density is then obtained as the number of dislocation lines crossing a given surface.

On the opposite, in the case of dislocation loops, a choice must be made: either the loop density is defined as a number of loops per unit volume, so that Z is in units of m, or the loop density can be expressed as the length of dislocation line per unit volume (in m^{-2}), so that Z is dimensionless. Let's consider that the sink efficiency Z is dependent on the loop radius r_L. It is then possible to convert the sink efficiency with the dimension of a length Z_{vol} to the dimensionless sink efficiency Z with:

$$Z_{\mathrm{vol}} = 2\pi r_L Z \tag{2.36}$$

2.6 Accelerated convergence technique

The explicit algorithm for equation (2.31) demands many calculation steps to reach the steady-state needed for Eq. (2.34). For Eq. (2.34), only the steady state is needed for sink efficiency calculation, and this steady state is unique. As a consequence, the path to reach the steady state does not have to follow a physical behaviour, as long as the steady state is physically determined. The proposed algorithm consists in correcting the value of the profile $X(\mathbf{r}, t)$ at each time interval θ in order to accelerate the convergence, as described below. In order to make this description, we adopt the following notations:

$$\begin{aligned} X_i^n(\mathbf{r}) &= X\left(\mathbf{r}, t = n\,\theta\Delta t\right) \\ X_i^{n+1}(\mathbf{r}) &= X\left(\mathbf{r}, t = (n+1)\,\theta\Delta t\right) \end{aligned} \tag{2.37}$$

From $X_i^n(\mathbf{r})$, the PF simulation is launched normally over θ time steps, giving the field $X_i^{n+1}(\mathbf{r})$. We assume that the evolution of the average PD composition calculated by the PF model follows a kinetic equation of a rate-theory type (see section 1.2.5):

$$\frac{\partial \bar{X}}{\partial t} = K_0 - Z\rho_s D\left[\bar{X}(t) - X^{\mathrm{eq}}\right] \sim K_0 - K(t)\bar{X}(t) \tag{2.38}$$

The so-called sink strength $K(t)$ can then be locally determined:

$$K(t) = \frac{K_0 - \frac{\partial \bar{X}}{\partial t}(t)}{\bar{X}(t)} = \frac{K_0 - \frac{\bar{X}_i^{n+1} - \bar{X}_i^n}{\theta}}{\bar{X}^{n+1}} = K^{n+1} \tag{2.39}$$

We assume that K^{n+1} can be used as an approximation of K^∞. Since the real converged average value is $\bar{X}^\infty = K_0/K^\infty$, the quantity $\bar{X}_{\mathrm{est}} = K_0/K^{n+1}$ can be used as a first estimation of $\bar{X}^\infty$.

The profile $X_i^{n+1}(\mathbf{r})$ is corrected by a proportionality factor in order to have an average composition $\bar{X}_{\mathrm{corr}}^{n+1}$ instead of $\bar{X}_i^{n+1}$:

$$X_{\text{corr}}^{n+1}(\mathbf{r}) = \bar{X}^{n+1}(\mathbf{r}) \left[1 + \xi \frac{\bar{X}_{\text{est}}^{n+1} - \bar{X}^{n+1}}{\bar{X}_{\text{est}}^{n+1}}\right] \tag{2.40}$$

where ξ is an *ad hoc* value that sets the homothetic transformation value.
Finally, for the next algorithm step, we consider:

$$X_i^{n+1} = X_{\text{corr}}^{n+1} \tag{2.41}$$

This means that the further PF calculation will be performed from the corrected value of the field.

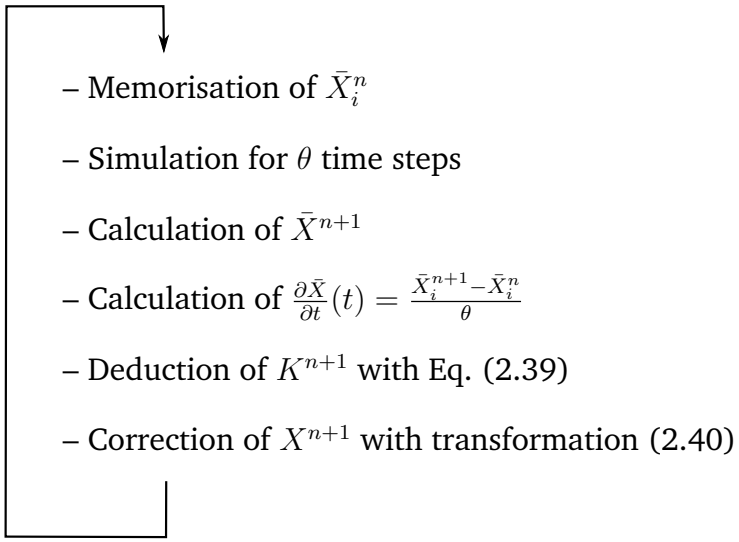

Figure 2.5: Accelerated convergence algorithm schematics.

The value of the parameter ξ is chosen in order to avoid instabilities during the calculation. Empirically, we observe that calculations remain stable for $\xi \lesssim 1.3$. The choice of θ is *a priori* crucial: a small period would lead to instabilities. In fact, we observe that whatever how low θ is chosen, simulations remain stable, even if θ less that 10 time steps. In addition, we remark that very long θ period have a tendency to make the simulations more unstable (approximated steady-state overestimated, leading to wrong composition adjustment). As a consequence, this parameter will be taken very small, in order to accelerate convergence and avoid instabilities. In general, calculation will be performed with $\xi = 1.0$ and $\theta = 10$.

This technique can be easily implemented in the PF code (around 30 code lines). The algorithm efficiency will be tested in chapters 3 and 5. For cases with θ is less than 100 time steps, calculation time spared can be more than 90 % (see for exemple Fig. 3.3). Sink efficiency calculations at low sink densities would have been impossible without this technique.

2.7 Advantages and limits of the method

2.7.1 Infinite microstructure

As the periodic boundary conditions are considered in this method, the modelled system is not isolated. Instead, it is an infinite microstructure reproduced in every direction. As a consequence, the calculated PD absorption rate is not the one of the isolated sink, but the one of the full microstructure. In this method, the sink-free volume shape is not arbitrary, which is always a questionable choice. For example, it has been shown by Dubinko et al. [37] that the sink efficiency of a toroidal sink is strongly affected if the sink-free volume is spherical or toroidal (see section 1.3.4.2 and in particular Fig. 1.11).

2.7.2 Realistic irradiation conditions

Instead of imposing the PD concentration far from the sink (like in the Laplace model), the PD creation is due to a uniform source term. This term corresponds to a geometrically random PD creation, which is closer to real irradiation conditions. It must be emphasised that the method also allows to have non uniform and non constant source terms, by means of a function of time and space instead of the scalar parameter K_0. As a consequence, it would be able to consider a charged particle defect creation, as a function of space.

2.7.3 No topological constraints

The definition of the order parameters η and λ is up to the operator. As a consequence, a wide range of microstructures can be modelled using this technique. It is possible to consider the effect of different types of dislocations (depending on the Burgers vector and the normal to the habit plane), or shapes (defined by the functions η and λ). This feature will be applied with success in this work to study dislocation straight lines (chapters 3 and 4), spherical sinks and circular dislocation loops (chapter 5).

2.7.4 Numerical solution of the stress field

Contrary to OKMC techniques [25, 26, 36, 45], the stress field or the elastic potential field is not an input of the calculation. Instead, the elastic potential field is a result of the PF calculation. The main consequence is that only easy to handle parameters are needed as input data: the PD Vegard coefficients tensors (obtained by *ab initio* calculations), the Burgers vector and the vector normal to the habit plane for the dislocation.

2.7.5 Freedom in material properties definition

The PF method allows to consider any elastic anisotropy of the system: in the PD shape, diffusion coefficients or the crystal elastic properties. This must be considered in comparison with various methods that are limited to isotropic properties [37]. As the properties of the system are defined by scalar and tensorial data, one can easily study various materials.

To obtain quantitative results, it is necessary to have a correct assessment of

the elastic and chemical driving forces, as well as the kinetic parameters. For this purpose, the model has been designed to be used in a multiscale approach, in which the thermodynamic (F_{chem}), kinetic ($\mathbf{M}$) and elastic (C_{ijkl}, ϵ_{ij}^{d0} and ϵ_{ij}^{00}) data are inputs of the calculation and specific to the real material under study. For example, these data can be obtained by atomistic calculations. More specifically, equation (2.7) for F_{chem} can be modified to incorporate the required thermodynamic data of the system. In that case, we will have to solve equation (2.22) instead of (2.29), as simplification described in equation (2.25) will not be possible. In addition, it is easy in the present model to consider anisotropy of diffusion as well as elastic properties of the crystal and point defects, since the microelasticity theory presented in section 2.3 is valid whatever the symmetry properties of the matrix, dislocations and PDs.

2.7.6 Limit: Sink region choice

As in analytical methods, the sink region shape and volume is arbitrarily chosen, and is not a consequence of the calculation. This problem is discussed for example in [28, 37].

2.7.7 Limit: Fixed dislocations

In this work, PD diffusion has been assumed to be much faster than dislocation climb, thus, dislocation cores have been considered immobile. In recent models, the dislocation climb due to the absorption of defects can be taken into account [84, 85]. The model presented in this article could take dislocation climb into account by solving a supplementary evolution equation for the order parameter η. However, these models have difficulties to properly describe the sink region. In addition, our calculations need to reach a steady state between irradiation and absorption of a given PD type. This steady state would be difficult to obtain if the dislocation core is moving. Finally, under irradiation conditions, the dislocation climb is due to the net flux of SIAs and vacancies. The calculation should then take into account the coexistence of both types of defects in the same system. Although the PF method can consider several PD types simultaneously, this study remains beyond the scope of this work. As a consequence, the dislocation climb will not be taken into account.

The growth of a dislocation loop is controlled by the PD flux which is already calculated in the present model by equation (2.23) in each cell of the calculation domain. As a consequence, η must obey a conservative equation (Cahn-Hilliard type) in which a source term equal to the net flux of point defects to the sink must be added. For example, in the case of an interstitial loop, the net flux $J^{\text{net}}(\mathbf{r})$ is the difference between the SIA and vacancy fluxes:

$$J^{\text{net}}(\mathbf{r}) = \lambda^{\text{eff}}\lambda(\mathbf{r})\left[X_{\text{i}}(\mathbf{r}) - X_{\text{i}}^{s} - X_{v}(\mathbf{r}) + X_{v}^{s}\right] \tag{2.42}$$

$J^{net}(\mathbf{r})$ is zero everywhere except in the capture zone defined by the order parameter λ. The resulting equation governing the evolution of η is given by:

$$\frac{\partial \eta}{\partial t}(\mathbf{r},t) = \boldsymbol{\nabla}\left[\mathbf{M}_{\eta}(\mathbf{r}) \cdot \boldsymbol{\nabla}\frac{\delta F}{\delta \eta}(\mathbf{r},t)\right] + J^{\text{net}}(\mathbf{r},t) \tag{2.43}$$

where M_η is a parameter controlling the minimization kinetics of the loop core and elastic energies under a continuous PD fluxes.

Moreover, the diffusion equation (2.22) of both interstitials and vacancies cannot be considered independently and should also include a reaction term due to the vacancy-interstitial recombination:

$$J^{\text{reac}}(\mathbf{r}) = -K\ X_{\text{i}}(\mathbf{r})\ X_v(\mathbf{r}) \tag{2.44}$$

where K is the recombination coefficient. The difficulty then rests in the dynamic control of the order parameter λ which must follow the moving dislocation core.

2.8 Summary

In this chapter, we gave the details of the method that will be used in the following chapters to calculate the sink efficiency of various sinks. The strategy rests on a PF model, that allows to take account the creation, diffusion and annihilation of PDs, considering elastic interaction with the dislocations. In order to calculate a dislocation line or loop, three order parameters are introduced (see section 2.2): the site fraction X, the dislocation platelet function η that corresponds to the stress field of the dislocation, and the new order parameter that determines the absorbing region of the sink λ. A free energy functional has been defined in section 2.3, and is used to simulate the evolution of the system, as described in section 2.4. When the simulation reaches the steady state, we are able to deduce the sink efficiency of the sink, as explained in section 2.5. In addition, in order to obtain faster results, an accelerated convergence algorithm has been developed (see section 2.6). It will be tested in the following chapters.

Our method allows to consider a wide range of microstructures (dislocation lines as well as loops) and of properties (isotropic or anisotropic elastic properties), while most existing models are limited to the case of the straight dislocation. In addition, the elastic potential field associated with the elastic interaction between the PDs and the dislocations is a result of the calculation, instead of an input. Finally, the PF technique is flexible enough to be easily adapted for other kinds of sinks, such as spherical sinks, or grain boundaries.

As a consequence, the main difference with methods from the literature is that the stress field of the microstructure doesn't need to be provided to the model, contrary to existing OKMC and continuous techniques (see section 1.3.3 and 1.3.4.2). To our knowledge, our model is the only existing method that allows to compute the sink efficiency of dislocation loops with isotropic or anisotropic elasticity, with periodic boundary conditions.

Chapter 3

A generic study of dislocation sink efficiency by phase field method

Contents

Sink efficiency calculation for dislocations has been a challenge for several years (see section 1.3.2), due to their stress field that attracts PDs towards the core. The attraction of PDs towards the dislocation line is well known for Cottrell atmospheres, where the carbon content in bcc iron is significantly higher close to dislocation cores.

Various analytical and numerical models have already been proposed. The goal of this chapter is to test the effectiveness and relevance of the method developed in chapter 2 on the case of straight dislocations. The model will first be applied to the simple case of the cylindrical sink, i.e. the dislocation core without elasticity. A particular interest will then be given on the effect of PD diffusion anisotropy. Results are compared to available solutions from the literature. Then, a second part fill focus on the diffusion of PDs in the complex stress field of straight dislocations. This will allow us to validate the elastic part of the PF model. Finally, the cylindrical sink and the stress field will be considered together to create a system that models a population of dislocations and the diffusion of PDs to the core.

It will be shown that the proper simulation of PD diffusion in a stress field

can be achieved with our PF model. The PF method will then be applied to more complex systems in chapters 4 and 5.

3.1 System description

In this work we present 2D simulations in planes perpendicular to the dislocation line. As the straight dislocations are invariant by translation along the line axis, the simulation can be performed in 2D. Since periodic boundary conditions are used along the three Cartesian directions, no spatial dependence of the fields is considered parallel to the z direction defined below. Using this geometry dislocation loops are transformed into parallel edge dislocation dipoles acting as sinks for PDs. It should be emphasised that, due to the periodic boundary conditions, the modelled microstructure is an infinite lattice of parallel straight dislocations, instead of an isolated line in a cylinder. A consistent way to define properly the order parameters $\eta(\mathbf{r})$ and $\lambda(\mathbf{r})$ for this configuration is illustrated in Fig. 2.3 (see section 2.2 for the definition of the order parameters).

In the two-dimensional calculation domain comprising $2N \times N$ grid cells, the dislocation lines are parallel to the z direction, with (010) slip plane and b Burgers vector oriented along x. It implies that η is equal to 0 in the whole simulation domain, except in the region around the line joining the two dislocation cores and parallel to $[100]$ (Fig. 2.3b)). More precisely, if the dislocation core centres are located at coordinates (x_1, y_1) and (x_2, y_1), then the η field is defined as follows:

$$\eta(x,y) \;=\; \frac{1}{2}\delta(y-y_1)\left[\tanh\left(\frac{x-x_1}{\sqrt{2}W}\right) - \tanh\left(\frac{x-x_2}{\sqrt{2}W}\right)\right] \tag{3.1}$$

where δ is the Dirac function ($\delta(x = 0) = 1, \delta(x \neq 0) = 0$). In the cases depicted in Fig. 2.3, $x_1 = Na_0/2$, $x_2 = 3Na_0/2$, $y_1 = Na_0/2$ and $W = \sqrt{2}a_0$. One can see that the dislocation cores are located at the centre of each $N \times N$ square that form the rectangular domain with dimensions $2N \times N$. This choice is made in order to have the most regular distribution of dislocations. However, the model enables to study less regular microstructures.

3.2 Results

The PF results are compared to the analytical models available in the literature for the four following cases:

1. Sink efficiency calculation with isotropic diffusion without elasticity (case 1).
2. Sink efficiency calculation with anisotropic diffusion and without elasticity (case 1 bis).
3. Composition profile calculation with elasticity, but without sink (case 2).
4. Sink efficiency calculation with elasticity (case 3).

In each simulation, only one type of sink s and PD n are considered, so the sink efficiency Z_n^s of sink s for PD n will be simply noted Z in the following parts. As a preliminary remark, since $K_0 = J^s$ at steady state, the value of Z can be deduced from equation (2.34). In all the simulations, $K_0^* = 3 \times 10^{-8}$, which corresponds to a few dpa per year. For dislocation lines, the sink density is in m^{-2} (length of dislocation per unit volume, noted ρ_l in the following parts), which implies that Z is dimensionless.

3.2.1 Sink efficiency without elastic interaction (case 1)

In the absence of elastic effects, the calculation domain is reduced to a square system with N^2 grid cells (see Fig. 2.3a)). The periodic boundary conditions create an infinite microstructure, instead of considering an outer boundary delimiting the reservoir, as usually done in rate theory. In this part, PDs are generated by irradiation at rate K_0 and absorbed by a central sink for which different values of the radius r_0 are considered and $X^s = 0$. Simulations run until steady state is reached. An example of the resulting transient ($t^* = 0$ through 2000) and steady-state ($t^* = 6000$) profiles are represented in Fig. 3.1 along $y = Na_0/2$ for $N = 64$ and $r_0 = 2\,a_0$. These profiles show the good behaviour of the sink and reveal that the absorption flux J^{abs} is efficient enough to maintain the composition in the sink at X^s.

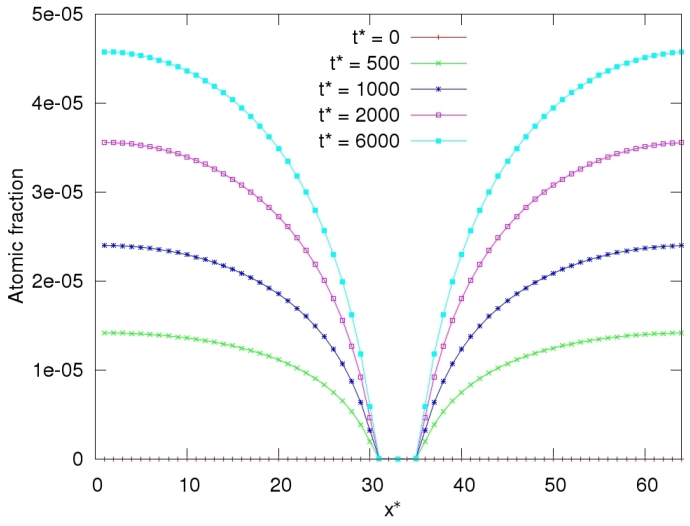

Figure 3.1: Site fraction profiles for different computation times. The sink is at the centre of the system.

In the PF simulations, N and r_0 vary respectively in the range $[32 - 1024]$ and $[2.58\,a_0 - 5.55\,a_0]$, i.e. the sink volume fraction $f_d = \pi {r_0}^2/(a_0 N)^2$ varies between 2×10^{-5} and 9.47×10^{-2}. For each simulation, the sink efficiency is obtained from equation (2.34) and all the PF results are compiled in Fig. 3.2. The data are also represented as a function of dislocation density by using the relation $f_d = \rho_l\, \pi {r_0}^2$ with $r_0 = 2\,\mathrm{nm}$.

The sink efficiencies calculated by Laplace, Poisson and Wiedersich models are

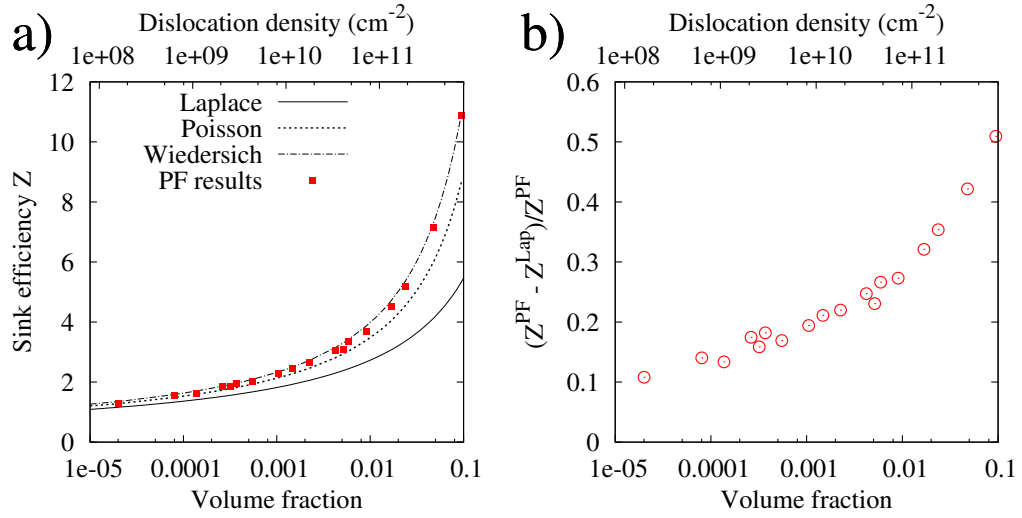

Figure 3.2: a) Sink efficiencies obtained by various analytical models (lines) and PF method (points) as a function of the sink volume fraction in the system. b) Relative difference between the Laplace and PF sink efficiency.

respectively noted Z^{Lap}, Z^{Pois} and Z^{W}. The sink efficiencies obtained with the PF method Z^{PF} are then compared to the analytical expressions available in the literature [28] (see section 1.3.2).

The analytical expressions are plotted in Fig. 3.2 together with the PF results. Our calculations are in very good agreement with Z^{W} and show significant differences with Z^{Lap} and Z^{Pois}. This behaviour can be easily understood since only the Wiedersich model solves the Poisson equation and considers the true average spatial composition $\bar{X}$ to calculate Z, which makes it very similar to the PF simulations (see equation (1.6)). Z^{PF} is slightly lower than Z^{W}, a trend that can be attributed to the difference between the system geometries (square in PF model versus circular in Wiedersich model).

This comparison constitutes a non trivial validation of the PF method used as a tool to predict the sink behaviour of straight dislocation. The same methodology can be applied to any type of structural defect (grain boundaries, cavities, etc.) whatever its morphology since the use of the order parameter $\lambda(\mathbf{r})$ allows to consider any shape in the simulation domain. The key point is to define properly J^{abs} in order to have a sink boundary condition equivalent to a Dirichlet one. This validation constitutes a necessary preliminary step before the implementation of an elastic drift in the diffusion equation.

Finally, it must be emphasized that the model predicts very different results on a large range of sink volume fraction values, as illustrated in Fig. 3.2b): for a dislocation density between 10^8 cm^{-2} and 10^{11} cm^{-2}, the relative difference $(Z^{\mathrm{PF}} - Z^{\mathrm{Lap}})/Z^{\mathrm{PF}}$ varies between 10 % and 30 %. These results suggest it is of first importance to solve the Poisson equation in the case of an irradiation uniformly applied on the system, and to consider the equivalence $X^{\mathrm{RT}} = \bar{X}$ instead of $X^{\mathrm{RT}} = X(R)$ (see section 1.3.1). The following parts show how these arguments can be generalised when elasticity effects are taken into account.

The algorithm explained in section 2.6 has been employed for most of the calculation presented in this chapter. The validation process is described as follows: a system with size 64×64 cells is created. A cylindrical sink analogous to the one in section 3.2.1 is used, with $r_0 = 3.5\, a_0$. PDs are generated at rate $K_0^* = 3 \times 10^{-8}$. The dimensionless time is chosen to be $\Delta t^* = 10^{-2}$. The evolutions of the average composition for various values of the period θ are compared in Fig. 3.3 along to $\bar{X}(t, \theta \to \infty)$ that is obtained without using the accelerated method.

The computation time is estimated for a 3 % accuracy with the steady-state average composition. The number of time steps needed to reach this accuracy are compiled in Table 3.1. The convergence is obtained 24 times faster with $\theta = 5$ than without the accelerated convergence algorithm ($\theta \to \infty$).

Table 3.1: Time steps needed to reach a 3 % accuracy as a function of θ.

θ (time steps)	Time steps for 3 % accuracy
∞	363000
50000	100000
5000	30000
1000	18000
100	15000
5	15000

The value of $\bar{X}_{\text{est}}^{n+1}$, calculated from Eq. (2.39) is plotted along $\bar{X}(\theta \to \infty)$ obtained with PF computation on Fig. 3.4. Even without the accelerated convergence algorithm, this simple local estimation of the steady state average composition gives good results. The steady state value is obtained 4 times faster by $\bar{X}_{\text{est}}^{n+1}$ than by directly considering $\bar{X}(\theta \to \infty)$.

3.2.2 Anisotropic diffusion (case 1 bis)

Woo et al. [49] showed that diffusion anisotropy of the SIA in Zr has a strong effect on sink efficiency and can lead to a significant absorption bias (see section 1.3.5.2).

It should be emphasised that, in their work, Woo and Goesele [49] considered the Laplace boundary conditions (fixed composition at the sink and reservoir boundaries, see section 1.3.2.1) to obtain these conclusions. As we showed that the Wiedersich conditions give different results from Laplace ones in the case of isotropic diffusion (see section 3.2.1), we can wonder in which extent results are modified by application of the Wiedersich conditions.

3.2.2.1 Model PF/W

In order to complete the study of Woo and Goesele, the PF technique is used (see chapter 2). We have shown that the PF boundary conditions are as realistic as the Wiedersich ones. Our PF code has been extended to allow anisotropic diffusion to be taken into account. The objective is to calculate the sink efficiency as a function of the diffusion coefficient anisotropy. As in the model by Woo and Goesele, elastic interactions are neglected. In this part, we consider that the vacancy has

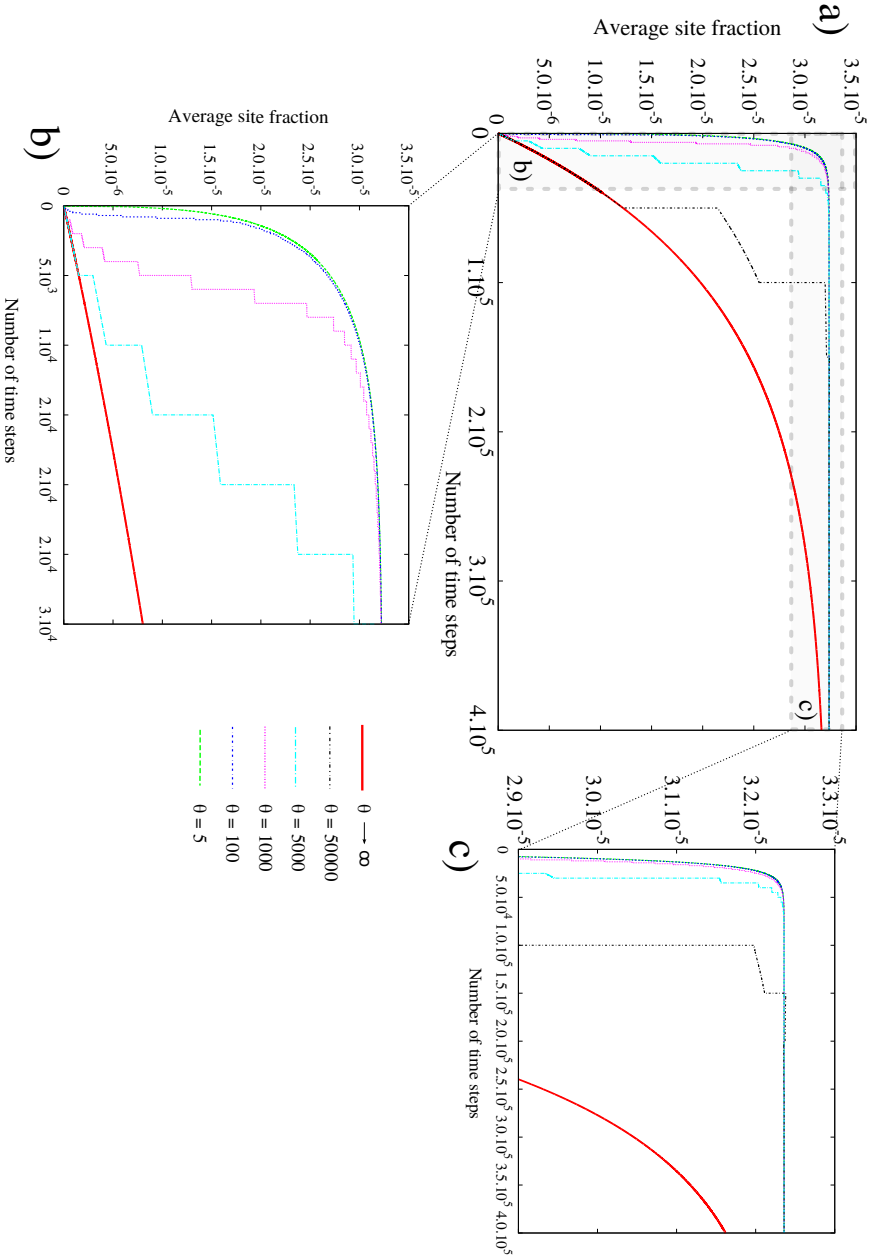

Figure 3.3: Average site fraction of PDs in a 64×64 system with various values of $\theta \in \{5, 100, 1000, 5000, 50000\}$. a) Evolution during the full simulation, b) a zoom on the first time steps, in order to see the quick growth of $\bar{X}$ in simulations with low θ values and c) zoom close to the steady-state site fraction. The thicker line corresponds to the calculation without the accelerated technique ($\theta \to \infty$). It is obvious that the steady-state is obtained faster for low values of θ.

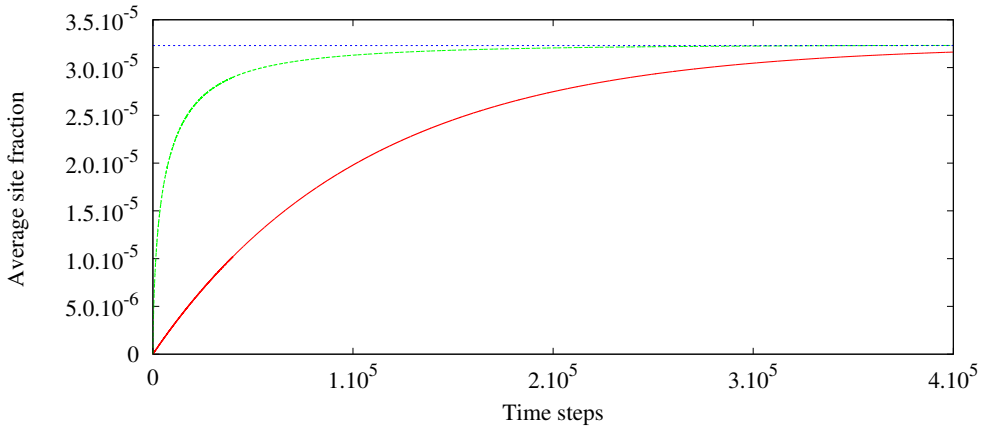

Figure 3.4: Average site fraction $\bar{X}(t)$ in the 64×64 system, with $\theta \to \infty$ (red solid line). Estimated steady-state average composition $\bar{X}_{\text{est}}^{n+1}$ from Eq (2.40) (green dashed line). It can be seen that the estimated composition approaches the true steady-state composition ($\bar{X} = 3.23 \times 10^{-5}$ (blue horizontal line)) way faster than the composition directly obtained from the calculation.

an isotropic diffusion tensor, while the SIA diffusion is anisotropic. As in the work of Woo and Goesele, we consider that the SIA has a diffusion coefficient D_a in the basal plane, and D_c in direction normal to it. Sink efficiencies are calculated for systems equivalent to Fig. 2.3a). The effect of the factor D_a/D_c is studied in this part. In our case, D_a is the diffusion coefficient in direction y and D_c is the diffusion coefficient in direction x. As a consequence, the modelled system is equivalent to that from section 1.3.5.2 with angle $\phi = \pi/2$. The calculations are made for factor D_a/D_c from 1 to 100, which is much higher than the validity domain of the Woo and Goesele expression. The sink efficiency is deduced from Eq. (2.34), with $D = \bar{D} = \sqrt{D_a/D_c}$. In this section, this model will be designated as PF/W.

3.2.2.2 Model PF/Lap

In addition to the framework described in section 3.2.2.1, the PF model is modified in order to consider boundary conditions close to those of the model of Woo and Goesele. It has been previously shown that imposing a flux J^{abs} given by equation (2.23) in the volume occupied by the sink is equivalent to imposing a composition X^s in the sink volume. This approach is therefore generalised to impose a composition $X(R)$ at the surface of a circular simulation domain of radius R. The part of the simulation domain outside this circle is subjected to a flux J^{prod} of the form:

$$J^{\text{prod}}(\mathbf{r}) = \lambda^{\text{prod}}(\mathbf{r}) \cdot \lambda^{\text{eff}} \cdot [X(\mathbf{r}, t) - X(R)] \tag{3.2}$$

where the order parameter λ^{prod} is equal to 0 inside the reservoirs of radius R centred on (x_1, y_1) and (x_2, y_1), and 1 outside. Equation (2.22) is modified to take into account this flux and K_0 is put to zero to reproduce the Laplace conditions. Therefore, to obtain results in conditions close to those of the Laplace model, the

following equation has to be solved:

$$\frac{\partial X}{\partial t}(\mathbf{r},t) = \boldsymbol{\nabla}\left[\mathbf{M}(X)\cdot\boldsymbol{\nabla}\mu(\mathbf{r},t)\right] - J^{\text{prod}} - J^{\text{abs}} \tag{3.3}$$

The corresponding geometrical configuration (noted PF/Lap) is represented in Fig. 3.5.

The sink efficiency is then defined as:

$$Z_{\text{PF/Lap}} = \frac{J_s}{\rho_l \bar{D} X(r=R)} \tag{3.4}$$

where:

$$J_s = \int_V J^{\text{abs}}(\mathbf{r})\mathrm{d}r \tag{3.5}$$

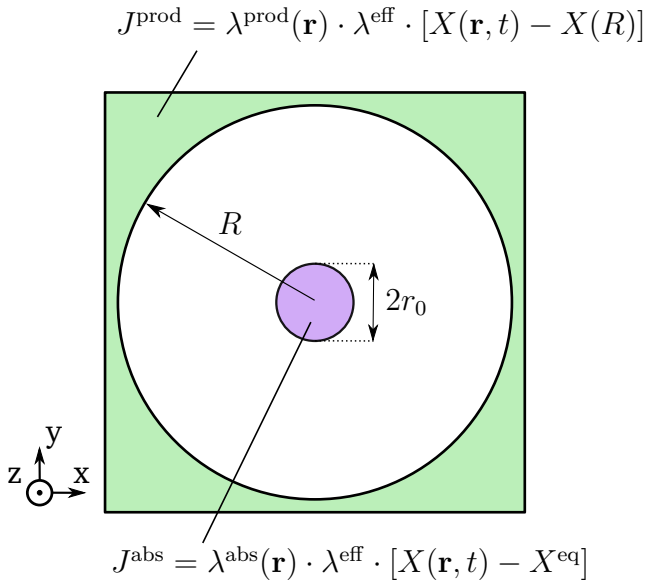

Figure 3.5: Diagram of the PF/Lap model. The sink region is in purple, the production region in light green.

3.2.2.3 Results

Sink efficiencies from PF/W, PF/Lap models and the analytical solution by Woo and Goesele are given in Fig. 3.6. The PF/W and PF/Lap are modelled in $N \times N$ domains with $N = 128$, $a_0 = 0.323\,\text{nm}$. We consider that the angle between the line direction **l** and axis $\langle c \rangle$ is 90°, hence $D_x = D_a$ and $D_y = D_c$. The bias from the analytical solution of Woo is defined as:

$$\begin{aligned} B^{\text{Woo}}(\phi = \pi/2) &= 1 - \frac{Z^{\text{Woo}}(D_a/D_c = 1)}{Z^{\text{Woo}}(D_a/D_c = D_a)} \\ &= 1 - \frac{Z^{\text{Lap}}}{Z^{\text{Woo}}(D_a/D_c = D_a)} \end{aligned} \tag{3.6}$$

with $Z^{\mathrm{Woo}}(D_a/D_c = D_a)$ given by Eq. (1.37). The biases obtained with the 3 methods are plotted in Fig. 3.7. Composition maps at steady state are plotted on Fig. 3.8.

It can be seen on Fig. 3.6 that with the PF/W model the sink efficiency decreases with the factor D_a/D_c, while the sink efficiency increases in the PF/Lap results and the analytical solution of Woo. It must be noted that the agreement between the PF/Lap model and the analytical solution is very good, as their boundary conditions are very close. In addition, at $D_a/D_c = 1$, the PF/W model gives a higher sink efficiency than the other models. This phenomenon is due to the difference in the boundary conditions, as described in section 3.2.1, and observed in particular in Fig. 3.2. While the sink efficiencies and biases of PF/Lap model and the analytical solution are increasing functions of D_a/D_c, the sink efficiency calculated with the PF/W model is a decreasing function of D_a/D_c.

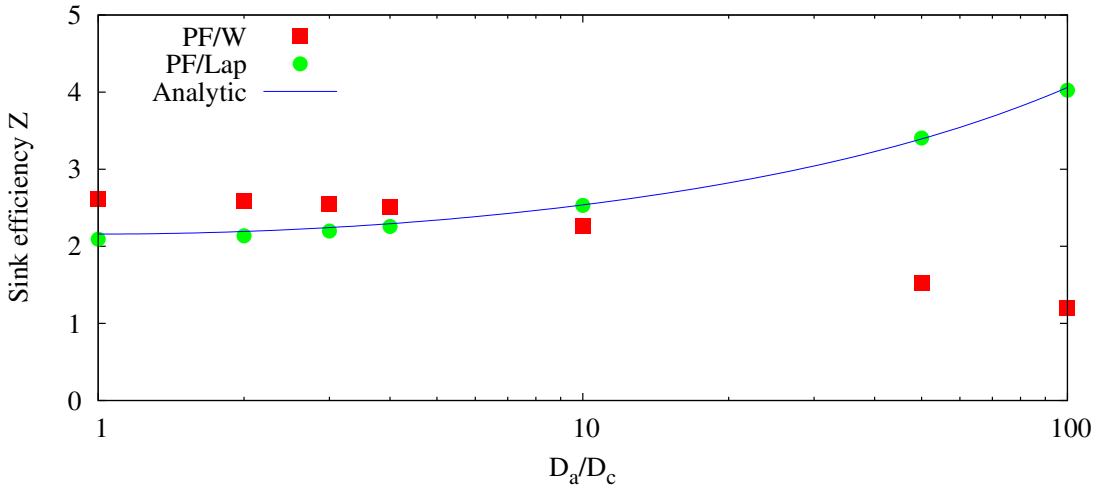

Figure 3.6: Sink efficiency of anisotropically diffusing SIAs, as a function of D_a/D_c. Results of PF/W model (red squares), PF/Lap (green circles) and Eq. (1.37) (solid blue line).

3.2.2.4 Lattice effect

Simulations performed in previous section have been made with the fast diffusion coefficient oriented in direction $[100]$ and the low diffusion coefficient oriented towards $[010]$. PF model induces periodic boundary conditions, dislocations are organised as a regular lattice in directions $[100]$ and $[010]$. We want to evaluate the effect of relative organisation of sinks and the main directions of the diffusion tensor.

In order to evaluate this effect, the same framework as PF/W is considered (see Fig. 2.3a)). The diffusion tensor is defined as:

$$D_{\mathrm{i}}(\theta) = \begin{pmatrix} D_{11}\cos^2\theta + D_{22}\sin^2\theta & (D_{22}-D_{11})\cos\theta\sin\theta & 0 \\ (D_{22}-D_{11})\cos\theta\sin\theta & D_{11}\sin^2\theta + D_{22}\cos^2\theta & 0 \\ 0 & 0 & D_{33} \end{pmatrix} \tag{3.7}$$

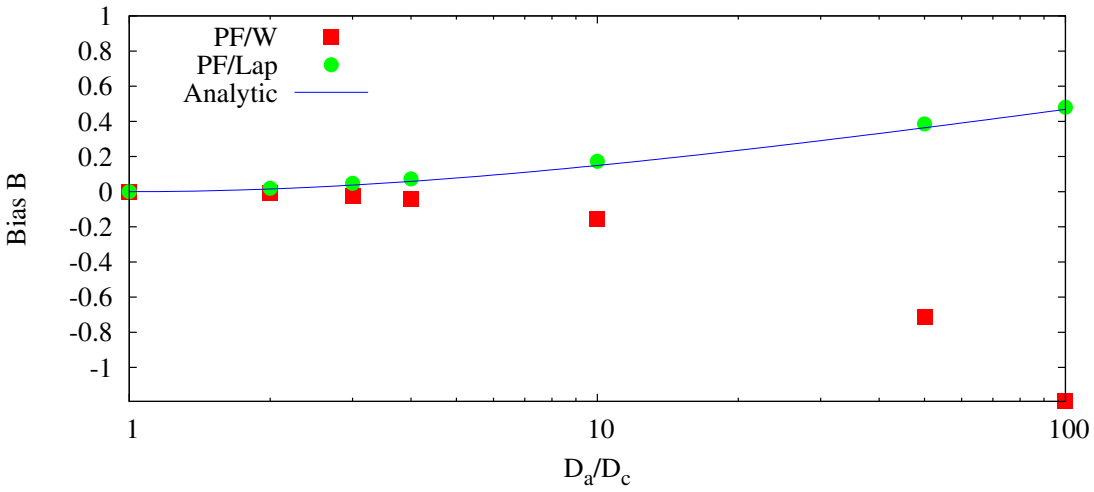

Figure 3.7: Absorption bias by a cylindrical sink by 3 different techniques: $B(\mathrm{Woo})$ is the analytical solution (1.37), $B(\mathrm{PF/Lap})$ is calculated with PF/Lap method (close to that of Woo, Fig. 3.15); $B(\mathrm{PF/W})$ is the PF/W method (see Fig. 2.3a)).

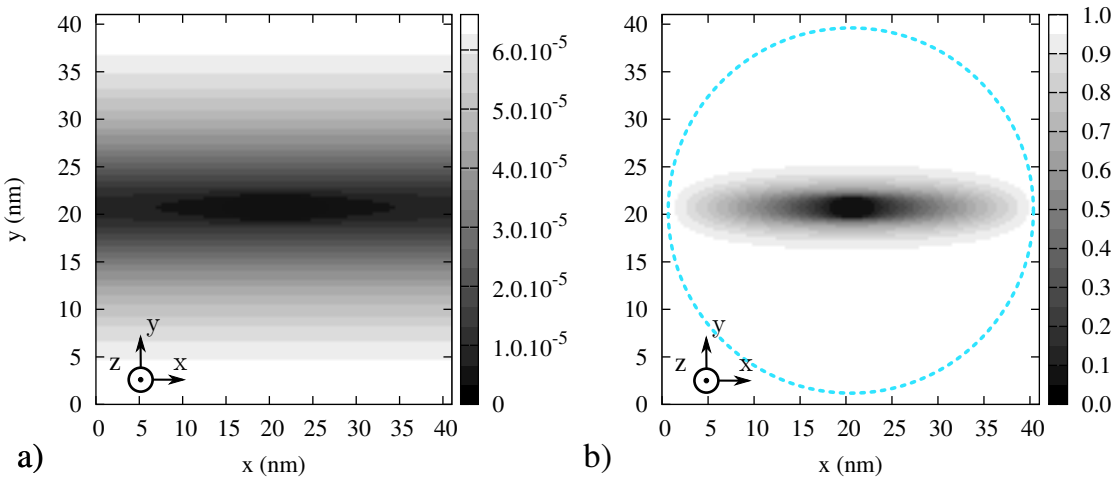

Figure 3.8: Atomic fraction maps at steady state for $D_a/D_c = 100$ in model PF/W (a) and PF/Lap (b) value of $X/X(r \geqslant R)$ in a 128×128 cells system. The blue dotted circle designates the inner boundary of the source region of radius R.

where θ is a rotation angle around axis $\langle z \rangle \parallel \mathbf{l}$. Simulations on a series of values $\theta \in [0, \pi/4]$ (that is between $[100]$ and $[110]$ orientations) are made. Due to the symmetries of the system (periodic with period $\pi/2$ and reflexive symmetry with respect with axis $\theta = \pi/4$), the sweep domain on θ is large enough to explore all possible orientations. In addition, calculations are made for $D_{11}/D_{22} \in \{4, 10, 50, 100\}$. Results are gathered in Fig. 3.9.

It can be seen that for $D_{11}/D_{22} = 4$, a maximum is attained when $\theta = 45°$ (equivalent to the fast diffusion direction oriented towards $[110]$). On the opposite, the sink efficiency is minimum when $\theta = 0$. For higher anisotropies ($D_{11}/D_{22} \geqslant 10$), $Z(\theta = 45°)$ is a local minimum. In addition, a new local minimum between 25° and 30° appears for even higher anisotropies ($D_{11}/D_{22} \geqslant 50$).

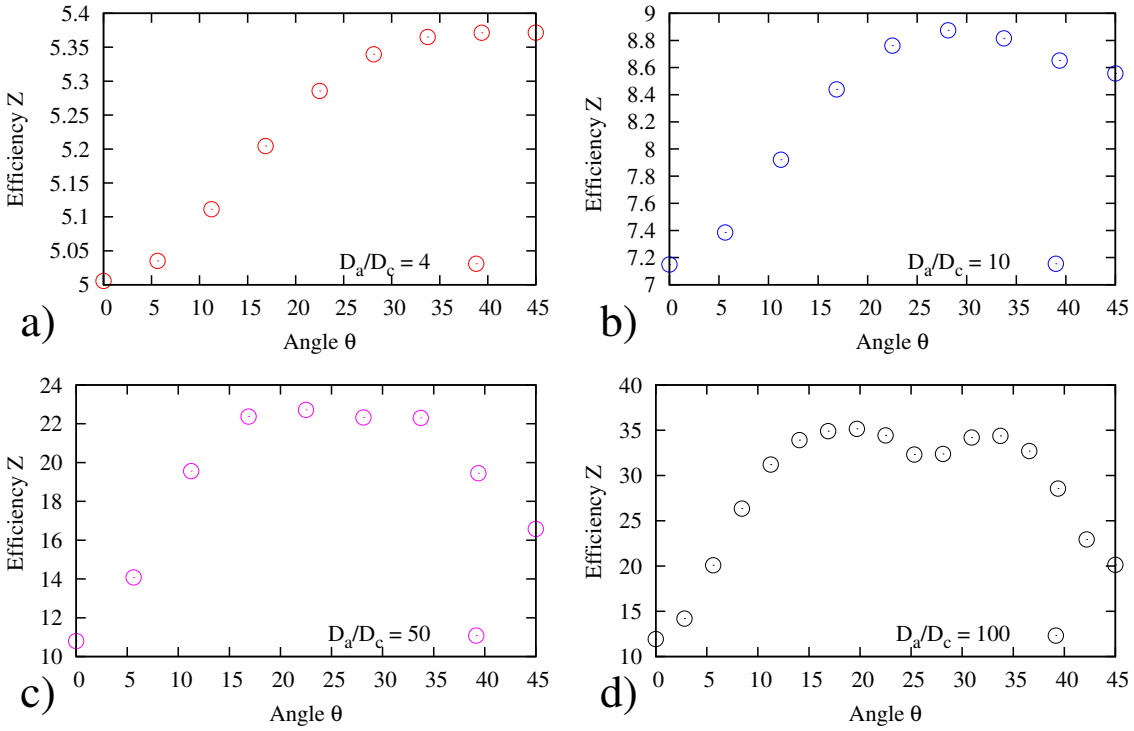

Figure 3.9: Absorption efficiencies of a dislocation lattice as a function of the angle θ between the fast diffusion direction and axis $[100]$. Results are given for: a) $D_{11}/D_{22} = 4$, b) $D_{11}/D_{22} = 10$, c) $D_{11}/D_{22} = 50$, d) $D_{11}/D_{22} = 100$.

3.2.2.5 Discussion

A striking result in Fig. 3.6 is that depending on the model, the sink efficiency can be an increasing or decreasing function of the factor D_a/D_c. This section is dedicated to the understanding of this phenomenon.

In order to better understand the limits of the boundary conditions proposed by Woo and Goesele, we propose a thought experiment. In the case of Laplace conditions, the sink efficiency is the consequence of the total flux from the reservoir border to the sink surface. Woo and Goesele showed that the anisotropic diffusion problem in a hollow cylinder with circular base is equivalent to the isotropic diffusion in a hollow cylinder with elliptical base (by means of space variable

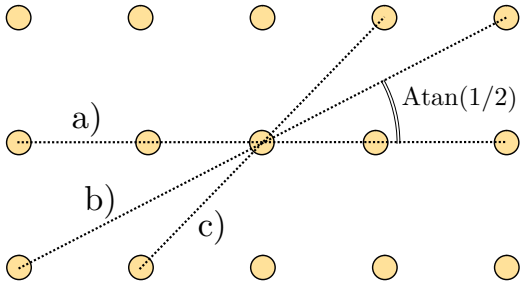

Figure 3.10: Schematics of the sink lattice as modelled in PF. 3 particular directions are highlighted: a) $\theta = 0$, b) $\theta = \mathrm{atan}(1/2)$, c) $\theta = 45°$. These directions correspond to local minima in Fig. 3.8d).

change). The main axis of the ellipse is smaller along fast diffusion directions (see Fig. 3.11). If the diffusion is strongly anisotropic, this is equivalent to shortening the distance between the reservoir and the sink, in one direction. As a consequence, this will create a local high flux zone, that will increase the calculated sink efficiency. In the limiting case of an infinite diffusion coefficient in one direction, it is equivalent to have a contact between sink and reservoir, by thus an infinite flux and an infinite sink efficiency.

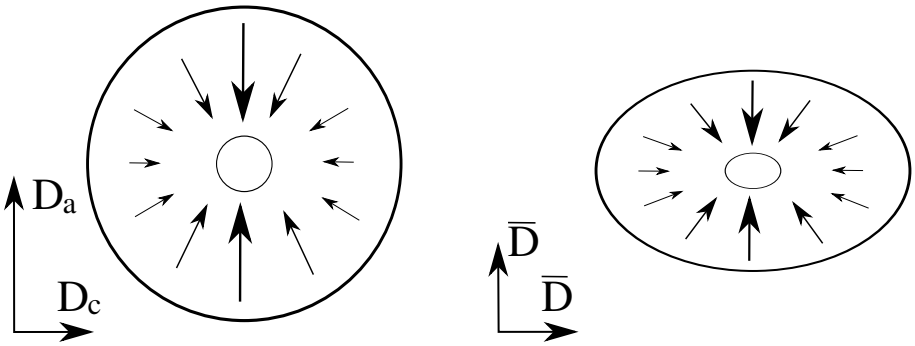

Figure 3.11: Diagram of diffusion of anisotropic migration PDs around a cylindrical sink. Left: anisotropic diffusion faster along $\langle a \rangle$ direction. The arrows represent the fluxes. Right: equivalent system in an ellipse-based cylindrical sink and isotropic diffusion coefficient $\bar{D} = (D_a/D_c)^{1/2}$. It is obvious that the higher the value of D_a the higher the flux towards the sink as the distance will be lower and lower.

Let's imagine the same case with the Wiedersich boundary conditions. If we start with isotropic diffusion, the boundary conditions are equivalent to the case described in section 1.3.2.3. If one direction is faster diffusing, the system can be considered as a pair of cylinders with elliptical base (see Fig. 3.12). When the cylinders are close to each other, the sink will lower the concentration, and by thus, increase the sink efficiency. However, in the other direction, the concentration will remain high. As a consequence, no matter how fast the PDs diffuse in a

given direction, there will remain a "trap zone" where PDs can accumulate. The average concentration will then be fixed by this region. The sink efficiency will remain finite, even for a very high diffusion coefficient in the fast diffusion direction. In these conditions (high value of D_a, hence $\bar{D}$, and finite value of $\bar{X}$), the sink efficiency will tend towards 0.

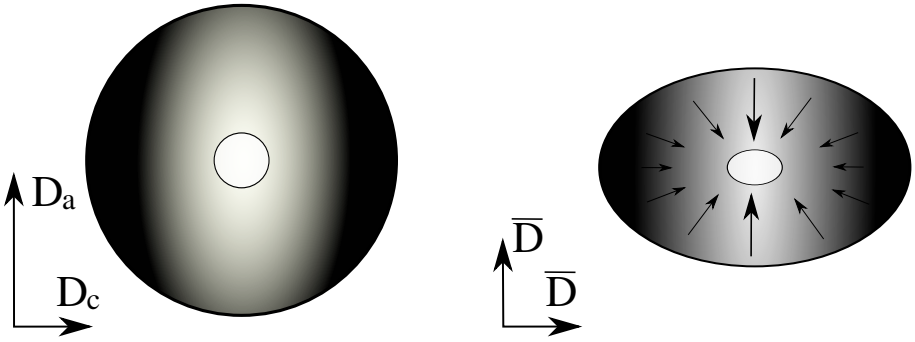

Figure 3.12: Diagram of diffusion of anisotropic migration PDs around a cylindrical sink, with $B_0 = 0$. Left: anisotropic diffusion faster along $\langle a \rangle$ direction. The dark zones are the enriched regions. Right: equivalent system in an ellipse-based cylindrical sink and isotropic diffusion coefficient $\bar{D}$. It is obvious that whatever the value of D_a, there will always be a "trap region" in directions normal to the $\langle a \rangle$ axis (vertical).

This thought experiment shows that in the case of anisotropic diffusion, the conditions used could lead to major discrepancy. This explains the fundamental difference in behaviour between PF/Lap and PF/W in Fig. 3.6. For high diffusion anisotropies, the use for the PF/W model is necessary for proper sink efficiency estimation. While it has been previously seen that Laplace conditions tend to underestimate the sink efficiency and elastic bias for isotropic elasticity (see sec. 3.2.1), they tend to overestimate the contribution of diffusion anisotropy.

Concerning the effect of the angle θ, it must be noted that local minima always correspond to a dislocation alignment direction. It is obvious that $[100]$ and $[110]$ are particular directions. In addition, it is remarkable that the minimum between 25° and 30° could correspond to direction $[210]$, for which $\theta = \mathrm{atan}(1/2) = 26°$ (see Fig. 3.10). As a consequence, the alignment of the fast diffusion direction with a particular direction of the lattice leads to a lower sink efficiency than for a random orientation. This is due to the effect of "trap zone". In this case, trap zones are parallel with the main axis of the dislocation lattice ($[100]$, $[110]$ and $[210]$), but are not aligned with sinks. A defect in this region will diffuse fast without being captured by a sink. The defect is then trapped in a "hallway". Defect concentration has then the capacity to build up, as they need a long time to be absorbed. As a consequence, this effect lowers the capacity of the microstructure to absorb the corresponding migrating defect.

This phenomenon has already been commented by Malerba et al. [23] on the case of the 1D diffusion of crowdions with OKMC. It is also considered the cause of vacancy nature defects alignment in irradiated metals: the defects would align

along fast diffusion directions of SIAs in order to lower their SIA capture efficiency, and by thus, their bias (see section 1.3.5.3).

This section showed the relevance of the PF method to study anisotropic diffusion and absorption by regular sink lattices. It should be emphasised that the PF method allows to include more than one sink in the system. As a consequence, it is easy to simulate a less regular sink distribution by randomizing the sinks locations.

3.2.3 PD diffusion in the stress field of a dislocation line (case 2)

The introduction of elasticity induces the specification of a space scale in the PF model. In the following, the grid spacing a_0 is systematically chosen equal to the Burgers vector $\mathbf{b}$. In this part, the calculations are performed using the configuration described in case 2 (see Fig. 2.3). The physical parameters are specified in Table 3.2: vacancies with a relaxation volume Ω_v diffuse in an elastically isotropic matrix characterized by its shear modulus μ and Poisson ratio ν. K^0 and J^{abs} are set at 0, and so the average composition $\bar{X}$ remains constant during the simulation. In order to describe every validation steps, the stress field of a straight dislocation has been compared to the analytical solution in the framework of isotropic elasticity in section A.1 (to be found in appendix). This section will focus on the diffusion of PDs in the stress field of this dislocation. In every of those steps, the numerical solution from PF model will be compared to analytical solutions.

Table 3.2: Physical parameters of the system when elasticity effects are taken into account.

Shear modulus μ, GPa	33
Poisson ratio ν	0.33
Temperature T, K	600
Atomic volume V_{at}, m^3	2.3×10^{-29}
Vacancy relaxation volume, Ω_v	$-0.6 \times V_{\text{at}}$
SIA relaxation volume, Ω_i	$+1.2 \times V_{\text{at}}$
Burgers vector b, nm	0.3

The PF model enables to compute the elastic diffusion drift of PDs in a stress field by solving equation (2.29). The site fraction field is initially uniform and set at a very low composition close to the thermal equilibrium value at $T = 600\ \text{K}$, $X(\mathbf{r}, t = 0) = 10^{-15}$. At thermal equilibrium, the presence of dislocations induce a PD compositional inhomogeneity that can be compared with Cottrell atmospheres in the case of carbon atoms surrounding dislocations in iron. The corresponding profile at $x = x_1$ is represented in Fig. 3.13.

In this specific case, the PF steady-state profile can be compared to an analytical solution. Indeed, for an elastically isotropic crystal with an isotropic Vegard tensor, the reduced elastic potential $\mu_{\text{el}}^{\text{iso}*}(\mathbf{r})$ can be expressed by Eq. (1.23).

The resulting steady-state profile can be easily calculated:

$$X(r, \theta) = \bar{X}\ \exp\left(-\mu_{\text{el}}^{\text{iso}*}(r, \theta)\right) \tag{3.8}$$

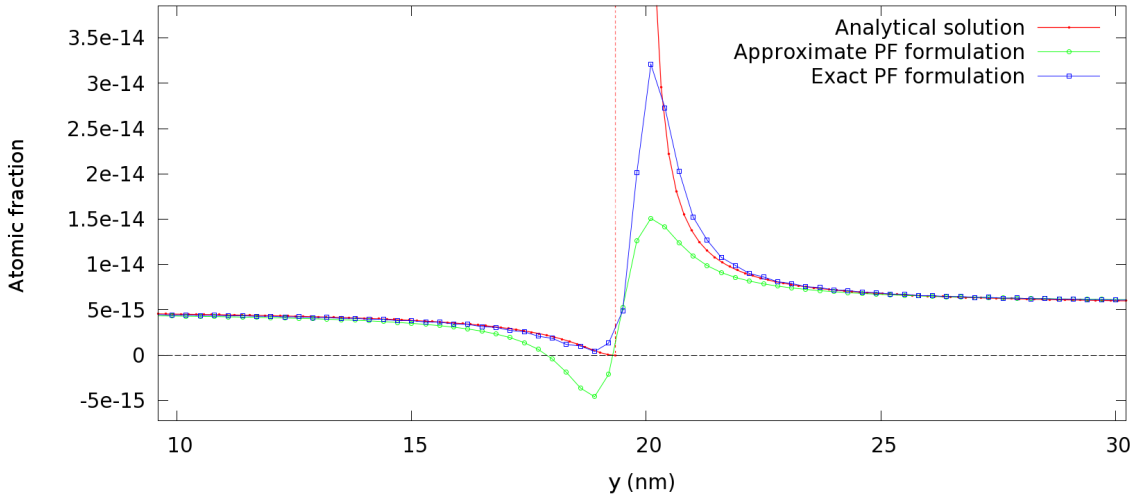

Figure 3.13: Composition profiles of vacancies at thermal equilibrium at 600 K around a dislocation core obtained with both approximate method (3.9) (circles) and the exact method (2.29) (squares), compared to analytical solution (3.8) (solid curve).

The analytical profile is also plotted in Fig. 3.13 and is quite close to the PF one, except near the dislocation core, where linear elasticity is not valid.

Equation (2.29) might be simplified by assuming that the composition in the drift term is uniform and equal to $\bar{X}$. This assumption must be verified. If $K_0 = J^{\text{abs}} = 0$, then equation (2.29) can be rewritten as:

$$\frac{\partial X}{\partial t} = D\nabla^2 X + \frac{D\bar{X}}{k_B T}\nabla^2\left(\frac{\partial E_{\text{el}}}{\partial X}\right) \tag{3.9}$$

which, in Fourier space, gives:

$$\widetilde{\frac{\partial X}{\partial t^*}}(\tilde{\mathbf{q}}^*, t^*) = -(\tilde{\mathbf{q}}^*)^2 \tilde{X}(\tilde{\mathbf{q}}^*, t^*) - (\tilde{\mathbf{q}}^*)^2\, \bar{X}\, \widetilde{\mu^*_{\text{el}}}(\tilde{\mathbf{q}}^*, t^*) \tag{3.10}$$

The approximate equation (3.10) requires less computational time (2 instead of 7 Fourier transforms to perform at each time step), which makes it very attractive to implement. As a consequence, it has been tested in the same conditions as the exact equation (2.29) to conclude on the validity of this assumption to simulate a Cottrell atmosphere. Both the exact and approximate solutions have been plotted on Fig. 3.13. The approximate method leads to an almost symmetrical profile on each side of the core, while the analytical solution leads to an exponential increase of the composition in the compression zone. Moreover, the approximate solution leads to negative compositions in the tensile region around the dislocation.

These results are a priori at odds with previous results reported in the literature [86] and based on this simplified solution. However, it must be emphasized that in Fig. 3.13, the approximate solution is tested in extreme conditions in comparison with the results of the literature. Indeed, the test has been performed

with (i) a high value of the Vegard coefficient (0.13 in our case *vs* 0.05 in [86]) and (ii) very low site fraction values. These two physical parameters combined with the approximation made to solve the diffusion equation explain the negative values. Since the approximate solution leads to non physical values of the compositions in the neighbourhood of the dislocations, the above assumption can not be made to solve equation (2.29). As a consequence, in conditions (i) and (ii) specific to irradiation, the exact formulation (2.29) must be systematically used to calculate sink efficiencies when typical values are considered for the main physical parameters (average PD compositions and strength of the elastic interactions).

3.2.4 Sink efficiency with elastic interactions (case 3)

It has been shown that the PF model is able to predict the diffusion of PDs around a sink without elasticity (section 3.2.1), and simulate the diffusion of PDs in the stress field of a dislocation (section 3.2.3). In this section, the dislocation lines are coupled with absorbing sinks modelled as cylinders centred on the dislocation cores. In the following we take $r_0 = 1.27\,\mathrm{nm}$ ($\approx 4\,a_0$) and the system configuration is represented in Fig. 2.3c). The evolution of PD population is simulated by solving equation (2.22). Several simulations are performed with different values of N between 20 ($\rho_l = 2.78\times10^{12}\mathrm{cm}^{-2}$) and 512 ($\rho_l = 4.24\times10^{9}\mathrm{cm}^{-2}$). As the relaxation volume of vacancies and SIAs have opposite signs (see Table 3.2), the equilibrium composition profiles are different and represented in Fig. 3.14) for $N = 128$. As expected, the depleted and enriched zones in vacancies correspond respectively to the traction and compression zones, whereas the opposite behaviour is observed for SIAs. It can be noticed that the centre of the composition isocurves do not coincide with the dislocation cores: they are in the traction zone for vacancies and in the compression zone for interstitials. This phenomenon is an expected effect of the elastic interaction: the enriched and depleted zones correspond to those of the Cottrell atmosphere (see section 3.2.3).

The PF sink efficiencies $Z_{\mathrm{el}}^{\mathrm{PF}}$ are plotted as a function of the dislocation density in Fig. 3.15 (filled squares): for both vacancies and SIAs, the sink efficiency increases with dislocation density.

The PF results are compared to the Rauh and Simon (RS) model [33] (see section 1.3.2.5). The RS analytical results are represented in full lines in Fig. 3.15 and are significantly different from the PF results. Several reasons may explain this discrepancy:

(i) The RS solution rests in the choice of a suitable boundary condition $X = X(R)$ at the surface of the reservoir, like in the Laplace model (see section 1.3.2.1). In the PF model, irradiation effects are taken into account via the creation rate K_0, like in the Poisson and Wiedersich models. Moreover, the RS model expresses J^s as a function of $(X(R) - X^{th})$ to deduce Z, like in the Laplace description, whereas the PF model uses $(\bar{X} - X^{th})$, like in the Wiedersich model. These choices were shown to induce significant differences in the obtained values of Z without elasticity (see section 3.2.1), so it is expected that the same considerations can be applied when elastic effects are considered.

(ii) In the RS model, the boundary condition at the surface of the reservoir does not depend on θ (see equation (1.21)), which corresponds to a perfectly circular

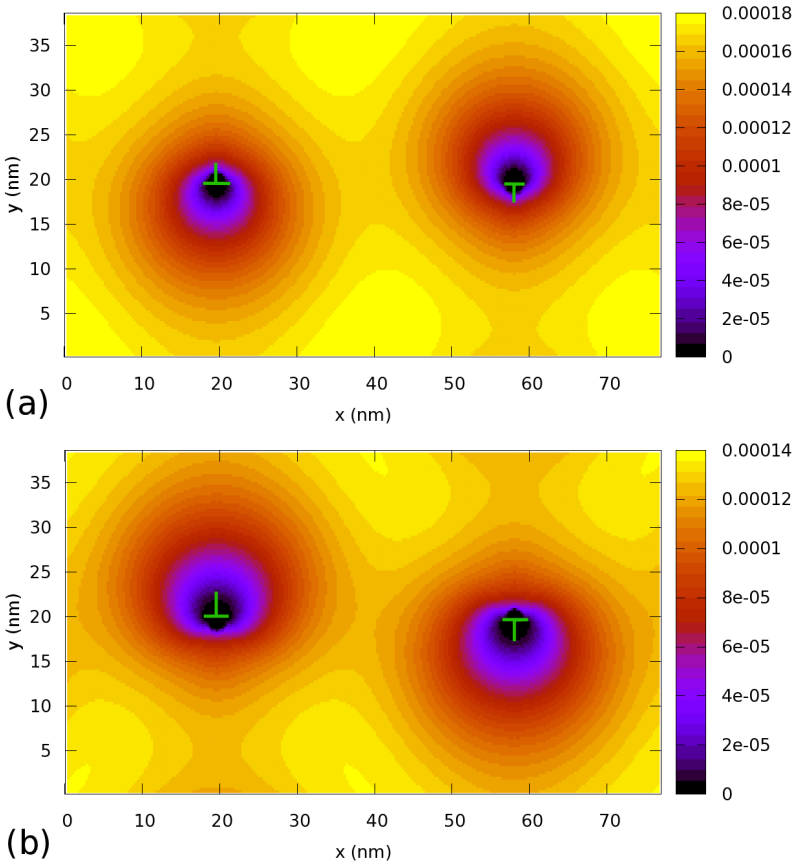

Figure 3.14: Steady-state composition map obtained by PF method for a) vacancies and b) self-interstitials. The edge dislocation positions and orientations are given in green. The rich and depleted regions for each PD are opposed, due to relaxation volumes with opposite sign.

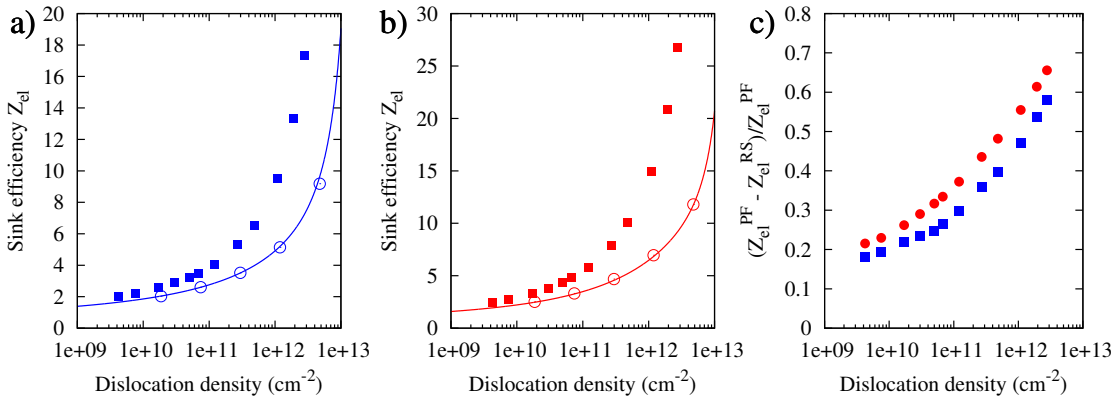

Figure 3.15: Sink efficiencies for a) vacancies and b) SIAs, obtained with the PF (filled squares), RS (full lines) and PFRS (empty circles) models. c) Relative difference between RS and PF sink efficiencies.

composition isocurve centred on the core of the dislocation. This assumption is quite arbitrary and is at odds with the PF composition maps represented in Fig. 3.14, which may lead to some differences between both models.

(iii) Elastic interactions between dislocations are ignored in the RS model, which limits its validity to low dislocation density. The proposed PF model does take into account all the elastic interactions between neighbouring dislocations (present in the simulation cell or obtained by periodic boundary conditions). These interactions may be important when a high dislocation density is considered.

(iv) Despite the validation of the PF model demonstrated in cases 1 and 2, numerical artefacts may lead to erroneous calculations when dealing with absorbing sinks in presence of elasticity effects.

To check these different arguments, the PF model is modified in order to integrate the main assumptions of the RS model. To this end, we considered a new order parameter that describes the source region, as in section 3.2.2.2. This approach is therefore generalised to impose a composition $X(R)$ at the surface of a circular simulation domain of radius R. The part of the simulation domain outside the circle is subjected to a flux J^{prod} defined by Eq. (3.2).

Equation (2.22) is modified to take into account this flux and K_0 is put to zero to reproduce the RS conditions. Therefore, to obtain results in conditions close to those of the RS model, equation (3.3) must be solved. This model is very close to the one proposed in section 3.2.2.2 for anisotropic diffusion. The difference in this section is that the diffusion tensors are considered isotropic, and that the dislocation stress field is taken into account. The sink efficiency Z_{RS} is deduced from an equation similar to Eq. 3.4, with $D = \bar{D}$.

The corresponding geometrical configuration (noted PFRS) is represented in Fig. 3.16 and is a convenient way to test points (i) and (ii) provided that $X(R)$ instead of $\bar{X}$ is used to calculate Z. To attenuate the effect mentioned in (iii), it has been necessary to use oversized systems ($N/2 \gg R$) to lower the elastic interaction between mirror dislocations and to approach the isolated dislocation case by this way, the dislocation were held sufficiently far from each other to neglect any interaction of the PD with neighbouring dislocations.

The sink efficiency obtained in the PFRS configuration is reported in Fig. 3.15: RS and PFRS results show very good agreement, which validates the PF methodology to calculate sink efficiency with elasticity. These results allow to discard the numerical argument (iv) as a possible explanation for the difference observed between the RS ans PF results and proves that the PF results are physically sound. It also confirms that the simplifying assumptions required to obtain the RS analytical solution can lead to significant discrepancy with real sink efficiencies evaluated in conditions close to those encountered in experimental situations: the relative difference $(Z_{\text{el}}^{\text{PF}} - Z_{\text{el}}^{RS})/Z_{\text{el}}^{\text{PF}}$ for vacancies (resp. SIAs) varies between 0.18 (resp. 0.22) for $\rho_l = 4.24 \times 10^9\ \text{cm}^{-2}$ and 0.58 (resp. 0.66) for $\rho_l = 2.78 \times 10^{12}\ \text{cm}^{-2}$ (see Fig. 3.15). This has a direct consequence on the bias factor B, defined in Eq. (1.34). The bias factor from the RS and PF models (respectively noted B^{RS} and B^{PF}) have been reported in Fig. 3.17.

It can clearly be seen that the RS model significantly underestimates the bias with respect to the PF model: B^{PF} (resp. B^{RS}) varies between 0.183 (resp. 0.147)

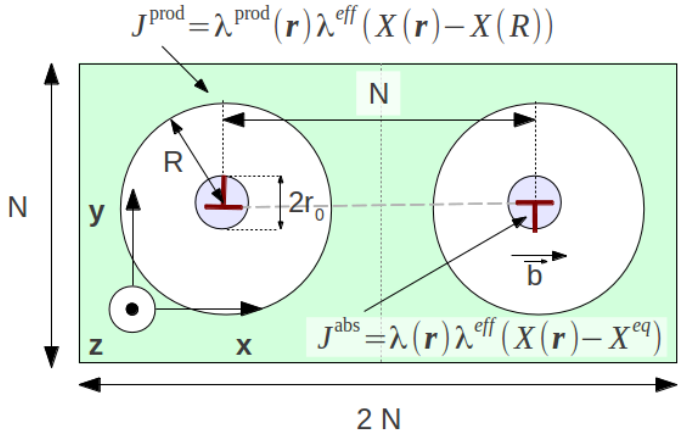

Figure 3.16: PFRS configuration.

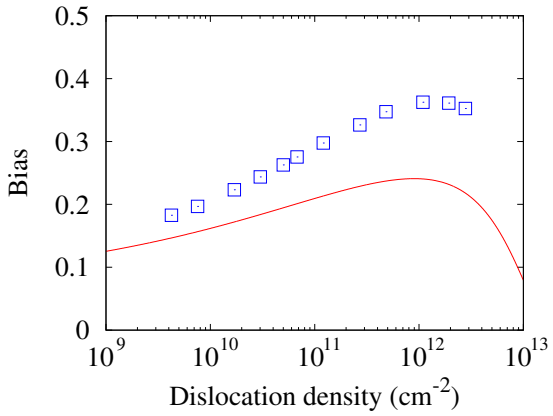

Figure 3.17: Comparison between B^{PF} (open squares) and B^{RS} (solid line) as a function of the dislocation density.

for $\rho_l = 4.24 \times 10^9\ \mathrm{cm}^{-2}$ and 0.363 (resp. 0.24) for $\rho_l = 1.09 \times 10^{12}\ \mathrm{cm}^{-2}$.

The RS and PF results are significantly different for typical values of ρ_l ($\approx 10^{10}\ \mathrm{cm}^{-2}$) in deformed or irradiated materials (see Fig. 3.15). This comparison allows to draw similar conclusions to those reported in section 3.2.1: (i) an irradiation uniformly applied on the system can not be properly taken into account by ad hoc conditions at the boundary of the reservoir (ii) the equivalence $X^{\mathrm{RT}} = \bar{X}$ instead of $X^{\mathrm{RT}} = X(R)$ (see Tab. 1.1) for the estimation of the sink efficiency should be systematically considered. In a previous work, Tomé et al. [38] calculated the sink efficiency of a straight dislocation by solving numerically the Poisson equation in presence of the elastic field generated by the dislocation. Although very innovative, this work did not draw special attention to the influence of (i) and (ii) on the resulting sink strength. Furthermore, the numerical solution adopted was explicitly developed to treat cylindrical geometries which implies strong restrictions on the reservoir geometry. Finally, in such approach, the elastic strain generated by the sink is an input field of the model while is it evaluated self-consistently in the

present approach. All these arguments justify the development of the new model presented in chapter 2.

As in section 3.2.1, the accelerated convergence algorithm (see section 2.6) should be validated when taking into account the stress field of the dislocations. An analogous system to the one of case 3 is used (Fig. 2.3c)), with a size 128×64 and a pair of dislocations characterised by $r_0 = 4\,a_0$, $b = a_0$, $\Omega_{\mathrm{PD}} = 0.6$ and the same elastic properties as in section 3.2.4. These results are compared to the function $\bar{X}(t)$ that is obtained without using the accelerated method ($\theta \to \infty$). The results are close to those without elasticity, except the occurrence of a slight bump in accelerated simulations. In the discussion, we will distinguish the bump occurring on the initial stage of Fig. 3.18 from the instability observed for high values of θ. In these cases, we can see that, instead of an increasing monotonous curve, a maximum is reached just after the rapid growth in the initial stage (see Fig. 3.18c)).

It must therefore be noted that:

- the value of the error in the bump is lower than 2 % at $N = 64$;
- the maximum error in the bump decreases with the size of the system, as revealed by supplementary simulations not reproduced in this manuscript for sake of brevity;
- this maximum error decreases when θ rises, but the disappearance of the bump is faster for simulation performed with low values of θ.

Despite the bump, the accelerated convergence algorithm is still faster than the limiting case of $\theta \to \infty$. In addition, in the case of small systems, it is easy to perform more calculation steps in order to ensure that the bump is properly suppressed. For large systems, increasing the number of time steps is costly, but the error due to the bump is lower than for small systems, since it never exceeds 2 %. As a consequence, the accelerated convergence algorithm is not limited to small domains. Surprisingly, this numerical artefact is not observed in the case of loops (see section 5.4.2). This case is very specific to straight dislocations with elasticity.

The computation time is estimated for a 3 % accuracy with the steady-state composition. The number of time steps needed to reach this accuracy are compiled in Table 3.3. The convergence is obtained 29 times faster with $\theta = 5$ than without the accelerated convergence algorithm ($\theta \to \infty$).

3.3 Discussion

The PF results allow an easy comparison between the capture efficiencies obtained with or without elasticity as a function of dislocation density. As shown in Fig. 3.19, the deduced relative difference $(Z_{\mathrm{el}}^{\mathrm{PF}} - Z^{\mathrm{PF}})/Z_{\mathrm{el}}^{\mathrm{PF}}$ for vacancies (resp. SIAs) varies between 0.12 (resp. 0.28) for $\rho_l = 4.24 \times 10^9\,\mathrm{cm}^{-2}$ and 0.22 (resp. 0.5) for $\rho_l = 1.09 \times 10^{12}\,\mathrm{cm}^{-2}$. This comparison confirms that taking into account elasticity is of first importance to correctly evaluate the capture efficiencies of dislocations. Moreover, the value of the shear modulus, taken equal to $33\,\mathrm{GPa}$ to

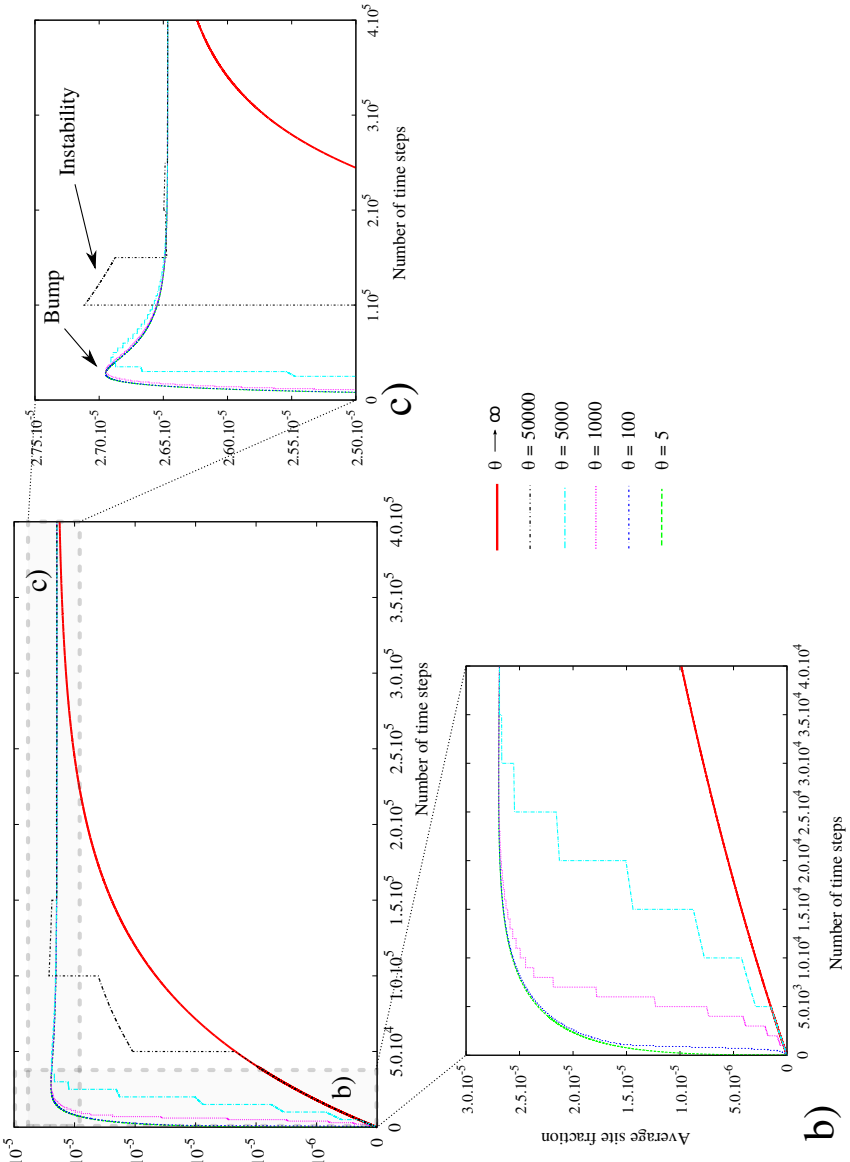

Figure 3.18: Average site fraction of PDs in a 128×64 system with various values of $\theta \in \{5, 100, 1000, 5000, 50000\}$. a) the evolution during the full simulation, b) a zoom on the first time steps, in order to see the quick growth of the low θ simulations and c) a zoom around the steady-state site fraction. The thicker line corresponds to the calculation without the accelerated technique ($\theta \to \infty$). It is obvious that the steady-state is obtained faster for low values of θ, in particular on a). The "bump" in the site fraction of low θ simulation can be seen on b). It is due to the acceleration technique is endemic to the case of straight dislocations with elasticity. In this graph, it can be noted that the bump is slightly higher for low θ values, but also that its disappearance is slower for high θ values.

Table 3.3: Time steps needed to reach a 3 % accuracy as a function of θ.

θ (time steps)	Time steps for 3 % accuracy
∞	291000
50000	99000
5000	29000
1000	18000
100	10000
5	10000

perform the calculations (see Table 3.2), must be compared to the shear modulus in other systems: for example, it is much lower than the value of C_{44} for bcc Fe ($\approx 120\,\mathrm{GPa}$). The application of the PF model to some real materials may then lead to enhanced elastic effects on Z calculation.

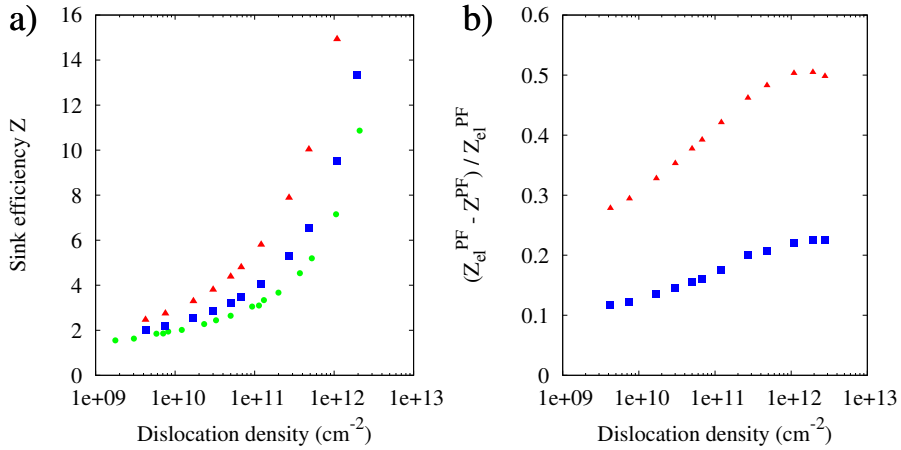

Figure 3.19: PF results: a) sink efficiencies without elasticity (circles) and with elasticity for vacancies (squares) and SIAs (triangles). b) Relative differences between elastic and non-elastic sink efficiencies for vacancies (square) and SIAs (triangles).

3.4 Conclusion

The validation procedure of the new PF model is divided into three steps. The first step shows that PDs absorption without elasticity is correctly modelled. In particular, the PF results are in good agreement with the Wiedersich model, but deviate from the Poisson and Laplace models. Indeed, PF and Wiedersich models rest on the same assumptions, namely an irradiation uniformly applied on the system via the production rate K_0 and the equivalence between the true average composition of the reservoir and X^{RT} for the estimation of the sink efficiency.

The method has been extended to anisotropic diffusion coefficients. It has been shown that the existing analytical solutions are good approximations in their validity domain, but the PF model gives a better estimation for high diffusion anisotropy. In addition, the anisotropic diffusion effect on absorption by regular microstructures has been studied. We showed that the Wiedersich boundary conditions must be used for anisotropic diffusing PDs. It is clear that the alignment of defects could be promoted by anisotropic diffusion.

The second step tests PDs segregation around the dislocation due to elasticity, but with no absorption of the defects by the dislocation. This reference case may appear as non physical but is nevertheless interesting, since it reveals that common simplifying assumptions made in PF models to deal with elastodiffusion can not be applied in the context of irradiation.

The third step tests the combined effect of the sink with elasticity. By comparison with the RS model, this paper reports original results on capture efficiencies with elasticity taking into account more realistically the influence of the microstructure. It has also been rigorously showed that the discrepancy between the PF and RS models is not due to a methodological mistake. In particular, for the case of straight dislocation line with elastic interactions, it is shown that the RS model underestimates the sink efficiency at dislocation densities which can be encountered in real irradiated materials.

Unlike the RS or other analytical models restricted to elastically isotropic systems, it must be emphasized that the PF model is able to deal with any anisotropic crystals. Moreover, the analytical models treat PDs as pure dilatation centres which is a simplification of the real cases. In the present formalism, it is possible to take into account the shape effect of PDs via a non isotropic Vegard tensor ϵ^{00}.

Finally, it is relevant to note that the PF model can either study regular or random microstructures. All these arguments show that the PF model constitutes a real improvement for the calculation of dislocation sink efficiency with respect to the analytical methods available in the literature. Since the PF method has been validated on a wide range of different cases, it can be applied to more realistic systems. Next chapter will focus on the practical case of zirconium.

Chapter 4

Elasticity effect on zirconium growth under irradiation

Contents

The PF model has been validated in the previous chapter. It is now relevant to consider a more practical case: hcp-zirconium. This crystal has a tendency to deform anisotropically under irradiation, which is is a major concern in the nuclear industry.

The material and the irradiation growth phenomenon will be described in the first part (section 4.1). Then, the methodology used in chapter 3 will be adapted (section 4.2) and applied to the case of straight dislocations in α-zirconium (section 4.3). The results, which show a preferential absorption of SIAs by prismatic loops, stem from the elastic interaction between dislocations and anisotropic point

defects. Our predictions are consistent with the observed radiation growth of Zr alloys.

4.1 Bibliography

4.1.1 Zirconium in nuclear industry

Pressurized light water reactors (PWR) have first been developed for submarine propulsion by Amiral Rickover in the Naval Propulsion program and put to the test in NAUTILUS device [87]. Their main features were device compacity and long autonomy. Light water plays the role of neutron moderator and coolant fluid. The high neutron cross section and the low mass of hydrogen enable light water to slow down fission neutrons in a small volume (in contrast with graphite or heavy water reactors, for example). However, hydrogen absorbs a significant fraction of thermal neutrons during the slowing process. It is then necessary to enrich the uranium fuel, in order to counterbalance the neutron absorption by light water and meet criticality conditions.

For security reasons, the fissile fuel and the coolant fluid have to be separated by an interfacing material: the *cladding material*. This material must have good mechanical properties in service conditions (400°C), corrosion resistance in hot water and low neutron absorption cross section. This last condition is critical: fuel enrichment is expensive and energy consuming. In addition, fuel enrichment is closely supervised, in order to prevent military grade fuel production and, by thus, nuclear weapon proliferation. It is then necessary to select a specific material that does not interact with neutrons: hcp zirconium (or α-zirconium) purified from hafnium happens to meet those conditions, and has been used since, in submarine as well as in nuclear power plants.

In spite of the small neutron cross section of zirconium, the cladding material is submitted to a high damage flux due to its vicinity with the fissile fuel and the absence of a moderating protective screen. Irradiation effects on zirconium alloys did not raise much attention until the 60's [88]. Cladding and guide tubes were elongating under irradiation. This phenomenon causes a risk of buckle of the fuel assembly and an enhanced risk of fracture.

4.1.2 Effect of irradiation on zirconium microstructure

In the 80's, much experimental work on irradiated hcp crystals has been performed and still constitutes the phenomenological basis for still-in-progress work [9, 88–92].

The microstructural defects created in irradiated hcp crystals can be listed as follows:

- prism-plane loop family,
- basal-plane loop family,
- voids.

Habit plane	Burgers vector $\mathbf{b}$	$\mathbf{b}$ norm	Type
$\{11\bar{2}0\}$	$1/3\langle 11\bar{2}0\rangle$	$a = 3.23\mathring{A}$	Int/Vac
$\{10\bar{1}0\}$	$1/3\langle 11\bar{2}0\rangle$	$a = 3.23\mathring{A}$	Int/Vac
$\{10\bar{1}1\}$	$1/3\langle 11\bar{2}3\rangle$	$\sqrt{a^2+c^2} = 6.07\mathring{A}$	Int
(0001)	$1/6\langle 20\bar{2}3\rangle$	$\sqrt{\frac{1}{3}a^2+\frac{1}{4}c^2} = 3.17\mathring{A}$	Vac
(0001)	$1/2[0001]$	$\frac{1}{2}c = 2.57\mathring{A}$	Vac
(0001)	$[0001]$	$c = 5.14\mathring{A}$	Vac

Table 4.1: Dislocation loops formed by irradiation observed in zirconium and its alloys [9, 60].

4.1.2.1 Prism-plane loops

Prism-plane loops (or $\langle a\rangle$-loops) generally form with their habit plane close to the prismatic plane $\{10\bar{1}0\}$ and have a Burgers vector $\mathbf{b} = 1/3\langle 11\bar{2}0\rangle$ [9]. Their nucleation begins very early during irradiation.

Unlike in fcc and bcc metals, $\langle a\rangle$-loops can be either of interstitial or vacancy nature [89]. They are stable and coexist during irradiation. The relative proportion of vacancy loops over interstitial is strongly dependent on irradiation temperature [9] (see Fig. 4.1). Stoller et al. [31] claim that the vacancy $\langle a\rangle$-loop maximum fraction temperature is analogous to the maximum swelling temperature in irradiated fcc crystals. In the vicinity of a grain boundary, this proportion is also dependent on the grain orientation. In thin samples irradiated with electrons, the vacancy loop fraction is dependent on the foil orientation. The vacancy loops are more frequent in foils where the normal is close to $\{0\bar{1}10\}$, while interstitial loops dominate when the foil normal is close to $[0001]$ [65].

Several works observed the alignment of $\langle a\rangle$-loops along dense directions $\{11\bar{2}0\}$ [9, 89, 92] (see Fig. 4.2). In particular, vacancy $\langle a\rangle$-loops are generally aligned as layers parallel with the trace of the basal plane. It has also been observed that the loops in a given row have the same Burgers vector [60]. This means that they also have the same nature, either interstitial or vacancy. A striking remark is that the specific alignment of defects has no link with the irradiating particle mass: the same phenomena are observed in electron [9, 65, 92, 93] as well as neutron [9, 65] irradiated crystals. This is a remarkable difference from fcc and bcc crystals, where void and SFT alignment has only been observed under neutron or ion irradiation [59].

It must be emphasised that a statistical study of $\langle a\rangle$-loops in irradiated hcp crystals is very difficult since [9]:

- Only a small percentage of the loops can be measured, due to their small size.

- The foil oxidation interferes with the observation of some loop orientation. As a consequence, the result can be biased towards particular loop orientations. This can raise important uncertainty, as we know that loop population

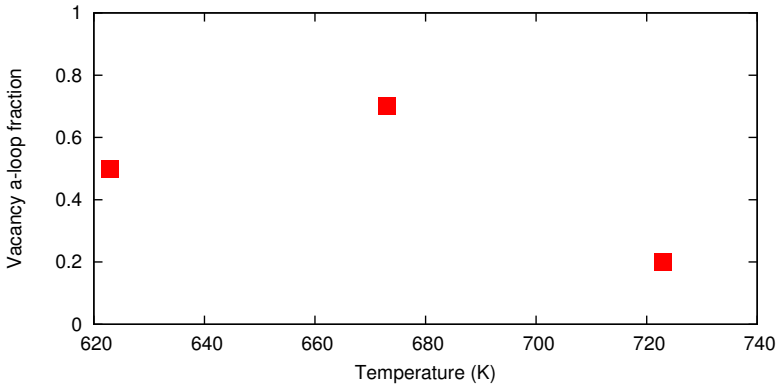

Figure 4.1: Proportion of vacancy $\langle a \rangle$-loops over the total $\langle a \rangle$-loops population in irradiated Zr as a function of irradiation temperature (in K). This proportion reaches a maximum of 70 % around 673 K. For irradiation temperature under 523 K, the interstitial loop type is dominant [94] (values from [9]).

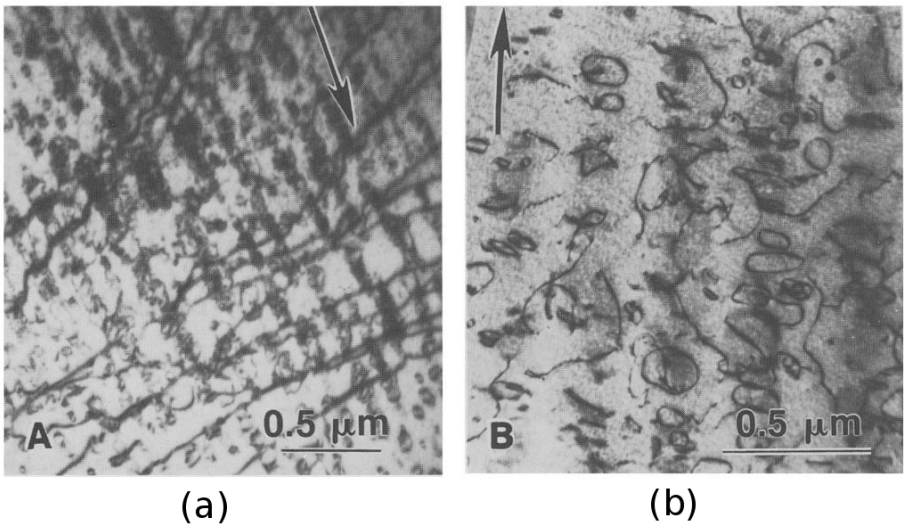

Figure 4.2: Alignment of $\langle a \rangle$ type dislocation loops in crystal-bar Zr following: (a) electron irradiation in a HVEM to ~ 0.2 dpa at 675 K; (b) neutron irradiation in EBR-II (*Experimental Breeder Reactor II*, Argonne National Laboratory, Idaho, USA) to a fluence of 1.5×10^{26} n.m^{-2} ($\sim$ 0.2 dpa) at about 700 K. Diffracting vector $\mathbf{g} = [11\bar{2}0]$ (indicated by black arrows), beam direction $\mathbf{B} \sim [1\bar{1}00]$ in each micrograph (from [9]).

is strongly dependent on foil orientation (see in particular, section 3.4 in ref. [92] and 3.4.1 in ref. [9]).

4.1.2.2 Basal-plane loops

The existence of basal loops in irradiated hcp crystal is not under debate anymore [9]. Basal loops have been observed in electron [9, 65, 93], neutron [9] and ion [95, 96] irradiated zirconium alloys. Griffiths even states that: "In general, basal plane **c**-component loops were observed in all Zr (and Zr-alloy) samples provided the dose was sufficiently high" [65]. It has also been observed that the probability of producing $\langle c \rangle$-loops increases with temperature. Except from specific cases, $\langle c \rangle$-loops are always of vacancy type [9]. In contrast with $\langle a \rangle$-loops, the $\langle c \rangle$-loops nucleate after an incubation period of typically 1 dpa. Samples where $\langle c \rangle$-loops are visible generally host a high density of $\langle a \rangle$-loops [65]. As a consequence, the $\langle c \rangle$-loops must be observed with a diffracting vector $\mathbf{B} = [0002]$, in order to vanish the $\langle a \rangle$-loop contrast. It is then hard to study both types of loops simultaneously. It has been seen [65] that those loops are frequently aligned as layers parallel to the trace of the basal plane (see Fig. 1.18).

$\langle c \rangle$-loop nucleation is sensitive to the materials purity, inhomogeneities, and regions of localized strain (mostly around edge dislocations) [65]. $\langle c \rangle$-loops nucleate more easily in low purity samples and in the vicinity of intermetallic precipitates [9]. The main explanations of this phenomenon given in the literature are:

1. partial dissolution of intermetallic $\mathrm{Zr_2(Fe, Ni)}$ precipitates creates iron platelets that act as nucleation sites for $\langle c \rangle$-loops [65]. These platelets should be too small and generate a contrast too low to be seen with TEM.

2. *Screening* effect of the precipitate between SIA clusters and vacancy type $\langle c \rangle$-loops. The precipitate is a barrier to the diffusion of 1D-diffusing SIA clusters. A vacancy defect is then "shadowed" from SIA cluster flux (see Fig. 1.17) as 1D-diffusing clusters would be blocked by the precipitate. An equivalent idea is proposed by Stoller for swelling in fcc crystals [31]. Griffiths (section 2 in [9]) remarks that voids, stacking fault tetrahedra and vacancy loops are more prone to nucleate close to precipitates and grain boundaries. The grain boundary can act as a barrier for SIA clusters, but won't necessarily induce a particular local chemistry, as needed for explanation 1. However, only few experimental works support this mechanism.

The nucleation of $\langle c \rangle$-loops in layers parallel to the basal planes is correlated with the existence of layers of small intermetallic precipitates. Nevertheless, we still do not know which of the following mechanisms is valid:

- the $\langle c \rangle$-loops nucleate preferentially as layers in the basal plane, and then capture impurities. Intermetallics would then precipitate as layers parallel with the basal plane, or

- the intermetallics nucleate as layers parallel to the basal plane, and then act as nucleation sites for $\langle c \rangle$-loops. $\langle c \rangle$-loops would then nucleate aligned as layers parallel with the basal plane.

It is obvious that the vacancy type $\langle c \rangle$-loops play a fundamental role in the irradiation growth of hcp crystals (see section 4.1.3). The acceleration of the irradiation growth (or "breakaway" growth) is directly correlated with the observation of such loops [95]. As a consequence, the understanding of the nucleation and growth of such defects is a key issue for predicting irradiation behaviour of hcp crystals.

4.1.2.3 Voids

Voids have been observed in most hcp crystals. Nevertheless, they are rarer than in fcc crystals. They form in hcp crystals irradiated with electrons between 625 and 775 K or with neutrons between 675 and 750 K [9]. In general, voids are not observed in crystals containing a high concentration of $\langle c \rangle$-loops. This is probably due to the faster nucleation of $\langle c \rangle$-loops that lower the vacancy supersaturation, and thus impede void nucleation.

Void existence strongly depends on the purity of the crystal and on the preinjection of insoluble gases. Some indications show that voids are more stable in impure crystals [9], but impurities can also stabilise vacancy loops, and thus decrease vacancy supersaturation [65]. Insoluble gases promote the nucleation of voids, as gas atoms aggregation is a nucleation site, and the internal gas pressure counterbalances the surface tension of the void. In the vicinity of a grain boundary (GB), the void nucleation depends on the GB orientation [9]: voids form close to grain boundaries perpendicular to the basal plane while no voids are observed near GBs parallel with it. Void alignment has been observed in irradiated Zr [97], Ti and Mg [65]. As voids are rare in Zr, they do not constitute a major concern.

4.1.3 Growth of zirconium and its alloys under irradiation

The main detrimental phenomena taking place in zirconium and its alloys under irradiation are [88, 94, 98, 99]:

hardening due to dislocation loop nucleation, that impede the movement of glissile dislocations;

irradiation creep due to the high supersaturation of mobile monodefects that accelerate dislocation climb; Dislocation climb will promote faster plastic deformation, as it will help dislocations to circumvent crystalline defects;

precipitate amorphization observed on intermetallics;

irradiation growth that is a spontaneous anisotropic deformation at constant volume in the absence of applied macroscopic stress.

In this section, we will present in more detail the phenomenon of irradiation growth, which is different from swelling. Swelling is an isotropic strain of the material due to the nucleation and growth of voids or bubbles, and the migration of SIAs to other sinks. It always leads to strictly positive macroscopic strain.

On the opposite, irradiation growth is an anisotropic deformation at constant volume of an unstressed material [49, 88]. An expansion in a given direction is then compensated by a contraction in at least one of the other directions. This

phenomenon is not correlated with the nucleation of voids and does only occur in hcp crystals. In the specific case of zirconium, it is admitted that the irradiation growth leads to a contraction along the **c** axis, and a growth in the directions parallel to the basal plane [100].

From an industrial point of view, this phenomenon has a technological impact. The guide tubes and fuel rods are shaped by a specific rolling process that leaves a *texture* on the final product. In other words, the crystallographic orientations of the grains are not randomly distributed in the final product. On the opposite, the mean **c** axis lays in the plane normal to the tube axis, with a 30° angle with the radial direction [87] (see Fig. 4.3 and 4.4). This grants the fuel assembly the best mechanical properties, but also enables macroscopical strain due to irradiation growth. In this precise case, the tubes and rods have a tendency to grow longer (positive strain along the tube axis), and the thickness to get thinner. This dimensional instability is a serious issue for the integrity of the first confinement barrier (protection against radioactive spread to the environment).

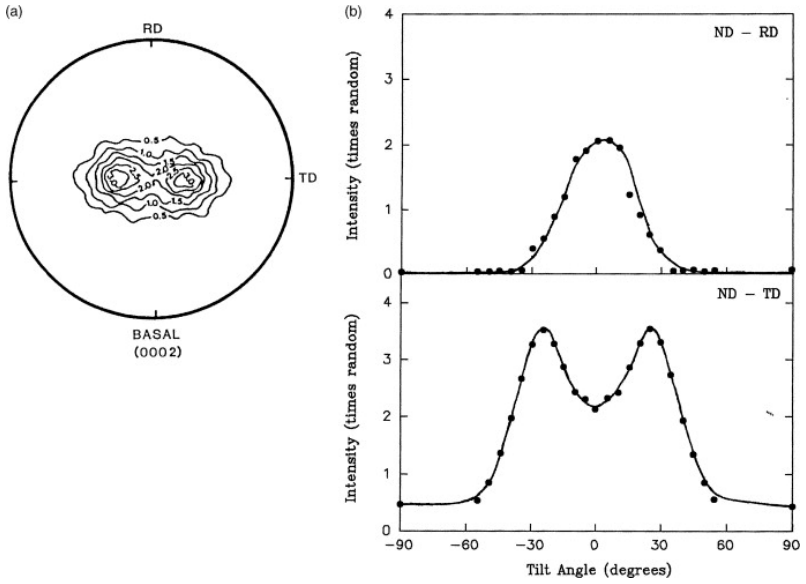

Figure 4.3: a) Basal (0002) pole distribution of a rolled zircaloy sheet exhibiting peak intensities at $\pm 30°$ from the normal to the sheet surface towards transverse directions (from [87]). RD stands for rolling direction, ND for normal direction (to the sheet) and TD transverse direction (relative to the rolling direction). b) ND–TD scan of basal pole intensity versus tilt angle depicting the characteristic bimodal distribution while the intensity continuously decreases from ND towards RD. A graphical interpretation of such graph is given in Fig. 4.4.

Irradiation growth is traditionally described as a 3-step process [99]:

Stage I: Initial high strain rate. The growth strain rate is a decelerating function of the dose, positive in the direction parallel to the basal plane, negative normal to it (see Fig. 4.5).

Stage II: Low growth stage. The strain rate is very low in every direction.

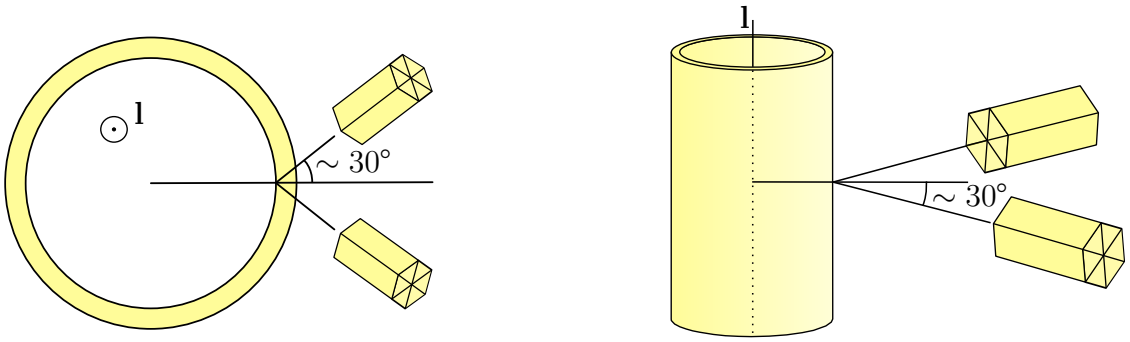

Figure 4.4: Diagram of the $\langle c \rangle$-axis orientation in cladding tubes. The $\langle c \rangle$-axis lays close to the plane normal to the rolling tube axis l (i.e. the *transverse direction*, see Fig.4.3) with a 30° from the radial direction of the tube [87]. As a consequence, the tube axis is close to a $\langle 11\bar{2}0 \rangle$ direction. The growth is always positive along the tube axis.

Stage III: "Breakaway" growth. After an incubation period of about 1 dpa, the strain rate accelerates in every direction. This phenomenon is strongly correlated with the nucleation and growth of basal vacancy loops [65].

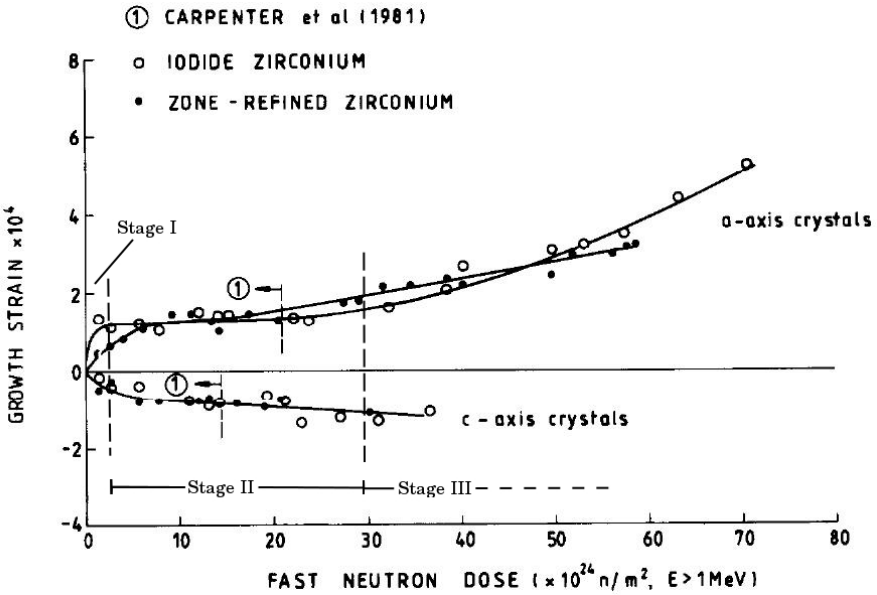

Figure 4.5: Irradiation growth in iodide and zone-refined zirconium single crystals at 553 K. The decomposition in 3 stages are clear for iodide refined zirconium (open circles): Stage I is from 0 to about $3 \times 10^{24}\,\mathrm{n.m^{-2}}$, followed by stage II up to $30 \times 10^{24}\,\mathrm{n.m^{-2}}$ (from [90]).

Cold worked materials experience no stage II. They go directly from stage I to III (see Fig. 4.6).

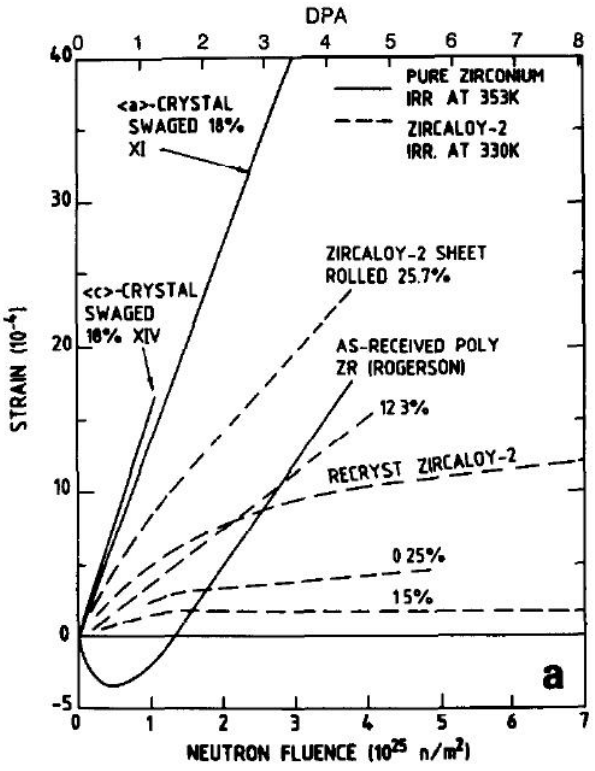

Figure 4.6: Comparison of the growth behaviour of the swaged crystals (i.e. deformed tubes with radial compression) with cold-worked zirconium and Zircaloy-2 irradiated at 353 K (from [99]).

Irradiation growth is not fully understood, but some mechanisms related to it have been identified [49]: the absorption of vacancies by edge dislocations generates a contraction of the crystal in the direction parallel to the dislocation Burgers vector. The opposite is true for the absorption of SIAs. Another way to describe the mechanism is to consider the edge dislocation as an excess half plane of atoms in the crystal. When this dislocation absorbs vacancies, it is equivalent to remove one layer of atoms. It is obvious that this phenomenon would generate irreversible deformation in the direction normal to this half plane (see Fig. 4.7), or parallel with the Burgers vector of the dislocation. This phenomenon can be rationalised as [49]:

$$V_j = \frac{J_i - J_v}{b_j} \ , \tag{4.1}$$

where V_j is the climb velocity of dislocation j and b_j its Burgers vector norm, J_i and J_v are respectively the interstitial and vacancy flux to dislocation j. Dislocations are supposed to be edge for simplicity.

The crystal strain is then related to the climb rates of every dislocation of type j through [49, 100]:

$$\frac{\mathrm{d}\varepsilon_{mm}}{\mathrm{d}t} = \sum_j \rho_j \, V_j \, b_j \, \cos^2 \phi_j \ , \tag{4.2}$$

where ρ_j is the j-type dislocation density and ϕ_j the angle between the Burgers vector b_j and the orientation m of the strain ε_{mm}. It is obvious from equation (4.2) that the climb of a given dislocation generates strain in a direction parallel to its Burgers vector (see Fig. 4.7).

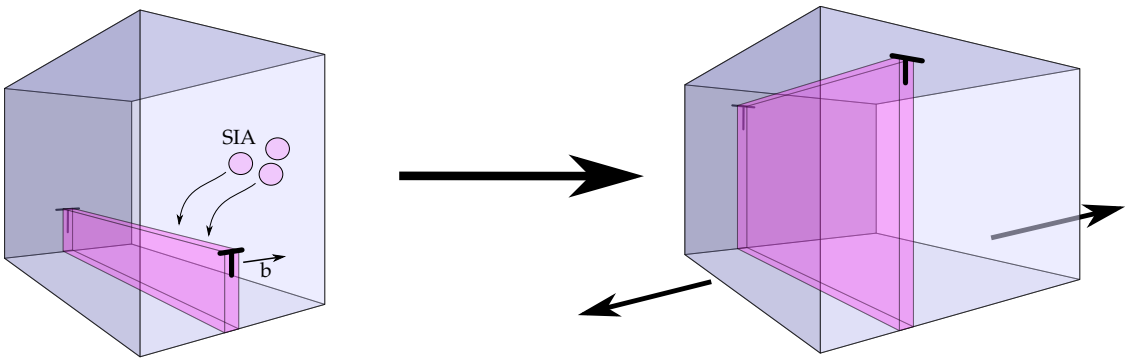

Figure 4.7: Growth of a crystal due to the exclusive absorption of SIAs by a dislocation (no applied stress). The climb of the dislocation is equivalent to the addition of an extra atomic plane with thickness equal to b normal to $\mathbf{b}$. The effect of the absorption of vacancies will produce the opposite effect, i.e. a contraction in the direction of $\mathbf{b}$.

It can then be understood that the absorption of monodefects by dislocations can lead to irreversible strain. In the case of irradiated materials, the defects of vacancy and interstitial nature are created in equal number. As a consequence, there can be a growth only if the absorption flux of vacancies and SIAs by dislocations are not equal. We define the *net flux* as the difference between the flux of SIAs and the flux of vacancies. Hence, if the net flux is zero, the absorption of SIAs is compensated by the absorption of an equal number of vacancies. Then, there must be an absorption *bias* of SIAs towards particular dislocations for the growth to take place. In the case of zirconium, we expect prismatic dislocations to receive a net flux of SIAs (positive net flux) and the basal loops to receive a net flux of vacancies (negative net flux). This is consistent with the fact that zirconium growth is faster after nucleation of vacancy type $\langle c \rangle$-loops.

As a consequence, we do understand how hcp crystals can grow under irradiation. The real question is then: why is there an absorption bias between prism-plane and basal plane loops?

In order to explain the origin of this bias, previous theories (see section 1.3.5) have been considered.

4.1.3.1 DAD

During the 80's, Woo developed a theory [49, 50] in order to explain zirconium growth (see section 1.3.5.2). The main idea is to consider that the SIA diffuse faster in the basal plane rather than in the **c** direction, while the vacancy diffuses

isotropically. This conditions can be expressed as:

$$\frac{D_i^a}{D_i^c} > \frac{D_v^a}{D_v^c}, \tag{4.3}$$

where D is the diffusion coefficient, indices i and v correspond respectively to SIA and vacancy, and superscript a denotes the diffusion coefficient in directions parallel to the basal plane and c in the direction perpendicular to it.

As a consequence, the SIAs are prone to be absorbed preferentially by dislocations normal to the basal plane rather than parallel to it. This would promote (i) the rapid growth of basal vacancy loops, (ii) the positive growth of the crystal in directions parallel with the basal plane and (iii) the contraction of the crystal in the axial direction. In order to properly describe irradiation effects in Zr, the fundamental assumptions of the model should be validated. There is still no consensus on the diffusional anisotropy of the SIA [16, 17, 101–105]. In general, the anisotropy calculated for both vacancies and SIAs are of the same order of magnitude ($D_i^a/D_i^c \sim D_v^a/D_v^c$) (see Tab. 4.2). Moreover, DFT calculations have shown the possibility of a faster migration of the SIA along the $\langle c \rangle$ axis than perpendicular to it [17, 105], which is opposite to the MD results and the assumption made in [50]. As a consequence, the DAD may not constitute a satisfactory explanation for zirconium growth.

Table 4.2: Diffusion coefficients for SIAs and vacancies at 600 K in Zr in directions parallel with the (0001) plane and normal to it.

Ref.	D_i^a/D_i^c (SIA)	D_v^a/D_v^c (vacancy)
[106, 107] (exp.)	-	1.66
[108] (MD)	4.25	1.0
[103] (*DFT*)	0.709	2.77
[102] (MD)	~ 4	~ 1.4
[16] (*DFT*)	2.03	2.64
[101] (MD/thermodynamical integration)	-	1.99
[105] (DFT)	~ 3	~ 5

4.1.3.2 Production bias model

Another theory has been recently developed by Golubov et al. [100] (see also section 1.3.5.3). The main idea is to apply the Production Bias Model to hcp crystals: irradiation creates not only monodefects, but also defect clusters, that have their own migration and interaction properties. In the case of zirconium, Golubov assumes that the irradiation damage creates SIA clusters along with monodefects. These SIA clusters are described as very small prismatic dislocation loops. The assumptions of the model are described as follows [100]:

1. The initial microstructure consists of prismatic and basal edge dislocations;
2. the primary cascade radiation damage consists of monoSIA, monovacancies and SIA clusters (20 % of interstitials are initially aggregated as clusters according to [100]);

3. monodefects migrate isotropically;

4. the SIA clusters migrate in 1D along $\langle 11\bar{2}0\rangle$ close-packed directions;

5. the elastic interaction of SIA clusters with $\langle c\rangle$ and $\langle a\rangle$ dislocations with the Burgers vector non-parallel to that of the clusters are neglected. As a consequence, SIA clusters can only be absorbed by dislocations with a same Burgers vector parallel to their own;

6. the difference in absorption properties of dislocation loops and edge dislocations for mobile point defects and SIA clusters is neglected (no dislocation shape effect);

7. any dislocation bias on the absorption of monodefects is neglected.

This is basically a simplified version of the PBM [31], with the additional assumption that SIA clusters only interact with dislocations having a Burgers vector parallel to that of the cluster. Golubov et al. then developed a rate-theory model based on these assumptions. The main conclusions of this work can be summarised as follows:

- SIA clusters cannot be absorbed by basal vacancy loops (assumption 5), as a consequence, as soon as $\langle c\rangle$-loops are nucleated, they will absorb a negative net flux and grow fast.

- As SIA clusters are absorbed by prismatic dislocations only, those dislocations will have a bias towards SIA objects, and will promote the positive growth strain of the crystal in the directions parallel with the basal plane.

- If the $\langle a\rangle$-dislocations Burgers vectors distribution is anisotropic, the SIA cluster flux in each direction is the same, as SIA clusters do only interact with dislocation having the same Burgers vector (assumption 5), whatever their density. On the opposite, the monodefects flux depend on the dislocation density only (assumptions 3, 6 and 7). As a consequence, each $\langle a\rangle$-dislocation will receive a given fraction of the remaining monoSIAs and monovacancies, in proportion to the dislocation density. However, as a fraction of SIAs have been created as SIA clusters, there are more available monovacancies than monoSIAs. As a consequence, the dislocations with the higher density will absorb more vacancies than SIAs (see Fig. 4.8 for a graphical interpretation). The main consequences of this conclusion are:

  - it is then possible to observe a temporary negative strain in one or two prismatic directions. This has already been experimentally observed (see for example Fig. 4.6), mostly in cold worked materials, which could have anisotropic distributions of dislocation Burgers vectors [88, 98, 99]
  - it is possible to have a cohabitation of both interstitial and vacancy type $\langle a\rangle$-loops, as long as they do not have the same Burgers vector.

- The 1D diffusion of SIA clusters would promote other effects (assumption 4):
  - alignment of vacancy type defects with a direction parallel with the basal plane, voids and $\langle c \rangle$-loops aligned with the trace of the basal plane [65],
  - vacancy $\langle a \rangle$-loops alignment along the close-packed directions.

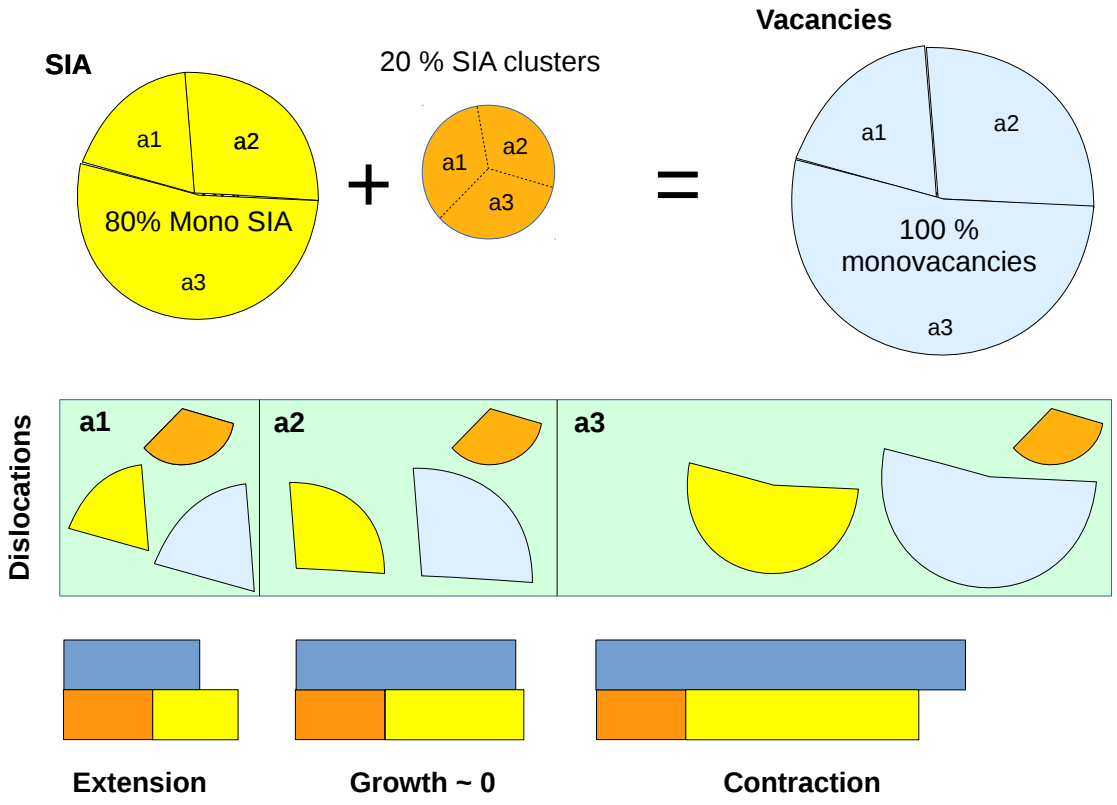

Figure 4.8: Diagram of the distribution of defects absorbed by prismatic dislocations (noted a_1, a_2 and a_3). Interstitial clusters will be absorbed in equal proportions by each dislocation type, whatever their relative density (represented by the surface of each blue rectangle). On the opposite, monodefects are absorbed proportionally to each dislocation Burgers density. As a consequence, dislocations a_3 will absorb a higher fraction of both SIAs and vacancies. As there is less monoSIAs than monovacancies, dislocations a_3 will absorb more vacancies than SIAs. The opposite will occur for dislocations a_1. The third line shows that the net flux of defects to each dislocation will not necessarily be zero. According to this theory, there can be a negative growth in $\langle a_3 \rangle$ direction, as long as the a_3 prismatic dislocations are available in a higher density than other dislocations.

This theory is the first one to propose an explanation to the temporary negative growth of zirconium along one $\langle a \rangle$-direction and the cohabitation of vacancy and interstitial $\langle a \rangle$-loops. However, some limitations must be raised.

The PBM has been widely used to explain the difference in microstructures of FCC crystals irradiated with electrons or neutrons [31]. In FCC metals, the alignment of stacking fault tetrahedra and voids happen only under heavy particle irradiation, as well as decoration of edge dislocation lines with small interstitial clusters [58, 59]. These effects have never been observed under electron irradiation (see also Fig. 1.14). This shows that the type of irradiation, hence the type of damage cascades (clusters or Frenkel pairs only), has a strong influence on the irradiated microstructure. On the opposite, in the case of zirconium, whereas the electron- and neutron irradiated microstructures differ, similar features are observed: vacancy prismatic and basal loops, as well as irradiation growth and void alignment, happened in various alloys irradiated either with electrons or heavy particles (see section 4.1.2.2). As a consequence, the role of interstitial clusters produced by irradiation cascades (also called *primary interstitial clusters* [31]) should be different in irradiated hcp crystals (see Fig. 4.9) than in fcc alloys.

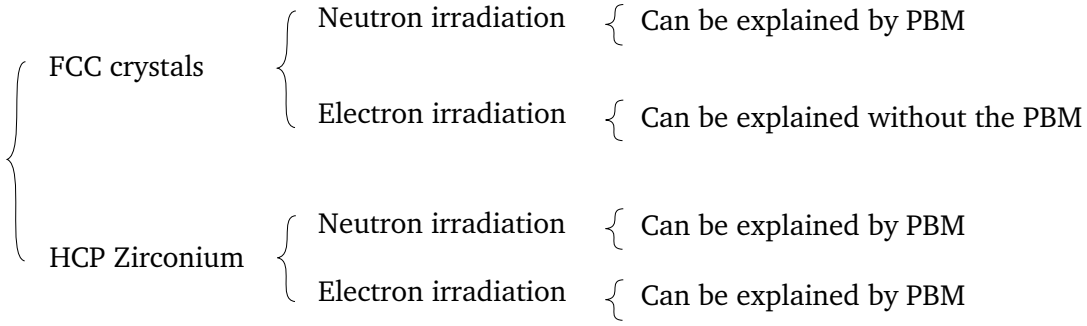

Figure 4.9: Summary of cases to which the PBM applies. It is surprising that while electron and neutron irradiation lead to major microstructural differences in FCC metals, irradiated hcp-Zr microstructures seems to be less dependent on the irradiated particle mass. As a consequence, it is difficult to sustain that the PBM, in its present version [100], is relevant for cases where primary clusters are produced by heavy particle collision.

In addition, the PBM predicts that HVEM irradiation would not produce any growth or formation of vacancy loops. In the framework of the PBM, the fraction of SIAs in clusters is 0 % under electron irradiation (assumption 2). Nevertheless, both irradiation growth and nucleation of vacancy loops have been observed in electron irradiated zirconium [65, 92, 93].

It should also be emphasised that the very same assumptions could be applied to any cubic metal (bcc or fcc). The only difference would be that they would not have 4 prismatic directions and no $\langle c \rangle$ direction. However, the conclusion on the coexistence of vacancy and interstitial loops would remain valid. In addition, it would be possible, for cold worked materials, to experience anisotropic growth if the Burgers vector distribution is anisotropic (see Fig. 4.8). To our knowledge, this has never been observed before, neither in bcc nor fcc crystal.

In heavy particle irradiated bcc and fcc crystals, the voids are aligned along close-packed directions (see Fig. 1.15). From the conclusions of the PBM on heavy particle irradiated FCC crystals, where voids align along close packed directions,

one could expect the voids to align along prismatic directions in magnesium. In the case of ion irradiated magnesium, while void do nucleate in layers parallel with the trace of the basal plane, they do not display any alignment along close-packed directions [97]. It is then possible that those voids nucleate as layers for other reasons.

The theories based on anisotropic diffusion (faster basal plane SIA diffusion for DAD or 1D-diffusing interstitial clusters for PBM) are generally used to explain the void alignment in layers parallel with the basal plane (see for example Fig. 1.15). In that case, voids in layers would minimise their SIA capture efficiency, and then maximise their growth rate and survival probability. In the case of Zr, the theory is applicable and is consistent with the alignment of both basal vacancy loops and voids as layers parallel with the basal plane. But in the case of Mg, which has almost the same c/a factor than Zr, a striking observation is that basal plane loops are interstitial in nature and always very wide ($\sim 0.5\,\mu$m) [65]. As in Zr, voids tend to form layers parallel with the trace of the basal plane (see Fig 4.10). If the void alignment could be explained by faster diffusion of SIAs in the basal plane, then it would be hard for basal interstitial loops to grow. On the opposite, if SIA clusters diffused along $\langle c \rangle$ direction, voids wouldn't align as layers parallel with the basal plane. It is possible that the void alignment and the formation of basal loops do not have the same reason. As a consequence, the anisotropic diffusion based theories converge to the same conclusions in the case of zirconium, but not in other hcp metals.

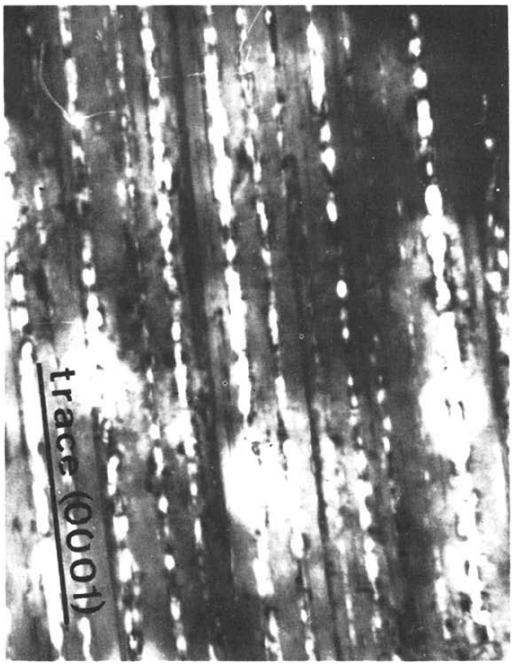

Figure 4.10: Magnesium irradiated at $3 \times 10^{21}\,\mathrm{n/cm^2}$ (E > 0.1 MeV). T= 55°C. Foil normal: $[11\bar{1}0]$. Zoom $\times 24000$. Voids are aligned as layers in the trace of the basal plane. The voids are randomly distributed in each layer (from [97]).

The fundamental assumption of the model is that 20 % of the SIA are created in the form of clusters (assumption 2). This fact has never been experimentally proven. In addition, MD simulation works on Zr that predicted the formation of SIA clusters in the annealing phase of the damage cascade rely on an empirical potential whose validity is still under debate [105, 109, 110].

Another striking observation has been made in [92] in electron irradiated zirconium thin foils at 675 K. The foil normal was $\mathbf{N} \sim [1\bar{2}11]$. Griffiths observed a mixed population of vacancy and interstitial loops. He wrote "only a small percentage of vacancy loops (< 20 %) have Burgers vector other than $\mathbf{b} = 1/3[\bar{1}2\bar{1}0]$". The direction is very important, as the prismatic direction $[\bar{1}2\bar{1}0]$ is the closest to the foil normal $\mathbf{N} \sim [1\bar{2}11]$. If we consider that the foil surface is an efficient sink for 1D diffusing SIA clusters with the Burgers vector close to the surface normal, this would promote the growth of vacancy $\langle a \rangle$-loops with the same Burgers vector (see Fig. 4.11). This would explain what is observed by Griffith, but this happened under electron irradiation, where there is no primary SIA clusters. As a consequence, some assumptions of the PBM are not necessary for the existence of prismatic vacancy loops. Golubov et al. claim that under electron irradiation, it is possible for monoSIAs to gather and form SIA clusters, and then promote a PBM-style behaviour [100]. In that case, the creation of clusters by aggregation of monoSIAs should also happen under other irradiation conditions, where the monoSIAs are believed to represent 80 % of the cascade product (see Fig. 4.9). This effect has been neglected in the present version of this model. It is probable that in the article describing the PBM model, these effects could have been compensated by proper parametrisation of the adjustable parameters, such as the SIA fraction in primary clusters. In order to consider the PBM as a reliable model for describing the microstructural evolution of hcp crystals, these contradictions should be first explained.

To the best of our knowledge, Molecular Dynamics calculations indicate the formation of such clusters in Ti and Zr [111]. These calculations rest on empirical potentials which were used to study point defects and clusters of point defects properties in Zr ([108, 112] among others). The validity of the potentials, and hence of the MD results, is however questioned by the fact that the configuration of the single SIA predicted by the interatomic potential used in [112] disagrees with *ab initio* calculations. As a consequence, there is no consensus concerning the main assumptions of the PBM model, i.e. the nature and proportion of these clusters, as well as their diffusion mechanisms. Moreover, this approach ignores the main characteristics of individual vacancies and SIAs whereas they are the two most important crystal defects created during the primary event of radiation damage. It is important to mention that zirconium alloys irradiated with electrons, which only produce individual Frenkel pairs, also develop vacancy loops [91]. This result highlights the importance of considering the interaction between dislocations and individual PDs as done in this work.

This shows, without a doubt, that the behaviour of the monodefects should be properly known in order to better simulate irradiated materials evolution, whatever the irradiation type. In summary, these previous models do not explain all the experimental facts associated with the zirconium growth. This may be due to the fact that the mainly ignore some main characteristics of PDs in zirconium. In-

deed, DAD postulates a higher diffusion anisotropy for SIAs, which is not proven, whereas PBM only considers clusters of defects, while SIAs and vacancy have identical behaviour.

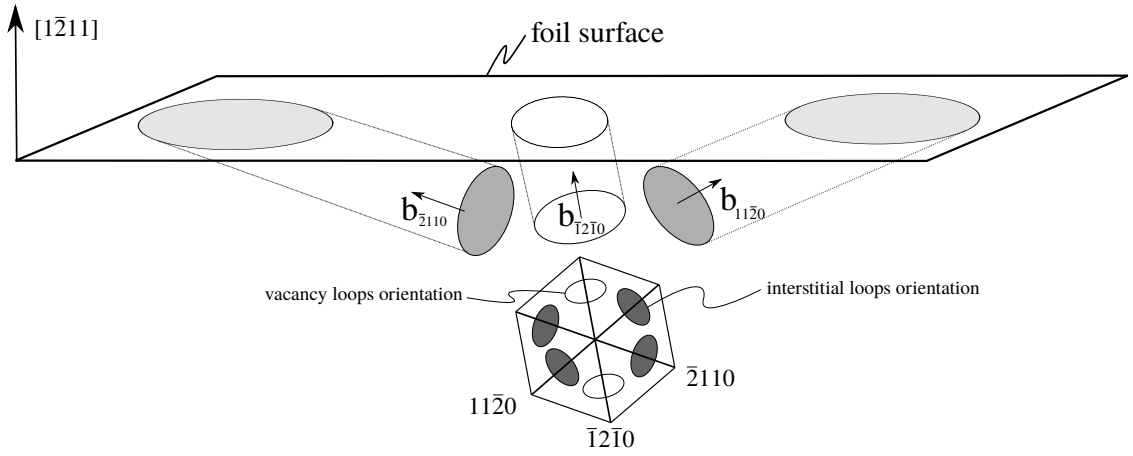

Figure 4.11: Diagram of the relative orientation between the foil surface and the 3 prismatic Burgers vectors in a HVEM irradiated zirconium sample in [92]. It is obvious that from a given depth, it is easier for a dislocation loop moving along axis $[\bar{1}2\bar{1}0]$ to reach the surface than for the 2 other glide directions. It would make the surface a more effective sink for dislocations with $\mathbf{b} = [\bar{1}2\bar{1}0]$ than for the others.

4.1.3.3 Dislocation bias

The dislocation bias has been considered to be unable to explain zirconium growth until now [65, 100]. This was due to the fact that the PDs were considered as dilatational centres. In metals, the relaxation volume of the SIA is larger than the vacancy in absolute value, then the dislocation bias as defined in Eq. (1.34) increases with the Burgers vector norm. As the perfect basal loop has a larger Burgers vector than the prismatic loop (see Tab. 4.1), the dislocation bias should be higher for the basal rather than the prismatic loops. Hence, zirconium would grow in the opposite direction to that observed experimentally. A priori, models based on dislocation bias are not able to explain Zr growth.

In fact, the elastic interactions between PDs and dislocations, and hence dislocation bias, are not well understood in zirconium, for several reasons:

(i) Elastic properties of PDs in their equilibrium and *a fortiori* saddle point configurations are difficult to determine. At the first order, it has been shown that the elastic interaction of one PD with an applied strain field created by the surrounding microstructure can be described by a dipole tensor P_{ij} [113, 114]. The isotropic and deviatoric parts of this tensor are respectively associated with the size and shape effects of the PD. This interaction can be refined by taking into account second order terms which are described by the elastic polarizability tensor [113–115]. State-of-the-art *ab initio* calculations turn out to be the most relevant tool for this kind of study.

(ii) The elastic interactions are by definition non local which means that PDs

interact with the entire microstructure. Their knowledge can be tracked by a mesoscale model while atomistic ones are less efficient. For this purpose, (PF) models have been applied to predict microstructure evolution under irradiation taking into account elasticity in presence of dislocation loops [73, 74] acting as sinks. However, a proper definition of the order parameters must be used, as discussed in chapter 2.

Chernov et al. [116] investigated the interaction between anisotropic PDs and straight dislocations in hcp Zr. They studied the configurations of the SIA by means of molecular statics, using a Finnis-Sinclair many-body interatomic potential [117], which they claim to properly reproduce the SIA diffusion behaviour. Then, they calculated the energy of each configuration in the vicinity of a straight dislocation, whose stress field was obtained within the anisotropic linear elasticity theory according to the algebraic method [8]. They investigated the case of dislocations with Burgers vector $1/3\langle 11\bar{2}0\rangle$, $1/3\langle 11\bar{2}3\rangle$ and $[0001]$ (see Tab. 4.1). The binding energy of SIAs with the dislocation has been computed in various locations and configurations around the dislocation core. They showed that the SIAs interact the most with $1/3\langle 11\bar{2}3\rangle$ in the screw dislocation configuration, while the vacancy is preferentially attracted towards $[0001]$ dislocations in the screw configuration. Surprisingly, the PDs are generally more elastically attracted towards screw dislocations than towards edge dislocations. This result is opposite to the previous works. Due to the diffusion anisotropy of the SIA, that was assumed in this work, the SIA is absorbed more easily by $1/3\langle 11\bar{2}3\rangle$ dislocation in the edge configuration. This is due to: (i) the high value of the Burgers vector norm, (ii) the orientation of the Burgers vector, that interacts with the SIA stablest configuration, (iii) the orientation of the dislocation that is not parallel with the basal plane, which leads to a DAD effect (see section 4.1.3.1). The main limit of this work is due to the use of the molecular statics, which is not reliable, as discussed in section 4.1.3.2, to compute the PD properties at saddle point and equilibrium configurations. According to more recent DFT calculations [17, 110], the stablest configurations of the SIA in Zr do not correspond to those obtained by Chernov et al. In addition, they considered a faster diffusion of the SIA parallel to the basal plane, a fact which has not been proven.

It follows from (i) and (ii) that a multiscale approach coupling PF and *ab initio* calculations should allow to take into account the specific elastic properties of PDs and their interaction with the microstructure.

Coming back to the initial problematic of dislocation loop formation in zirconium, some recent works allowed to make advances in that direction. As outlined by (i), a comprehensive study of the elastic interactions requires a precise knowledge of the structure and energetics of PDs in zirconium which were not available in the literature up to now. This lack has been recently fulfilled by *ab initio* calculations which have reported that SIAs in zirconium may adopt different configurations with very similar formation energies [17, 110].

Formation energies of different configurations have been computed using DFT method (MD results are too uncertain to be considered [16]). Several configurations for the SIA have been considered: octahedral (O), split $\langle 0001\rangle$ dumbbell (S), crowdion (C), tetrahedral (T), basal octahedral (BO), basal split (BS), basal crowdion (BC), basal tetrahedral (BT) [118], buckled crowdion (C' [17] or *dd* [16]

for *double dumbbell*), BC' [17] (or *ddp2* [16]) and "rotated split" configuration (ST [16]). Recent results show that the supercell should include at least 200 atoms to lead to an acceptable convergence [17]. The dumbbell fractions assumed in such calculations are overestimated (more than 10^{-3}). As a consequence, SIAs are influenced by long-range interactions with their mirror images due to the periodic boundary conditions. For supercells hosting less than 150 atoms, the most stable SIA configuration is octaedral (O). For larger supercells, the basal octaedral (BO) and basal split (BS) have relatively low formation energies. A larger number of atoms in the supercell generally leads to more reliable results, as the interactions between the modelled defect and its mirror images vanish with the distance between them. Energies obtained in the literature are compiled in Table 4.3.

The most stable configurations (BO, BS, BC, BT and BC') are all "basal" configurations, i.e. the strain induced by those defects is mostly oriented in directions parallel with the basal plane [16, 17]. According to Vérité [103] and Peng [118], configurations BC and BT spontaneously decay to configuration BO. As a consequence, the main relevant configurations are BO, BS and DDP2. The anisotropic strain due to those defects may induce particular interaction with dislocations, the specificity of which has not been taken into account in DAD or PBM models.

This contrasts with the situation observed in cubic materials for which the average SIA is isotropic. It is then essential to quantify how this shape effect of SIAs influences the sink efficiencies of dislocations in order to better understand the microstructure evolution in irradiated zirconium. This task is complicated due to the high diversity of dislocation loops encountered in this system. In addition, taking into account this particular effect is complicated since it introduces another source of anisotropy in the problem. In particular, the orientation of the PD with respect to the orientation of the dislocations becomes essential and it is crucial when studying strongly anisotropic microstructures. The PF model can easily take into account those anisotropies. In order to address this problem, we propose a combination of atomic scale modelling based on DFT calculations to evaluate the PDs properties and the PF model described in chapter 2. It requires as input data the PD properties in zirconium which are provided by *ab initio* calculations the reliability of which has been discussed above. Dislocations orientations and Burgers vectors used in the calculations are those experimentally determined for irradiated zirconium alloys in the literature. The results given in section 4.3 allow to compare the elastic biases calculated for basal and prismatic loops. The main conclusion is that they are consistent with the observed growth of basal dislocation loops of vacancy type.

4.2 Methodology

4.2.1 Phase-field model

The methodology described in chapter 2 is applied to zirconium to calculate sink strengths. In particular, it means that the same assumptions are adopted in this chapter, that is:

- isotropic diffusion coefficients;

Table 4.3: Formation energies of SIA configurations in Zr, at 0 K, from the literature. N_{sc} represents the number of atoms in the computation supercell.

Ref.	N_{sc}	O	BO	BS	C	S	C'	BC'	ST	T	BC	BT
[119] (PWSCF, GGA)	37	3.04	3.14	3.39	3.52	3.28	-	-	-	-	-	-
[120] (VASP,PAW)	37	3.22	3.45	-	3.63	3.56	-	-	-	-	3.76	4.84
[120](VASP,PAW)	37	2.94	2.98	-	3.25	3.12	-	-	-	-	2.95	4.14
[16] (VASP,USPP)	97	2.96	2.99	3.11	3.27	3.16	3.05	2.99	3.07	-	-	-
[16] (VASP,USPP)	201	2.92	2.85	2.97	3.26	3.08	3.05	2.87	3.06	-	-	-
[16] (VASP,PAW)	201	2.94	2.86	2.97	3.28	3.09	3.06	2.88	3.07	-	-	-
[118] (VASP,PAW)	36	3.05	3.24	3.53	3.56	3.44	-	-	-	3.44	3.23	4.65
[118] (VASP,PAW)	96	2.97	2.98	3.08	3.34	3.19	-	-	-	3.19	2.98	4.23
[118] (VASP,PAW)	180	2.98	2.82	2.96	3.37	3.17	-	-	-	3.17	2.82	2.82
[118] (VASP,PAW)	288	2.92	2.78	2.87	-	3.08	-	-	-	-	-	-
[110] (QE,GGA)	37	3.00	3.14	3.43	-	3.32	-	-	-	-	-	-
[110] (VASP,GGA)	37	2.94	3.17	3.49	-	3.31	-	-	-	-	-	-
[110] (QE,GGA)	97	2.97	2.90	3.03	-	3.10	-	-	-	-	-	-
[110] (VASP,GGA)	97	2.85	2.87	3.00	-	3.06	-	-	-	-	-	-
[110] (QE,GGA)	241	2.93	2.75	2.87	-	3.02	-	-	-	-	-	-
[110] (QE,GGA)	241	2.93	2.74	2.84	-	3.05	-	-	-	-	-	-
[110] (QE,GGA)	301	2.91	2.75	2.89	-	2.97	-	-	-	-	-	-
[17] (SIESTA,PAW)	289	3.16	3.03	3.26	3.43	3.20	-	3.11	-	-	-	-
[17] (VASP,PAW)	289	2.81	2.70	2.79	3.14	2.92	-	2.72	-	-	-	-
[17] (VASP,PAW)	491	2.84	2.70	2.79	-	2.94	-	2.73	-	-	-	-
[105] (QE,GGA)	145	2.92	2.77	2.90	-	3.02	3.16	2.82	-	-	-	-
[105] (VASP,GGA)	145	2.80	2.73	2.88	-	2.98	-	-	-	-	-	-

- ideal solution approximation for PDs;
- uniform and constant generation of PDs;
- negligible elastic interaction between defects;
- X^s is assumed to be equal to the thermal equilibrium composition X^{th};
- periodic boundary conditions.

The specific features of the present chapter lies in the anisotropy of the properties of zirconium, while chapter 3 considered only isotropic elastic properties. The parameters specific to Zr are then the properties of PDs ϵ_{ij}^{00}, dislocation loops ϵ_{ij}^{d0} and elastic constants of Zr C_{ijkl}.

4.2.2 Input data

4.2.2.1 Properties of PDs

In the framework of the Phase Field model, PDs are described by their Vegard tensor ϵ_{ij}^{00} which is an input parameter that can be determined by first principle calculations. The DFT results reported here have been obtained with the VASP code [14,121] in the PAW framework [122] with a kinetic-energy cutoff of 250 eV. If the kinetic-energy cutoff is increased to 400 eV the changes in the formation energy of the various PDs investigated is modified by ~ 0.01 eV. Twelve electrons are included in the valence band. All calculations were performed using the GGA and the PW91 functional [123]. Comparable results [17] were obtained using the PBE [124] functional. For metallic alloys, the standard GGA functionals work well as pointed out in recent reviews [15], the case of insulators and/or strongly correlated materials being more problematic to treat and often needs the use of heavier methods like hybrid-functionals, the LDA+U or the GW method [15,125]. For the Brillouin zone integration, we used the Methfessel-Paxton smearing scheme [126] with a smearing value of 0.2 eV. Convergence tests were performed in Zr using different supercells sizes as mentioned by Vérité [17]. The k-points density was not less than that of a $15 \times 15 \times 12$ grid for a 2 atom hcp unit cell. According to Vérité [17], accurate enough results are obtained for a $5 \times 5 \times 4$ supercell (200 atoms) for the vacancy and for a $6 \times 6 \times 4$ supercell (288 atoms) for the SIAs with a $3 \times 3 \times 3$ k-points grid. To determine the Vegard tensor for each type of PD, a full supercell relaxation under no external stress was performed. During the simulation, the periodic box containing N_{sc} atomic sites (288 for SIAs and 200 for the vacancy) and one PD is allowed to minimise its energy by taking a homogeneous strain ε_{ij}. The Vegard coefficients are given by:

$$\epsilon_{ij}^{00} = N_{\text{sc}} \varepsilon_{ij} \tag{4.4}$$

To calculate ϵ_{ij}^{00}, a relaxed supercell of n atoms representing the perfect crystal is used as a reference. The corresponding supercell vectors are noted $\mathbf{A_1}$, $\mathbf{A_2}$ and $\mathbf{A_3}$ and expressed in the orthonormal basis $\mathfrak{R}_0 = (\mathbf{x_1}, \mathbf{x_2}, \mathbf{x_3})$ basis, with $\mathbf{x_1} \parallel [\bar{1}2\bar{1}0]$, $\mathbf{x_2} \parallel [\bar{1}0\bar{1}0]$ and $\mathbf{x_3} \parallel [0001]$. The matrix A is then defined as:

$$A = \begin{pmatrix} A_1^1 & A_2^1 & A_3^1 \\ A_1^2 & A_2^2 & A_3^2 \\ A_1^3 & A_2^3 & A_3^3 \end{pmatrix}_{\mathfrak{R}_0} \tag{4.5}$$

where A_i^j is the jth coordinate of vector $\mathbf{A_i}$.

Then, a single defect (SIA or vacancy) is inserted in the supercell, leading to a total number of atoms of $(N_{\text{sc}} - 1)$ for the vacancy or $(N_{\text{sc}} + 1)$ for the SIA in the defected supercell. The supercell relaxation due to the defect introduction is then simulated using an atomic scale method. The new vectors $\mathbf{A_1'}$, $\mathbf{A_3'}$ and $\mathbf{A_3'}$ are extracted.

During the relaxation, the supercell is submitted to a deformation T that can be expressed as a transformation matrix F:

$$A' = FA, \tag{4.6}$$

where F is an unknown matrix that is obtained as:

$$F = A'A^{-1}, \tag{4.7}$$

where A^{-1} is the inverse of matrix A.

The strain ε experienced by the supercell is [127]:

$$\varepsilon(T) = {}^1\!/_2 \left(F^t \colon F - \mathbb{I}_3\right), \tag{4.8}$$

where F^t is the transposed matrix of F and $\mathbb{I}_3$ is the identity matrix.

Following this procedure for vacancies, the corresponding Vegard tensor $\epsilon_{ij}^{00,v}$ is reported in Tab. 4.4. It has a tetragonal form, being isotropic in the basal plane with $|\epsilon_{33}^{00,v}| > |\epsilon_{11}^{00,v}|(= |\epsilon_{22}^{00,v}|)$. This tetragonality or shape anisotropy of vacancies stems from the hexagonal symmetry. The strain is stronger, in absolute value, along the $\langle c \rangle$-axis (-0.185) than along directions parallel with the basal plane (-0.131) (see Tab. 4.4). Like for SIAs, this anisotropy will be taken into account by PF calculation.

The calculation of the Vegard tensor for SIAs is more complicated due to the different types identified in zirconium and published in [17]. Assuming that the equilibrium population of PDs is reached in a few atomic jumps, it is possible to associate to SIAs an average Vegard tensor $\bar{\epsilon}_{ij}^{00,i}$:

$$\bar{\epsilon}_{ij}^{00,i} = \sum_n F_B^n \epsilon_{ij}^{00,n}, \tag{4.9}$$

where n refers to the type of SIA, $\epsilon_{ij}^{00,n}$ is the value of the Vegard tensor of the SIA of type n averaged over its ν_n variants and F_B^n is the Boltzmann factor defined as:

$$F_B^n = \frac{\nu_n \exp(-E_f^n / k_B T)}{\sum_n \nu_n \exp(-E_f^n / k_B T)} \tag{4.10}$$

ν_n and E_f^n are respectively the multiplicity and formation energy of the SIA of type n. In this work, all the calculations are performed at 600 K which is close

to the operating temperature of the cladding tubes. Among all the SIAs studied by Vérité [17], only those with a Boltzmann factor greater than 1 % have been considered to calculate $\bar{\epsilon}_{ij}^{00,i}$ and their Vegard tensors are given in Table 4.4.

Table 4.4: Relevant properties of point defects in Zr. For each PD type the components of its Vegard tensor averaged over the PD variants are given. The thermodynamic average of the Vegard tensor was performed at 600 K using Eq. (4.9). t refers to the tetragonality factor, t^1 corresponds to values obtained in this work (see text) and t^2 to values from [17].

PD	E_f (eV)	ν	F_B	ϵ_{11}^{00}	ϵ_{33}^{00}	t^1	t^2
BC'	2.7	6	74.3 %	0.564	0.02	0.61	0.57
BO	2.69	1	13.8 %	0.486	0.21	0.82	0.56
BS	2.77	3	8.4 %	0.637	−0.07	0.51	0.43
O	2.79	1	1.3 %	0.334	0.347	1.07	1.17
C'	2.91	6	2.0 %	0.352	0.281	1.22	1.35
avg. SIA			–	0.551	0.053	0.64	0.58
Vacancy	1.96		–	−0.131	−0.185	1.19	–

The resulting $\bar{\epsilon}_{ij}^{00,i}$ tensor is also tetragonal, but with an opposite behaviour to the one of vacancies since $\bar{\epsilon}_{33}^{00,i} < \bar{\epsilon}_{11}^{00,i} (= \bar{\epsilon}_{22}^{00,i})$. A tetragonality factor t quantifying the shape anisotropy can be associated with each type of PD by means of the dipole tensor P_{ij}, $t = P_{33}/P_a$, where $P_a = [(2(P_{11}^2 + P_{22}^2 + 2P_{12}^2) + (P_{11} + P_{22})^2)/8]^{1/2}$ [128]. In our work, the value of P_{ij} can be deduced from the relation $P_{ij} = V_{\mathrm{at}} C_{ijkl} \epsilon_{kl}^{00}$, with V_{at} the atomic volume and C_{ijkl} the elastic constants of pure zirconium taken from [129] in the R_0 basis: $C_{11} = 155\,\mathrm{GPa}$, $C_{12} = 67\,\mathrm{GPa}$, $C_{13} = 65\,\mathrm{GPa}$, $C_{33} = 173\,\mathrm{GPa}$ and $C_{44} = 36\,\mathrm{GPa}$. The corresponding value of t is reported in Table 4.4. The values obtained in [17] were directly calculated from the stress tensors determined at constant volume using SIESTA [130] which may explain the small differences with our values. On the whole, t obtained in this work is higher than in [17] for defects with a preferential deformation in the basal plane and lower for the other defects. The present average t is closer to the experimental one (1.1 ± 0.2 [128]), although comparison with this last value is not straightforward since experiments were performed at 6 K, this temperature being probably too low for application of Boltzmann statistics. The numerical values of t are different from 1, which means that PDs in zirconium, especially SIAs, do not behave like pure dilatational centres. Although these conclusions are drawn from a particular set of *ab initio* calculations, there is a general agreement among the recently published works about the preferential basal distortion of the most stable SIAs in Zr [16, 103, 110, 118–120]. As a conclusion, $\bar{\epsilon}_{ij}^{00,i}$ (resp. $\epsilon_{ij}^{00,v}$) are considered as the effective Vegard tensor characterizing SIAs (resp. vacancies) and then used as input parameters in the PF model.

4.2.2.2 Dislocation loop characteristics

The normal to the habit plane $\mathbf{n}_{dl}$ and the Burgers vector $\mathbf{b}_{dl}$ of each type of loop dl observed in zirconium under irradiation [9, 60, 131] are given in Table 4.5. In particular, it is observed that, for prismatic loops with a Burgers vector $1/3\langle 11\bar{2}0\rangle$,

the normal to the habit plane can vary between $\langle 11\bar{2}0\rangle$ and $\langle 10\bar{1}0\rangle$. Then, an intermediate orientation of the loop represented by $\mathbf{U_1}$ at $15°$ with $\langle 11\bar{2}0\rangle$ is also considered in this work (see Fig. 4.12). The symbols pl and bl will respectively refer to the prismatic and basal loops in the following. Knowing the normal $\mathbf{n}_{dl}$ and the Burgers vector $\mathbf{b}_{dl}$, it is then possible to calculate ϵ_{ij}^{dl0} used in the PF model from Eq. (2.2) for each type of loop given in Table 4.5.

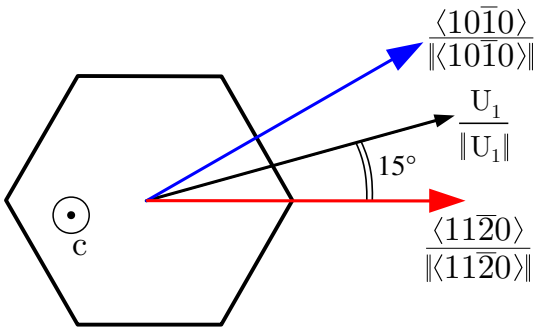

Figure 4.12: Normal to the different prismatic loops considered in this work.

Table 4.5: Characteristics and computed $\bar{B}$ values (see text for details) of dislocation loops observed in zirconium under irradiation.

	Habit plane	$\mathbf{b}_{dl}$	$\|\mathbf{b}_{dl}\|$ (Å)	Nature	$\bar{B}$
Prismatic	$\{11\bar{2}0\}$	$1/3\langle 11\bar{2}0\rangle$	3.23	Int./Vac.	0.392
	$\mathbf{U_1}$	$1/3\langle 11\bar{2}0\rangle$	3.23	Int./Vac.	0.389
	$\{10\bar{1}0\}$	$1/3\langle 11\bar{2}0\rangle$	3.23	Int./Vac.	0.383
Basal	(0001)	$1/6\langle 20\bar{2}3\rangle$	3.17	Vac.	0.218
	(0001)	$1/2[0001]$	2.57	Vac.	0.135
	(0001)	$[0001]$	5.14	Vac.	0.208

All the calculations presented here were performed in 2D and assuming that the loops are large enough to be locally assimilated to straight dislocations. The main steps of the PF methodology to investigate the loop sink efficiencies are described as follows. Each loop of Table 4.5 is decomposed into its constitutive dipoles of straight dislocations, as schematically represented in Fig. 4.13a). Each dipole is then characterized by its angle θ with a reference direction defined as $\mathbf{l}_{pl}^0 \parallel [0001]$ and $\mathbf{l}_{bl}^0 \parallel [\bar{1}2\bar{1}0]$, for prismatic and basal loops, respectively. In this approach, the study of one loop requires a series of 2D simulations, each one corresponding to one value of θ. The basis attached to the 2D calculation domain is then $(\mathbf{n}_{dl}, \mathbf{m}_{dl}^{\theta}, \mathbf{l}_{dl}^{\theta})$ (see Fig. 4.13b).

Whatever the type of loop dl and the value of θ, the calculation domain is constituted of $2N \times N$ grid cells of size a_0, in which the distance between the dislocation core centres is noted L, which means they are located at coordinates $(a_0(N - \frac{L}{2}), Na_0/2)$ and $(a_0(N + \frac{L}{2}), Na_0/2)$. All the calculations have been performed with $a_0 = 0.323$ nm and $r_0 = 1.275$ nm.

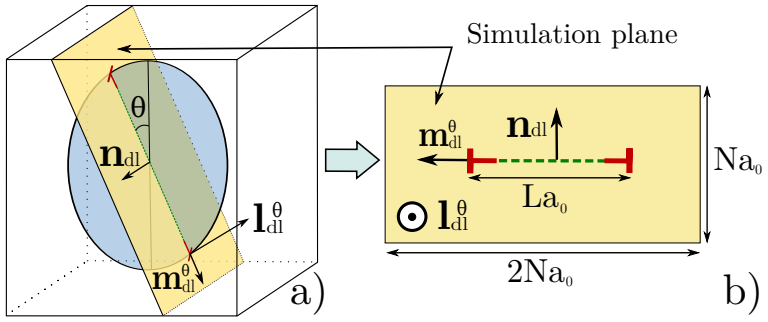

Figure 4.13: Decomposition of an interstitial loop (a) into its constitutive dipoles of straight dislocations (b).

For each simulation, the elastic properties of the system must be expressed in the $(\mathbf{n}_{dl}, \mathbf{m}^{\theta}_{dl}, \mathbf{l}^{\theta}_{dl})$ basis, and then depend on the type of loop dl and on the angle θ according to the relations:

$$\begin{aligned}
\bar{\epsilon}^{00,i}_{ij}(dl,\theta) &= T^{dl,\theta}_{il} T^{dl,\theta}_{jm} \bar{\epsilon}^{00,i}_{lm}(R_0),\\
\epsilon^{00,v}_{ij}(dl,\theta) &= T^{dl,\theta}_{il} T^{dl,\theta}_{jm} \epsilon^{00,v}_{lm}(R_0),\\
\epsilon^{dl0}_{ij}(dl,\theta) &= T^{dl,\theta}_{il} T^{dl,\theta}_{jm} \epsilon^{dl0}_{lm}(R_0),\\
C_{ijkl}(dl,\theta) &= T^{dl,\theta}_{ig} T^{dl,\theta}_{jh} C_{ghmn}(R_0) T^{dl,\theta}_{km} T^{dl,\theta}_{ln},
\end{aligned} \tag{4.11}$$

with $T^{dl,\theta}_{ij}$ the transformation matrix from R_0 to $(\mathbf{n}_{dl}, \mathbf{m}^{\theta}_{dl}, \mathbf{l}^{\theta}_{dl})$.

4.3 Results and discussion

4.3.1 Sink efficiencies of dislocation loops

As mentioned in Eq. (2.34), the calculation of Z and consequently B requires the knowledge of the average composition $\bar{X}$ at steady-state. It is calculated from the composition map which is an output of the PF model. Some examples of composition maps for SIAs and vacancies are represented for two specific dipoles $d_p = (\mathbf{l} \parallel \mathbf{c}, \mathbf{b} = 1/3[11\bar{2}0])$ and $d_b = (\mathbf{l} \parallel [\bar{1}2\bar{1}0], \mathbf{b} = [0001])$, each one being respectively representative of the dipoles constitutive of the prismatic $1/3\langle 11\bar{2}0\rangle\{11\bar{2}0\}$ loop and the basal $[0001](0001)$ loop. The sink efficiencies can then be deduced from Eq. (2.34) and are indicated by points P and B in Fig. 4.14.

Whatever the type of loop dl, The specific choice of $\mathbf{l}^0_{dl}$ implies that $Z(\theta) = Z(-\theta)$ and it is obvious that $Z(\theta) = Z(\theta + \pi)$. As a consequence, the SIA and vacancy sink efficiencies, respectively noted Z_i and Z_v, have been calculated for θ between $0°$ and $90°$. The results represented in Fig. 4.14 correspond to $N = 128$ and $L = N$. The resulting bias B is defined as Eq. (1.34).

Due to the symmetries of the problem, Z (and then B) does not depend on angle θ for $[0001](0001)$ and $1/2[0001](0001)$. These two loops are identical, except for the norm of their Burgers vector. A larger Burgers vector promotes elastic interactions between the dislocation and PDs, which results in larger sink efficiencies of

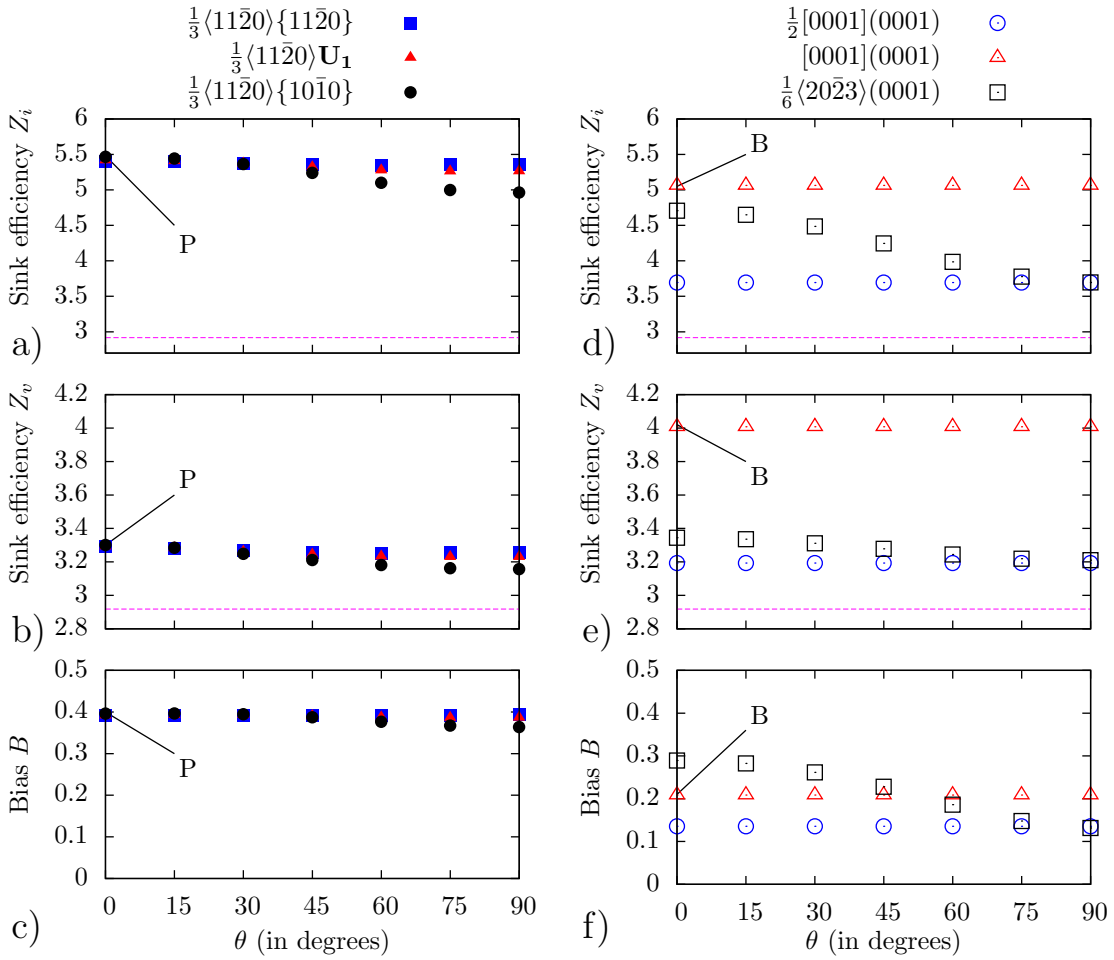

Figure 4.14: a), b) and c): Sink efficiencies and bias for the prismatic loops. d), e) and f): Sink efficiencies and bias for the basal loops. The dotted horizontal lines give the sink efficiency obtained if no elastic interaction is considered, with the Wiedersich equation for cylindrical sinks [28].

SIAs and vacancies for $[0001](0001)$ in comparison to $1/2[0001](0001)$. As expected, the resulting bias is also larger for $[0001](0001)$. The results obtained for the basal $1/6\langle 20\bar{2}3\rangle(0001)$ loop are qualitatively different, since the computed variations of Z and B with θ are significant. This is due to the change of the dislocation character along this loop, as represented in Fig. 4.15. When the tangent to the loop is parallel to $[\bar{1}2\bar{1}0]$ ($\theta = 0°$), the dislocation is purely edge, which corresponds to the case of a high elastic interaction with PDs. Then, the maxima of Z and B are reached for this value of θ. On the contrary, the edge character of the dislocation line is strongly attenuated for the maximum of $\mathbf{l}_{dl}^{\theta}.\mathbf{b}_{dl}$, reached at $\theta = 90°$, resulting in the lowest values of Z and B. In this case, the $1/6\langle 20\bar{2}3\rangle(0001)$ dipole has the same Burgers vector component in $[0001]$ as the $1/2[0001](0001)$ dipole. As the influence of the "screw" component of the line is negligible, both systems are almost equivalent. As a consequence, the computed efficiencies and bias give very close values (see Fig. 4.14d), e) and f)).

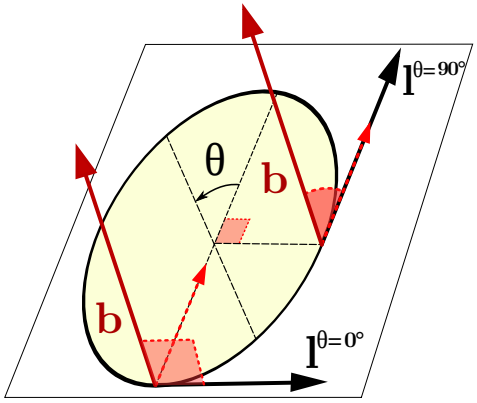

Figure 4.15: Representation of a $^1/_6\langle 20\bar{2}3\rangle(0001)$ loop. The dashed arrows represent the projection of $\mathbf{b}$ on the loop plane. It clearly appears that when $\theta = 0°$, $\mathbf{b}$ and $\mathbf{l}^\theta$ are normal to each other, while when $\theta \neq 0°$, $\mathbf{b}.\mathbf{l}^\theta \neq 0$.

The same type of argument allows to explain the variation of Z and B for the prismatic loops $^1/_3\langle 11\bar{2}0\rangle\mathbf{U_1}$ and $^1/_3\langle 11\bar{2}0\rangle\{10\bar{1}0\}$. Indeed, the more the normal to the loop habit plane deviates from the direction of the Burgers vector, the larger the variation magnitude of Z and B is. However, these variations are less pronounced for the prismatic loops than for $^1/_6\langle 20\bar{2}3\rangle(0001)$. On the whole, concerning the prismatic loops, the variations of Z and B with θ and the habit plane orientation are small.

In order to assess the preferential absorption of vacancies by the prismatic or basal loops, we consider a simplified system in which only these two types of sinks are present at the same density. If the basal (resp. prismatic) loops are characterized by the average sink efficiencies $\bar{Z}_{bl}$ (resp. $\bar{Z}_{pl}$) and biases $\bar{B}_{bl}$ (resp. $\bar{B}_{pl}$), then the net flux of vacancies to basal loops J_{net} is given by:

$$J_{\text{net}} = K_0 \left(\frac{\bar{Z}_{v,bl}}{\bar{Z}_{v,bl} + \bar{Z}_{v,pl}} - \frac{\bar{Z}_{v,bl}}{\bar{Z}_{v,bl} + \bar{Z}_{v,pl} R_B} \right) \tag{4.12}$$

with $R_B = (1 - \bar{B}_{bl})/(1 - \bar{B}_{pl})$. From Eq. (4.12), it is easy to demonstrate that $J_{\text{net}} > 0$ is equivalent to $\bar{B}_{bl} < \bar{B}_{pl}$. If J_{net} is positive, it means that the growth of basal loops of vacancy type is promoted by the elastic interactions with PDs. Then, under the simplifying assumptions mentioned above, only the determination of these two biases are required to conclude on the elastic effect, hence they are calculated through the following two-step procedure:

(i) For each type of loop, the bias is averaged over θ and the resulting value $\bar{B}$ is given in Table 4.5.

(ii) $\bar{B}_{bl}$ (resp. $\bar{B}_{pl}$) is the average value of $\bar{B}$ over all the basal (resp. prismatic) loops, assuming the same density of each type of loop.

The overall comparison between the prismatic and basal loops reveals that $\bar{B}_{bl} < \bar{B}_{pl}$ (19 % *vs* 39 %), which is consistent with the preferential growth of vacancy-type basal loops. It should also be noticed that the bias of prismatic loops is larger than that of any basal loop.

These results have been obtained for an arbitrary value of the dislocation den-

sity ρ_s and for a homogeneous distribution of the dislocations in the system corresponding to $L/N = 1$ but we can wonder whether such conclusions still hold for varying values of ρ_s and L/N. Since an overall small variation of the sink efficiency with θ is observed whatever the type of the loop (except $^1/_6\langle 20\bar{2}3\rangle(0001)$), we selected the dipole corresponding to $\theta = 0$ for each type of loop. These reference cases were used first to study the effect of the density ρ_s (N varies between 64 and 1024) with L/N set at 1. The results for Z_i, Z_v and B are respectively represented in Fig. 4.16a), b) and c). As expected, these quantities decrease with density, but still, the respective positions of the curves do not change, which means that the previous conclusions hold.

The same type of analysis has been conducted for different values of L (between $10\,a_0$ and $256\,a_0$) and a given density corresponding to $N = 256$, leading to Fig. 4.17a), b) and c): Z_i, Z_v and B increase with L but the ranking is conserved, like in Fig. 4.16.

In order to understand the physical origin of these conclusions, a thorough analysis of the numerical results is performed. In particular, an intriguing fact is that $\bar{B}_{[0001](0001)} < \bar{B}_{pl}$, which is *a priori* at odds with the fact that $\|\mathbf{b}\|_{[0001](0001)} > \|\mathbf{b}\|_{pl}$ ($5.14\,\mathring{A}$ *vs* $3.23\,\mathring{A}$). These results, obtained by rigorous solution of Eq. (2.22), cannot be understood in terms of PD relaxation volumes and Burgers vector norm only, as shown in the next section.

4.3.2 Anisotropy effects on sink efficiency

To interpret the previous numerical results, it is required to investigate the role of anisotropies in the system, which has two distinct origins:

- the anisotropy of the Vegard tensor ϵ_{ij}^{00} associated with PDs, referred as PD anisotropy in the following,
- the anisotropy of the elastic constants C_{ijkl} of the system considered as homogeneous and constituted of pure hcp zirconium

We do know that with fully isotropic properties, the dipole d_b defined in section 4.3.1 should always have a larger absorption bias than d_p (see Chap. 3), due to its larger Burgers vector. In order to better explain the bias inversion, the PF method was used to study separately each anisotropy effect. For this purpose, three simulation cases are compared for various dislocation densities:

- Case AA: anisotropic elastic constants and anisotropic PDs.
- Case IA: isotropic elastic constants and anisotropic PDs.
- Case AI: anisotropic elastic constants and isotropic PDs.

For case AI, the *isotropic PD* is defined so that its relaxation volume is equivalent to those calculated in section 4.2.2.1:

$$\varepsilon_{ii}^{00,\mathrm{iso}} = \frac{\mathrm{Tr}(\varepsilon^{00})}{3}, \tag{4.13}$$

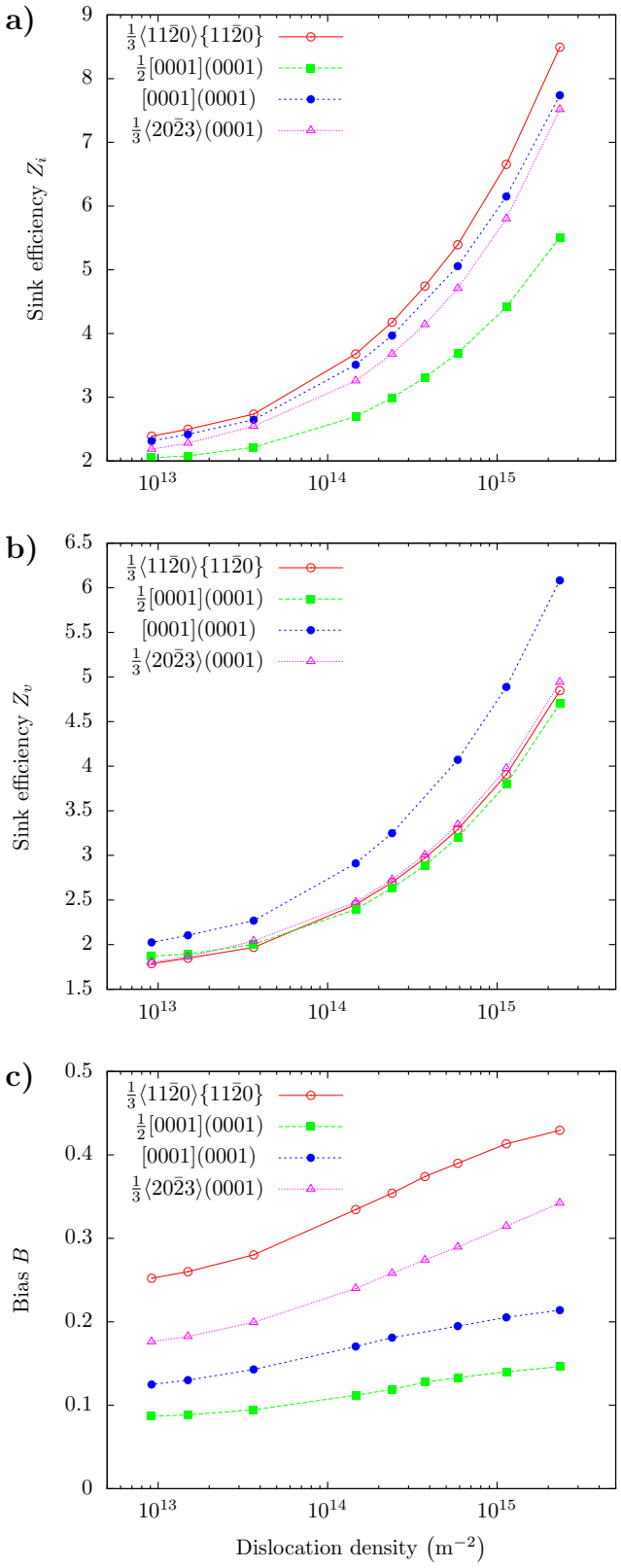

Figure 4.16: Sink efficiencies for a) SIAs, b) vacancies, and c) bias as a function of the dislocation density.

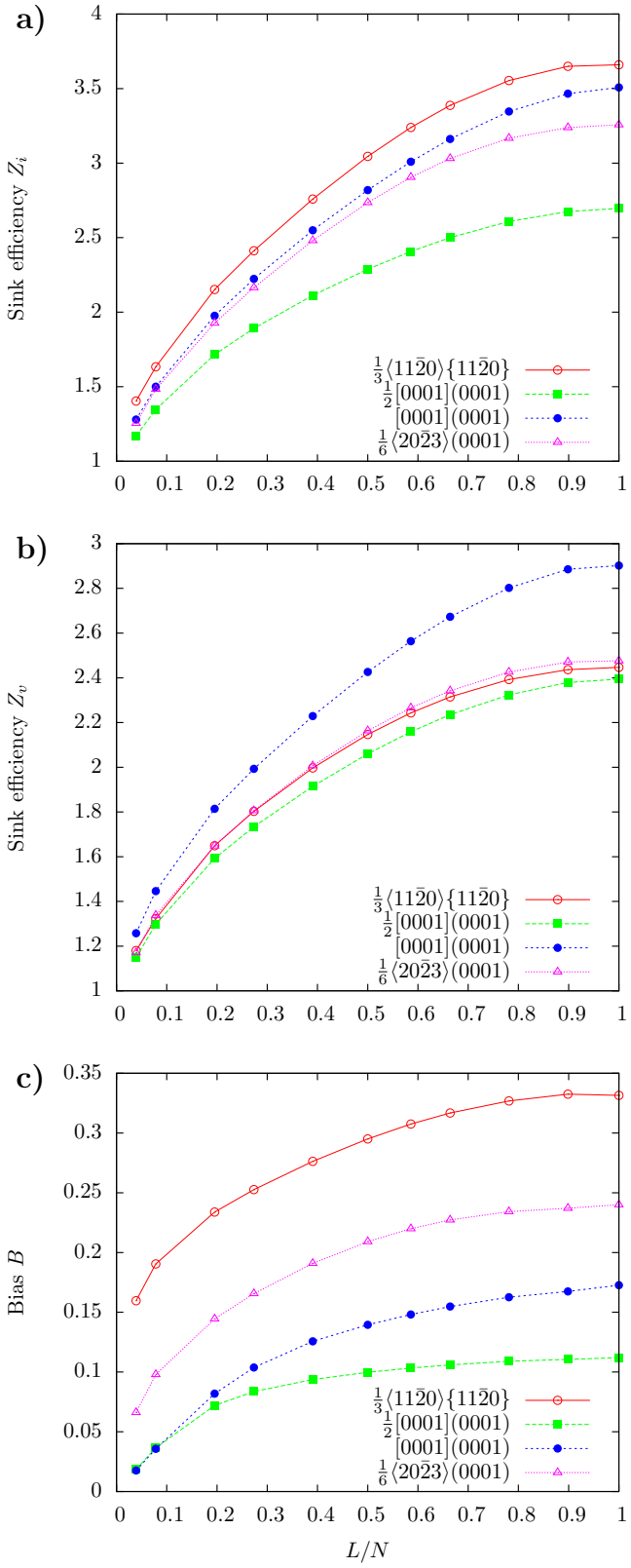

Figure 4.17: Sink efficiencies for a) SIAs, b) vacancies, and c) bias as a function of the distance between the dislocation cores.

which gives $\varepsilon_{ii}^{00,\mathrm{iso}} = +0.38$ for SIAs and $\varepsilon_{ii}^{00,\mathrm{iso}} = -0.15$ for vacancies.

The isotropic elastic constants C_{ijkl}^{iso} were calculated so that $C_{11}^{\mathrm{iso}} = C_{11} = 155\,\mathrm{GPa}$ and $C_{44}^{\mathrm{iso}} = C_{44} = 36\,\mathrm{GPa}$.

Results are gathered in Fig. 4.18. One can see in Fig. 4.18c) that in case IA, d_p still has the higher absorption bias values (for a given density), which is similar to case AA (see Fig. 4.18a)). On the contrary, for case AI (Fig. 4.18b)), d_b has the higher absorption bias, which is the same result as the one what would be expected for fully isotropic properties (C_{ijkl} and ϵ^{00}).

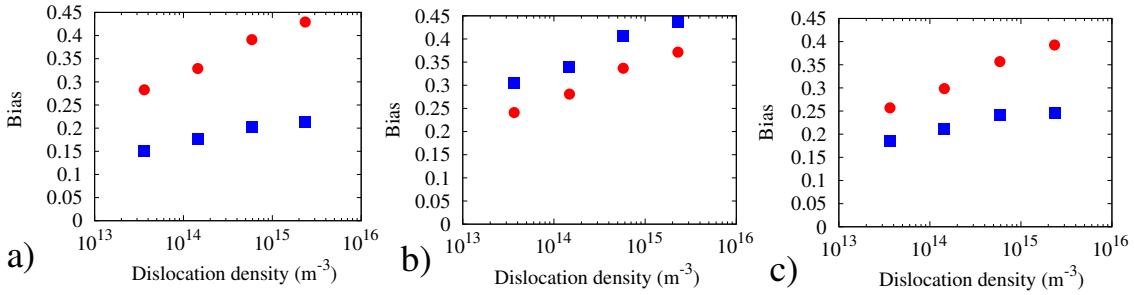

Figure 4.18: Absorption bias of d_b (blue squares) and d_p (red circles) in a) case AA, b) case AI and c) case IA as a function of dislocation densities.

As a consequence, the PD anisotropy is more decisive than the anisotropy of the elastic constants. This was expected, as zirconium has slightly anisotropic elastic constants, while the SIA has one order of magnitude between its Vegard coefficients. The main parameter is then the relative orientation of the Burgers vector and the eigenvectors of the Vegard tensor: the highest value of the sink efficiency is obtained when the direction of highest strain is parallel to the Burgers vector. The following part will then be dedicated to the specific study of PD anisotropy.

4.3.3 The SAS effect

To simplify the problem, only the results related to d_b and d_p are considered in this part and the corresponding sink efficiencies are noted Z_{d_b} and Z_{d_p} in the following. The strength of the elastic interactions can be conveniently quantified by means of the elastic potential. The Vegard tensor of PDs being diagonal (see section 4.2.2.1), the elastic potential μ_{el} is given by the expression $V_{\mathrm{at}}\epsilon_{ii}^{00}\sigma_{ii}(\mathbf{r})$ (see Eq. (2.18)), in which only the diagonal terms of the stress tensor are present. The diagonal stress fields maps are represented for d_b (resp. d_p) in Fig. 4.19 (resp. Fig. 4.20): the largest component is σ_{33} for d_b, whereas it is σ_{22} for d_p (in both cases, it corresponds to σ_{ii}, where i refers to the direction $\mathbf{n}_{dl}$). Concerning SIAs, the comparison of the elastic potentials for both dipoles represented in Fig. 4.21 reveals that they are approximately of the same magnitude, which is in fact the result of two antagonistic effects:

(i) $\|\mathbf{b}\|_{d_b} > \|\mathbf{b}\|_{d_p}$ ($5.14\,\mathring{A}$ *vs* $3.23\,\mathring{A}$), which should induce larger elastic interactions between SIAs and d_b.

(ii) However, for the dipole d_b, its main stress component σ_{33} interacts with $\bar{\epsilon}_{33}^{00,i}$, which is ten times lower than the other Vegard coefficients. As a consequence,

its contribution to the elastic potential is negligible. For the dipole d_p, the situation is opposite since its main stress component σ_{22} interacts with $\bar{\epsilon}_{22}^{00,i}$, which is the largest Vegard coefficient.

From (ii) and the previous results, it clearly appears that SIAs will preferentially interact with prismatic dislocations rather than with the basal ones. In the following, we refer to this phenomenon as the *Shape Anisotropy of SIAs* (SAS) effect.

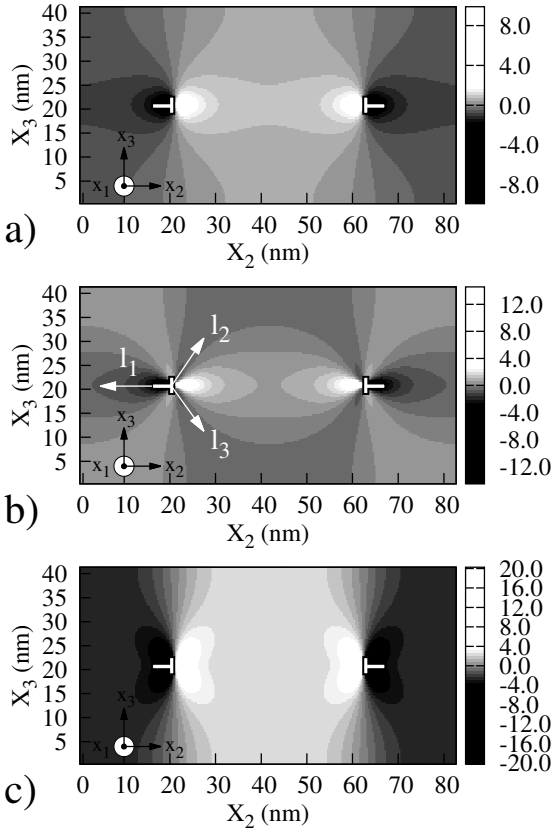

Figure 4.19: Steady-state maps of a) σ_{11}, b) σ_{22} and c) σ_{33} for d_b. Stress values are given in units of k_BT/V_{at}.

As a result of these antagonistic effects, the sink efficiencies for SIAs is slightly larger for d_p than for d_b (see points P and B in Fig. 4.14). The same explanation applies to any dislocation dipole constitutive of the prismatic $^1/_3[11\bar{2}0]\{11\bar{2}0\}$ loop since whatever this dipole, it is always the largest component of the stress field which interacts with the largest Vegard coefficient. As a consequence, the sink efficiency for SIAs in Fig. 4.14a) weakly depends on θ, which reveals a qualitative difference with the DAD effect [50]. Indeed, the latter predicts preferential absorption of SIAs by dislocation lines parallel to **c** and not by any dislocation line constitutive of a prismatic loop.

For vacancies, there is also a shape anisotropy effect which is opposite to the SAS effect ($|\epsilon_{33}^{00,v}| > |\epsilon_{11}^{00,v}|$ whereas $|\bar{\epsilon}_{33}^{00,i}| < |\bar{\epsilon}_{11}^{00,i}|$, see section 4.2.2.1). Moreover, the anisotropy is less pronounced for $\epsilon_{ij}^{00,v}$ than for $\bar{\epsilon}_{ij}^{00,i}$. As a consequence, effect (i)

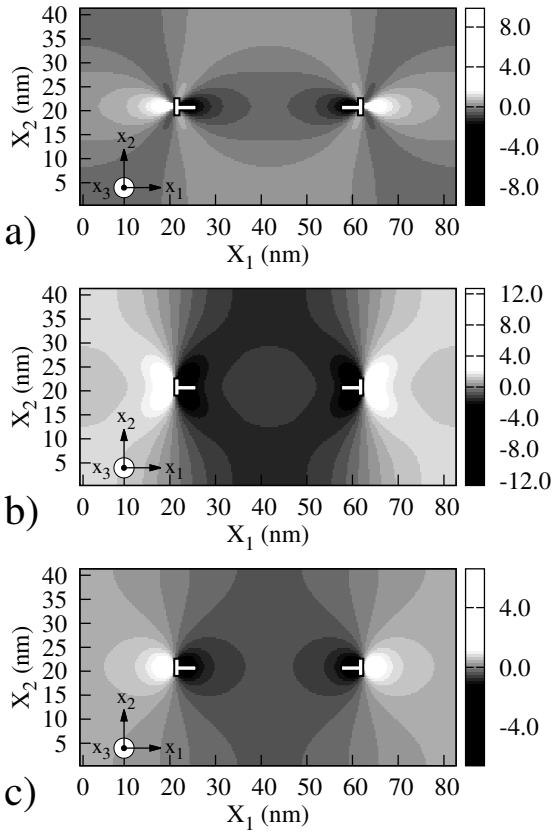

Figure 4.20: Steady-state maps of a) σ_{11}, b) σ_{22} and c) σ_{33} for d_p. Stress values are given in units of k_BT/V_{at}.

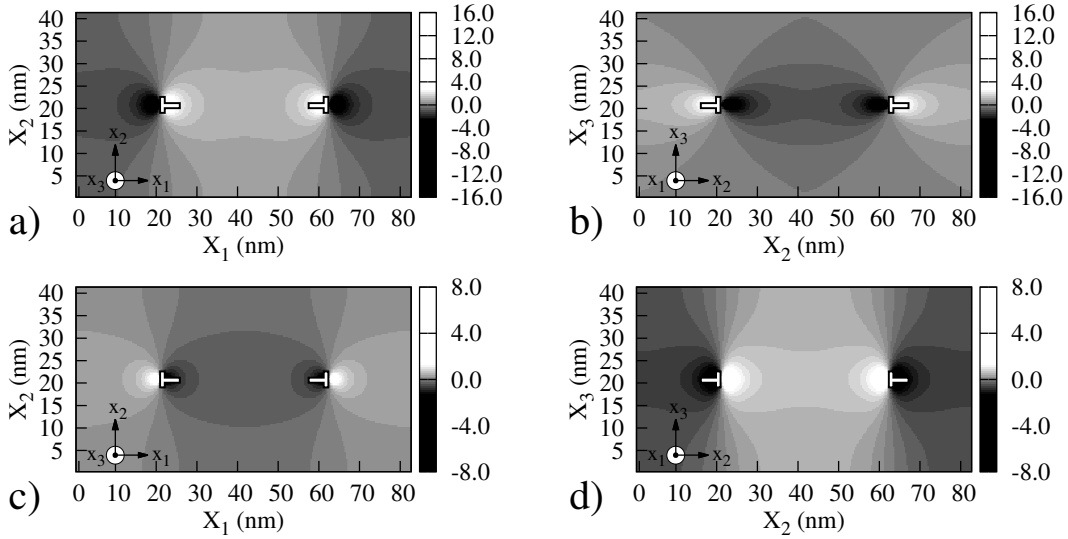

Figure 4.21: Elastic potential maps of SIAs (resp. vacancies) around d_p in a) (resp. c)) and d_b in b) (resp. d)). Elastic potentials are given in units of k_BT/V_{at}.

described above is slightly enhanced by the shape anisotropy of vacancies and Z_v is then larger for d_b than for d_p. It results from $Z_{i,d_p} \approx Z_{i,d_b}$ and $Z_{v,d_p} < Z_{v,d_b}$ a significant difference in biases, $B_{d_p} > B_{d_b}$ as shown in Fig. 4.14. The SAS effect has been illustrated for one couple of dipoles, but the same conclusion is valid whatever the choice of the dipoles representative of the basal and prismatic loops.

The SAS effect is also visible on the steady-state composition profiles represented in Fig. 4.22. Considering for example Fig. 4.22c) corresponding to vacancy diffusion around d_p, the composition profiles are qualitatively close to the profiles represented in Fig. 3.14 dedicated to elastically isotropic systems: as the relaxation volume of vacancies is negative, the depleted and enriched zones in vacancies correspond respectively to the traction and compression zones. Moreover, the isocurves are almost circular but their centre do not coincide with the dislocation cores: they are in the traction zone for vacancies. These similarities are not surprising since in our case, the elastic constants of zirconium matrix are slightly anisotropic and the Vegard tensor of vacancies is close to a pure compression. Comparing Fig. 4.22b) (SIA diffusion around d_b) with Fig. 4.22c) reveals the SAS effect: beyond the fact that the behaviour is opposite for SIAs (the depleted and enriched zones corresponds respectively to the compression and traction zones due to a positive relaxation volume), the SIA isocurves are also qualitatively different from the vacancy ones since they clearly exhibit three directions more depleted in SIAs, as indicated in Fig. 4.22b) by vectors $\mathbf{l}_1$ to $\mathbf{l}_3$. The angle between $\mathbf{l}_1$ and $\mathbf{l}_2$ or $\mathbf{l}_1$ and $\mathbf{l}_3$ is approximately $130°$. This is related to the specific variations of σ_{22} (see Fig. 4.19b)) with which SIAs preferentially interacts for d_b (negligible interaction with σ_{33} due to $\bar{\epsilon}_{33}^{00,i} \ll \bar{\epsilon}_{22}^{00,i}$ and $\sigma_{22} > \sigma_{11}$) and which exhibits negative values along the same directions $\mathbf{l}_1$ to $\mathbf{l}_3$.

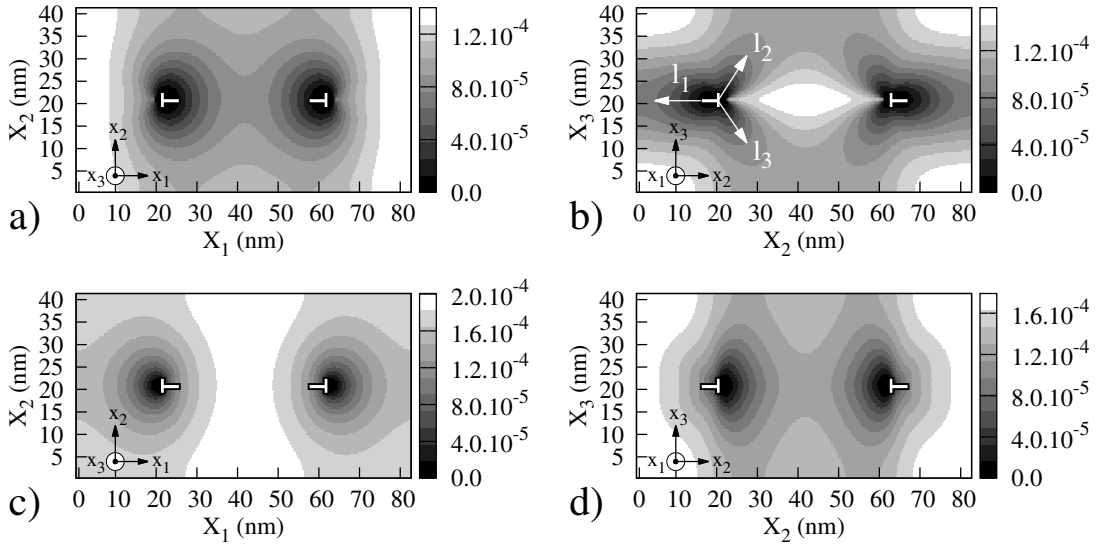

Figure 4.22: Steady-state composition maps of SIAs (resp. vacancies) around d_p in a) (resp. c)) and d_b in b) (resp. d)). Values are given in site fractions.

4.3.4 Limits of the model

The PF model allowed to revisit the calculation of the elastic biases for dislocations in zirconium by taking into account the specific deformation induced by PDs in the matrix. It must be mentioned that it is often believed that the positive elastic bias for dislocations, due to a larger relaxation volume of SIAs than vacancies, only promotes the growth of interstitial loops, and hence cannot explain the unusual presence of vacancy-type basal loops in zirconium alloys. It has been shown that such conclusions do not hold anymore when considering shape anisotropy of PDs.

Our analysis rests on isotropic diffusion tensor, as shown in Eq. (2.21). This assumption is at odds with previous models proposed to explain the development of these microstructural defects in zirconium. Indeed, among the physical origins proposed up to now, the DAD between SIAs and vacancies assumed by Woo et al. [49, 50] has been considered as an appealing explanation. The questionable point is that there is no experimental nor simulations results based on state-of-the-art density functional calculations that confirm that the assumptions of reference [50] are verified for Zr (see section 4.1.3.1). All these results clearly show that the migration anisotropy of point defects in zirconium is still a matter of debate. It is obviously expected that the crystal lattice anisotropy and the anisotropy of the SIA configurations (SAS) should imply a non isotropic diffusion of both point defects but no quantification of the correlation between SIAs structure on one hand and SIAs diffusion on the other hand has been established until now. Since this task is beyond the goal of this chapter, we choose to assume isotropic diffusion due to a lack of reliable data. It is important however to emphasize that our results show that there is no need to suppose a strong SIAs diffusion anisotropy to explain the existence of vacancy basal dislocation loops in Zr alloys under irradiation, the observation that originally motivated the development of the DAD model. In addition, the methodology proposed in this paper can easily incorporate diffusion anisotropy and if we consider this effect, the magnitude of the main result of the work (i.e. the preferential bias of SIAs for prismatic loops) would be reinforced instead of being weakened.

It must be mentioned that other effects known as *Stress Induced Preferential Absorption* (SIPA) have been overlooked in this paper due to a lack of data in the literature. These are related to the impact of a stress field —the dislocation one in our case— on sink strengths. In SIPA I, the role of the polarizability tensor, which arises from the difference in the elastic properties between the inclusion and the matrix [35], is crucial. However, the polarizability tensors for PDs in zirconium are not available in the literature. Moreover, it can be shown that this tensor can be related to the change of the elastic constants of the crystal induced by the presence of the defects [113, 114]. The formalism of the PF model proposed in this paper assumes homogeneous elastic constants and then should be adapted to the case of inhomogeneous elasticity. Previous methods have been proposed to solve such an issue [86, 132–134] in PF models and could be easily incorporated in the formalism of this paper. The SIPA-SAPSE effect (Saddle Point Shape Effect) is related to the characteristics of PDs in their saddle point position. Indeed, it has been shown that in an elastic strain field the anisotropy of the saddle-point configuration leads to an anisotropic diffusion at the origin of the SIPA-SAPSE

effect [38, 39]. Studying this effect supposes to know the deformation induced by PDs in their saddle point configurations. These values still need to be determined.

As previously indicated, we took for X^s in Eq. (2.34) the thermal equilibrium value at 600 K. Since dislocation loops that absorb PDs are prone to climb, there is a climbing force per unit length F_{pk} acting on them that generates a supersaturation X^d of PDs at the loop cores that is given by [8]:

$$X^d = X^s \exp\left(\frac{F_{pk} V_{\mathrm{at}}}{k_B T b}\right), \tag{4.14}$$

with $F_{pk} = [(\sigma \cdot \mathbf{b}) \wedge \mathbf{l}] \cdot \mathbf{n}$ (with σ the local stress tensor, $\mathbf{l}$ the normalised vector tangent to the line and $\mathbf{n}$ the normalised climb direction) the Peach-Köhler force per unit length acting on the loop and generated by the external load and/or by sources of internal stress in the microstructure. In our calculations, the maximum value of σ was determined by considering the stress generated by a dislocation at 3 nm away from the line, the minimum distance between dislocations used in this work ($L/N = 0.04$ in Fig. 4.17). This value leads to a ratio $X^d/X^s < 100$ in the case of the perfect basal loop, and $X^d/X^s < 20$ for the other cases. Such an increase does not affect the calculated sink efficiency, even for dislocation lines considered very close.

Rigorously, we should have solved one diffusion equation of the same form as Eq. (2.22) per type and orientation of SIA. To circumvent this difficulty, an ensemble average for the SIA concentration was assumed, that allows to define an effective Vegard tensor (Eq. (4.9)) and then to treat only one diffusion equation for all SIAs. We think that this approach is sufficient to grasp the main tendencies of SIA behaviours in the stress field of a dislocation, and more particularly the SAS effect. However, provided the transition rates between the different types of SIAs are known, it would be an interesting extension of this work to study the quantitative effect of such an assumption on sink strengths.

4.4 Conclusion

Phase-field calculations have shown that, despite the greater Burgers vector of perfect basal loops, the basal configuration of SIAs leads to the highest capture bias for prismatic loops. As a consequence, while prismatic loops absorb more SIA, basal loops will experience a net flux of vacancies. The Shape Anisotropy of SIAs (SAS) could therefore be a major factor for basal vacancy loops growth in irradiated zirconium alloys. Based on state-of-the-art *ab initio* results and on a rigorous PF model applied to sink efficiency calculations, this work clearly points out the necessity of properly taking into account elastic interactions and in particular the SAS effect. The consideration of SAS for other crystals may also help to better understand the evolution of loops in irradiated materials. This approach could be generalised to other migrating defects: as the strain properties of small defect clusters in irradiated metals are strongly anisotropic [100], the study of this type of effect on their diffusion could be a perspective of this work.

Chapter 5

Sink efficiency of dislocation loops in metals

Contents

While dislocation loops are commonly observed defects in irradiated metals, their migrating defect sink efficiencies have been much less studied than those of straight dislocations (see section 1.3.4), due to the 3D nature of the problem (see section 1.3.4). The geometry of the dislocation line was described by 2 independent variables: ρ_l and r_0, while the dislocation loop geometry need 3 of those: the loop density ρ_{vol}, the loop radius r_L and the core radius r_0. The literature concerning the loop sink efficiency calculation is still incomplete: no systematic study of the effect of the boundary conditions have been performed and calculations with anisotropic elasticity have never been carried out. In order to better understand

the microstructure evolution in irradiated metals, dislocation loops should benefit of the same efforts as those dedicated to straight dislocation lines. Because of the lack of systematic studies on dislocation loops, this chapter is dedicated to the separated investigation on the effects of each variable on sink efficiency.

Most recent techniques make simplifying assumptions (Laplace boundary conditions) or must be coupled with other models to provide the PD elastic potential around the dislocation (see section 1.3.4.2). In this chapter, the methodology for computing sink efficiencies of dislocation loops in various conditions will be explained. Original application and results will be presented and discussed. In particular, this chapter aims at assessing the validity of the PF model for 3D calculations of sink efficiencies, whereas results presented in chapters 2, 3 and 4 only concern 2D simulations. The same approach to that used in chapter 3 will be followed:

- Validation of the model by comparison with the simple case of the spherical sink for which an analytical solution is available (section 5.1).
- Computation of sink efficiency of a toroidal sink (i.e. a dislocation loop without elasticity, see section 5.1.2).
- Evaluation of the effect of elasticity on sink efficiency of dislocation loops with isotropic elastic properties (section 5.2).
- Application of the method to the practical case of zirconium (section 5.3).
- Validation of the accelerated convergence algorithm for toroidal sinks and dislocation loops (section 5.4).

This systematic approach enables to consider each parameter separately. We will be able to comment on the effects of the loop properties on the sink efficiency.

In this chapter, the expression *toroidal sink* will be used for simulations without elasticity, while *dislocation loop* concern calculations taking into account the elastic interactions between PDs and the dislocations.

5.1 3D sink efficiency calculations without elastic interaction

This section will focus on the particular cases of the spherical sink and the toroidal sink, for which analytical solutions are known.

5.1.1 Spherical sink

Before applying the PF model to dislocation loops, we study the simpler case of the spherical sink which constitutes a preliminary 3D validation. These simulations are performed without taking elasticity into account, i.e. $\eta = 0$.

The spherical sink has been studied analytically (see section 1.2 and Tab. 1.2). Laplace solution leads to a sink efficiency independent of the sink density, depending only on the sink radius. This solution is acceptable for very low sink densities.

The limiting case for which $R \to \infty$ leads to the asymptotic Laplace solution exposed in Eq. (1.20). On the opposite, Wiedersich sink efficiency grows with sink radius and sink density (see Tab. 1.2). All those solutions converge for very low sink densities to the value of Eq. (1.20).

Phase-field calculations on the spherical sink case have been performed and compared to analytical solutions. Toroidal sink efficiencies can be rigorously calculated using only 2 order parameters. The first order parameter is the point defect site fraction field X, the second one is the shape function λ of the sink (see Fig. 5.3). In the PF code, the λ order parameter set at 1 if the cell is located at a distance lower than a given radius r_0' from a point c, and 0 otherwise (0 otherwise, see Fig. 5.1):

$$(x - x_c)^2 + (y - y_c)^2 + (z - z_c)^2 \leqslant (r_0')^2 \Rightarrow \lambda(x, y, z) = 1 \tag{5.1}$$

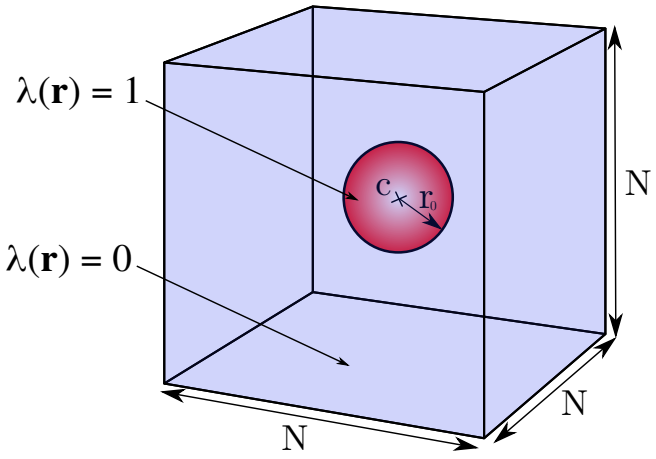

Figure 5.1: PF computation domain in the case of a spherical sink centred on point c, with radius r_0.

As it is hard to properly describe a sphere with radius r_0' in a cubic mesh, the effective radius r_0 must be deduced from the number of cells in the sink. For the analytical solutions, the radii r_0 and R have been estimated as:

$$r = (3N_{\text{cell}}/4\pi)^{1/3} a_0, \tag{5.2}$$

with N_{cell} the number of cells located in the sink for $r = r_0$, or the number of cells in the computational domain for $r = R$. It must be noted that $r_0 < r_0'$.

With this choice, the analytical and numerical sinks share the same volume. Nevertheless, it must be noted that:

- PF sinks are not perfect spheres,
- the PF calculation domain is a cube instead of a sphere of radius R, like in the analytical models.

The results of the sink efficiency calculations by PF are plotted on Fig. 5.2. Like in the cylindrical sink case (see chap. 3), the Wiedersich solution gives a higher

sink efficiency than the Laplace one. In addition, PF results give values slightly lower than those of Wiedersich, but very close to it. We remark that PF results do fit perfectly the Wiedersich solution calculated for a sink radius of r_0^{corr} instead of r_0:

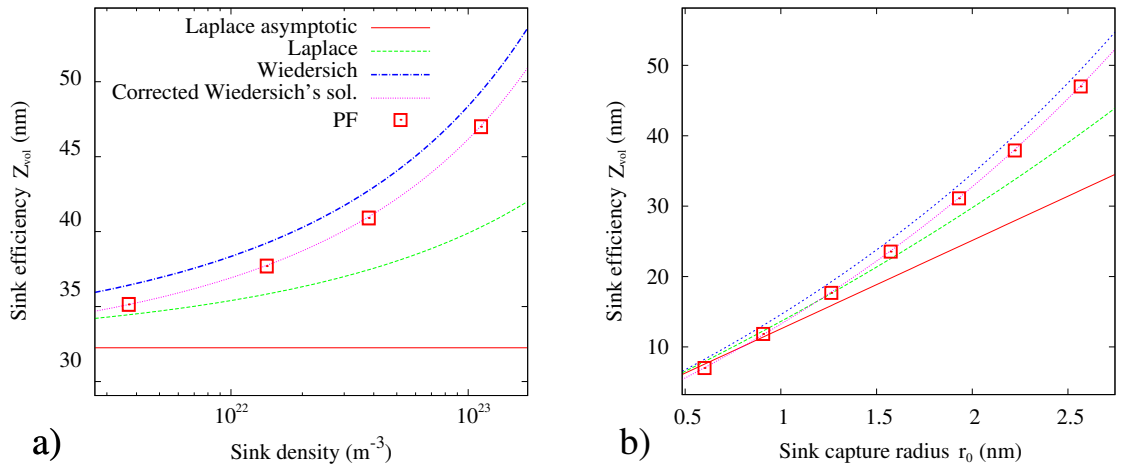

Figure 5.2: a) Sink efficiencies of the spherical sink as a function of spherical sink density, given for $64 \leqslant N \leqslant 200$ and $r_0' = 8\,a_0 \Rightarrow r_0 = 7.94\,a_0$. b) Sink efficiencies as a function of the spherical sink radius, given for 0.8 nm $\leqslant r_0' \leqslant 2.56$ nm and $N = 64$. The lines represent various analytical solutions, the squares are PF results. *Corrected Wiedersich solution* is the plot of the Wiedersich solution with correction given in equation (5.3). The agreement between PF results and the corrected Wiedersich solution is excellent.

$$r_0^{\text{corr}} = r_0 - 0.25\,a_0, \tag{5.3}$$

which is a non trivial assumption. In other words, that means that equation (5.2) overestimates the radius of the numerical sink by $0.25\,a_0$. To our opinion, the main reasons are: (i) the modelled spherical sink isn't a perfect sphere and (ii) the boundary condition imposed in the sphere is close but not perfectly equivalent to the Dirichlet boundary condition. The same correction has been tested on the case of the cylindrical sink, and the conclusions of chapters **??** and 4 remain unchanged. In the following, the correction (5.3) will be taken systematically into account.

5.1.2 Sink strength of the toroidal sink (without elasticity)

The calculation tool has been calibrated in the case of spherical sinks (see section 5.1.1), for which several analytical solutions are known. Only one expression is given for the toroidal sink neglecting elastic interactions (see Eq. (1.29)).

The system is described as a toroidal sink isolated in an infinite medium (see Fig. 5.3). Furthermore, Dubinko [37] showed that the result is highly dependent on the reservoir geometry (see section 1.3.4.2). In fact, the choice between a spherical and a toroidal reservoir gives close results for small loop radii only (see Fig. 1.11).

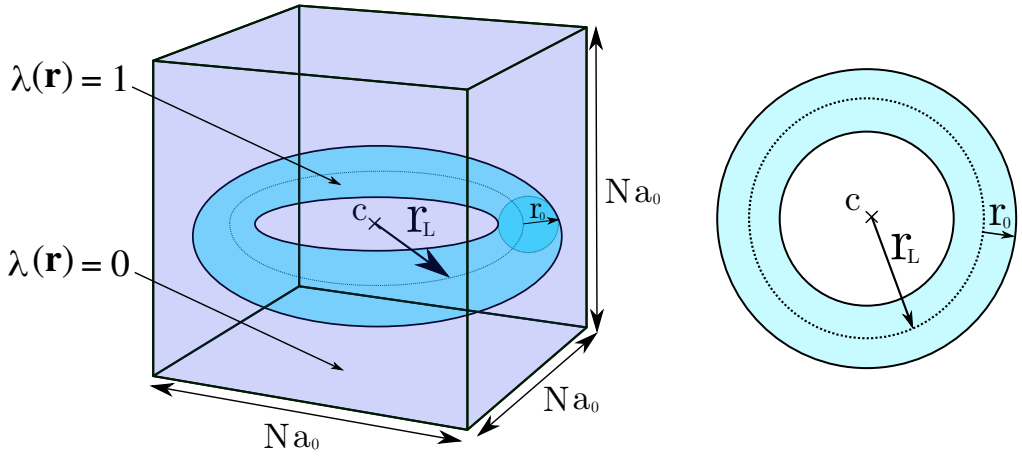

Figure 5.3: Schematic of the toroidal sink with major radius r_L and minor radius r_0. Note that $\eta(\mathbf{r})$ is null everywhere in the calculation domain since no elasticity effect is taken into account in this part.

Toroidal sink efficiencies can be rigorously calculated using only 2 order parameters. The first order parameter is the point defect site fraction field X, the second one is the shape function λ of the sink (see Fig. 5.3). $\lambda(\mathbf{r})$ is set at 1 inside the torus of centre c, major radius r_L and minor radius r_0. In the case where the habit plane of the torus is parallel to the (xy) plane, the (x, y, z) coordinates of any point located inside the the torus verify:

$$\left[r_L - \sqrt{(x-x_c)^2 + (y-y_c)^2}\right]^2 + (z-z_c)^2 < {r'_0}^2, \tag{5.4}$$

with (x_c, y_c, z_c) the coordinates of point c.

Toroidal sink efficiencies have been calculated for a wide range of parameters, which are the sink density per unit volume ρ_{vol}, the torus major radius r_L and the minor radius r_0 (see Tab. 5.1). The calculated sink efficiencies are compared to the analytical solution (1.29) in Fig. 5.4, 5.5 and 5.6. In addition, the accelerated convergence algorithm has been applied in these calculations with $\theta = 10$ and $\xi = 1.0$, its validation will be given in section 5.4.1.

Table 5.1: Input data for the toroidal sink.

Properties	Value
Cell size a_0 (nm)	0.323
Domain size N (cells)	$64 \leqslant N \leqslant 200$
System size (nm^3)	$20.7^3 \leqslant (Na_0)^3 \leqslant 64.6^3$
Sink density (m^{-3})	$3.7 \times 10^{21} \leqslant \rho_{\text{vol}} \leqslant 1.13 \times 10^{23}$
Atomic volume V_{at} (m^3)	2.3×10^{-29}

Figure 5.4 shows the convergence between PF and analytical results for very low sink volumetric densities (with $r_0 = 1.05\,\text{nm}$ ($r'_0 = 1.13\,\text{nm}$) and $r_L = 6.46\,\text{nm}$).

However, even for $\rho_{\text{vol}} \simeq 10^{21}\,\text{m}^{-3}$ (for $N = 256$ and $a_0 = 0.323$ nm, $\rho_{\text{vol}} = 1.77 \cdot 10^{21}\,\text{m}^{-3}$), the relative difference is still about 20 %. Since densities $\rho_{\text{vol}} > 10^{21}\,\text{m}^{-3}$ are experimentally observed in various irradiated materials (W [135], Zr [89,136, 137], α-Fe and its alloys [66]), Eq. (1.29) is not a satisfactory approximation to explain those experiments.

In Fig. 5.5, the sink efficiency of the toroidal sink is plotted as a function of the major radius r_L ($N = 64$, $\rho_{\text{vol}} = 1.13 \cdot 10^{23}\,\text{m}^{-3}$ and $r_0 = 1.05\,\text{nm}$). When $r_0 \simeq r_L$ (between 1 and 2 nm), there is a very good agreement between the Wiedersich solution $Z_{\text{vol}}^{\text{W}}$ (see Tabl 1.2) for a sphere of radius $r_s = r_L + r_0$ and the results obtained with the PF model $Z_{\text{vol}}^{\text{PF}}$. This is due to the fact that, for very low r_L, the torus degenerates into a sphere. For any value of r_L the sink efficiency calculated by PF is higher than the Nichols analytical solution. $Z_{\text{vol}}^{\text{PF}}$ is a concave function, while $Z_{\text{vol}}^{\text{Ni}}$ (Eq. (1.29)) is a convex function of r_L.

Finally, Fig. 5.6 shows that the effect of the minor radius r_0 on a sink population of density $\rho_{\text{vol}} = 1.13{\cdot}10^{23}\,\text{m}^{-3}$ with $r_L = 6.46\text{nm}$ is far stronger than expected from the analytical solution. As a consequence, future works should pay a particular attention to the choice of this parameter.

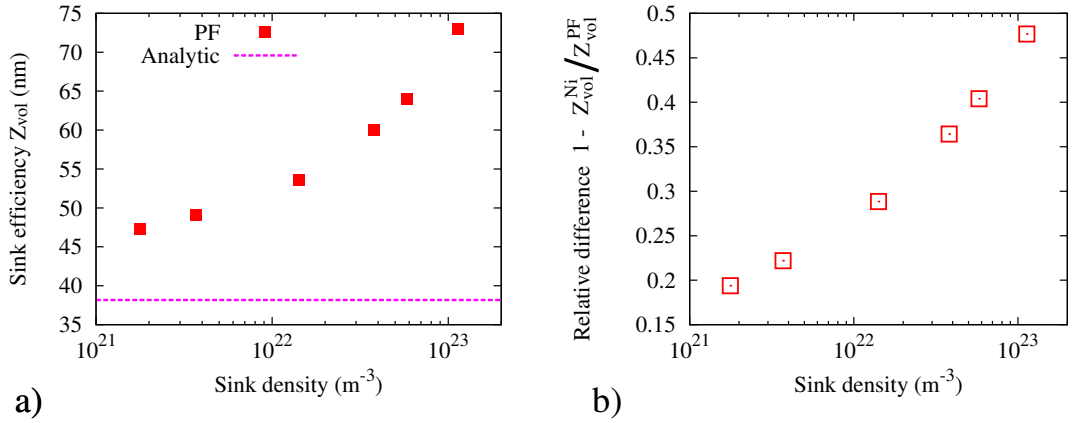

Figure 5.4: a) Sink efficiencies calculated by PF with $64 \leqslant N \leqslant 256$ (filled squares), compared to the analytical solution (1.29) (pink dashed line) as a function of loop density ($r_0 = 1.05\,\text{nm}$ and $r_L = 6.46\,\text{nm}$). b) Relative difference between PF and analytical solution $Z_{\text{vol}}^{\text{Ni}}$ (1.29). The difference remains non negligible, even for low sink volumetric densities.

5.1.3 Summary

The present section has been first focused on 3D simulations without elasticity. The first step was a validation of the PF method described in chapter 2 for the case of the spherical sink, for which analytical solutions are available. This section has shown that a correction (Eq. 5.3) is necessary in the PF method in order to properly model systems in 3D. With this correction on the sphere radius r_0, the agreement between the analytical solution of Wiedersich and the PF results is excellent, whatever the sink density or radius (see Fig. 5.2). The correction on r_0

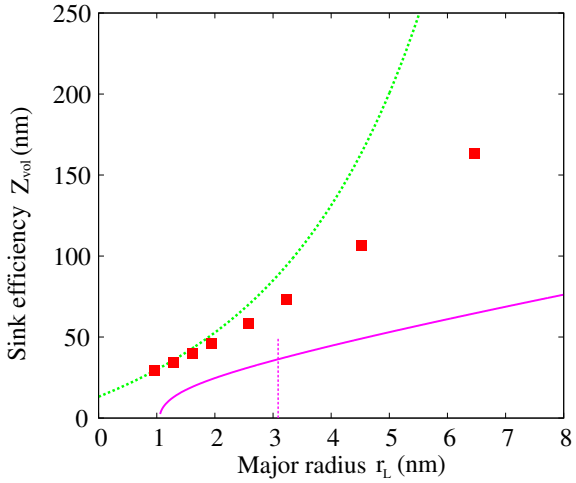

Figure 5.5: Sink efficiency of a toroidal sink, as a function of the torus major radius r_L, with $r_0 = 1.05\,\mathrm{nm}$ and $N = 64$ ($\rho_{\mathrm{vol}} = 1.13 \times 10^{23}\,\mathrm{m}^{-3}$). PF results (squares) are compared to various analytical solutions: toroidal sink (Eq. (1.29)) (pink solid line), spherical sink with radius $r_0 + r_L$ with Wiedersich conditions (see Tab. 1.2) (green dotted line).

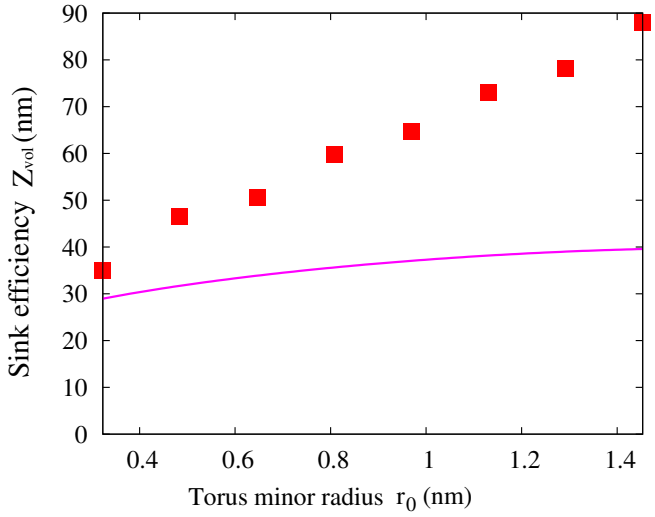

Figure 5.6: Sink efficiency of a toroidal sink, as a function of the torus minor radius r_0, with $r_L = 3.23\,\mathrm{nm}$ and $N = 64$ ($\rho_{\mathrm{vol}} = 1.13 \times 10^{23}\,\mathrm{m}^{-3}$). Squares: PF results, pink solid line: toroidal sink efficiency analytical solution (1.29). The slight oscillations are due to the difficulty to define exactly the minor radius in a cubic mesh.

has been reported on further calculation on the minor radius of the toroidal sinks.

According to the PF results on toroidal sinks, the analytical solution (1.29) is an acceptable approximation for very low sink densities. However, PF method has disagrees with it on the following aspect: the sink efficiency of toroidal sinks is strongly dependent on sink density, in the range of densities studied here. In particular, Eq. (1.29) is not able to model the absorption of defects for sink densities above $\rho_l = 10^{21}\ \mathrm{m}^{-3}$ (see Fig. 5.4).

For low values of the torus major radius $r_L \lesssim r_0$, the torus can be approximated by a spherical sink with radius $r_L + r_0$.

These calculations have been made without taking into account elasticity. The next step will follow the same approach an chapter 3: the stress field generated by the loops will be considered in the framework of isotropic elasticity.

5.2 Sink strength of a dislocation loop (isotropic elasticity)

Few works are dedicated to the sink efficiency calculation of dislocation loops by considering the elastic interactions with the migrating defects. As shown in previous chapters (see chap. 3), PF method is able to simulate the diffusion of PDs in the stress field of any dislocation network, and deduce the dislocation sink efficiency. As we have shown that the PF method is relevant to simulate toroidal sinks, this conclusion will be used to explore the case of dislocation loops.

5.2.1 System description

In this section, $\lambda(\mathbf{r})$ and $X(\mathbf{r})$ are defined in the same way as in section 5.1.2. In order to take into account the elastic interactions between the dislocation loop and PDs, a dislocation order parameter η is introduced (see chap. 2.2). This order parameter is shaped as a platelet, whose border is located along the core of the dislocation line (Fig. 5.7 b)). The stress-free strain properties of the platelet is then defined by Eq. (2.2).

The loop is modelled by means of the order parameter $\eta(\mathbf{r})$ equal to 1 inside the platelet and 0 outside. In the habit plane, η is defined as follows (its value is 0 elsewhere):

$$\eta(\mathbf{r}) = \delta(z - z_c)\frac{1}{2}\left[1 - \tanh\left(\frac{\sqrt{(x-x_c)^2 + (y-y_c)^2} - r_L}{\sqrt{2}\,W}\right)\right], \tag{5.5}$$

with $W = \sqrt{2}$ in our case. According to this definition, the value of η changes sharply from 0 to 1 in the direction normal to the habit plane, while in any direction in the habit plane, η increases smoothly from its minimal to its maximal value. In our case, a disk-shaped platelet with radius r_L is considered, hence, the dislocation is a circular loop (see Fig. 5.7 a)).

Both order parameters η and λ have the same centre c and radius r_L. As a consequence, it is required that the dislocation core (border of the platelet defined

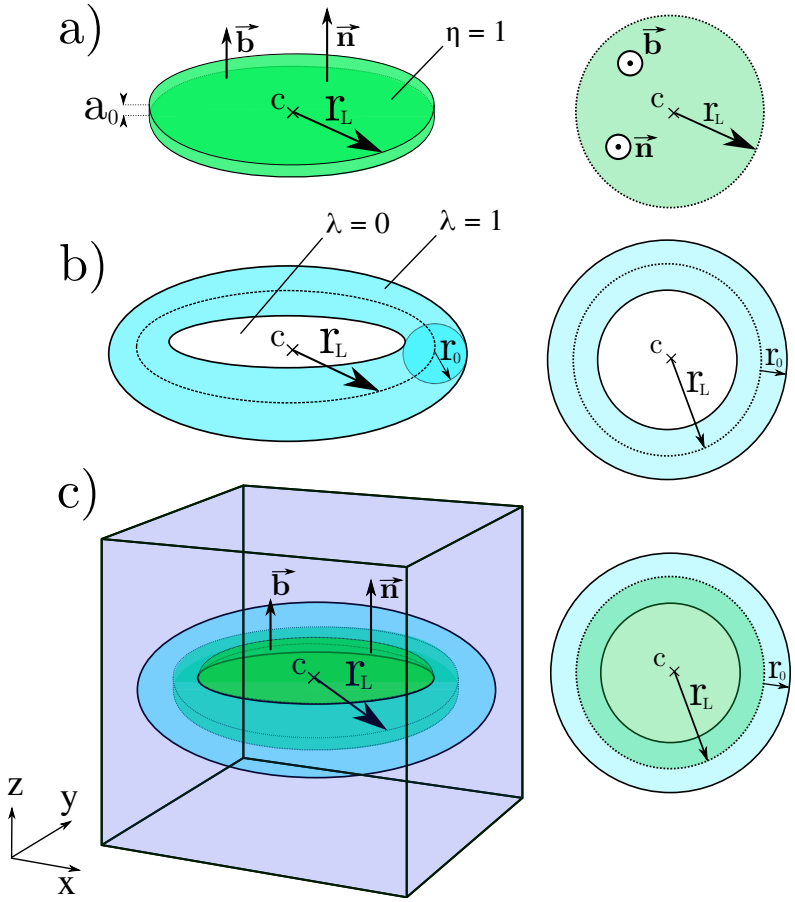

Figure 5.7: a) Definition of the platelet (with the same centre c as the torus) that represents a dislocation loop with thickness a_0 by means of η. b) Definition of the toroidal sink domain centred on c with radius r_L and core radius r_0 by means of λ. c) Coexistence of both order parameters in the simulated system.

by η) is located inside the toroidal region defined by λ: the core region is fully embedded in the sink region. Note that the value of r_0 is given after correction given by Eq. (5.3).

5.2.2 Results

The simulations are performed with the parameters of table 5.2. The dislocation loops are considered to be of interstitial nature, with the Burgers vector $\mathbf{b}$ collinear to the vector $\mathbf{n}$ normal to the habit plane and oriented in the same direction ($\mathbf{b} \cdot \mathbf{n} > 0$) (see Fig. 5.7). The loop density is taken relatively high ($1.13 \cdot 10^{23}\,\mathrm{m}^{-3}$), but is close to bcc Fe irradiated at 0.8 dpa at 340 K, where Zinkle et al. [138] measured loop densities up to $\sim 6.0 \cdot 10^{22}\,\mathrm{m}^{-3}$ with average loop diameter of $4\,\mathrm{nm}$. In addition, it must be noted that the observation techniques (TEM) used to measure defect densities generally ignore defects whose size is less than 1 nm. As a consequence, the real defect densities is higher than the measured ones.

Like in the case of the toroidal sink (see section 5.1.2), the accelerated convergence algorithm has been used in this section. The algorithm will be validated in

section 5.4.2.

Table 5.2: Input data adopted in section 5.2.2 for the dislocation loop sink efficiency calculation (elastic isotropic properties).

Properties	Value
Shear modulus μ, GPa	33
Poisson ratio ν	0.33
Burgers vector norm (nm)	0.323
Temperature (K)	600
Cell size a_0 (nm)	0.323
System size (nm^3)	$20.7 \times 20.7 \times 20.7$
Dislocation loop density (m^{-3})	1.13×10^{23}
Atomic volume V_{at} (m^3)	2.3×10^{-29}
Dislocation core radius r_0 (nm)	1.21
Dislocation loop radii r_L (nm)	$1.62 - 6.46$
SIA relaxation volume Ω_i	$+1.2 \times V_{\text{at}}$
Vacancy relaxation volume Ω_v	$-0.6 \times V_{\text{at}}$

The steady-state maps of PD site fractions obtained by PF are plotted on Fig. 5.8. The effect of the relaxation volume sign is obvious. It can be seen that the compressive region ("inside" the loop) is depleted in SIAs and enriched in vacancies. The opposite is true for the tensile zone.

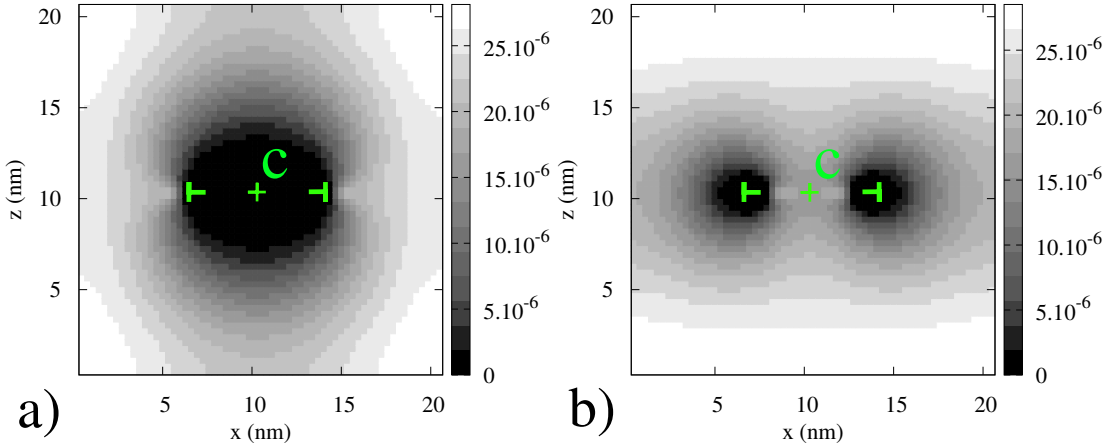

Figure 5.8: PD Site fraction maps for a) SIAs and b) vacancies in the case of an interstitial loop ($r_L = 3.23$ nm). The cut is made parallel to the (xz) plane, and contains the centre c of the loop. The intersections between the loop and the cutting plane are indicated by a green "$\top$". The inside region of the loop is depleted in SIAs, due to the strong compressive stress in this region, and enriched with vacancies. These maps can be compared to Fig. 3.14.

The sink efficiencies obtained by PF are given in Fig. 5.9. As expected, the elastic interaction leads to a sink efficiency increase, this effect being enhanced by for higher absolute values of the relaxation volume. As a consequence, the

dislocation loop has a higher sink efficiency for SIAs than for vacancies. This effect is even stronger at large loop radius (see Fig. 5.10). This difference in sink efficiencies between vacancies and SIAs leads to the bias represented in Fig. 5.11.

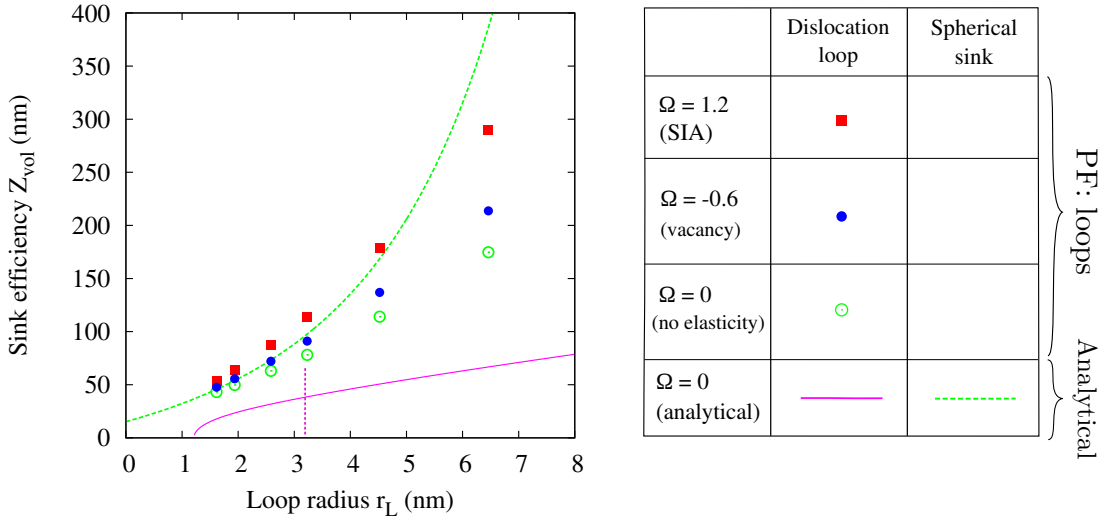

Figure 5.9: Sink efficiencies of a dislocation loop as a function of the loop radius r_L: analytical solution for torus (1.29) (pink solid line), Wiedersich analytical solution for the spherical sink with radius $r_0 + r_L$ (green dotted line), PF results without elasticity (green open circles), PF results for vacancies (blue filled circles) and SIAs (red filled squares). The dashed vertical line indicates the lower validity limit of the analytical solution for the toroidal sink (Eq. (1.29)).

5.2.3 Loop vs straight dislocation

The PF model allows an easy investigation of the influence of the dislocation line configuration, i.e. straight line or circular loop, via the order parameters $\eta(\mathbf{r})$ and $\lambda(\mathbf{r})$: for loops, they are defined in Fig. 5.7 whereas for straight dislocations, they are represented in Fig. 2.3. In this chapter, the sink density has been defined as the number of loops per unit volume, or volumetric loop density. Nevertheless, it is also possible to define the sink density as the dislocation line density ρ_l, i.e. the length of dislocation line per unit volume (see section 2.5 and in particular Eq. 2.36). In this section, we compare the loop sink efficiency to the straight dislocation sink efficiency, as a function of the dislocation line density ρ_l.

To this end, the sink efficiency of dislocation loops Z_{vol} (in units of m) has been converted into the dimensionless dislocation sink efficiency Z using Eq. (2.36). Results obtained with straight dislocations presented in section 4.3.1 (in particular in Fig. 4.16) are plotted together with the results from section 5.3. In the case of straight dislocations, the density depends only on N, i.e. the size of the system, as there are always 2 dislocations per $2N \times N$ cells. On the contrary, the equivalent dislocation density of loops is given by:

$$\rho_l = 2\pi r_L \rho_{\text{vol}} = \frac{2\pi r_L}{(a_0 N)^3} \tag{5.6}$$

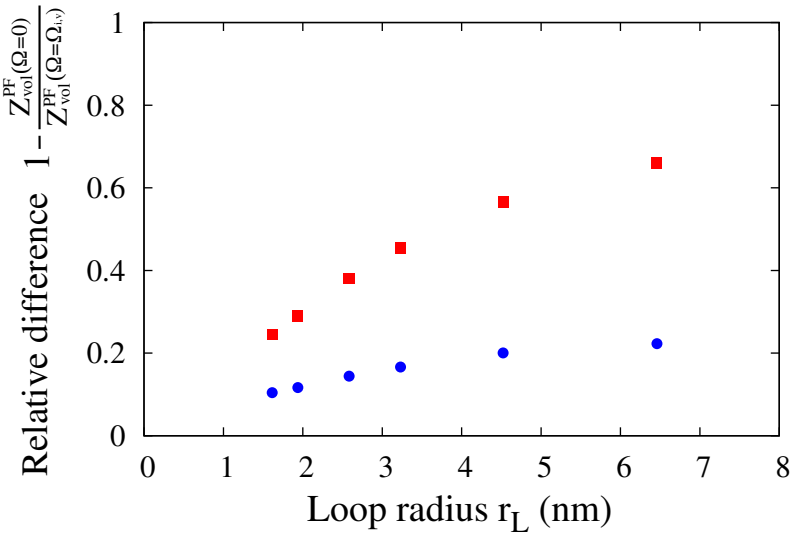

Figure 5.10: Relative difference between sink efficiencies of a dislocation loop for SIAs ($\Omega_i = +1.2 \times V_{\mathrm{at}}$, red squares) and vacancies ($\Omega_v = -0.6 \times V_{\mathrm{at}}$, blue circles) and a toroidal sink computed by PF, as a function of loop radius r_L. The results show that the elastic effect is strongly related to the loop radius.

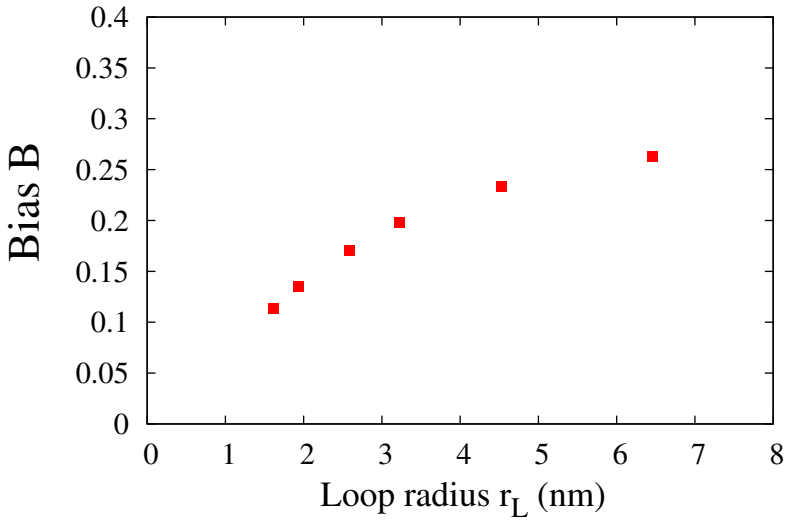

Figure 5.11: Dislocation loop bias B, as a function of the loop radius r_L, obtained with values of Tab. 5.2.

The equivalent dislocation line density of loops depends on loop volumetric density ρ_{vol} and on the loop radius r_L.

For this purpose, the quantity $Z_{\mathrm{vol}}^{\mathrm{PF,dl}}$ for the loops in Fig. 5.9 has been converted into $Z^{\mathrm{PF,dl}}$ in Fig. 5.12. The sink efficiencies $Z^{\mathrm{PF,sd}}$ for straight dislocations (sd) corresponding to the same dislocation line density ρ_l have been reported in the figure.

For loops, the curve $Z^{\mathrm{PF,dl}}(\rho_l)$ without elasticity (toroidal sink) is not monotonous: it decreases for small values of ρ_l, reaches a minimum around $\rho_l = 2 \cdot 10^{15}\,\mathrm{m}^{-2}$ and slightly increases for larger dislocation densities. This behaviour is qualitatively different from the curve $Z^{\mathrm{PF,sd}}(\rho_l)$ for straight dislocations, which continuously increases. This is due to the fact that the dimensionless sink efficiency is equivalent to an efficiency per unit length of dislocation. For small loops, the sink can be approximated by a spherical sink (see section 5.1.2). When the loop radius tends to zero, the sink efficiency tends to a positive finite value equal to the sink efficiency of the spherical sink. As a consequence, the sink efficiency per unit length of dislocation tends to infinity. Both curves intersect at $\rho_l = 1.8 \cdot 10^{15}\,\mathrm{m}^{-2}$. Beyond this point, their behaviour are qualitatively similar. Indeed, in the limiting case of an infinite dislocation loop, each of its segment tends to behave like a straight dislocation (as the curvature radius tends to infinity). However, a larger value of r_L not reached in our simulations would be necessary to have a quantitative agreement between both curves.

The sink efficiency of loops for vacancies $Z_v^{\mathrm{PF,dl}}$ reaches a minimum around $\rho_l = 1.5 \cdot 10^{15}\,\mathrm{m}^{-2}$, while minimum for $Z_i^{\mathrm{PF,dl}}$ is not reached, but would be obtained for $\rho_l < 1.25 \cdot 10^{15}\,\mathrm{m}^{-2}$. At high densities, the loops and the straight dislocations tend to have a qualitatively equivalent behaviour, although the loops have lower sink efficiencies than the straight dislocations. At $\rho_l = 4.6 \cdot 10^{15}\,\mathrm{m}^{-2}$, we have: $Z_i^{\mathrm{PF,dl}} = 7.51$, $Z_v^{\mathrm{PF,dl}} = 5.27$ and $Z^{\mathrm{PF,dl}} = 4.01$. These results shows that the sink efficiency increase with the PD relaxation volume, which is higher in absolute value for the SIA than for the vacancy. These results are consistent with those obtained for straight dislocations.

5.2.4 Influence of the nature of the loop

In comparison with chapter 3, where only straight dislocations where considered, the dislocation loop nature has now to be taken into account. The same system as the one described in section 5.2.1 is considered, with parameters of Tab. 5.3. One difference lies in the fact that $\epsilon_{ij}^{d0,I} = -\epsilon_{ij}^{d0,V}$, where the superscripts I and V stand for parameters of the interstitial and vacancy loop type, respectively.

Biases calculated with PF are plotted in Fig. 5.13. Whatever the type of loop, they are increasing functions of the loop radius. This last result is expected: large loops tend to be equivalent to straight dislocations, for which it is meaningless to define an interstitial or a vacancy nature.

For a given loop radius, the dislocation bias of a vacancy loop is always higher than the one of the interstitial loop. Again, the bias increases with the loop radius, and the difference in bias between the loop natures decreases with r_L. If both types of loops coexist in the same crystal with the same loop radius, vacancy loops receive a net flux of SIAs, while interstitial loops receive a net flux of vacancies.

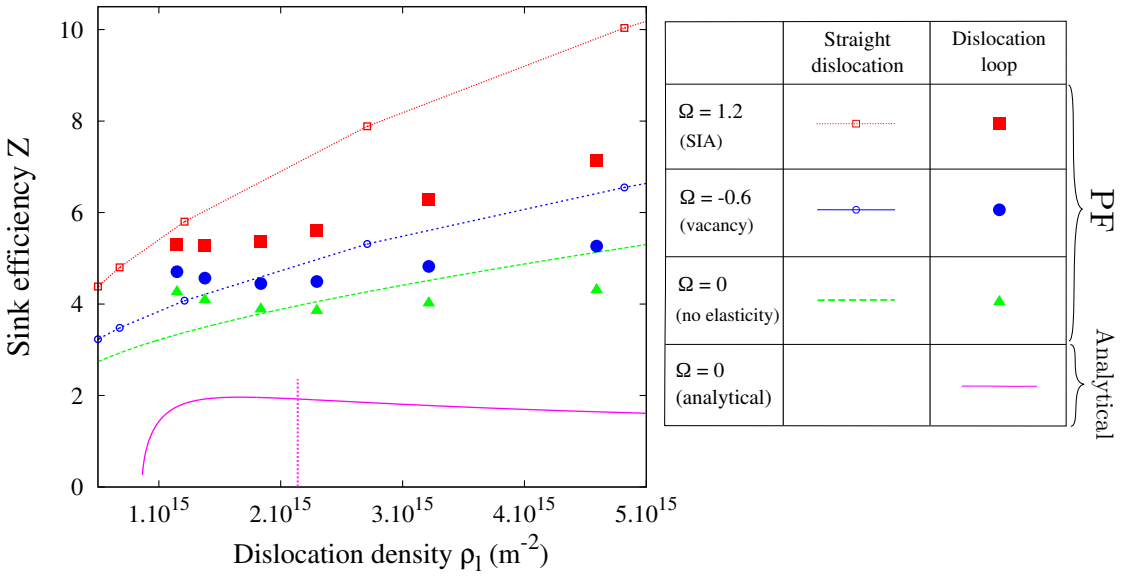

Figure 5.12: Z as a function of the dislocation line density ρ_l. For dislocation loops, the variation of ρ_l is due to the evolution of the loop radius. The analytical solution for the torus (Eq. (1.29)) (solid line) is also plotted. All the cases plotted in this figure are depicted in the table on the right. For example, filled squares correspond to the sink efficiency fo a dislocation loop for SIA obtained by PF.

Table 5.3: Input data adopted in section 5.2.4 for dislocation loop sink efficiency calculation (isotropic elastic properties).

Properties	Value
Shear modulus μ, GPa	44.5
Poisson ratio ν	0.301
Burgers vector norm b (nm)	0.323
Temperature (K)	600
Cell size a_0 (nm)	0.323
System size (nm^3)	$20.7 \times 20.7 \times 20.7$
Dislocation loop density (m^{-3})	1.13×10^{23}
Atomic volume V_{at} (m^3)	2.3×10^{-29}
Dislocation core radius r_0 (nm)	1.05
Dislocation loop radii r_L (nm)	$1.62 - 6.46$
SIA relaxation volume Ω_i	$+1.15 \times V_{\text{at}}$
Vacancy relaxation volume Ω_v	$-0.45 \times V_{\text{at}}$

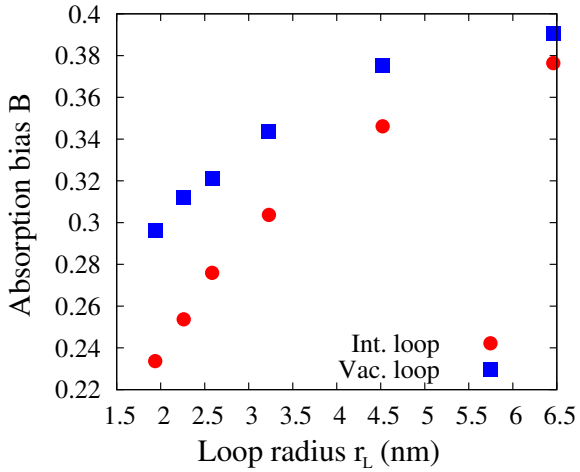

Figure 5.13: Dislocation bias as a function of the loop radius r_L, in the case of interstitial (red circles) and vacancy (blue squares) loops (obtained witht the parameters of Tab. 5.3). For a given loop radius, vacancy loops have a higher bias than interstitial loops. For large radii, the bias becomes independent of the loop nature, as the loop becomes equivalent to straight dislocation lines.

As a consequence, it is impossible for both types of loops to coexist in the same crystal with the same loop radius. This conclusion is opposite to what is observed in irradiated hcp crystals [9,91]. The model of dislocation bias in its present form cannot explain the coexistence of interstitial and vacancy loops with the same Burgers vector. Indeed, chapter 4 shows the essential role of the SAS effect to explain this phenomenon, effect which will be taken into account in section 5.3.

5.2.5 Loop cohabitation effect

According to the results from section 5.2.4 show that the cohabitation of interstitial and vacancy loops with the same Burgers vector and radius is impossible. However, the cohabitation of interstitial and vacancy loops has been observed in hcp crystals (see section 4.1.2). The previous section is not able to describe this phenomenon. All the previous calculations have been performed considering only one sink in the simulation domain. We have seen that the interaction between mirror images of sinks play a major role in the final computed sink efficiency. In hcp crystals, prismatic loops have been observed aligned as rows parallel to the basal plane (see Fig. 4.2). However, one could ask: what is the effect of the cohabitation of several sinks with different properties in the same system?

As a consequence, 3 systems should be compared: (i) sink efficiency calculation of a sink of type 1 in the calculation domain A, (ii) a sink of type 2 in the calculation domain B, and (iii) sinks 1 and 2 in a calculation domain C, equal to A+B. In cases (i) and (ii), the sink is embedded in an infinite lattice of sinks with the same properties as itself. On the opposite, case (iii) is composed of a mixed population of two types of sinks that can induce a behaviour different from the ones observed in (i) and (ii). The PF model presented in chapter 2 can easily handle case (iii). In this part, we consider 2 sinks: an interstitial loop (sink 1) and a

vacancy loop (sink 2). Major radii of loops 1 and 2 are noted $r_{L,1}$ and $r_{L,2}$, respectively, and the core radii are noted $r_{0,1}$ and $r_{0,2}$. Those two loops are centred in c_1 and c_2. The Vegard tensors are noted $\epsilon_{ij}^{d0,1}$ and $\epsilon_{ij}^{d0,2}$ for loop 1 and 2, respectively. It is then necessary to introduce new order parameters:

- the single order parameter η dedicated to the description of the elastic stress field of the dislocation loop will be replaced by η_1 for sink 1 and η_2 for sink 2. Each one of them is a function of space, equal to 1 in the platelet that represents the loop, and 0 outside. The platelet is defined by Eq. (5.5), with the particularity of being centred on c_1 for loop 1 and c_2 for loop 2. The elastic behaviour of each loop is associated with a stress-free strain tensor $\epsilon_{ij}^{d0,1}$ or $\epsilon_{ij}^{d0,2}$, defined by Eq. (2.2).

- The absorption regions are now represented by means of 2 order parameters λ_1 and λ_2. Each of those order parameters are defined as a torus by Eq. (5.4), with centre, major and minor radii imposed for each loop.

Except from these two new order parameters, the model remains the same, especially concerning the order parameter representing PD site fraction two other order parameter X_i and X_v associated with SIAs and vacancies.

However, the sink efficiencies of the cohabitating loops cannot be deduced from Eq. (2.34): this equation determines the sink efficiency of the *whole system*. In other words, this equation does not allow to separate the effect of each individual sink. In order to tackle this problem, another definition of the sink efficiency Z_s of sink s, given by (2.35).

Calculations have been performed with the same isotropic elastic properties as in section 5.2.4 (see Tab. 5.3). Two loops are present in the same calculation domain of size $N \times N \times 2N$: an interstitial loop centred on c_1 of coordinates $x_{c_1} = N/2\,a_0$, $y_{c_1} = N/2\,a_0$ and $z_{c_1} = N/2\,a_0$ and a vacancy loop centred on c_2 of coordinates $x_{c_2} = N/2\,a_0$, $y_{c_2} = N/2\,a_0$ and $z_{c_2} = 3N/2\,a_0$ (see Fig. 5.14). Both loops have opposite Burgers vectors, with equal norm. In this part, $K_0^* = 3.23 \times 10^{-8}$ and $\Delta t^* = 10^{-2}$. Simulations are run until the steady-state is reached, and the sink efficiency Z_{vol} of each loop are deduced from Eq. (2.35). They are plotted in Fig. 5.15 and the corresponding biases in Fig. 5.16, for which $r_{0,1} = r_{0,2} = 3.25\,a_0$ and $1.94\text{ nm} \leqslant r_{L,1} = r_{L,2} \leqslant 6.46\text{ nm}$. The obtained microstructure corresponds to the alignment, parallel to a prismatic direction, of prismatic loops of alternated nature. This kind of alignment has been observed in Zr (see Fig. 4.2) and Ti [57].

At a loop density $\rho_{\text{vol}} = 1.13 \cdot 10^{23}\,\text{m}^{-3}$, the interstitial loop bias goes from 0.25 at $r_L = 1.94\,\text{nm}$ to 0.39 at $r_L = 6.46\,\text{nm}$ while vacancy loop bias goes from 0.26 at $r_L = 1.94\,\text{nm}$ to 0.35 at $r_L = 6.46\,\text{nm}$. This means that the bias of interstitial loop is higher than that of vacancy loop for loop radii larger than $r_L = 2.2\,\text{nm}$. At a loop density $\rho_{\text{vol}} = 3.80 \cdot 10^{22}\,\text{m}^{-3}$, the interstitial loops bias goes from 0.21 at $r_L = 1.94\,\text{nm}$ to 0.35 at $r_L = 6.46\,\text{nm}$ while vacancy loop bias goes from 0.25 at $r_L = 1.94\,\text{nm}$ to 0.30 at $r_L = 6.46\,\text{nm}$. In this case, the intersection between both curves occurs at functions appears at $r_L^c = 3.1\,\text{nm}$ instead of $2.2\,\text{nm}$.

It means that, for $r_L > r_L^c$, the interstitial loops absorb more SIAs than vacancy ones, the opposite being true true for vacancies. This result must be compared to

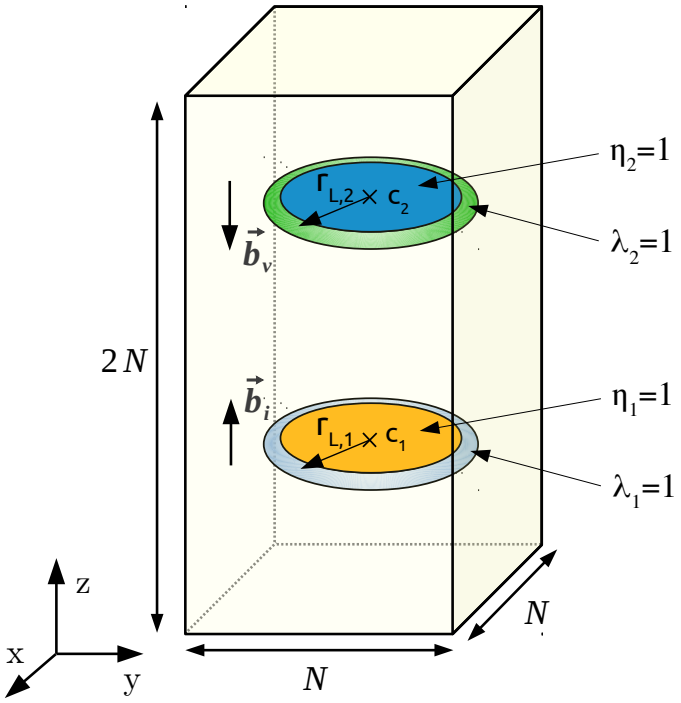

Figure 5.14: Description of the system for the cohabitation effect study.

Fig. 5.13: when the system contains only one type of loop, the vacancy loop has a stronger bias than the interstitial loop. In the case of two population of loops with opposite nature, there can be a wide range of configurations in which the opposite behaviour is obtained.

The effect of loop interaction (that is, the difference in behaviour between cohabiting loops (Fig. 5.16), and calculation with one loop population (Fig. 5.13)) is due to elastic interaction. For $N = 64$, the distance between the loop centres $d_{c_1,c_2}(N = 64)$ is $20.6\,\mathrm{nm}$ while $d_{c_1,c_2}(N = 92) = 29.7\,\mathrm{nm}$. We have seen that the intersection between the biases curves happens $r_L^c(N = 64) = 2.2\,\mathrm{nm}$ and $r_L^c(N = 92) = 3.1\,\mathrm{nm}$. In the limiting case of $d_{c_1,c_2} \to \infty$, the intersection radius r_L^c tends to the infinity. As the stress field of a loop decreases with the distance to this loop, the elastic interaction and the cohabitation effect, decreases with the distance between loops.

5.2.6 Summary

After the PF method has been validated in the case of the toroidal sink, the stress field of dislocation loops is taken into account. By means of the order parameter η provided with the right stress-free strain tensor ϵ_{ij}^{d0}, the stress field of any dislocation loop can be simulated. By adding this order parameter, it is possible to simulate the diffusion of isotropic PDs towards toroidal sinks, and the effect of elasticity on their absorption.

The results show a significant effect of the loop radius r_L on the sink efficiency Z_{vol} and the bias B (see Fig. 5.11). This effect can be considered analogous to

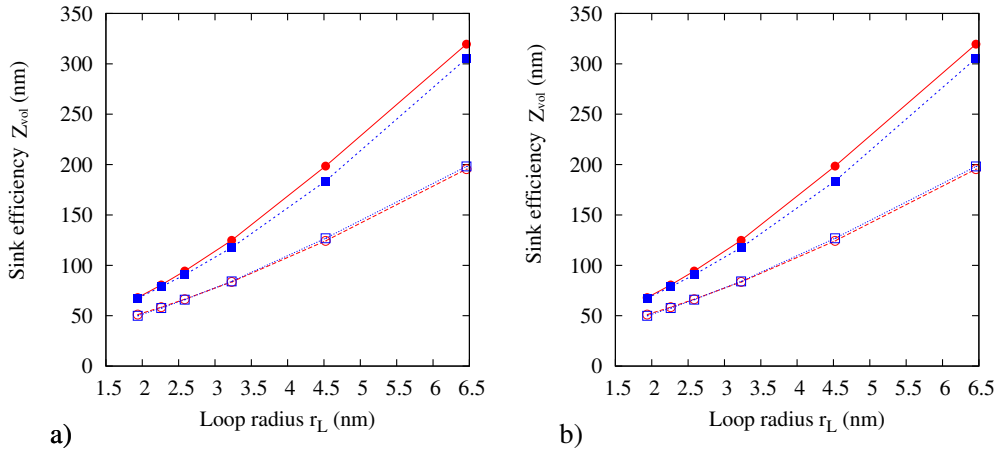

Figure 5.15: Sink efficiency of interstitial (red circles, filled for SIAs, open for vacancies) and vacancy loops (blue squares, filled for SIAs, open for vacancies) with isotropic elastic properties as a function of the loop radii r_L, for a) $N = 64$ ($\rho_{\text{vol}} = 1.13 \times 10^{23}\,\text{m}^{-3}$) and b) $N = 92$ ($\rho_{\text{vol}} = 3.80 \times 10^{22}\,\text{m}^{-3}$). It must be noted that in these calculations, *both loops have the same radius*.

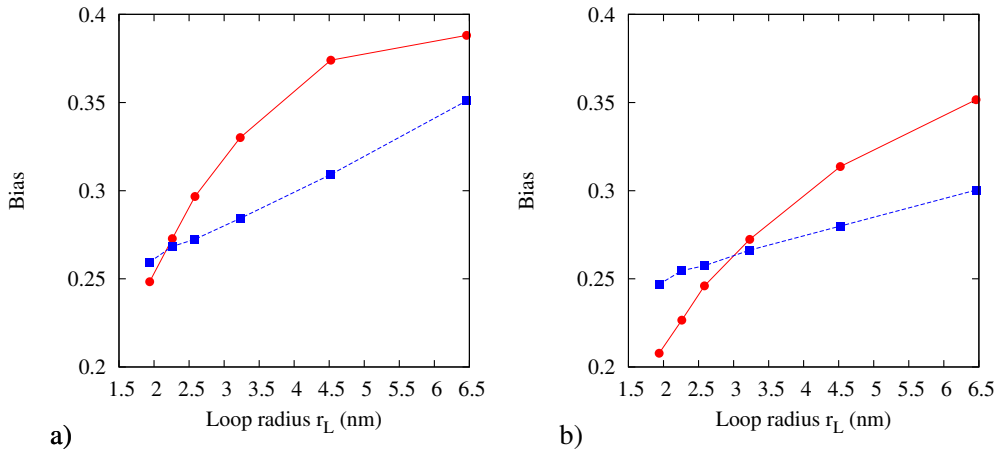

Figure 5.16: Bias of interstitial (red circles) and vacancy loops (blue squares) with isotropic properties as a function of the loop radii r_L, for a) $N = 64$ ($\rho_{\text{vol}} = 1.13 \times 10^{23}\,\text{m}^{-3}$) and b) $N = 92$ ($\rho_{\text{vol}} = 3.80 \times 10^{22}\,\text{m}^{-3}$). It must be noted that in these calculations, *both loops have the same radius*.

the result on dislocation line density presented in chapters 3 (see for example Fig. 3.15) and 4 (see Fig. 4.16).

In order to compare the properties of dislocation loops and straight dislocation, the sink efficiency Z_{vol} (in units of m) has been converted into the dimensionless quantities Z, and the loop volumetric density ρ_{vol} into the dislocation line density ρ_l. This allows us to directly compare the sink efficiency of theses two types of sinks (see Fig. 5.12). It has been shown that the line configuration plays an important role on sink efficiency. Even for the highest loop radii studied in this part ($r_L = 6.49$ nm), the loop still cannot be approximated as a straight line, and the equivalence would be reached for much larger loop radii.

The nature of the dislocation loop plays an important role on its sink efficiency. This effect has been tested, and it has been shown that the vacancy loop has a higher bias than the interstitial loop (see Fig. 5.13). This is opposite to the assumption of Dubinko [37], who considered that the absorption efficiency of a dislocation loop did not depend on the loop nature. As a consequence, the coexistence of both interstitial and vacancy loops would be impossible in the same crystal: the vacancy loops would absorb a net flux of SIAs, while the interstitial loops would absorb a net flux of vacancies, leading to the shrinkage of both types assuming that the radii of both types of loops are equal.

Finally, as the cohabitation of prismatic loops had been assessed by experimental observations, we computed the sink efficiency of dislocation loops with opposite nature in the same calculation domain. The results show that the elastic interaction between loops can counterbalance the phenomenon previously described (see Fig. 5.16). This effect is stronger at high loop densities, i.e. when loops are close to each other. Indeed, the elastic interactions are strongly dependent on the distance between loops.

As in chapter 2, the present section has been limited to the case of isotropic elasticity. The next section is dedicated the case of anisotropic zirconium. It will allow us to check if the results and conclusion established for straight dislocation in chapter 4 are still valid for loops.

5.3 Dislocation loops in zirconium

Sink efficiencies of straight dislocations in zirconium have been calculated with the PF model in chapter 4. This section aims at generalising this study to dislocation loops. The same elastic properties as those adopted in chapter 4 are used (see section 4.2.2.1 and Tab. 4.4). Then, the elastic properties of the crystal as well as the PD Vegard tensors are anisotropic. The dislocation loops modelled in this part are (see Tab. 4.1 for further detailed information):

- Interstitial $1/3\langle 11\bar{2}0\rangle$ prismatic loop;
- Vacancy $1/2[0001]$ basal loop;
- Vacancy $1/6\langle 20\bar{2}3\rangle$ basal loop;
- Vacancy $[0001]$ basal loop.

The sink efficiencies Z_{vol} of each type of dislocation loops are computed with r_L varying between 1.9 and $6.4\,\text{nm}$ with 3 loop densities $\rho_{\text{vol}} = 1.13 \cdot 10^{23}\,\text{m}^{-3}$, $3.80 \cdot 10^{22}\,\text{m}^{-3}$ and $1.41 \cdot 10^{22}\,\text{m}^{-3}$. The results are plotted on Fig. 5.17.

On Fig. 5.17a),c) and e), the sink efficiency for SIAs of $1/3\langle 11\bar{2}0\rangle$ is the highest, followed by $[0001]$, $1/6\langle 20\bar{2}3\rangle$ and $1/2[0001]$ loops, for a given loop radius. On Fig. 5.17b),d) and e), the sink efficiency for vacancies of $[0001]$ is the highest, followed by $1/3\langle 11\bar{2}0\rangle$, $1/6\langle 20\bar{2}3\rangle$ and $1/2[0001]$ loops, for a given loop radius. These conclusions are verified for every value of r_L and ρ_{vol}. The increase of the loop radius r_L or the loop density ρ_{vol} leads to higher sink efficiencies Z_{vol}: for $r_L = 6.5$ nm, the sink efficiency for vacancies of $[0001]$ loops is $Z_{\text{vol}} = 146$ nm at $\rho_{\text{vol}} = 1.41 \times 10^{22}\,\text{m}^{-3}$, $Z_{\text{vol}} = 184$ nm at $\rho_{\text{vol}} = 3.80 \times 10^{22}\,\text{m}^{-3}$ and $Z_{\text{vol}} = 259$ nm at $\rho_{\text{vol}} = 1.13 \times 10^{23}\,\text{m}^{-3}$.

The results are consistent with those obtained in chapter 4 (see in particular Fig. 4.16a) and b)):

- Z_{vol} increases with the dislocation line density (here, the dislocation density increases with the loop radius);
- Z_{vol} for vacancies is higher for larger Burgers vector dislocations,
- Z_{vol} for SIAs does follow a non trivial rule: the highest sink efficiency is obtained for prismatic loops, while the basal loops sink efficiencies are increasing functions of the Burgers vector norm.

In figures 5.18, it can be seen that, whatever the loop density, the bias of the $1/3\langle 11\bar{2}0\rangle$ prismatic loop is always higher than that of the basal loops. This result is also consistent with the results of section 4.3: the SAS effect can lead to a higher bias towards prismatic loops rather than basal ones, despite the larger Burgers vector of the $[0001]$ basal loops. In particular, the difference between the bias of prismatic loops and basal loops is larger than in the case of straight dislocations (see in particular Fig. 4.16c)).

In addition, for the higher density calculations (Fig. 5.18a)), a negative bias is obtained for $[0001]$ basal loop if the radius r_L is higher than 4.5 nm. It should also be noted that for $r_L > 2.5$ nm, the bias of $[0001]$ loops is lower than that of $1/2[0001]$ ones. These phenomena are due to the SAS: while the sink efficiency of $[0001]$ loops for vacancies is significantly larger than $1/2[0001]$ (due to the Burgers vector norm), these two loop types have close sink efficiencies for SIAs, as elasticity plays a minor role in this case. As a consequence, the behaviour of these dislocation loops is opposed to the classical assumption that the higher the Burgers vector norm, the higher the bias. It must be noted that in this case, the loop diameter is about 10 nm, while the cubic box side is 20.3 nm. Nevertheless, unlike the case of straight dislocations, the bias of basal loops is a non monotonous function of the radius: they all display a maximum, around 2.5 nm for $1/2[0001]$ loop, around 4 nm for $1/6\langle 20\bar{2}3\rangle$ loop and $[0001]$ loop bias is always decreasing. For lower loop densities, this effect is less intense: except from the case of $[0001]$ basal loop at $3.80 \times 10^{22}\,\text{m}^{-3}$ (Fig. 5.18b)), the bias of basal loops is an increasing function of the loop radius.

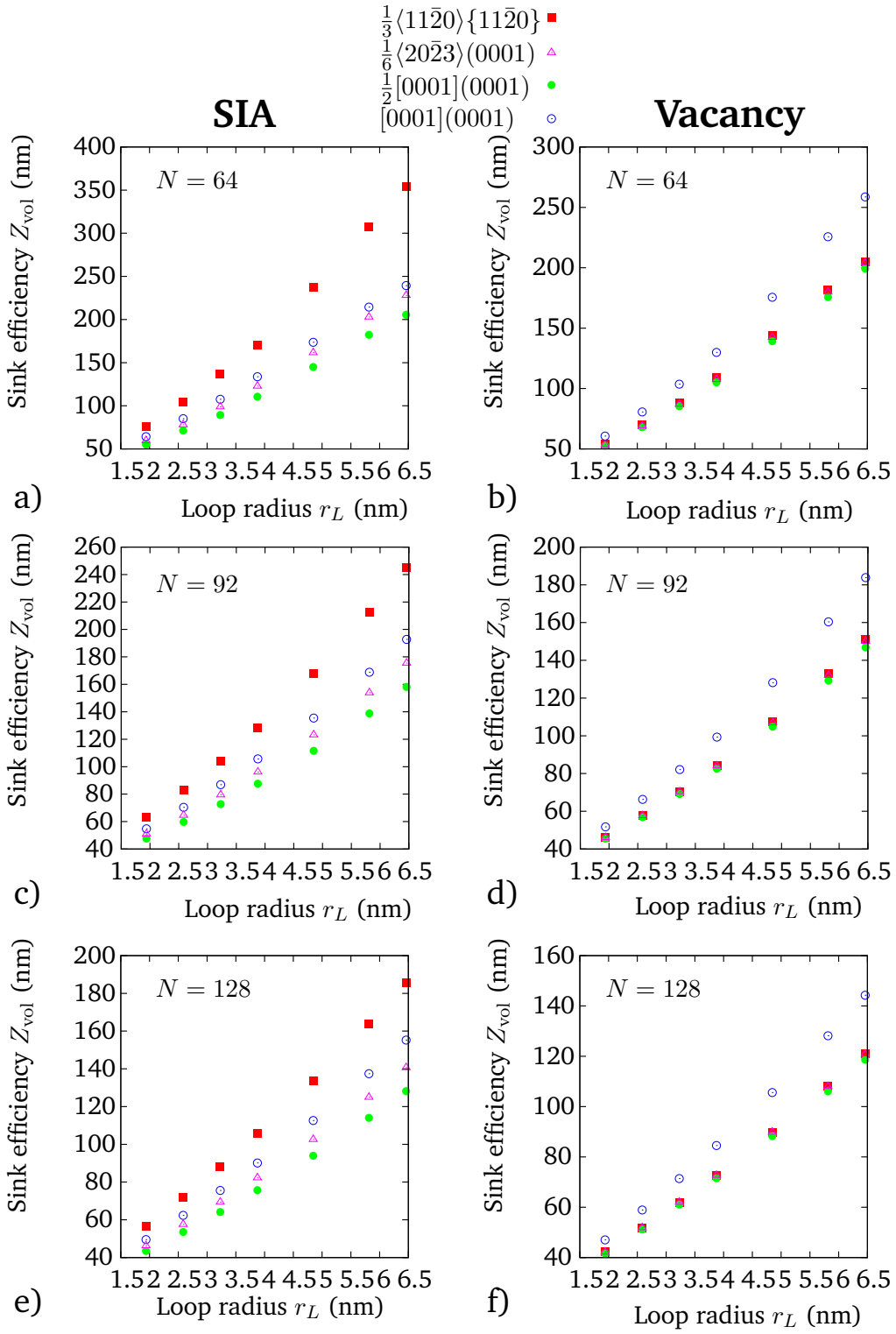

Figure 5.17: Sink efficiency of different dislocation loops for a), b) $\rho_{\mathrm{vol}} = 1.13 \times 10^{23}\,\mathrm{m}^{-3}$, c), d) $3.80 \times 10^{22}\,\mathrm{m}^{-3}$ and e), f) $1.41 \times 10^{22}\,\mathrm{m}^{-3}$, as a function of the loop radius r_L. Interstitial $1/3\langle 11\bar{2}0\rangle$ prismatic loop (filled squares), vacancy $1/2[0001]$ basal loop (filled circles), vacancy $1/6\langle 20\bar{2}3\rangle$ basal loop (open triangles) and vacancy $[0001]$ basal loop (open circles) are investigated.

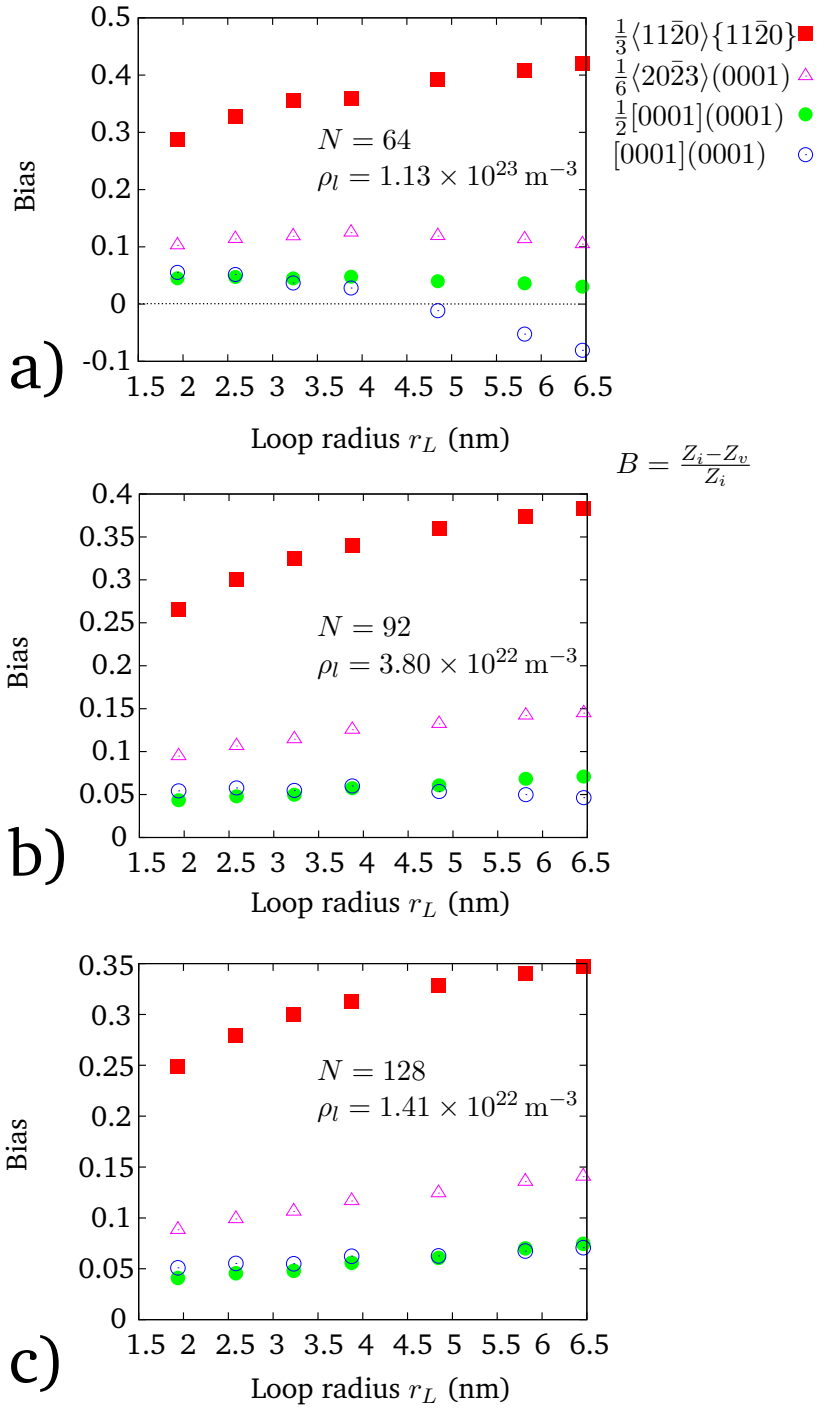

Figure 5.18: Bias of different dislocation loops for a) $\rho_{\mathrm{vol}} = 1.13 \times 10^{23}\,\mathrm{m}^{-3}$, b) $3.80 \times 10^{22}\,\mathrm{m}^{-3}$ and c) $1.41 \times 10^{22}\,\mathrm{m}^{-3}$, as a function of the loop radius r_L. Interstitial $1/3\langle 11\bar{2}0\rangle$ prismatic loop (filled squares), vacancy $1/2[0001]$ basal loop (filled circles), vacancy $1/6\langle 20\bar{2}3\rangle$ basal loop (open triangles) and vacancy $[0001]$ basal loop (open circles).

5.3.1 Comparison with straight dislocations

In section 5.2.3, a comparison has been made between the straight dislocation and the dislocation loop sink efficiencies. A similar investigation is proposed in this part for Zr in order to study the effect of the system size, we plot the sink efficiency of dislocation loops as a function of ρ_l for $N = 64$, $N = 92$ and $N = 128$ in Fig. 5.19. In fact, Z does not only depend on the dislocation line density ρ_l, but is a complex function of N and r_L.

Some conclusions are similar to those of section 5.2.3:

- at low loop radius (i.e. low dislocation density), sink efficiency of loops is higher than that of straight dislocations (this phenomenon is explained in section 5.2.3).
- Sink efficiency of loops is not a monotonous function of dislocation line density: it exists a minimum that depends on N: around $\rho_l = 2 \cdot 10^{15}$ m^{-2} for $N = 64$, around $\rho_l = 7 \cdot 10^{14}$ m^{-2} for $N = 92$ and around $\rho_l = 4 \cdot 10^{14}$ m^{-2} for $N = 128$.
- After the minimum, the loop sink efficiency generally tends to follow the same trend as the sink efficiency of straight dislocation.
- We can wonder what is the value of r_L^∞ from which the loop behaves like straight dislocations. 7 nm is clearly below this value.
- Basal loops have a lower bias than prismatic ones, due to the SAS effect (see section 4.3.3).

On the contrary, there are several specific features relative to loops in zirconium:

- At high basal loop densities (Fig. 5.19a)), $Z(\rho_{\text{vol}})$ for SIAs reaches a plateau. This effect does not occur in the case of vacancies. This leads to a negative bias for $[0001]$ loops (see Fig. 5.20).
- For a given dislocation density, the sink efficiency of dislocation loops and straight dislocations for vacancy has the following feature in common: $[0001]$ has a higher sink efficiency, while the other dislocation types have lower sink efficiencies very close to each other. This is different for the SIAs: $\frac{1}{3}\langle 11\bar{2}0\rangle$, $[0001]$ and $\frac{1}{6}\langle 20\bar{2}3\rangle$ straight dislocation sink efficiencies have close values, while $\frac{1}{2}[0001]$ have much lower values. In comparison, sink efficiency of $\frac{1}{3}\langle 11\bar{2}0\rangle$ loops is significantly higher than that of $[0001]$, $\frac{1}{6}\langle 20\bar{2}3\rangle$ and $\frac{1}{2}[0001]$ loops.
- The difference in biases between prismatic and basal dislocation loops is large in comparison with straight dislocations. Prismatic loops are here considered as interstitial, while basal loops are of vacancy nature. It has been shown that, in the case of isotropic elasticity, vacancy loops have a tendency to have a higher bias than interstitial ones, for a given loop radius r_L (see Fig. 5.13). As a consequence, it was expected to obtain a lower difference

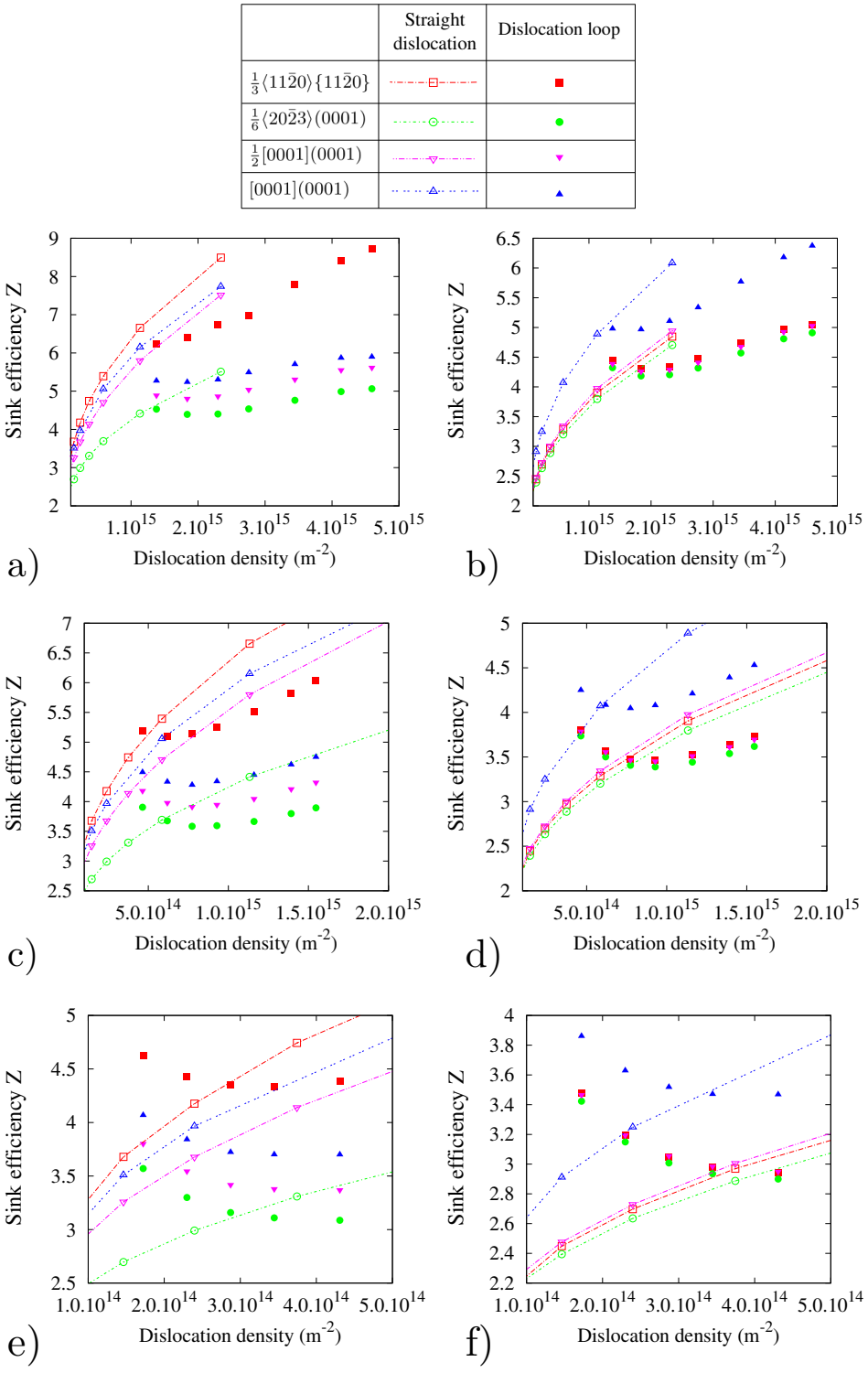

Figure 5.19: Sink efficiency of straight dislocations (open points with lines) and dislocation loops (filled points) for a), b) $\rho_{\text{vol}} = 1.13 \times 10^{23}\,\text{m}^{-3}$, c), d) $\rho_{\text{vol}} = 3.80 \times 10^{22}\,\text{m}^{-3}$ and e), f) $\rho_{\text{vol}} = 1.41 \times 10^{22}\,\text{m}^{-3}$ as a function of the linear dislocation density. Interstitial $^1/_3\langle 11\bar{2}0\rangle$ prismatic loop (squares), vacancy $^1/_2[0001]$ basal loop (circles), vacancy $^1/_6\langle 20\bar{2}3\rangle$ basal loop (turned down triangles) and vacancy $[0001]$ basal loop (turned down triangles).

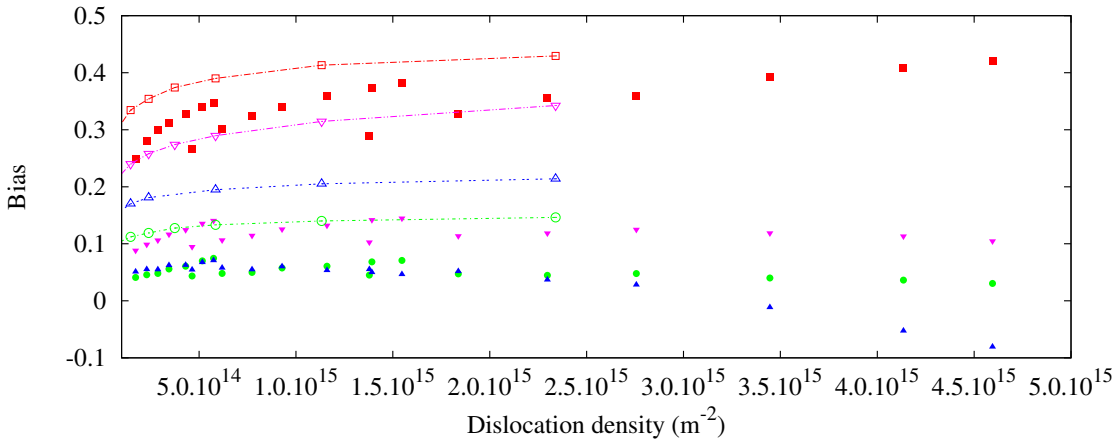

Figure 5.20: Bias of straight dislocations (open points with lines) and dislocation loops with varying radii and loop number density (filled points) as a function of the dislocation line density. Interstitial $1/3\langle 11\bar{2}0\rangle$ prismatic loop (squares), vacancy $1/2[0001]$ basal loop (circles), vacancy $1/6\langle 20\bar{2}3\rangle$ basal loop (turned down triangles) and vacancy $[0001]$ basal loop (turned down triangles).

in bias between interstitial and vacancy loops. It turns out that these arguments do not hold when the SAS is taken into account.

The main conclusions of this section is that the results are consistent with those of chapter 4: the SAS effect explains the higher bias of prismatic loops than basal vacancy loops. In addition, the SAS effect is stronger for loops than for straight dislocations: the difference in biases between prismatic and basal dislocations is larger for loops (see in particular Fig. 5.20). These results also show that the dislocation loops cannot be approximated by straight dislocations in Zr.

5.3.2 Influence of the nature of the loop

Both vacancy and interstitial prismatic loops ($\mathbf{b} = 1/3\langle 11\bar{2}0\rangle$, $\mathbf{n} = 1/3\langle 11\bar{2}0\rangle/\|\mathbf{n}\|$) have been observed in irradiated zirconium (see section 4.1.2.1). As a consequence, the effect of the nature of the loop must be studied.

We applied the same methodology as in section 5.2.4 to the case of prismatic loops in zirconium. The $(\mathbf{a_1}, \mathbf{a_2}, \mathbf{c})$ basis is used, with $\mathbf{a_1} = 1/3[\bar{1}2\bar{1}0]/a$, $\mathbf{a_2} = 1/\sqrt{3}[\bar{1}0\bar{1}0]/a$ and $\mathbf{c} = [0001]/c$. The coordinates of the Burgers vector are $[0\ 0\ b]$ with $b = 0.323$ nm and habit plane normal is $[0\ 0\ 1]$. Calculations of the sink efficiency of prismatic loops are made for $N = 64$ ($\rho_{\text{vol}} = 1.13 \times 10^{23}$ m^{-3}) and $N = 92$ ($\rho_{\text{vol}} = 3.80 \times 10^{22}$ m^{-3}). We have $1.94 \leqslant r_L \leqslant 6.46$ nm and $r_0 = 1.05$ nm.

Calculated biases for both types of loop are given in Fig. 5.21. For $N = 64$, the bias of prismatic loops goes from 0.23 for $r_L = 1.94$ nm to 0.37 for $r_L = 6.46$ nm. At the same loop density, the bias of vacancy loops goes from 0.208 for $r_L = 1.94$ nm to 0.39 for $r_L = 6.46$ nm. For $N = 92$, the bias of prismatic loops goes from 0.208 for $r_L = 1.94$ nm to 0.33 for $r_L = 6.46$ nm. At the same loop density, the bias of vacancy loops goes from from 0.264 for $r_L = 1.94$ nm to 0.39 for $r_L = 6.46$ nm.

For high loop radii, the difference between biases decreases. In any case, for a given value of r_L the bias of vacancy loops is always higher than that of prismatic loops. The effect of the loop density is consistent with the previous results: lower loop densities mean lower biases. As a consequence, the conclusions of section 5.2.4 remain true: according to those calculations, vacancy and interstitial loops with similar radii could not cohabit.

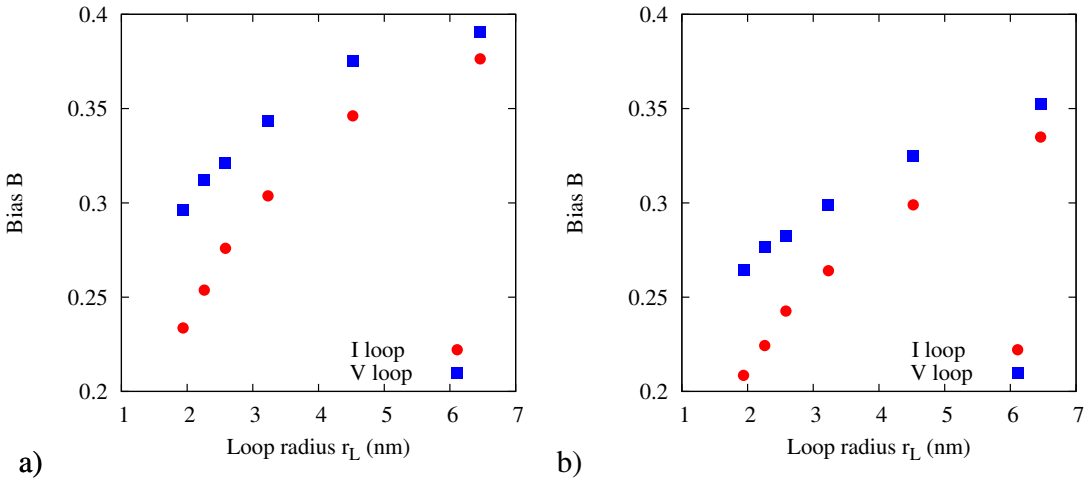

Figure 5.21: Dislocation bias of prismatic dislocation loops at density a) $\rho_{\text{vol}} = 1.13 \times 10^{23}\ \text{m}^{-3}$ ($N = 64$) and b) $\rho_{\text{vol}} = 3.80 \times 10^{22}\ \text{m}^{-3}$ ($N = 92$), as a function of the loop radius r_L, in the case of loops of interstitial (blue squares) and vacancy (red circles) nature (parameters given in text).

5.3.3 Loop cohabitation effect

The methodology presented in section 5.2.5 is considered in this part. Two prismatic loops ($\mathbf{b} = 1/3\langle 11\bar{2}0\rangle$, $\mathbf{n} = 1/3\langle 11\bar{2}0\rangle/\|\mathbf{n}\|$) with opposite nature (one of vacancy type, the other of interstitial type) are simulated in the same domain (see Fig. 5.14). The properties are those of the chapter 4: $\mathbf{x} \parallel \langle 11\bar{2}0\rangle$, $\mathbf{y} \parallel \langle 10\bar{1}0\rangle$ and $\mathbf{z} \parallel [0001]$ in Fig. 5.14. In this part, $K_0^* = 3.23 \times 10^{-8}$ and $\Delta t^* = 10^{-2}$. Sink efficiencies are deduced from Eq. (2.35) and plotted on Fig. 5.22 while the biases are plotted on Fig. 5.23. Sink efficiency values display the same behaviour as in Fig. 5.15, however, the sink efficiency values are slightly higher. On Fig. 5.23, there is an intersection between the biases of interstitial and vacancy loops. The biases are higher than the ones obtained with isotropic elasticity B_{iso} ($0.35 < B < 0.5$ whereas $0.25 < B_{\text{iso}} < 0.4$), but they cross each other for the same values of r_L: for $N = 64$, $r_L > 2.2\,\text{nm} \Rightarrow B_I > B_V$ and for $N = 92$, $r_L > 3.15\,\text{nm} \Rightarrow B_I > B_V$. It is surprising that the loop cohabitation effect is weakly dependent on the system properties.

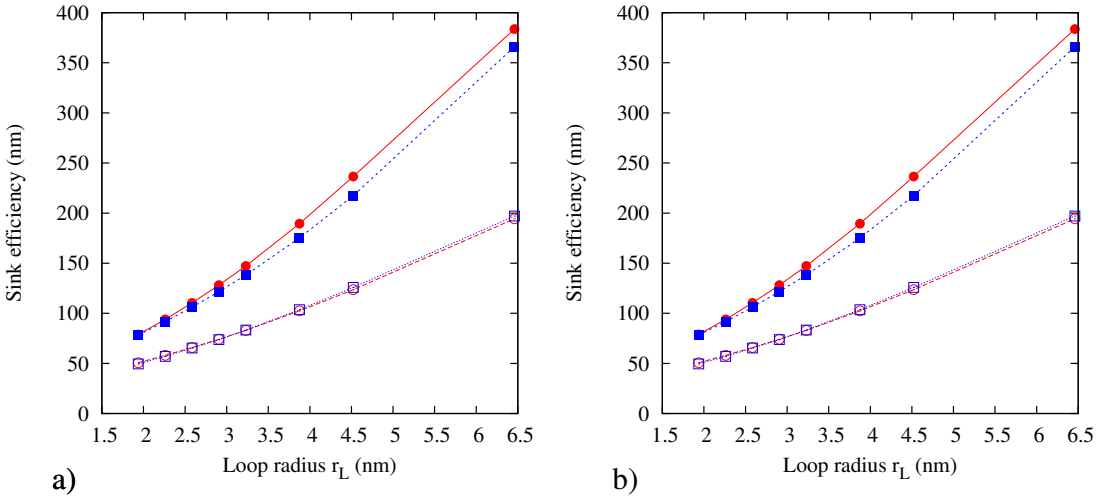

Figure 5.22: Sink efficiency of interstitial (red circles, filled for SIAs, open for vacancies) and vacancy loops (blue squares, filled for SIAs, open for vacancies) in zirconium as a function of the loop radii r_L, for a) $N = 64$ ($\rho_{\text{vol}} = 1.13 \times 10^{23}\,\text{m}^{-3}$) and b) $N = 92$ ($\rho_{\text{vol}} = 3.80 \times 10^{22}\,\text{m}^{-3}$). It must be noted that in these calculations, *both loops have the same radius*.

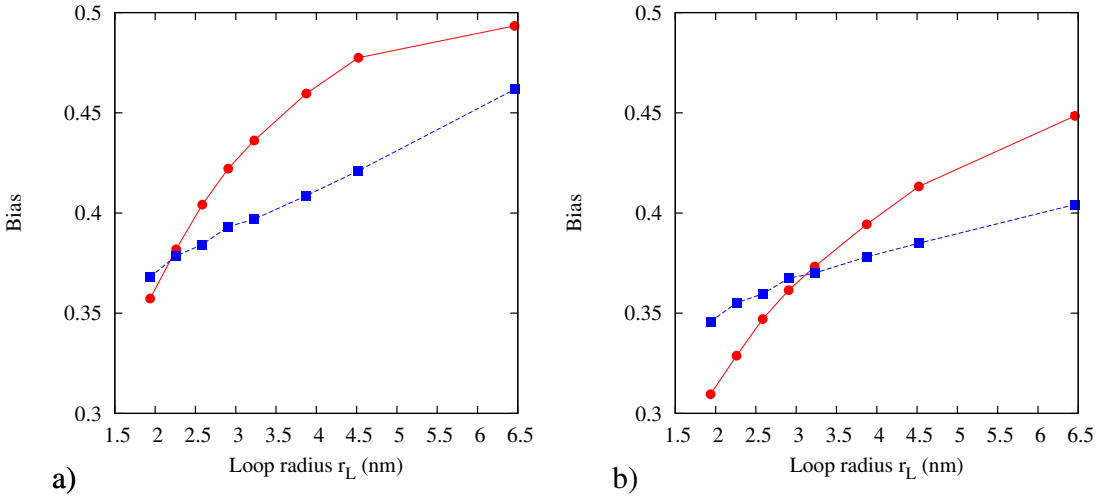

Figure 5.23: Bias of interstitial (red circles) and vacancy loops (blue squares) in zirconium as a function of the loop radii r_L, for a) $N = 64$ ($\rho_{\text{vol}} = 1.13 \times 10^{23}\,\text{m}^{-3}$) and b) $N = 92$ ($\rho_{\text{vol}} = 3.80 \times 10^{22}\,\text{m}^{-3}$). It must be noted that in these calculations, *both loops have the same radius*.

5.3.4 Summary

The methodology described in section 5.2 for dislocation loops with isotropic elasticity is applied to the case of anisotropic zirconium already studied in chapter 4. Hence, the absorption of anisotropic PDs by 4 types of dislocation loops is simulated. At a first glance, results show that previous conclusions of chapter 4 are quantitatively unchanged for dislocation loops:

- Prism-plane $1/3\langle 11\bar{2}0\rangle$ loops have a higher bias than basal ones.
- This effect is due to the SAS (see section 4.3.3).

However, supplemental remark have been raised:

- The effect of SAS on the bias difference between prismatic and basal dislocations is stronger in the loop configuration than in the straight line configuration.
- At high loop densities, a negative bias can be obtained for $[0001](0001)$ vacancy loops.
- The bias of $[0001](0001)$ loop has proven to be lower than $1/2[0001](0001)$ loops at high loop densities. This is surprising since it disagrees with the general assumption that the larger the Burgers vector norm, the higher the bias. Due to the SAS, this assessment is not valid.
- A loop with a radius $r_L \leqslant 6.5\ \mathrm{nm}$ is too small to be approximated by straight dislocation lines, whatever the loop type.

As the coexistence of prismatic interstitial and vacancy loops have been experimentally observed in irradiated zirconium, we have investigated the effect of their cohabitation by PF. Results show a very similar behaviour to the one obtained in isotropic elasticity (see section 5.2.5). The intersection between bias curves occur for the same loop radii, and there is a lower cohabitation tendency for lower loop densities, as expected.

5.4 Validation of the accelerated convergence algorithm

5.4.1 No elasticity

Like in section 3.2.1, the accelerated convergence algorithm (see section 2.6) should be validated for toroidal sinks. An analogous system to the one of section 5.1.2 is used, with a size $64 \times 64 \times 64$ with a centred toroidal sink with $r_0 = 3.75\, a_0$ and $r_L = 10\, a_0$. Results obtained by PF calculations are compared to the function $\bar{X}(t)$ without using the accelerated method ($\theta \to \infty$) on Fig. 5.24. For every simulations, $K_0^* = 3.23 \cdot 10^{-8}$ and $\Delta t^* = 10^{-2}$, $r_L = 10\, a_0$ and $r_0 = 3.75\, a_0$. Unlike the case of straight dislocations with elasticity (see section 3.2.4), it can be seen that no local overestimation of the steady state composition occurs in Fig. 5.24. This

means that the acceleration method is effective, whatever the value of θ for the case of toroidal sinks.

Again, it can be seen that the steady-state composition is independent of the value of θ (as long as no instability occurs).

The computation time is estimated for a 3 % accuracy with the steady-state composition. The number of time steps needed to reach this accuracy are compiled in table 5.4. Calculation with $\theta = 5$ reach the 3 % accuracy more than 23 times faster than the calculation run in the limiting case of $\theta \to \infty$.

Table 5.4: Number of time steps needed to reach a 3 % accuracy as a function of θ for a toroidal sink.

θ (time steps)	Number of time steps
∞	$>$ 400000
50000	123000
5000	30000
1000	17000
100	14000
5	14000

5.4.2 With isotropic elasticity

As in section 5.4.1, the accelerated convergence algorithm (see section 2.6) should be validated again, taking into account the stress field of the dislocations. An analogous system to the one of the previous sections is used, with a size $64 \times 64 \times 64$ with a centred toroidal sink with $r_0 = 3.75\, a_0$ and $r_L = 10\, a_0$. $b = a_0 = 0.323$ nm, $V_{\mathrm{at}} = 2.3 \times 10^{-29}$ m^{-3} and $\Omega_{\mathrm{PD}} = +0.6$, $T = 600$ K, $\mu = 33$ GPa and $\nu = 0.33$. These results are compared to the function $\bar{X}(t)$ that is obtained without using the accelerated method ($\theta \to \infty$). Again, it can be seen that the steady-state composition is independent of the value of θ (as long as no instabilities are experienced). In addition, there are no "bump" as observed for the case of the straight dislocations with elasticity (see section 3.2.4 and Fig. 3.18b)). As a consequence, there will be no need to take care of the "bump", as the increase of $\bar{X}$ is monotonous in the case of dislocation loops or toroidal sinks (see also section 5.4.1, Fig. 5.24).

In order to better estimate the effectiveness of the method, we compare the number of calculation steps needed for a 3 % accuracy in comparison with the steady-state, as a function of θ. The number of time steps needed to reach this accuracy are compiled in table 5.5. The calculation with $\theta = 5$ reaches a 3 % accuracy 27 times faster than with $\theta \to \infty$.

5.5 Conclusions

The PF method presented in chapter 2 is applied to 3D simulations. While most works on sink efficiency are limited to 2D systems, or neglect elastic interaction

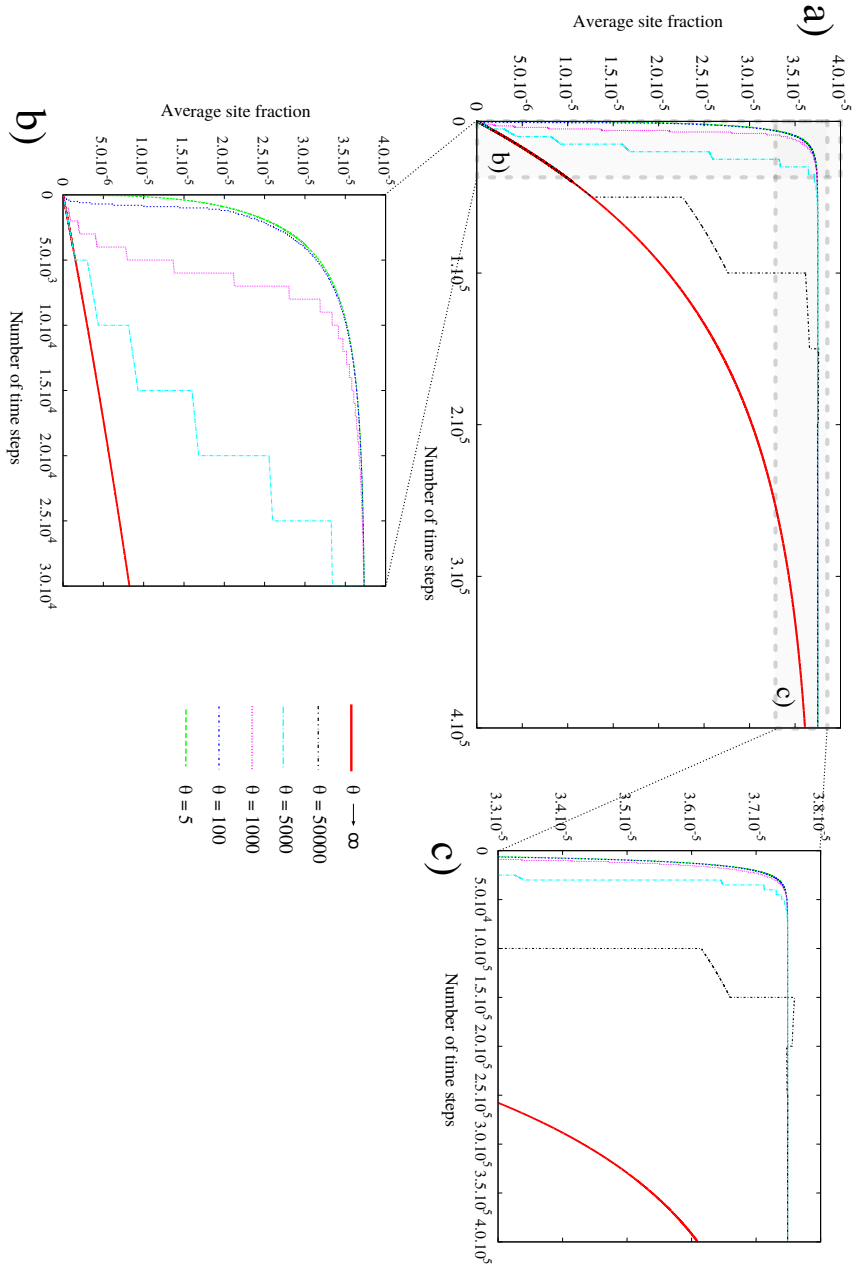

Figure 5.24: Average site fraction of PDs in a $64 \times 64 \times 64$ system with various values of $\theta \in \{5, 100, 1000, 5000, 50000\}$. a) Evolution during the full simulation, b) zoom on the first time steps, where the quick growth of the low θ simulations can be seen and c) zoom around the steady-state site fraction. The thicker line corresponds to the calculation without the accelerated technique ($\theta \to \infty$). It can be seen on a) that there is no "bump" (the slight overestimation for $\theta = 50000$ is due to an instability of the method, which occurs for high values of θ).

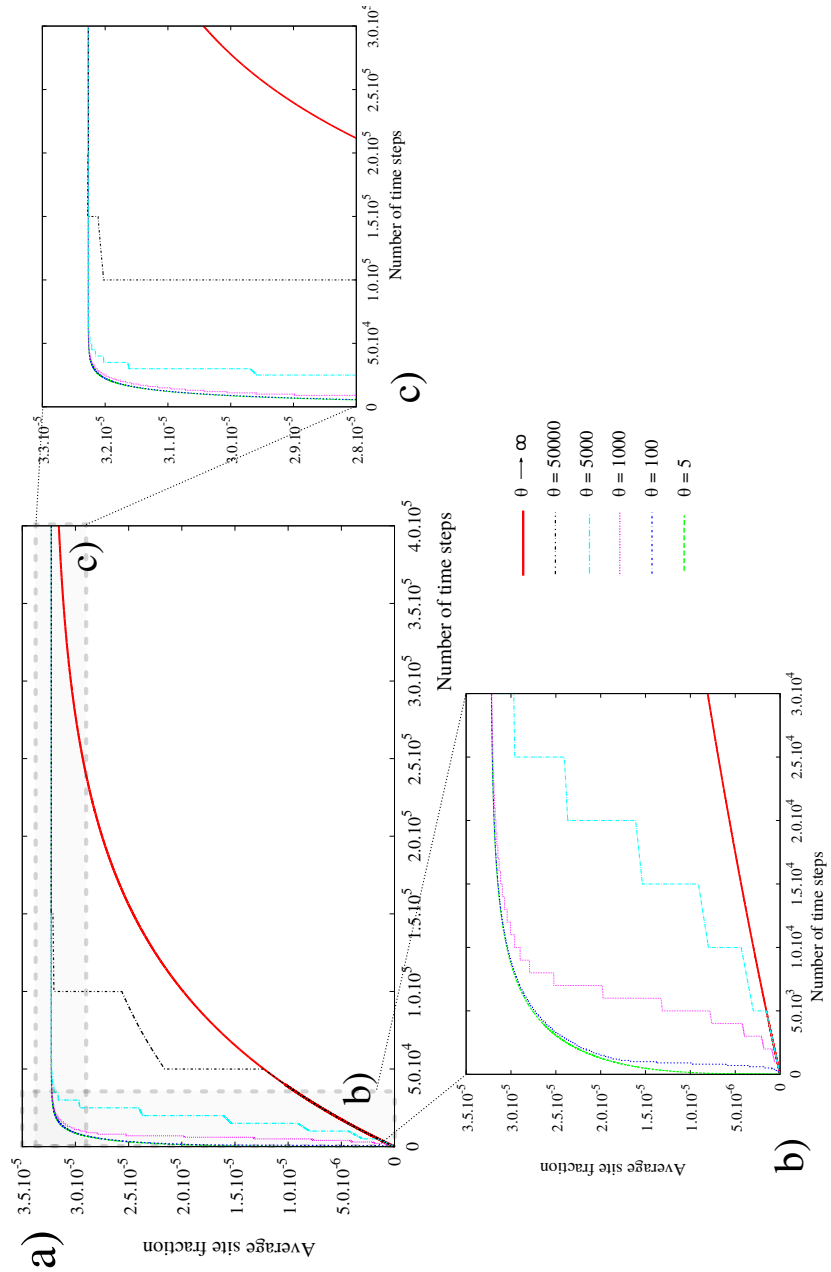

Figure 5.25: Average site fraction of PDs in a $64 \times 64 \times 64$ system with various values of $\theta \in \{5, 100, 1000, 5000, 50000\}$. a) the evolution during the full simulation, b) a zoom on the first time steps, in order to see the quick growth of the low θ simulations and c) a zoom around the steady-state site fraction. The thicker line corresponds to the calculation without the accelerated technique ($\theta \to \infty$). It is obvious that the steady-state is obtained faster for low values of θ, in particular on a). It can be seen on a) that there is no "bump". Again, the acceleration algorithm can be considered effective for the case of dislocation loops.

Table 5.5: Time steps needed to reach a 3 % accuracy as a function of θ for a dislocation loop.

θ (time steps)	Time steps for 3 % accuracy
∞	356000
50000	100000
5000	30000
1000	16000
100	13000
5	13000

between dislocations and PDs, the PF model has proven its effectiveness in the field of dislocation loop sink efficiency calculation.

The methodology has been organised in 3 main parts:

- calculations without elasticity for comparison with the analytical solutions and validation;
- calculations with isotropic elasticity;
- application to the practical case of zirconium, i.e. with anisotropic elastic constants and anisotropic PD shape and realistic dislocation properties.

From a computer science point of view, the reliability of the results are assessed in section 5.4.

The first step (see section 5.1) has been focused on the case of spherical sink, for which analytical solutions are available. We showed that, due to the limits of the cubic mesh, a correction term on r_0 should be considered for a better accuracy. The correction on r_0 has also been reported in the following calculations on the minor radius of the toroidal sinks and the dislocation loops. Then, the PF results for toroidal sinks have shown that the analytical solutions available in the literature are only valid for very low loop densities. In general, the Wiedersich boundary conditions should be used for toroidal sinks and loops.

The second stage of the study has been focused on the effect of elasticity on the sink efficiency of dislocation loops of both interstitial and vacancy nature, either with only one type of loops in the domain, or both types coexisting in the same domain. It can be concluded that:

- the sink efficiency is dependent on loop radius and loop density;
- the sink efficiency is dependent on the dislocation loop nature, in particular, vacancy type loops have a higher bias than interstitial ones;
- when interstitial and vacancy loops present in the same domain, the elastic interactions make it possible for interstitial loops to have a higher bias than vacancy ones;
- the loop should have a radius larger than 7 nm to be approximated by straight dislocations.

Third, the method has been applied to the particular case of hcp zirconium. The properties of zirconium, PDs and dislocations considered are the same as in chapter 4. Results show the remarkable conclusions of chapter 4 established for straight dislocations remain relevant for loops. In addition, the SAS effect is stronger for loops than for straight dislocations (see Fig. 5.20). As both interstitial and vacancy prismatic loops have been observed in irradiated hcp-Zr, their cohabitation has been modelled. A system with both types of loop has been simulated and leads to results close to those obtained in the framework of isotropic elasticity: at high loop densities and large radii, the bias of interstitial loops can be higher than vacancy ones.

As the accelerated convergence algorithm described in section 2.6 has been extensively used in this chapter, the last section is focused on the validation of the technique. It has shown that the algorithm is effective for calculation of toroidal sinks or dislocations loops. Unlike the case of the straight dislocation with elasticity, no bump in the average PD site fraction has been obtained in accelerated simulations.

The present chapter showed the versatility of the PF method to model and simulated a wide range of microstructures: spherical and toroidal sinks, dislocation loops with isotropic and anisotropic elasticity, and cohabitation of different types of loops. To our knowledge, This work is the first one to propose a systematic study of dislocation loop sink efficiency in zirconium. Now that it has been validated, the method could then be extended to more complex systems, in particular with several sinks in the same domain.

Conclusion

In order to better understand the microstructural evolution of irradiated materials, numerical methods have been developed. During this PhD, a PF model is proposed to properly describe the creation of migrating point defects, their diffusion in the stress field of dislocations and their absorption by microstructural defects. The main advantages of the method is that it naturally takes into account complex contributions to the stress field: dislocation lines and loops can easily be simulated, whatever their type, shape, and in elastically isotropic or anisotropic crystals.

For 2D simulations, the model is accurate for straight dislocations, with or without elasticity. However, calculations showed that the effect of elasticity is underestimated by most analytical solutions in the literature. In addition, as we performed a systematic comparison between different models, we assessed that sink efficiency calculations should always consider Wiedersich boundary conditions. The rigorous validation of the proposed model allow us to be confident in the results obtained for more realistic systems: the straight dislocations in zirconium. The PF model allowed us to properly take into account recent findings from DFT calculations, and deduce larger scale conclusions from them. In particular, we have shown that the SAS promotes the growth of zirconium under irradiation, even without applied stress.

The PF model has been pushed further to 3D simulations. Again, validation has been performed on the case of spherical sinks. By means of a simple correction rule, it is possible to simulate a wide range of dislocation loops. Calculations without elasticity showed that the analytical solution available already underestimates sink efficiency of loops, in particular for high defect densities. Dislocation loops in elastically isotropic crystals have been performed and have assessed the interest of the PF model: the capacity to easily describe any kind of dislocation loop in any crystal. In order to make the best use of the method, the dislocation loops have been modelled in zirconium. Results have shown that conclusions that had been obtained for straight dislocations remained valid for loops. As a consequence, our theory of the SAS effect on zirconium growth has been validated for both straight dislocations and small loops.

The approach that has been carried out on zirconium could be easily adapted to other metals, as long as the necessary input is available: the dislocations Burgers vectors and habit planes, the crystal elastic constants and the PD Vegard tensors. The last ones constitute the hardest data to obtain, as recent atomic scale calculations are necessary. By generalising our approach to other metals, it would be possible to compare the SAS effect on other metals. In particular, with the

PD properties of magnesium, we would find out if the growth of basal interstitial loops is consistent with the SAS. In addition, the model could be applied to bcc iron in order to model the PWR nuclear vessel, or bcc tungsten for the fusion reactor divertor.

As the sink shape had to be accurately described, it has been necessary to consider a small numerical grid spacing, close to the atomic radius. Due to the finite difference algorithm used in this work, sink efficiency of low sink densities needed a large calculation domain, i.e. a high number of computational cells with constant grid spacing. As a consequence, it has been difficult to compute the sink efficiency of very low sink densities. In order to save time, we developed an accelerated convergence algorithm and made use of parallel programming. Even in those conditions, the calculation at lower sink density, or for systems with several sinks, in particular for loops, should be performed with a variable grid spacing. Indeed, except from the regions close to the sinks, the stress field and the diffusion do not need to be simulated using refined mesh. Using a variable grid spacing, it may be possible to compute the sink efficiency of dislocation loops with volumetric densities down to $10^{19}\,\mathrm{m}^{-3}$.

In this work, we have considered that the PD recombination has a negligible effect on the sink efficiency. This assumption should be investigated, using a modified version of the model. To this end, equation (2.22) can be adapted, by adding a source term proportional to the PD concentration.

In our work, the diffusion of PDs depended only on the elastic stress gradient, and independent of the uniformly applied stress. We could adapt the PF model to consider the migrating clusters, which are elastically strongly anisotropic [31, 59, 100]. In comparison with the PDs modelled in this work, clusters would have a strongly anisotropic diffusion tensor (almost 1D), and an anisotropic Vegard tensor, calculated from equation (2.2). The PF model could also be improved for systems with anisotropic dumbbells or clusters with several variants, such as bcc iron. Details are given in section A.2.

Then, the model could also be improved to take into account the saddle point configurations of the PD on its diffusion path by means of a diffusion coefficients tensor $D^*_{ij}(\mu^{\mathrm{sp}}_{\mathrm{el}}(\mathbf{b}))$ dependent on the saddle point configuration elastic potential $\mu^{\mathrm{sp}}_{\mathrm{el}}$.

Appendix A

Contents

A.1 Dislocation stress field validation

The stress fields due to the edge dislocation can be computed with the PF model. It is then possible to compare the obtained stress fields with the analytical solution for the edge dislocation in an isotropic crystal.

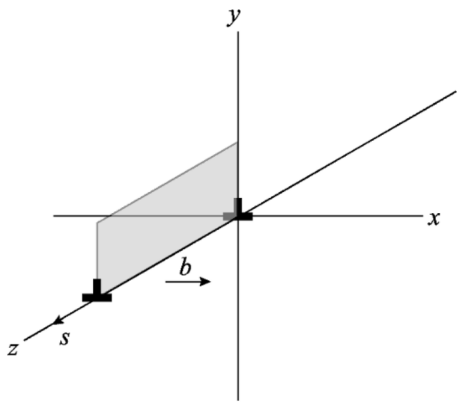

Figure A.1: Edge dislocation in a cartesian base, from [1].

$$\begin{cases} \sigma_{xx} = -\dfrac{\mu b}{2\pi(1-\nu)}\dfrac{y(3x^2+y^2)}{(x^2+y^2)^2} & \text{(A.1a)} \\ \sigma_{yy} = \dfrac{\mu b}{2\pi(1-\nu)}\dfrac{y(x^2-y^2)}{(x^2+y^2)^2} & \text{(A.1b)} \\ \sigma_{xy} = -\dfrac{\mu b}{2\pi(1-\nu)}\dfrac{x(x^2-y^2)}{(x^2+y^2)^2} & \text{(A.1c)} \\ \sigma_{zz} = \nu(\sigma_{xx}+\sigma_{yy}) = -\nu\dfrac{\mu b}{2\pi(1-\nu)}\dfrac{2y}{(x^2+y^2)} & \text{(A.1d)} \\ \sigma_{xz} = \sigma_{yz} = 0 & \text{(A.1e)} \end{cases}$$

with μ the shear modulus and ν the Poisson coefficient. The coordinates are those indicated in Fig. A.1. The system is described in Fig. A.2, and the physical values are given in Tab. 3.2. In this case, we have $N = 512$ and $a_0 = 0.3\,\mathrm{nm}$. The dislocation cores are located on $(256, 256)$ and $(256, 768)$.

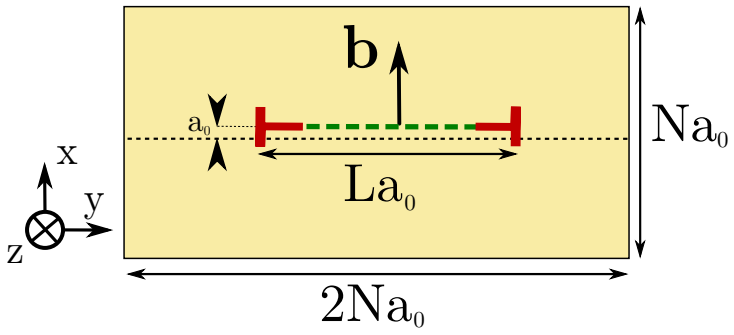

Figure A.2: System used for stress field validation. The black dashed line represents the direction of the profile for stress field plot.

The comparison between PF results and the analytical solution is given in Fig. A.3 to A.6. It can be seen that for any of those stress directions, the fit is very good, except near the dislocation core. Anyway, the analytical solution is not realistic in this region, as the stress values diverge close to the core.

A.2 Sink efficiency calculation with numerous variants

The PF model can be adapted to take into account the variant of a given PD or defect cluster. To this end, we may consider populations of each variant, that can rotate into other variants in order to minimise their energy. Technically, each variant n would be considered as an order parameter X_n. It is possible to add, in the kinetic equation (2.31), an exchange term in order to consider the capacity of the variant n to rotate into configuration m.

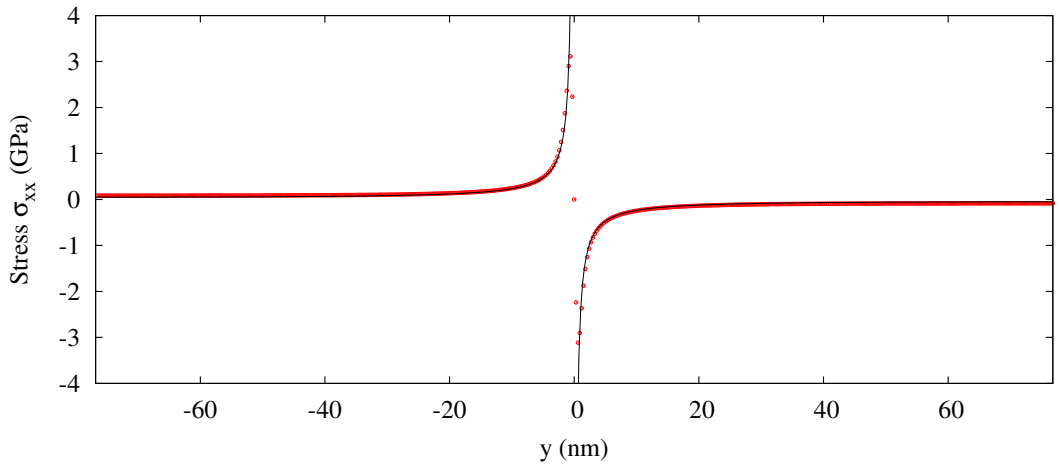

Figure A.3: Profile of the stress σ_{xx} along y at $x = 255$.

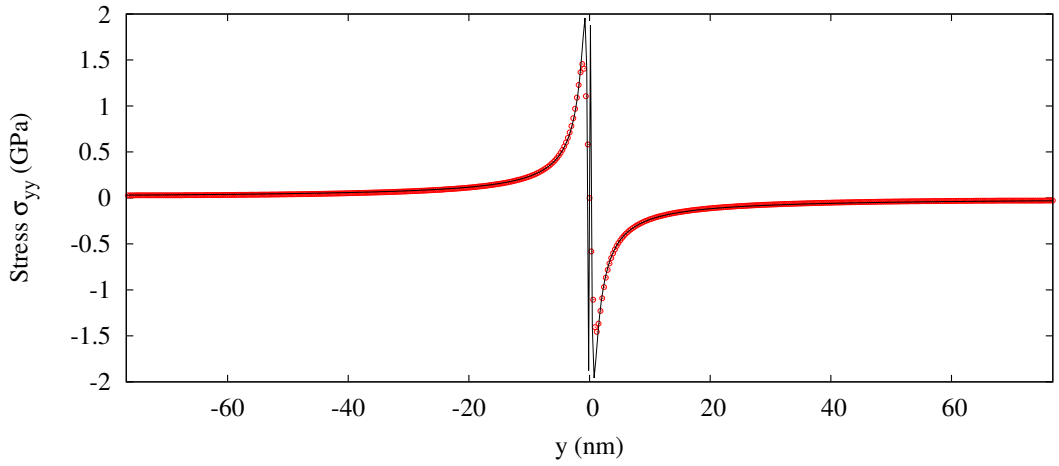

Figure A.4: Profile of the stress σ_{yy} along y at $x = 255$.

$$\left(\frac{\partial X_n}{\partial t}\right)_{\text{rot}} = \sum_{m \neq n} \left[-v_{n\to m} X_n(\mathbf{r}) + v_{m\to n} X_m(\mathbf{r})\right] \tag{A.2}$$

with :

$$v_{n\to m}(\mathbf{r}) = \nu_0 \exp\left\{-\frac{E_r + \frac{1}{2}\left[\mu_m^{\text{elas}}(\mathbf{r}) - \mu_n^{\text{elas}}(\mathbf{r})\right]}{k_B T}\right\} \tag{A.3}$$

where E_r is the rotation energy, ν_0 the attempt frequency of rotation.
The sink efficiency can be deduced as:

$$Z = \frac{K_0}{D\rho_s \sum_n (\bar{X}_n - X_n^s)} \tag{A.4}$$

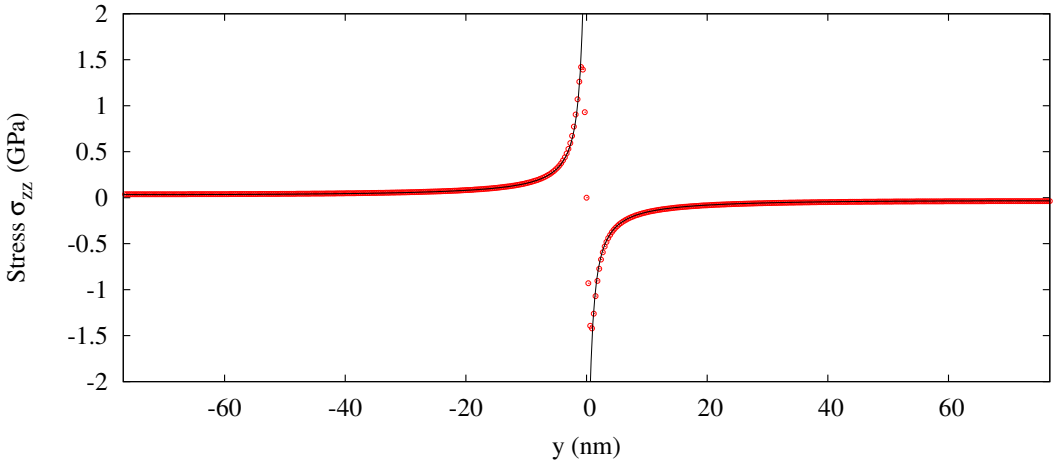

Figure A.5: Profile of the stress σ_{zz} along y at $x = 255$.

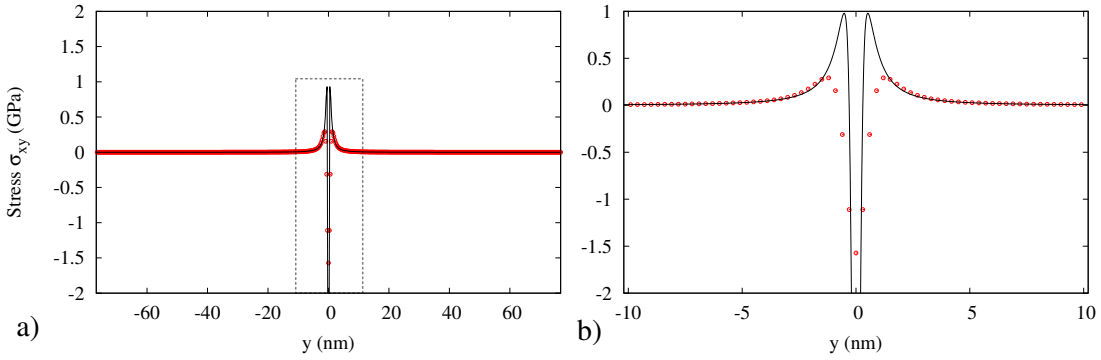

Figure A.6: Profile of the shear stress σ_{xy} along y at $x = 255$.

Bibliography

[1] Gary S. Was. *Fundamentals of Radiation Materials Science - Metals and alloys*. Springer, 2007.

[2] H. Ullmaier and W. Schilling. *Radiation damage in metallic reactor materials*. International Atomic Energy Agency, Vienna, 1980.

[3] C.H. Woo, A.A. Semenov, and B.N. Singh. Analysis of microstructural evolution driven by production bias. *Journal of Nuclear Materials*, 206(2-3):170–199, 1993.

[4] B.N. Singh, H. Trinkaus, and C.H. Woo. Production bias and cluster annihilation: Why necessary? *Journal of Nuclear Materials*, 212-215(PART 1):168–174, 1994.

[5] B.N. Singh and C.H. Woo. Consequences of intra-cascade clustering on defect accumulation and materials performance. *Radiation Effects and Defects in Solids*, 144(1-4):119–143, 1998.

[6] R.E. Stoller. *Primary radiation damage formation*, volume 1. 2012.

[7] F.R.N. Nabarro. *Theory of Crystal Dislocations*. Clarendon Press, Oxford, England, 1967.

[8] J.P. Hirth and J. Lothe. *Theory of Dislocations – Second edition*. Wiley-Interscience Publication, 1982.

[9] M. Griffiths. A review of microstructure evolution in zirconium alloys during irradiation. *J. Nucl. Mater.*, 159:190–218, 1988.

[10] A.D. Brailsford and R. Bullough. The rate theory of swelling due to void growth in irradiated metals. *Journal of Nuclear Materials*, 44(2):121 – 135, 1972.

[11] Michael P. Suhr, Jess B. Sturgeon, and Wilhelm G. Wolfer. Void nucleation, growth, and coalescence in irradiated metals. *J. Nucl. Mater.*, 378:86–97, 2008.

[12] S.I. Porollo, A.M. Dvoriashin, Y.V. Konobeev, and F.A. Garner. Microstructure and swelling of neutron irradiated nickel and binary nickel alloys. *Journal of Nuclear Materials*, 442(1-3 SUPPL.1):S809–S812, 2013.

[13] R. Schibli and R. Schäublin. On the formation of stacking fault tetrahedra in irradiated austenitic stainless steels - a literature review. *Journal of Nuclear Materials*, 442(1-3 SUPPL.1):S761–S767, 2013.

[14] G. Kresse and J. Furthmuller. *Phys. Rev. B*, 54:11169, 1996.

[15] J.-P. Crocombette and F. Willaime. 1.08 - ab initio electronic structure calculations for nuclear materials. In Rudy J.M. Konings, editor, *Comprehensive Nuclear Materials*, pages 223 – 248. Elsevier, Oxford, 2012.

[16] Petrica Gasca. *Zirconium – Modélisation ab initio de la diffusion des défauts ponctuels*. PhD thesis, Université Lille 1 – Sciences et technologies — École doctorale Sciences de la Matière, du Rayonnement et de l'Environnement, 2010.

[17] G. Vérité, C. Domain, Chu-Chun Fu, P. Gasca, A. Legris, and F. Willaime. Self-interstitial defects in hexagonal close packed metals revisited: Evidence for low-symmetry configurations in ti, zr, and hf. *Phys. Rev. B*, 87:134108, Apr 2013.

[18] Céline Varvenne, Fabien Bruneval, Mihai-Cosmin Marinica, and Emmanuel Clouet. Point defect modeling in materials: Coupling ab initio and elasticity approaches. *Phys. Rev. B*, 88:134102, 2013.

[19] Roger E. Stoller. Molecular dynamics simulations of high energy cascades in iron. volume 373, pages 21–26, 1995.

[20] Roger E. Stoller and Lawrence R. Greenwood. From molecular dynamics to kinetic rate theory: a simple example of multiscale modeling. volume 538, pages 203–210, 1999.

[21] L. Malerba. Molecular dynamics simulation of displacement cascades in α-fe: A critical review. *Journal of Nuclear Materials*, 351(1-3):28–38, 2006.

[22] D. Terentyev, C. Lagerstedt, P. Olsson, K. Nordlund, J. Wallenius, C.S. Becquart, and L. Malerba. Effect of the interatomic potential on the features of displacement cascades in α-fe: A molecular dynamics study. *Journal of Nuclear Materials*, 351(1-3):65–77, 2006.

[23] L. Malerba, C. S. Becquart, and C. Domain. Object kinetic monte carlo study of sink strengths. *J. Nucl. Mater.*, 360:159–169, 2007.

[24] Ville Jansson. *Radiation-induced nanostructure evolution models for Fe alloys*. PhD thesis, University of Helsinki, 2013.

[25] Zhongwen Chang, Par Olsson, Dmitry Terentyev, and Nils Sandberg. Dislocation bias factors in fcc copper derived from atomistic calculations. *Journal of Nuclear Materials*, 441:357–363, 2013.

[26] A.B. Sivak, V.M. Chernov, V.A. Romanov, and P.A. Sivak. Kinetic monte-carlo simulation of self-point defect diffusion in dislocation elastic fields in bcc iron and vanadium. *Journal of Nuclear Materials*, 417(1-3):1067–1070, 2011.

[27] R.G.A. Veiga, M. Perez, C.S. Becquart, E. Clouet, and C. Domain. Comparison of atomistic and elasticity approaches for carbon diffusion near line defects in α-iron. *Acta Materialia*, 59(18):6963–6974, 2011.

[28] F.A. Nichols. On the estimation of sink-absorption terms in reaction-rate-theory analysis of radiation damage. *J. Nucl. Mater.*, 75:32–41, 1978.

[29] T. Okita and W.G. Wolfer. A critical test of the classical rate theory for void swelling. *Journal of Nuclear Materials*, 327(2-3):130–139, 2004.

[30] F. Christien and A. Barbu. Cluster dynamics modelling of irradiation of zirconium single crystals. *J. Nucl. Mater.*, 393:153–161, 2009.

[31] S. I. Golubov, A. V. Barashev, and R. E. Stoller. Radiation damage theory. In Rudy J.M. Konings, editor, *Comprehensive Nuclear Materials, vol. 1*, pages 357–391. Elsevier, Oxford, 2012.

[32] I.G. Margvelashvili and Z.K. Saralidze. *Fiz. Tverd. Tela.*, 15:2665, 1973.

[33] H. Rauh and D. Simon. *Phys.Sta.Sol.*, 46:499, 1978.

[34] F.S. Ham. *Journal of Applied Physics*, 30:915, 1959.

[35] W. G. Wolfer and M. Ashkin. Diffusion of vacancies and interstitials to edge dislocations. *J. Appl. Phys.*, 47:791, 1976.

[36] A.B Sivak, V.A Romanov, and V.M Chernov. Influence of stress fields of dislocations on formation and spatial stability of point defects (elastic dipoles) in v and fe crystals. *Journal of Nuclear Materials*, 323(2-3):380 – 387, 2003.

[37] V.I. Dubinko, A.S. Abyzov, and A.A. Turkin. Numerical evaluation of the dislocation loop bias. *J. Nucl. Mater.*, 336:11–21, 2005.

[38] C. N. Tomé, H. A. Cecatto, and E. J. Savino. Point-defect diffusion in a strained crystal. *Phys. Rev. B*, 25(12):7428–7440, 1982.

[39] B.C. Skinner and C.H. Woo. Shape effect in the drift diffusion of point defects into straight dislocations. *Physical Review B*, 30(6):3084–3097, 1984.

[40] Dariush Seif and Nasr M. Ghoniem. Effect of anisotropy, {SIA} orientation, and one-dimensional migration mechanisms on dislocation bias calculations in metals. *Journal of Nuclear Materials*, 442(1-3):S633 – S638, 2013.

[41] N.Smetniansky-De Grande, A. Sarce, E.J. Savino, and C.N. Tome. Sink strengths for hcp magnesium. *Journal of Nuclear Materials*, 159(0):379 – 385, 1988.

[42] V. Jansson, L. Malerba, A. De Backer, C.S. Becquart, and C. Domain. Sink strength calculations of dislocations and loops using okmc. *Journal of Nuclear Materials*, 442(1-3):218–226, 2013.

[43] A.B. Sivak, V.M. Chernov, N.A. Dubasova, and V.A. Romanov. Anisotropy migration of self-point defects in dislocation stress fields in {BCC} fe and {FCC} cu. *Journal of Nuclear Materials*, 367-370, Part A:316–321, 2007.

[44] A.B. Sivak, V.A. Romanov, and V.M. Chernov. Diffusion of self-point defects in body-centered cubic iron crystal containing dislocations. *Crystallography Reports*, 55(1):97–108, 2010.

[45] A.B. Sivak and P.A. Sivak. Efficiency of dislocations as sinks of radiation defects in fcc copper crystal. *Crystallography Reports*, 59(3):407–414, 2014.

[46] A. Seeger and U. Gösele. Steady-state diffusion of point defects to dislocation loops. *Physics Letters A*, 61(6):423–425, 1977.

[47] R. Bullough, M.R. Hayns, and C.H. Woo. The sink strength of dislocation loops and their growth in irradiated materials. *Journal of Nuclear Materials*, 84(1-2):93–100, 1979.

[48] W. G. Wolfer and M. Ashkin. Stress-induced diffusion of point defects to spherical sinks. *Journal of Applied Physics*, 46:547–557, 1975.

[49] C.H. Woo and U. Gösele. Dislocation bias in an anisotropic diffusive medium and irradiation growth. *J. Nucl. Mater.*, 119:219–228, 1983.

[50] C.H. Woo. Theory of irradiation deformation in non-cubic metals: effect of anisotropic diffusion. *J. Nucl. Mater.*, 159:237–256, 1988.

[51] C.H. Woo, B.N. Singh, and H. Heinisch. A diffusion approach to modelling of irradiation-induced cascades. *Journal of Nuclear Materials*, 174(2-3):190–195, 1990.

[52] C.H. Woo, B.N. Singh, and F.A. Garner. Production bias: a proposed modification of the driving force for void swelling under cascade damage conditions. *Journal of Nuclear Materials*, 191-194(PART B):1224–1228, 1992.

[53] H. Trinkaus, V. Naundorf, B.N. Singh, and C.H. Woo. On the experimental determination of the migrating defect fraction under cascade damage conditions. *Journal of Nuclear Materials*, 210(3):244–253, 1994.

[54] C.H. Woo, B.N. Singh, and A.A. Semenov. Recent advances in the understanding of damage production and its consequences on void swelling, irradiation creep and growth. *Journal of Nuclear Materials*, 239(1-3):7–23, 1996.

[55] H. Trinkaus, B.N. Singh, and A.J.E. Foreman. Glide of interstitial loops produced under cascade damage conditions: Possible effects on void formation. *Journal of Nuclear Materials*, 199(1):1–5, 1992.

[56] B.A. Loomis, S.B. Gerber, and A. Taylor. Void ordering in ion-irradiated nb and nb-1% zr. *Journal of Nuclear Materials*, 68(1):19–31, 1977.

[57] M.a Griffiths, C.D.b Cann, and R.C.b Styles. Neutron irradiation damage in 64% cold-worked titanium. *Journal of Nuclear Materials*, 149(2):200–211, 1987.

[58] W. Jäger and H. Trinkaus. Defect ordering in metals under irradiation. *Journal of Nuclear Materials*, 205(C):394–410, 1993.

[59] M. Kiritani. Similarity and difference between fcc, bcc and hcp metals from the view point of point defect cluster formation. *Journal of Nuclear Materials*, 276(1):41–49, 2000.

[60] C.H. Woo. Defect accumulation behaviour in hcp metals and alloys. *J. Nucl. Mater.*, 276:90–103, 2000.

[61] V.I. Dubinko and A.A. Turkin. Self-organization of cavities under irradiation. *Applied Physics A: Solids and Surfaces*, 58(1):21–34, 1994.

[62] V.I.a Dubinko, A.G.a Guglya, and S.E.b Donnelly. Radiation-induced formation, annealing and ordering of voids in crystals: Theory and experiment. *Nuclear Instruments and Methods in Physics Research, Section B: Beam Interactions with Materials and Atoms*, 269(14):1634–1639, 2011.

[63] J. H. Evans. Simulations of the effects of 1-d interstitial diffusion on void lattice formation during irradiation. *Philosophical Magazine*, 85(11):1177–1190, 2005.

[64] H.L. Heinisch and B.N. Singh. Kinetic monte carlo simulations of void lattice formation during irradiation. *Philosophical Magazine*, 83(31-34):3661–3676, 2003.

[65] M. Griffiths. Evolution of microstructure in hcp metals during irradiation. *Journal of Nuclear Materials*, 205(C):225–241, 1993.

[66] A. Hardouin Duparc, C. Moingeon, N. Smetniansky-De-Grande, and A. Barbu. Microstructure modelling of ferritic alloys under high flux 1 mev electron irradiations. *Journal of Nuclear Materials*, 302(2-3):143–155, 2002.

[67] John W. Cahn and John E. Hilliard. Free energy of a nonuniform system. i. interfacial free energy. *Journal of Chemical Physics*, 28(2):258–267, february 1958.

[68] Samuel M. Allen and John W. Cahn. Ground state structures in ordered binary alloys with second neighbor interactions. *Acta Metallurgica*, 20(3):423–433, 1972.

[69] D. Rodney, Y. Le Bouar, and A. Finel. Phase field methods and dislocations. *Acta Materialia*, 51:17–30, 2003.

[70] Y. U. Wang, Y. M. Jin, A. M. Cuitiño, and A.G. Khachaturyan. Nanoscale phase field microelasticity theory of dislocations: Model and 3d simulations. *Acta Materialia*, 49:1847–1857, 2001.

[71] F.R.N. Nabarro. *Philos. Mag.*, 42:1224, 1951.

[72] A.G. Khachaturyan. *Theory of Structural Transformations in Solids*. Wiley, 1983.

[73] Yulan Li, Shenyang Hu, Charles H. Henager, Huiqiu Deng, Fei Gao, Xin Sun, and Moe A. Khaleel. Computer simulations of interstitial loop growth kinetics in irradiated bcc fe. *J. Nucl. Mater.*, 427:259–267, 2012.

[74] Shenyang Hu, Charles H. Henager, Yulan Li, Fei Gao, Xin Sun, and Moe A. Khaleel. Evolution kinetics of interstitial loops in irradiated materials: a phase-field model. *Modelling and Simulation in Materials Science and engineering*, 20, december 2012.

[75] Paul C. Millett and Michael Tonks. Application of phase-field modeling to irradiation effects in materials. *Current Opinion in Solid State and Materials Science*, 15:125–133, 2011.

[76] Paul C. Millett, Anter El-Azab, Srujan Rokkam, Michael Tonks, and Dieter Wolf. Phase-field simulation of irradiated metals ; part i: Void kinetics. *Computational Materials Science*, 50:949–959, 2011.

[77] Srujan Rokkam, Anter El-Azab, Paul Millet, and Dieter Wolf. Phase field modeling of void nucleation and growth in irradiated metals. *Modelling and simulation in materials science and engineering*, 17, 2009.

[78] Paul C. Millett, Anter El-Azab, and Dieter Wolf. Phase-field simulation of irradiated metals ; part ii: Gas bubble kinetics. *Computational Materials Science*, 50:960–970, 2011.

[79] Paul C. Millett and Michael Tonks. Phase-field simulations of gas density within bubbles in metals under irradiation. *Computational Materials Science*, 50:2044–2050, 2011.

[80] Paul C. Millett, Michael Tonks, S.B. Biner, Liangzhe Zhang, K. Chockalingam, Liangzhe Zhang, and Yongfeng Zhang. Phase-field simulation of intergranular bubble growth and percolation in bicrystals. *J. Nucl. Mater.*, 2011.

[81] K. Chockalingam, P.C. Millett, and M.R. Tonks. Effects of intergranular gas bubbles on thermal conductivity. *Journal of Nuclear Materials*, 430(1-3):166–170, 2012.

[82] P.C. Millett, D. Wolf, T. Desai, S. Rokkam, and A. El-Azab. Phase-field simulation of thermal conductivity in porous polycrystalline microstructures. *Journal of Applied Physics*, 104(3), 2008.

[83] P.C. Millett and M. Tonks. Meso-scale modeling of the influence of intergranular gas bubbles on effective thermal conductivity. *Journal of Nuclear Materials*, 412(3):281–286, 2011.

[84] Pierre-Antoine Geslin. *Contribution à la modélisation champ de phase des dislocations*. PhD thesis, Université Pierre et Marie Curie, 2013.

[85] P.-A. Geslin, B. Appolaire, and A. Finel. A phase field model for dislocation climb. *Applied Physics Letters*, 104(1), 2014.

[86] S. Y. Hu and L. Q. Chen. Solute segregation and coherent nucleation and growth near a dislocation – a phase-field model integrating defect and phase microstructures. *Acta Materialia*, 49:463–472, 2001.

[87] K. Linga Murty and Indrajit Charit. Texture development and anisotropic deformation of zircaloys. *Progress in Nuclear Energy*, 48(4):325 – 359, 2006.

[88] V. Fidleris. The irradiation creep and growth phenomena. *Journal of Nuclear Materials*, 159(C):22–42, 1988.

[89] A. Jostsons, P.M. Kelly, and R.G. Blake. The nature of dislocation loops in neutron irradiated zirconium. *Journal of Nuclear Materials*, 66(3):236–256, 1977.

[90] A. Rogerson. Irradiation growth in zirconium and its alloys. *Journal of Nuclear Materials*, 159(C):43–61, 1988.

[91] M. Griffiths, D. Faulkner, and R.C. Styles. Neutron damage in α-titanium. *Journal of Nuclear Materials*, 119(2-3):189–207, 1983.

[92] M. Griffiths, M.H. Loretto, and R.E. Smallmann. Electron damage in zirconium - i. defect structure and loop character. *J. Nucl. Mater.*, 115:313–322, 1983.

[93] M. Griffiths, M.H. Loretto, and R.E. Smallman. Electron damage in zirconium. ii. nucleation and growth of c-component loops. *Journal of Nuclear Materials*, 115(2-3):323–330, 1983.

[94] S.I. Choi and J.H. Kim. Radiation-induced dislocation and growth behavior of zirconium and zirconium alloys – a review. *Nuclear engineering and technology*, 45(3):385, June 2013.

[95] L. Tournadre, F. Onimus, J.-L. Béchade, D. Gilbon, J.-M. Cloué, J.-P. Mardon, and X. Feaugas. Toward a better understanding of the hydrogen impact on the radiation induced growth of zirconium alloys. *Journal of Nuclear Materials*, 441(1-3):222–231, 2013.

[96] L. Tournadre, F. Onimus, J.-L. Béchade, D. Gilbon, J.-M. Cloué, J.-P. Mardon, X. Feaugas, O. Toader, and C. Bachelet. Experimental study of the nucleation and growth of c-component loops under charged particle irradiations of recrystallized zircaloy-4. *Journal of Nuclear Materials*, 425(1-3):76–82, 2012.

[97] A. Risbet and V. Levy. Ordre de cavites dans le magnesium et l'aluminium irradies aux neutrons rapides. *Journal of Nuclear Materials*, 50(1):116–118, 1974.

[98] R.H. Zee, G.J.C. Carpenter, A. Rogerson, and J.F. Watters. Irradiation growth in deformed zirconium. *Journal of Nuclear Materials*, 150(3):319–330, 1987.

[99] G.J.C. Carpenter, R.H. Zee, and A. Rogerson. Irradiation growth of zirconium single crystals: A review. *Journal of Nuclear Materials*, 159(C):86–100, 1988.

[100] Stanislav Golubov, Roger Stoller, Alexander Barashev, and Bachu Singh. Breakthrough in understanding radiation growth of zirconium. 17th International Symposium on Zirconium in the Nuclear Industry, Hyderabad, India (oral presentation), 3-7 February 2013.

[101] Haohua Wen and C.H. Woo. Temperature dependence and anisotropy of self- and mono-vacancy diffusion in α-zr. *J. Nucl. Mater.*, 159:237–256, 1988.

[102] C.H. Woo and X. Liu. Atomistic calculation of point-defect diffusion anisotropy and irradiation growth in alpha-zirconium. *Philos. Mag.*, 87:2355, 2007.

[103] Guillaume Vérité. *Structure, stabilité et mobilité des défauts ponctuels dans le zirconium hexagonal compact : étude ab initio*. PhD thesis, Université Pierre et Marie Curie – Paris, 2007.

[104] G. Vérité, F. Willaime, and Chu Chun Fu. Anisotropy of the vacancy migration in ti, zr and hf hexagonal close-packed metals from first principles. *Solid State Phenomena*, 129:75–81, 2007.

[105] G.D. Samolyuk, A.V. Barashev, S.I. Golubov, Y.N. Osetsky, and R.E. Stoller. Analysis of the anisotropy of point defect diffusion in hcp zr. *Acta Materialia*, 78:173–180, 2014.

[106] G.M. Hood, H. Zou, D. Gupta, and R.J. Schultz. *J. Nucl. Mater.*, 223:122, 1995.

[107] G.M. Hood, H. Zou, R.J. Schultz, N. Matsuura, J.A. Roy, and J.A. Jackman. *Defect Diffusion Forum*, 49:143, 1997.

[108] Y.N. Osetsky, D.J. Bacon, and N. de Diego. Anisotropy of point defect diffusion in alpha-zirconium. *Metallurgical and Materials Transactions A*, 33A:777–782, 2002.

[109] N. de Diego, Yu. N. Osetsky, and D. J. Bacon. Structure and properties of vacancy and interstitial clusters in α-zirconium. *Jour. Nucl. Mater.*, 374:87–94, 2008.

[110] G.D. Samolyuk, S.I. Golubov, Y.N. Osetsky, and R.E. Stoller. Self-interstitial configurations in hcp zr: a first principles analysis. *Philos. Mag. Lett.*, 93(2):93–100, 2013.

[111] S. J. Wooding, L. M. Howe, F. Gao, A. F. Calder, and D. J. Bacon. A molecular dynamics study of high-energy displacement cascades in α-zirconium. *J. Nucl. Mater.*, 254:191–204, 1998.

[112] N. de Diego, Yu. N. Osetsky, and D. J. Bacon. Structure and properties of vacancy and interstitial clusters in α-zirconium. *J. Nucl. Mater.*, 374:87–94, 2008.

[113] P.H. Dederichs, C. Lehmann, H.R. Schober, A. Scholz, and R. Zeller. Lattice theory of point defects. *J. Nucl. Mater.*, 69-70:176–199, 1978.

[114] W.G. Wolfer. 1.01 - fundamental properties of defects in metals. In Rudy J.M. Konings, editor, *Comprehensive Nuclear Materials*, pages 1–45. Elsevier, Oxford, 2012.

[115] Dan Mordehai and Georges Martin. Enhanced annealing of the dislocation network under irradiation. *Phys. Rev. B*, 84:014115, 2011.

[116] V.M. Chernov, D.A. Chulkin, and A.B. Sivak. Interaction of intrinsic point defects with dislocation stress fields in hcp zirconium crystal. *Crystallography Reports*, 55(1):83–96, 2010.

[117] M.W. Finnis and J.E. Sinclair. Simple empirical n-body potential for transition metals. *Philosophical Magazine A: Physics of Condensed Matter, Structure, Defects and Mechanical Properties*, 50(1):45–55, 1984.

[118] Qing Peng, Wei Ji, Hanchen Huang, and Suvranu De. Stability of self-interstitials atoms in hcp-zr. *J. Nucl. Mater.*, 429:233–236, June 2012.

[119] F. Willaime. *Ab initio* study of self-interstitials in hcp-zr. *J. Nucl. Mater.*, 323:205–212, 2003.

[120] C. Domain and A. Legris. *Ab initio* atomic-scale determination of point-defect structure in hcp zirconium. *Philos. Mag.*, 85(4-7):569–575, 2005.

[121] G. Kresse and J. Furthmuller. *Comput. Mater. Sci.*, 6:15, 1996.

[122] G. Kresse and D. Joubert. From ultrasoft pseudopotentials to the projector augmented-wave method. *Phys. Rev. B*, 59:1758–1775, Jan 1999.

[123] John P. Perdew, J. A. Chevary, S. H. Vosko, Koblar A. Jackson, Mark R. Pederson, D. J. Singh, and Carlos Fiolhais. Atoms, molecules, solids, and surfaces: Applications of the generalized gradient approximation for exchange and correlation. *Phys. Rev. B*, 46:6671–6687, Sep 1992.

[124] John P. Perdew, Kieron Burke, and Matthias Ernzerhof. Generalized gradient approximation made simple. *Phys. Rev. Lett.*, 77:3865–3868, Oct 1996.

[125] Chris G. Van de Walle and Anderson Janotti. Advances in electronic structure methods for defects and impurities in solids. *physica status solidi (B)*, 248(1):19–27, 2011.

[126] M. Methfessel and A. T. Paxton. High-precision sampling for brillouin-zone integration in metals. *Phys. Rev. B*, 40:3616–3621, Aug 1989.

[127] Jean Salençon. *Mécanique des milieux continus, Tome 1 : Concepts généraux*. Ellipses, 2005.

[128] P. Ehrhart and B. Schönfeld. Self-interstitial-atoms and their agglomerates in hcp metals. In Kiritani M. Tokamura I., Doyama M., editor, *Point Defects and Defects Interactions in Metals*. University of Tokyo Press, 1982.

[129] G. Simmons and H. Wang. *Single crystal elastic constants and calculated aggregate properties: a handbook*. Cambridge (MA): MIT Press, 1971.

[130] J. M. Soler, E. Artacho, J. D. Gale, A. Garcia, J. Junquera, P. Ordejon, and D. Sanchez-Portal. *J. Phys. Condens. Mater.*, 14:2745, 2002.

[131] F. Onimus and J. L. Béchade. Radiation effects in zirconium alloys. In Rudy J.M. Konings, editor, *Comprehensive Nuclear Materials, vol. 4*, pages 1–31. Elsevier, 2012.

[132] Guillaume Boussinot, Yann Le Bouar, and Alphonse Finel. Phase-field simulations with inhomogeneous elasticity: Comparison with an atomic-scale method and application to superalloys. *Acta Materialia*, 58(12):4170 – 4181, 2010.

[133] L. Thuinet, A. Debacker, and A. Legris. Phase-field modeling of precipitates evolution dynamics in elastically inhomogeneous low-symmetry systems: application to hydride precipitation in zr. *Acta Materialia*, 60:5311–5321, 2012.

[134] Ludovic Thuinet, Alexandre Legris, Lingfei Zhang, and Antoine Ambard. Mesoscale modeling of coherent zirconium hydride precipitation under an applied stress. *J. Nucl. Mater.*, 438:32–40, 2013.

[135] X. Yi, M.L. Jenkins, M. Briceno, S.G. Roberts, Z. Zhou, and M.A. Kirk. In situ study of self-ion irradiation damage in w and w-5re at 500 c. *Phil. Mag.*, 93(14):1715–1738, 2013.

[136] R.A. Holt. Microstructure dependence of irradiation creep and growth of zirconium alloys. *Journal of Nuclear Materials*, 90(1-3):193–204, 1980.

[137] Léa Tournadre. *Vers une meilleure compréhension des mécanismes de déformation par croissance libre sous irradiation des alliages de zirconium*. PhD thesis, Université de La Rochelle, 2012.

[138] S.J. Zinkle and B.N. Singh. Microstructure of neutron-irradiated iron before and after tensile deformation. *Journal of Nuclear Materials*, 351(1-3):269 – 284, 2006.